Title

Field shift fractionations in novel isotope systems

Permalink

https://escholarship.org/uc/item/99t1j03g

Author

Sedlak, Alexander

Publication Date

2024

UNIVERSITY OF CALIFORNIA

Los Angeles

Field shift fractionations in novel isotope systems

A dissertation submitted in partial satisfaction of the requirements for the degree Doctor of Philosophy in Geochemistry

by

Alexander Paul Woodward Sedlak

2024

ABSTRACT OF THE DISSERTATION

Field shift fractionations in novel isotope systems

by

Alexander Paul Woodward Sedlak

Doctor of Philosophy in Geochemistry

University of California, Los Angeles, 2024

Professor Edwin Arthur Schauble, Chair

Measurements of isotope fractionation have long focused on mass dependent fractionations, though mass independent effects have long been recognized. One mechanism of mass independent fractionation is the nuclear field shift. Field shift isotope fractionation was first proposed by Bigeleisen (1996) and Nomura et al. (1996) as a mechanism explain to patterns of redox-driven uranium isotope fractionation. This thesis aims to model the nuclear field shift using *ab initio* methods in multiple isotope systems, in relevant natural species, as well as to explore potential applications of field shift fractionation measurements for these systems. The main method used is the DFT-PAW method of Schauble (2013), which makes it possible to determine field shifts in solids and complex aqueous species.

In the uranium isotope system, $^{238}U/^{235}U$ is predicted to be ~1-2‰ higher in U(IV) than coexisting U(VI) species at 25ºC. U(V) species are either intermediate or similar to U(IV) species. Fractionations of up to 0.6‰ are predicted between species in the same oxidation state.

In the case of plutonium and neptunium, Pu(V) and Pu(IV) species thought to be relevant to natural systems are found to be isotopically similar to each other, whereas Pu(VI) species will be approximately 2‰ lower in ^{242}Pu/^{239}Pu than Pu(V) or Pu(IV), and Pu(III) species will have approximately 3‰ higher ^{242}Pu/^{239}Pu than Pu(IV) or Pu(V). Np(VI) will be 0.6‰ lower in ^{237}Np/^{235}Np than coexisting Np(V) species, whereas Np(IV) and Np(III) will have approximately 1.3‰ higher ^{237}Np/^{235}Np. In the final study, field shift effects in platinum and iridium are studied, using Mössbauer isomer shifts according to the method of Schauble (2023) in to investigate iridium. Predicted field shifts for both ^{198}Pt/^{194}Pt and ^{193}Ir/^{191}Ir are relatively modest, approximately $\leq$0.1‰ at ambient temperatures for most species (e.g., mass dependent fractionation effects likely dominate for these elements at low temperatures). Notably, Pt in an Fe-alloy (as a possible analog for the Earth's core) is predicted to show an equilibrium fractionation of 0.09‰ at 3000 K relative to Pt^{II} substituted in an olivine crystal structure (as a speculative analog for the silicate mantle), which could explain observed superchondritic ^{198}Pt/^{194}Pt found in Archean mantle samples.

The dissertation of Alexander Paul Woodward Sedlak is approved

Peng Ni

Lars P. Stixrude

Edward Donald Young

Edwin Arthur Schauble, Committee Chair

University of California, Los Angeles

2024

Dedication:

To my mother who fostered a lifelong curiosity in me and who always ensured her children would have every possible opportunity.

Table of Contents

List of Figures

List of Tables

Acknowledgments

I must first start by thanking the people most responsible for directly aiding me in the completion of this dissertation. My advisor Edwin Schauble is the most brilliant scientist I have ever met, and I've met a great number of them over the course of my studies. I know it hasn't always been easy guiding me along to figure some of the complexities of this project out, and I could not be more grateful for your patience. Thank you as well to my committee members Lars Stixrude, Ed Young, and Peng Ni. Your insights into the writing of this manuscript, and especially in understanding the complexities of the PGEs, has been invaluable. I would also like to thank the other professors at UCLA who have aided me along the way. Craig Manning helped me to better understand igneous petrology, magma oceans, and all manner of topics through his reading groups. Tina Treude helped me to become a better geochemist and to understand redox chemistry more effectively through her course. I didn't do a whole lot of biology while I was here, but Dave Jacobs' course is one of my all-time favorites. In the Chemistry department, Richard Kaner taught my Inorganic Chemistry class that was so unbelievably helpful in my work. I would also like to thank the professors for whom I taught, for making life as a TA just a little bit easier. Finally amongst my teachers over the years I would like to thank my advisor from when I was at CSULB, Richard Behl, and my sedimentology professor from Arizona State University, L. Paul Knauth. It is through learning from these two that I finally began to go from liking the science of geology to loving it.

Of course, it isn't just professors who help you along the way during your studies. The staff at UCLA has been amazing. I would like to thank Lauri Holbrook for all her help along the way while she was here, as well as everyone else in the department. My fellow students have also been absolutely vital to my survival during this (far too long) journey. I would first like to thank Mojhgan, for being the most supportive person I know but also occasionally asking me "Why aren't you done yet?" to put a fire under me. I would also like to thank Sebastian Krause, Jeff Osterhaut, Rob Ulrich, and David Yousavitch for those years doing Biogeocheminar. Those were great times that did a ton for my appreciation of science and I know you will all do great in your careers. I would also like to thank my office mate over the past few years Yang Li. Thank you for all of the conversation, the help with coding, and these last few months of attempting to work out what we do next with our degrees.

Finally I would like to thank my friends and family. To all my longtime friends from ASU, CSULB, FVHS, and my summer job at Camp James, thank all of you for always believing in me and what I could accomplish. I've been blessed to have friends who were not shy about telling me these things. To my best friend Harry who I have known for quite literally as long as I can remember, thank you for always keeping me grounded and teaching me to simply relax and enjoy life every now and then. To my girlfriend Victoria, thank you for all the patience as I've tried frantically to finish this whole thing up so we can move on with our future together. You were my rock and I could not have done this without you. I love you and I can't wait to see what our future together holds. And finally to my family: none of this would have been possible without your help, it really was a collaborative effort. I would first like to thank my dearly departed abuelita. In times of need I often feel better by simply remembering how much you loved me. I miss you dearly every day. To my brother Joseph and my sister Diana, you may not have realized it, but because you always treated me as a peer and didn't talk down to me just because I was so much younger, I always pushed myself just a little bit harder to reach your level. To my father Robert, thank you for aiding me in everything that has ever come up outside of school, from moving to car issues to taxes, you always make life easier. I want you to know just how much you help and how much I appreciate it. And to my mother Maria and my niece Zinnia, I dedicate this dissertation to you. Mom, you passed your boundless curiosity about the world down to me, and it’s the most wonderful gift any son could have asked for. It’s no accident how many degrees your children have. Zinnia, when you are old enough to read this, I hope you take it as a sign that you are capable of incredible things if you are willing to put in the work. You have a tío who loves you very much and will always be there for you.

Vita

Alexander Paul Woodward Sedlak

Education

- University of California, Los Angeles
    - PhD candidate in Geochemistry
    - Master of Science in Geochemistry
- California State University, Long Beach
    - Master of Science in Geology
- Arizona State University
    - Bachelor of Science in Geology
    - Minors in Chemistry, Mathematics, and Geography

Presentations

- UCLA Geochemistry department seminar (2023)
- UCLA Geochemistry department seminar (2022)
- Goldschmidt poster (2019)
- American Geophysical Union poster (2018)
- Monterey and Related Sediments Project presentation (2016, 2017)
- American Association of Petroleum Geologists presentation (2016)
- American Association of Petroleum Geologists poster (2015)

Teaching

- Igneous Petrology (2022, 2023)
- Mineralogy (2020, 2021, 2022)
- Sedimentary Petrology (2018)
- Paleontology (2019)
- Earth and Evolutionary History (2020)
- Major Events in the History of Life (2021)
- Oceanography (2016, 2017, 2018, 2019)

Awards

- 2nd place (Pacific Division) – Imperial Barrel Award
- Johnson-Conrey Fellowship (2014)
- National Hispanic Scholar (2010)

Chapter 1

Introduction to isotope fractionation, ab initio methods, and dissertation

1. Introduction

The theory of stable isotope chemistry began with a few early studies (Lindemann and Aston, 1919; Lindemann, 1919; Urey and Greiff, 1935), with Harold Urey's discovery of deuterium being arguably the most significant. Measurements were eventually made of variations in the abundances of oxygen, carbon, nitrogen, and sulfur isotopes as well. H, C, N, O, and S are typically referred to as the "traditional" stable isotope systems. At equilibrium, each of these isotope systems displays abundance variations controlled mainly by mass dependent fractionation, the theory of which was developed extensively in seminal works including those of Urey (1947) and Bigeleisen and Mayer (1947). These early-studied elements each display large mass differences between their stable (non-radioactive and non-radiogenic) isotopes, which results in larger, more easily detected fractionations. They could also be quantitatively purified and processed into vapor-phase molecules in the laboratory. This enabled analysis with gas source isotope ratio mass spectrometers (IRMS), which were the main high precision instruments for measuring isotope abundance variations for most of the 20th century. With the advent of multi-collector inductively coupled plasma mass spectrometry (MC-ICP-MS) in the 1980s and 1990s, however, new isotope systems became possible to analyze (Date and Gray, 1988; Houk and Thompson, 1988; Jarvis et al., 1992; Koppenaal, 1992; Halliday et al., 1995). Motivated by this new technology, improving computer power, and software advances, *ab initio* electronic structure methods using computational chemistry software have been increasingly used to guide geochemists as to what might be expected in all of these new, "nontraditional" stable isotope systems.

Theoretical studies of isotope fractionation precede the development of modern computing. Lindemann (1919) performed the first theoretical calculations of isotope fractionation in the lead system. Urey and Greiff (1935), Urey (1947), and Bigeleisen and Mayer (1947) also performed theoretical calculations of isotope fractionation. These theoretical calculations derive from a simplified thermodynamic model of the quantum mechanics of molecular vibration and rotation. Later techniques for estimating isotope fractionations involved the use of force field and quantum mechanical methods (Kotaka and Kakihana, 1977; Kotaka et al., 1978; Hanschmann, 1984). *Ab initio* methods make it possible to accurately determine the equilibrium mass dependent isotope fractionations through estimation of the force constants of solids via the determination of phonons of solids or vibrational frequencies of molecules. Early studies utilizing vibrational frequencies examined the traditional isotopes (e.g., Harris, 1995) but *ab initio* methods are now regularly applied to the nontraditional isotope systems. With increasing computing power, it is now possible to consider more complex and accurate models. In recent years, *ab initio* methods have also been employed to look at an equilibrium mass independent fractionation phenomenon known as the nuclear field shift effect. First observed in laboratory fractionation experiments on uranium, Bigeleisen (1996) and Nomura et al. (1996) laid the theoretical framework to explain this effect and made the first estimates of its magnitude using isotope fractionation measurements and literature spectroscopic data. Later measurements of the $^{238}U/^{235}U$ system confirmed a redox-dependent effect on isotope composition (Stirling et al. 2005, 2006, 2007; Weyer et al. 2008), which was modeled by Schauble (2006) and Abe (2008ab, 2010). The fact that all isotopes of uranium are radioactive, yet chemical fractionations between isotopes are still measurable suggests that perhaps “stable isotope geochemistry” is better referred to as simply "isotope geochemistry," as radioactive elements may also display detectable fractionations due to this effect.

In this thesis, we estimated the magnitude of the field shift effect for a variety of elements using the DFT-PAW method. In the first chapter, we aim to produce the most in-depth characterization of the field shift effect in uranium to date, including solids and the bonding to different ligands in addition to redox effects. In the second chapter, we performed the first known estimates of equilibrium isotope fractionation in plutonium and neptunium. In the final chapter, we extend this technique to the platinum group elements, in particular to platinum, with an additional preliminary analysis of iridium.

1.2. Stable isotope theory

1.2.1. Mass dependent isotope fractionation

For the general case of thermodynamic equilibrium, in an isotope exchange reaction for molecules A and B with light isotope X and heavy isotope X', the reaction can be written as follows:

$$\mathrm{AX} + \mathrm{BX'} \leftrightarrow \mathrm{AX'} + \mathrm{BX}$$

The equilibrium constant for this reaction would be:

$$\mathrm{K_{eq}} = \frac{[\mathrm{X'A}][\mathrm{XB}]}{[\mathrm{XA}][\mathrm{X'B}]}$$

The isotope fractionation factor α can be defined as follows, assuming that only one isotope is being exchanged:

$$\alpha_{\mathrm{XA-XB}} = \frac{(\mathrm{X'/X})_{\mathrm{XA}}}{(\mathrm{X'/X})_{\mathrm{XB}}}$$

The close relationship between K_{eq} and α can be seen from these equations – in fact they are identical if exactly one atom is exchanged and a correction for molecular symmetry is made. Isotopic fractionations are sometimes reported as β values, which can be thought of as a fractionation between the species of interest and dissociated, non-interacting atoms of that element:

$$\mathrm{AX + X' \leftrightarrow AX' + X}$$

We can then rewrite the fractionation factor α between two species XA and XB as follows:

$$\alpha_{\mathrm{XA-XB}} = \frac{\beta_{\mathrm{AX}}}{\beta_{\mathrm{BX}}}$$

This relation allows us to determine the value for α by determining the β values for the substances of interest and taking their ratio. If fractionation is assumed to be mass dependent, and the electronic structure and energies of stationary molecules are insensitive to isotope substitution, then isotope reactions need only consider the dynamic energy of atomic motion. If molecules are assumed to vibrate as harmonic oscillators and rotate as rigid rotors, a further simplification is possible to separate the vibrational, translational, and rotational components of the free energy of motion. Using these assumptions and the Redlich-Teller product rule, which makes it possible to express the isotopic effects on translational and rotational partition functions in terms of the vibrational frequencies, Bigeleisen and Mayer (1947) derived the equation for β in a molecule in gas phase as follows:

$$\beta_{\mathrm{AX}} = \left[\prod_{\mathrm{i}=1}^{3\mathrm{N}-6} \frac{\nu_{\mathrm{i}}}{\nu'_{\mathrm{i}}} \text{ x } \frac{1 - \mathrm{e}^{-h\nu'_{\mathrm{i}}/(k\mathrm{T})}}{\mathrm{e}^{-h\nu'_{\mathrm{i}}/(2k\mathrm{T})}} \text{ x } \frac{\mathrm{e}^{-h\nu_{\mathrm{i}}/(2k\mathrm{T})}}{1 - \mathrm{e}^{-h\nu_{\mathrm{i}}/(k\mathrm{T})}}\right]^{1/\mathrm{n}}$$

The number of atoms in the molecule is N, n is the number of exchangeable atoms, h is Planck's constant, T is temperature, k is the Boltzmann constant, and ν and ν' are the vibrational frequencies for species A with isotopes X and X' respectively. Note that this is for the case of a nonlinear molecule; a linear molecule has 3N-5 vibrational degrees of freedom and so an additional term appears in the product.

Bigeleisen and Mayer (1947) also determined that it is possible to estimate the mass dependent component of fractionation for a species utilizing only force constants acting to hold the atom of interest in its molecular site, therefore bypassing the necessity of determining all isotope-sensitive vibrational frequencies for isotopically substituted molecules. Their derivation can be rearranged slightly to yield the following equation:

$$\beta_{\mathrm{AX}} \approx 1 + \frac{h}{96\pi^2 k \mathrm{T}^2} \frac{\mathrm{m}' - \mathrm{m}}{\mathrm{m}'\mathrm{m}} \mathrm{A}$$

Where m' refers to the heavy isotope and m refers to the light isotope. In the Bigeleisen and Mayer formulation, it is possible to determine the constant A by perturbing an atom of the element of interest in the three cartesian directions. A is then the sum of the restoring force constants.

Schauble (2004) qualitatively summarized the observed patterns of equilibrium mass dependent fractionation as follows:

1. Equilibrium isotope fractionations tend to decrease as temperature increases, roughly in proportion to $1/\mathrm{T}^2$
2. Isotope fractionations are largest for light elements and smaller for heavier elements, due to the higher relative differences in the reduced masses of isotopically substituted molecules
3. At equilibrium, the heavy isotope will tend to be incorporated into the substance that forms the bonds with the highest spring (force) constants. These "stiffer" bonds are usually short and strong. Shorter and stronger bonds in turn tend to be those for

substances of higher oxidation state, bonds involving elements near the top of the periodic table, highly covalent bonds between similarly electronegative atoms, lower coordination numbers, and/or involve transition elements in low spin configurations. Substances where the element being considered is bonded to hydrogens or in a low mass molecule will not be as enriched as expected, however.

1.2.2. Field shift effect

Nuclear field shift effects are an equilibrium thermodynamic phenomenon that results from the finite volume and/or nonspherical shape of atomic nuclei. The differences in the size and shape of isotopes result in differences in the Coulomb potential felt by bound electrons. This in turn results in a difference in the electronic structure and energy. Nuclear field shifts have long been observed in atomic spectra (Van Vleck, 1936; King, 1984) but Bigeleisen (1996) and Nomura et al. (1996) were the first to posit that the same phenomenon could produce chemical fractionation of isotopes. Chromatographic uranium isotope separation experiments showed that ^{238}U tended to preferentially incorporate into reduced species of uranium (Shimokaua and Kobayashi, 1970; Florence et al. 1975; Fukuda et al. 1983; Fujii et al., 1989ab). Bigeleisen (1996) and Nomura et al. (1996) showed that uranium isotope separation via ion exchange columns did not track the mass of the nuclei but instead tracked their nuclear charge radii. The nuclear field shift also scales with the difference in the electron density inside of the nucleus of the atom of interest within the fractionating species. We can examine the field shift effect through the following approximate relation adapted by Schauble (2013) from previous Mössbauer spectroscopy literature:

$$\delta E_{FS} \propto (|\psi(0)_A|^2 - |\psi(0)_B|^2)\, \Delta\langle r^2_{isotopes}\rangle$$

Where δE_{FS} is the volume component of the nuclear field shift effect, $\left|\psi(0)_{A,B}\right|^2$ are the contact densities (i.e. electron densities at the nucleus) of the fractionating species, and $\Delta\langle r^2_{isotopes}\rangle$ is the difference in the mean squared charge radii of the isotopic nuclei.

Knyazev and Myasoedov (2001) used relativistic electron structure calculations to show that field shift isotope fractionation will tend to increase at higher atomic number, primarily because relativistic contraction of s-electrons near charged nuclei increases the electron density. They also observed that covalent bonding would tend to reduce nuclear volume fractionations relative to what one would expect in ionically-bonded materials. Schauble (2006; 2007; 2013) and Abe (2008 ab; 2010) directly modeled the electronic structure of uranium, thallium, mercury, and cadmium species in order to estimate the magnitude of the field shift effect for these elements. Schauble (2007) summarized the general patterns observed for the nuclear field shift effect. For oxidation/reduction reactions where *d*, *p*, or *f*-orbital occupancies change, the heavy isotope will tend to concentrate in the reduced phase, while for oxidation/reduction reactions in which *s*-orbital occupancies change, the heavy isotope will concentrate in the oxidized phase. It can be observed that in the first case, the field shift acts in the opposite direction of the expected mass dependent component of fractionation, while in the second case, the field shift acts in the same direction. Additionally, in multiple-isotope systems there will likely be odd-even staggering for the field shift due to nuclear charge radius changing nonlinearly with increasing mass (Bigeleisen, 1996).

1.3. Ab initio methods

The properties of any material can, in principle, be determined from the laws of quantum mechanics describing the interactions between nuclei and electrons. For the purposes of the present studies, we are interested in determining the mass dependent and field shift components of fractionation through *ab initio* calculations. Exact calculations on any but the simplest systems are impossible, but they can be made tractable with a series of approximations, such as the Born-Oppenheimer approximation, which considers the rapid movement of electrons to be decoupled from the slower movement of atomic nuclei. With this assumption, it is possible to simplify Schrödinger's equation for electrons so that the positions of the nuclei are fixed external parameters. The energy of the system is therefore a function of the positions of the atomic nuclei. Nuclear dynamics can be determined via consideration of the movement of the nuclei on a potential energy surface.

There are two primary methods of solving Schrödinger's equation in *ab initio* calculations. The first is the Hartree-Fock method (Roothaan, 1951), which combines single particle wavefunctions (i.e. orbitals). The other method is Density Functional Theory (Hohenberg and Kohn, 1963). This formulation is distinct from Hartree-Fock in that it determines electronic energies from the electron densities. DFT methods are particularly useful for modeling complex aqueous systems and crystals. There are also hybrid methods such as B3-LYP (Becke, 1993), which incorporate aspects of both methods, and higher precision methods that more accurately capture effects such as electron correlation (e.g., coupled cluster theory; Cizek, 1966).

Electronic wavefunctions for electronic structure calculations are typically represented as a linear combination of a finite set of fixed functions – a basis set. These functions can be localized on the position of the atoms (e.g. atomic orbitals) or can consist of periodic plane waves (solutions for the Schrödinger equation of a free particle). In general, a localized basis set is most suitable for calculations of molecules, while a plane wave basis set is better suited for crystalline solids because of the periodic boundary conditions of crystallographic unit cells. The computational cost of such calculations can be quite high, so an additional approximation is made via the utilization of pseudopotentials, which replaces the potential created by the atomic nucleus and core electrons, allowing the calculation to consider only the valence electrons that significantly participate in bonding and ionization.

The determination of mass dependent components of fractionation for molecules is a three-step process. In the first step, the geometry of a molecule is optimized – i.e., relaxed – into the minimum energy configuration that is consistent with the model parameters. From an initial guess geometry, the forces on each atom and the stress distorting the entire cell are determined. As a result of these calculations, a new guess geometry is determined iteratively to minimize the forces and reduce the overall energy, a process that continues until the residual forces and stresses are reduced to the cutoff set for that calculation. Optimized geometries for crystals are obtained via a similar method to molecules, but the volume and shape of the cell is also allowed to vary. After this minimum energy geometric configuration is determined, the force constants for the atoms are determined by differentiation of forces or double differentiation of energy with respect to atomic positions – at the simplest, numerical differentiation via displacement of the atoms from their equilibrium positions. The vibrational frequencies are then determined via a calculation with the appropriate isotopic masses and model force constants (Baroni et al., 2001). This process can be repeated for a different isotopic mass by recycling the matrix of force constants. The resulting vibrational frequencies can then be used in the equation of Urey (1947) to determine the mass dependent component of fractionation for a species. Vibrational analysis of solids represents a different challenge than *in vacuo* molecules, because long range interactions in solids cause vibrational modes (phonons) to occupy a continuum rather than a finite number of discrete frequencies. In practice, this requires sampling of vibrational modes from the continuum, so as to represent the overall vibrational frequency spectrum.

In addition to modeling solid and gas phase species, it is often of interest to geologists to consider aqueous species. However, there are considerable difficulties examining these species compared to solid or gas phase species, stemming from the dynamic nature of aqueous environments. An ion or molecule dissolved in water will interact with its environment in a continuously changing configuration, with potentially multiple coordination spheres of water. The large number of atoms in these coordination spheres, and the often weak and variable bonding interactions involving water molecules, results in computationally intensive calculations. Therefore, it is typically advantageous to make approximations in order to simplify such calculations. One method is to explicitly solvate the species of interest only a limited number of coordination spheres of water. The configuration of the water molecules may be obtained as a snapshot from a molecular dynamics simulations, rather than attempting a complete thermodynamic integration over the all possible solvent molecule positions. This truncated explicit solvation (or simply "explicit solvation") method is still computationally intensive, however, and may necessitate the use of multiple configurations to achieve a reliable sampling of the aqueous species. It is also possible to instead approximate solvation by creating a spherical cavity around the central molecule of interest that is modeled *in vacuo*, and for all the space outside of this cavity, assume a structureless continuum that has properties consistent with a polarizable solvent with a dielectric constant equal to water (Cossi et al., 2002). This is known as a polarizable continuum model (PCM), a method of implicit solvation, and is often performed even in calculations utilizing explicit solvation shells in order to approximate long range effects in solution. In the present work, in general, implicit solvation is used to represent all water molecules that are not directly bonded to the atom or molecule of interest.

Estimates of field shift fractionations require accurate determination of electron densities. For atomic nuclei of elements with high atomic numbers, accurate determinations of electron densities must take into account relativity, typically using the Dirac equation, which is the relativistic counterpart to the Schrödinger equation. In order to provide an accurate depiction of the electronic environment at the nucleus, calculations also take into account every electron in the material. This contrasts with pseudopotential methods that typically only consider valence electrons. It turns out that some all-electron relativistic methods also allow the possibility to vary the nuclear charge radius to directly determine the energy differences that result from isotope substitution, which is convenient for the present study. These calculations can be very accurate, but they are computationally intensive and therefore limited in the scope of materials that can be modeled to relatively simple molecules and ions. Schauble (2013) proposed a method of expanding the utility of all-electron calculations via the DFT-PAW method. In this method, a set of simple molecules is modeled via fully relativistic Dirac-Fock calculations. Corresponding DFT models for the same species are then determined, built using Projector-Augmented-Wave datasets (Blöchl, 1994), which are very similar to pseudopotential methods with the advantage of preserving information about core electronic orbitals. This makes it possible to reconstruct changes in electron density at the nucleus even when the core electrons aren’t being modeled explicitly (Zwanziger, 2009). Correlation of all-electron and DFT-PAW model results produces a calibration line and makes it possible to determine (by interpolation or extrapolation) the field shift effect for any material so long as it is possible to create a DFT-PAW model. This allows the possibility of determining the field shift effect in solid materials and large aqueous complexes, though the accuracy of such models is limited by the initial calibration set. This overall calibration/interpolation procedure is here called the DFT-PAW method, and is the basis of the remaining chapters of this study.

1.4. Introduction to Chapter 2: Uranium isotope fractionation

The first estimates of the nuclear field shift effect on equilibrium isotope fractionation were made by Bigeleisen (1996) and Nomura et al. (1996) in order to explain the tendency of ^{238}U to incorporate into the reduced phase of uranium during chromatographic separation (Shimokaua and Kobayashi, 1970; Florence et al. 1975; Fujii et al., 1989ab; Fukuda et al. 1983). Subsequent advancements in mass spectrometry made it possible to measure $^{238}U/^{235}U$ to a high degree of precision (Stirling et al. 2005, 2006, 2007; Weyer et al. 2008). With the development of the $^{238}U/^{235}U$ isotope system, geochemists have taken an interest in performing uranium isotope measurements of sedimentary rocks as well as zircons. The uranium isotope system is now commonly used as a paleoredox proxy, used to track the oxygenation of the world's oceans through time by measuring the $^{238}U/^{235}U$ of carbonate sediments (Zhang et al., 2018; 2020) as well as reduced sediments (Lau et al., 2019). Experimental studies have been performed for both uranium incorporated into carbonates (Chen et al., 2016) and abiotic and biotic reduction of uranium (Wang et al., 2015ab). Measurements of zircons have shown large fractionations of 5‰ (Hiess et al., 2012) as well as smaller fractionations of -0.60‰ to -0.12‰ (Tissot et al., 2019).

We use the DFT-PAW method in order to determine both the nuclear field shift and the mass dependent component of fractionation for a variety of natural materials in the uranium system, including solids. Earlier all-electron *ab initio* studies were limited to smaller, vapor phase species (Schauble, 2006; Abe et al., 2008ab, 2010) while recent studies are still unable to model solids (Sato et al., 2021). This study aims to expand study of the field shift to solids and more complex aqueous species, in order to provide direct comparison to previous experiments and measurements. We also aim to provide an examination of the chemical properties may control the nuclear field shift in addition to redox state, such as bond length, bond partner, coordination number, and solvation, which may be of utility for this system as well as other isotope systems. We determined that U(IV) species are expected to be 1-2‰ heavier than U(VI) species, while U(V) species are expected to be 1-1.5‰ heavier than U(VI) species at 298 K. Select ligands can influence fractionations by up to 0.6‰ as well, even in the absence of changes in the oxidation state of uranium.

1.5. Introduction to Chapter 3: Neptunium and plutonium isotope fractionation

With the advent of nuclear technology, multiple radioactive isotopes were created at a large scale at the Earth's surface for the first time. Nuclear detonations, nuclear accidents, and nuclear waste from the fuel cycle all can result in the release of radioactive elements. The presence of these radioactive elements is now a primary environmental concern. The actinides plutonium and neptunium are among the elements released since 1945, and nearly all of their abundance today can be attributed to anthropogenic sources. Isotope ratios of Pu are frequently measured for the purpose of monitoring release of nuclear materials. Different (nuclear) sources of Pu have different isotopic ratios, which in principle makes it possible to trace them via isotope abundance analyses. Plutonium and neptunium behave similarly in the environment to uranium, in that the oxidized actinyl species are highly soluble while the reduced species tend to be insoluble (Maher et al., 2013). Pentavalent and hexavalent species tend to form highly soluble, linear AnO_2 molecules coordinated equatorially by various ligands. Tetravalent species tend to form insoluble oxides, hydroxides, and colloids. Trivalent species are relatively understudied.

These behaviors are common across all three elements; the main difference between them being the relative stabilities of these redox states at surface conditions.

Owing to their geochemical similarities and large atomic nuclei, it seems likely that the same field shift fractionation processes that act on the uranium system will act on these elements as well, and potentially at a similar magnitude, with the nuclear field shift being more significant than the mass dependent component of fractionation and consequently causing reduced species to be enriched in larger (and more massive) isotopes. Therefore, using some of the isotopes for Pu and Np with half-lives that are significant on human timescales, we aim to develop the first estimates of isotope fractionations for these elements using the DFT-PAW method. We determined that exchange between species with actinides in the +3 and +6 oxidation states will drive the largest field shift fractionations, whereas fractionations involving intermediate (+4 and +5) oxidation states are somewhat weaker, and in fact these oxidation states are very similar isotopically. For instance, for the ^{242}Pu/^{239}Pu system, Pu^{III} species are ~3‰ more enriched in ^{242}Pu than Pu^{IV} and Pu^{V} species, while Pu^{VI} species are ~2‰ lighter than Pu^{IV} and Pu^{V} species. In settings in which the isotopic composition of a source is well-characterized, such as in the case of nuclear waste disposal, this study may provide a framework for monitoring the behavior of these elements in the environment.

1.6. Introduction to Chapter 4: Platinum group element isotope fractionation

The platinum group elements (PGEs) are a cohort of transition metals with broadly similar chemical properties that are distinct from neighboring transition metals. PGEs are strongly siderophile, which means that they preferentially alloy with metallic iron rather than bonding with silicates; they are also chalcophile within the conditions relevant to the Earth's mantle, preferentially bonding with sulfur rather than oxygen. Experiments consistently find very strong partitioning of the PGEs into the metal phase during metal-silicate differentiation experiments (Capobiano, 1995; Borisov et al., 1994; Ohtani et al., 1997; Holzheid et al., 2000; Fortenfant et al., 2003; Righter et al., 2003; Cottrell and Walker, 2006; Ertel et al., 2006; Righter et al., 2008; Brenan and McDonough, 2009; Cottrell et al., 2009). Within the context of geochemistry, this partitioning is important because it predicts that the PGEs were preferentially incorporated into the metallic core during planetary differentiation, and as a consequence are depleted in the silicate mantle and crust. While these elements are indeed strongly depleted in the Earth's mantle and crust relative to undifferentiated meteorites, their measured concentrations are notably than higher metal-silicate partitioning experiments appear to predict (Ringwood, 1966; Chou, 1978; Jagoutz, 1979; Righter, 2003; Day et al., 2016). Two leading explanations for this anomaly are the Late Veneer hypothesis and the magma ocean hypothesis. The Late Veneer hypothesis (Kimura et al., 1974; Chou, 1978; Holzeid et al., 2000; Dauphas and Marty, 2002) states that the final 0.1-1.0% of the mass of the Earth accreted after core formation was largely complete. The addition of this material, likely a mix of chondrites and other extraterrestrial material, increased the abundance of PGEs in the bulk silicate Earth over time (Maier et al., 2009). The magma ocean hypothesis relies on observations from experiments with higher pressure, higher temperature, and varying oxygen fugacity, which results in less extreme partitioning of the PGEs into the metallic phase than initial experiments displayed (Brett, 1971; Ringwood, 1977; Brett, 1984; Murthy, 1991; Capobianco et al., 1993; Righter and Drake, 1997; Li and Agee, 2001). However, even high pressure/high temperature experiments cannot fully reproduce the observed mantle & crust abundance anomalies for all elements within the group (Ertel et al., 2006; Mann et al., 2012).

Owing to the field shift effect's 1/T temperature dependence, in contrast to the $1/T^2$ temperature dependence for mass dependent fractionations, field shift effects are likely to become more significant relative to mass dependent effects at higher temperatures, such as would be expected during core-mantle differentiation. We focus this study on using the DFT-PAW method to study ^{198}Pt/^{194}Pt fractionations, an isotope system which has been measured in a variety of materials of significance to core-mantle differentiation (Creech et al., 2017), with a secondary focus on using Mössbauer isomer shifts to develop a framework for ^{193}Ir/^{191}Ir field shift fractionations, a stable isotope system for which a measurement technique has been developed but has yet to see focused use in the geosciences (Zhu et al., 2017).

We find that platinum isotopes likely to be dominantly mass-dependent at most Earth-surface and crustal temperatures, whereas the field shift becomes (relatively) more important at higher temperatures. Platinum bound within an iron or nickel alloy is predicted to have the highest electron density of all species modeled (favoring depletion in large, massive platinum isotopes), while Pt^{II} substituting into the divalent site within an olivine structure is expected to have the lowest electron density (favoring enrichment in large, massive platinum isotopes). At conditions relevant to core-mantle differentiation (3000 K) we expect an equilibrium fractionation of 0.09‰, with the mantle having a higher ^{198}Pt/^{194}Pt. This may result in a primitive, unmixed mantle having measurably higher ^{198}Pt/^{194}Pt as a consequence of the field shift and Rayleigh fractionation. Alternative potential Pt-bearing reservoirs in silicate, such as sulfide species, are expected to be more weakly fractionated in equilibrium with iron-rich metallic liquid.

References

Abe M, Suzuki T, Fujii Y, et al (2008a) An ab initio molecular orbital study of the nuclear volume effects in uranium isotope fractionations. The Journal of Chemical Physics 129:164309. https://doi.org/10.1063/1.2992616

Abe M, Suzuki T, Fujii Y, et al (2010) Ligand effect on uranium isotope fractionations caused by nuclear volume effects: An ab initio relativistic molecular orbital study. The Journal of Chemical Physics 133:044309. https://doi.org/10.1063/1.3463797

Abe M, Suzuki T, Fujii Y, Hada M (2008b) An ab initio study based on a finite nucleus model for isotope fractionation in the U(III)–U(IV) exchange reaction system. The Journal of Chemical Physics 128:144309. https://doi.org/10.1063/1.2898541

Becke AD (1993) A new mixing of Hartree–Fock and local density-functional theories. The Journal of Chemical Physics 98:1372–1377. https://doi.org/10.1063/1.464304

Bigeleisen J (1996) Nuclear Size and Shape Effects in Chemical Reactions. Isotope Chemistry of the Heavy Elements. J Am Chem Soc 118:3676–3680. https://doi.org/10.1021/ja954076k

Bigeleisen J, Mayer MG (1947) Calculation of Equilibrium Constants for Isotopic Exchange Reactions. The Journal of Chemical Physics 15:261–267. https://doi.org/10.1063/1.1746492

Blöchl PE (1994) Projector augmented-wave method. Phys Rev B 50:17953–17979. https://doi.org/10.1103/PhysRevB.50.17953

Brett R (1984) Chemical equilibration of the Earth’s core and upper mantle. Geochimica et Cosmochimica Acta 48:1183–1188. https://doi.org/10.1016/0016-7037(84)90054-1

Capobianco CJ, Jones JH, Drake MJ (1993) Metal-silicate thermochemistry at high temperature: Magma oceans and the “excess siderophile element” problem of the Earth’s upper mantle. Journal of Geophysical Research: Planets 98:5433–5443. https://doi.org/10.1029/92JE02742

Chen X, Romaniello SJ, Herrmann AD, et al (2016) Uranium isotope fractionation during coprecipitation with aragonite and calcite. Geochimica et Cosmochimica Acta 188:189–207. https://doi.org/10.1016/j.gca.2016.05.022

Chou C-L (1978) Fractionation of Siderophile Elements in the Earth’s Upper Mantle. In: Proceedings of the 9th Lunar and Planetary Science Conference. Lunar and Planetary Institute, pp 219–230

Čížek J (1966) On the Correlation Problem in Atomic and Molecular Systems. Calculation of Wavefunction Components in Ursell-Type Expansion Using Quantum-Field Theoretical Methods. The Journal of Chemical Physics 45:4256–4266. https://doi.org/10.1063/1.1727484

Cossi M, Scalmani G, Rega N, Barone V (2002) New developments in the polarizable continuum model for quantum mechanical and classical calculations on molecules in solution. The Journal of Chemical Physics 117:43–54. https://doi.org/10.1063/1.1480445

Creech JB, Baker JA, Handler MR, et al (2017) Late accretion history of the terrestrial planets inferred from platinum stable isotopes. Geochem Perspect Lett 3:94–104. https://doi.org/10.7185/geochemlet.1710

Date AR, Gray AL (1989) Applications of inductively coupled plasma mass spectrometry. Blackie, Chapman, and Hall, New York

Dauphas N, Marty B (2002) Inference on the nature and the mass of Earth's late veneer from noble metals and gases. Journal of Geophysical Research: Planets 107:12-1-12–7. https://doi.org/10.1029/2001JE001617

Ertel W, Walter MJ, Drake MJ, Sylvester PJ (2006) Experimental study of platinum solubility in silicate melt to 14GPa and 2273K: Implications for accretion and core formation in Earth. Geochimica et Cosmochimica Acta 70:2591–2602. https://doi.org/10.1016/j.gca.2006.02.015

Florence TM, Batley GE, Ekstrom A, et al (1975) Separation of uranium isotopes by uranium(IV)-uranium(VI) chemical exchange. Journal of Inorganic and Nuclear Chemistry 37:1961–1966. https://doi.org/10.1016/0022-1902(75)80925-0

Fujii Y, Nomura M, Okamoto M, et al (1989a) An Anomalous Isotope Effect of 235U in U(IV)-U(VI) Chemical Exchange. Zeitschrift für Naturforschung A 44:395–398. https://doi.org/10.1515/zna-1989-0507

Fujii Y, Nomura M, Onitsuka H, Takeda K (1989b) Anomalous Isotope Fractionation in Uranium Enrichment Process. Journal of Nuclear Science and Technology 26:1061–1064. https://doi.org/10.1080/18811248.1989.9734427

Fukuda J, Fujii Y, Okamoto M (1983) A Fundamental Study on Uranium Isotope Separation Using U(IV)—U(VI) Electron Exchange Reaction. Zeitschrift für Naturforschung A 38:1072–1077. https://doi.org/10.1515/zna-1983-1005

Halliday AN, Lee D-C, Christensen JN, et al (1995) Recent developments in inductively coupled plasma magnetic sector multiple collector mass spectrometry. International Journal of Mass Spectrometry and Ion Processes 146:21–33. https://doi.org/10.1016/0168-1176(95)04200-5

Hanschmann G (1984) Reduzierte Zustandssummenverhältnisse isotoper Moleküle auf quantenchemischer Grundlage: VI. Mitt. MNDO-MO-Berechnungen zur 28Si/30Si-, 32S/34S- und 35Cl/37Cl-Substitution. Isotopenpraxis Isotopes in Environmental and Health Studies 20:437–439. https://doi.org/10.1080/10256018408623405

Harris NJ (1995) A systematic theoretical study of harmonic vibrational frequencies and deuterium isotope fractionation factors for small molecules. The Journal of Physical Chemistry 99:14689–14699. https://doi.org/10.1021/j100040a017

Hiess J, Condon DJ, McLean N, Noble SR (2012) 238U/235U Systematics in Terrestrial Uranium-Bearing Minerals. Science 335:1610–1614. https://doi.org/10.1126/science.1215507

Hohenberg P, Kohn W (1964) Inhomogeneous electron gas. Physical review 136:B864–B871. https://doi.org/10.1103/physrev.136.b864

Holzheid A, Sylvester P, O'Neill HSC, et al (2000) Evidence for a late chondritic veneer in the Earth's mantle from high-pressure partitioning of palladium and platinum. Nature 406:396–399. https://doi.org/10.1038/35019050

Houk RS, Thompson JJ (1988) Inductively coupled plasma mass spectrometry. Mass Spectrometry Reviews 7:425–461. https://doi.org/10.1002/mas.1280070404

Jarvis KE, Gray AL, Houk RS, et al (1992) Handbook of inductively coupled plasma mass spectrometry. Chapman and Hall, New York

Kimura K, Lewis RS, Anders E (1974) Distribution of gold and rhenium between nickel-iron and silicate melts: implications for the abundance of siderophile elements on the Earth and Moon. Geochimica et Cosmochimica Acta 38:683–701. https://doi.org/10.1016/0016-7037(74)90144-6

King WH (1984) Isotope shifts in atomic spectra. Springer New York, New York

Knyazev DA, Myasoedov NF (2001) Specific Effects of Heavy Nuclei in Chemical Equilibrium. Separation Science and Technology 36:1677–1696. https://doi.org/10.1081/SS-100104758

Koppenaal DW (1992) Atomic mass spectrometry. Analytical chemistry 64:320–342. https://doi.org/10.1021/ac00211a015

Kotaka M, Kakihana H (1977) Thermodynamic isotope effect of trigonal planar and tetrahedral molecules. Bulletin of the Research Laboratory for Nuclear Reactors (Tokyo Institute of Technology) 2:

Kotaka M, Shono T, Ikuta E, Kakihana H (1978) Thermodynamic isotope effect of some octahedral hexahalo complexes. Bulletin of the Research Laboratory for Nuclear Reactors (Tokyo Institute of Technology) 3:

Lau KV, Romaniello SJ, Zhang F (2019) The Uranium Isotope Paleoredox Proxy. Elements in Geochemical Tracers in Earth System Science. https://doi.org/10.1017/9781108584142

Lindemann FA (1919) XII. Note on the vapour pressure and affinity of isotopes. The London, Edinburgh, and Dublin Philosophical Magazine and Journal of Science 38:173–181. https://doi.org/10.1080/14786440708635937

Lindemann FA, Aston FW (1919) XLVIII. The possibility of separating isotopes. The London, Edinburgh, and Dublin Philosophical Magazine and Journal of Science 37:523–534. https://doi.org/10.1080/14786440508635912

Maher K, Bargar JR, Brown GEJr (2013) Environmental Speciation of Actinides. Inorg Chem 52:3510–3532. https://doi.org/10.1021/ic301686d

Maier WD, Barnes SJ, Campbell IH, et al (2009) Progressive mixing of meteoritic veneer into the early Earth's deep mantle. Nature 460:620–623. https://doi.org/10.1038/nature08205

Mann U, Frost DJ, Rubie DC, et al (2012) Partitioning of Ru, Rh, Pd, Re, Ir and Pt between liquid metal and silicate at high pressures and high temperatures - Implications for the origin of highly siderophile element concentrations in the Earth's mantle. Geochimica et Cosmochimica Acta 84:593–613. https://doi.org/10.1016/j.gca.2012.01.026

Miller CA, Peucker-Ehrenbrink B, Schauble EA (2015) Theoretical modeling of rhenium isotope fractionation, natural variations across a black shale weathering profile, and potential as a paleoredox proxy. Earth and Planetary Science Letters 430:339–348. https://doi.org/10.1016/j.epsl.2015.08.008

Murthy VR (1991) Early differentiation of the Earth and the problem of mantle siderophile elements: a new approach. Science 253:303–306. https://doi.org/10.1126/science.253.5017.303

Nomura M, Higuchi N, Fujii Y (1996) Mass Dependence of Uranium Isotope Effects in the U(IV)−U(VI) Exchange Reaction. J Am Chem Soc 118:9127–9130. https://doi.org/10.1021/ja954075s

Righter K, Drake MJ (2003) Partition coefficients at high pressure and temperature. Treatise on geochemistry 2:568. https://doi.org/10.1016/B0-08-043751-6/02010-7

Ringwood AE (1966) Chemical evolution of the terrestrial planets. Geochimica et Cosmochimica Acta 30:41–104. https://doi.org/10.1016/0016-7037(66)90090-1

Roothaan CCJ (1951) New developments in molecular orbital theory. Reviews of modern physics 23:69. https://doi.org/10.1103/RevModPhys.23.69

Sato A, Bernier-Latmani R, Hada M, Abe M (2021) Ab initio and steady-state models for uranium isotope fractionation in multi-step biotic and abiotic reduction. Geochimica et Cosmochimica Acta 307:212–227. https://doi.org/10.1016/j.gca.2021.05.044

Schauble EA (2006) Equilibrium uranium isotope fractionation by nuclear volume and mass-dependent processes. AGU Fall Meeting Abstracts 21:V21B-0570

Schauble EA (2004) Applying Stable Isotope Fractionation Theory to New Systems. Reviews in Mineralogy and Geochemistry 55:65–111. https://doi.org/10.2138/gsrmg.55.1.65

Schauble EA (2007) Role of nuclear volume in driving equilibrium stable isotope fractionation of mercury, thallium, and other very heavy elements. Geochimica et Cosmochimica Acta 71:2170–2189. https://doi.org/10.1016/j.gca.2007.02.004

Schauble EA (2013) Modeling nuclear volume isotope effects in crystals. PNAS 110:17714–17719. https://doi.org/10.1073/pnas.1216216110

Schauble EA (2023) Nuclear volume isotope fractionation of europium and other lanthanide elements. Geochemical Journal 57:118–133. https://doi.org/10.2343/geochemj.GJ23010

Shimokaua J, Kobayashi F (1970) Separation of Uranium Isotopes by Chemical Exchange. Isotopenpraxis Isotopes in Environmental and Health Studies 6:170–176. https://doi.org/10.1080/10256017008621706

Stirling CH, Andersen MB, Potter E-K, Halliday AN (2007) Low-temperature isotopic fractionation of uranium. Earth and Planetary Science Letters 264:208–225. https://doi.org/10.1016/j.epsl.2007.09.019

Stirling CH, Halliday AN, Porcelli D (2005) In search of live ^{247}Cm in the early solar system. Geochimica et Cosmochimica Acta 69:1059–1071. https://doi.org/10.1016/j.gca.2004.06.034

Stirling CH, Halliday AN, Potter E-K, et al (2006) A low initial abundance of ^{247}Cm in the early solar system and implications for r-process nucleosynthesis. Earth and Planetary Science Letters 251:386–397. https://doi.org/10.1016/j.epsl.2006.09.023

Tissot FLH, Ibanez-Mejia M, Boehnke P, et al (2019) ^{238}U/^{235} U measurement in single-zircon crystals: implications for the Hadean environment, magmatic differentiation and geochronology. Journal of Analytical Atomic Spectrometry 34:2035–2052. https://doi.org/10.1039/C9JA00205G

Urey H (1947) The thermodynamic properties of isotopic substances. J Chem Soc 562–581. https://doi.org/10.1039/JR9470000562

Urey HC, Greiff LJ (1935) Isotopic exchange equilibria. Journal of the American Chemical Society 57:321–327. https://doi.org/10.1021/ja01305a026

Van Vleck JH (1936) On the Isotope Corrections in Molecular Spectra. The Journal of Chemical Physics 4:327–338. https://doi.org/10.1063/1.1749853

Wang X, Johnson TM, Lundstrom CC (2015a) Isotope fractionation during oxidation of tetravalent uranium by dissolved oxygen. Geochimica et Cosmochimica Acta 150:160–170. https://doi.org/10.1016/j.gca.2014.12.007

Wang X, Johnson TM, Lundstrom CC (2015b) Low temperature equilibrium isotope fractionation and isotope exchange kinetics between U(IV) and U(VI). Geochimica et Cosmochimica Acta 158:262–275. https://doi.org/10.1016/j.gca.2015.03.006

Weyer S, Anbar AD, Gerdes A, et al (2008) Natural fractionation of ^{238}U/^{235}U. Geochimica et Cosmochimica Acta 72:345–359. https://doi.org/10.1016/j.gca.2007.11.012

Zhang F, Algeo TJ, Romaniello SJ, et al (2018) Congruent Permian-Triassic δ^{238}U records at Panthalassic and Tethyan sites: Confirmation of global-oceanic anoxia and validation of the U-isotope paleoredox proxy. Geology 46:327–330. https://doi.org/10.1130/G39695.1

Zhang F, Lenton TM, del Rey Á, et al (2020) Uranium isotopes in marine carbonates as a global ocean paleoredox proxy: A critical review. Geochimica et Cosmochimica Acta 287:27–49. https://doi.org/10.1016/j.gca.2020.05.011

Zhu Z, Meija J, Zheng A, et al (2017) Determination of the Isotopic Composition of Iridium Using Multicollector-ICPMS. Anal Chem 89:9375–9382. https://doi.org/10.1021/acs.analchem.7b02206

Zwanziger JW (2009) Computation of Mössbauer isomer shifts from first principles. J Phys: Condens Matter 21:195501. https://doi.org/10.1088/0953-8984/21/19/195501

Chapter 2

Chemical fractionation of $^{238}U/^{235}U$ in natural systems using first principles methods

Abstract

Uranium is one of the few systems known in which mass independent fractionation at equilibrium is the primary determinant of the isotopic composition. Laboratory experiments and natural sample suites indicate a significant fractionation between U(VI) and U(IV) species that appears to be driven primarily by the nuclear field shift effect. Previous theoretical studies of this effect have focused on all-electron relativistic electronic structure calculations on simple molecular species (Schauble 2006; Abe et al., 2008ab) and while recent studies have been extended to more complex species (Sato et al., 2021) these calculations are computationally intensive for many environmentally relevant species, and are not feasible for solids. In this study we use the DFT-PAW method of Schauble (2013) in order to examine field shift fractionation in solids as well as complex aqueous species. The results indicate that equilibrium fractionations at ambient temperatures between U(VI) and U(IV) species are generally on the order of 1‰, up to as much as 2‰, with higher $^{238}U/^{235}U$ in reduced U(IV) species. We also predict that U(V) species will generally have a similar isotopic composition to U(IV) species and may have even higher $^{238}U/^{235}U$ at surface temperatures in some cases. Non-redox speciation effects, while generally small, can also potentially cause measurable $^{238}U/^{235}U$ fractionation. These non-redox effects can be as large as approximately 0.6‰ in some species with organic ligands. Finally, we find that model procedures that account for solvation beyond the first coordination sphere can have a significant effect on estimated fractionations involving aqueous uranium species. An implicit solvation model is generally adequate to capture these outer-shell solvation effects;

incorporation of a realistic inner shell coordination structure, including water molecules, is crucial.

2.1. Introduction

The purpose of this study is to estimate both mass-dependent and nuclear volume (field shift) components of $^{238}U/^{235}U$ isotopic fractionations for environmentally relevant species using electronic structure calculations. We compare our results to fractionation measurements in experiments and natural samples. We also quantify the impact of oxidation and reduction reactions on the nuclear field shift effect, as well as non-redox changes in bonding environment, with the goal of providing a framework for future computational studies and measurements.

In nature, uranium occurs primarily in the U(VI) and U(IV) states. In oxygenated environments, U(VI) generally occurs as soluble and highly mobile linear uranyl-type species (UO_2^{2+}) with additional ligands such as H_2O or CO_3^{2-} bound equatorially to the uranium atom. In the ocean, various uranyl-bearing carbonate complexes dominate the mass balance of dissolved uranium. Endrizzi and Rao (2014) calculate that $Ca_2UO_2(CO_3)_3$ makes up 58% of total uranium in solution at seawater pH (~8.2), $CaUO_2(CO_3)_3^{2-}$ and $MgUO_2(CO_3)_3^{2-}$ account for 18% each, and the species $UO_2(CO_3)_3^{4-}$ accounts for 6%. When fixed into a carbonate mineral lattice, these species are incorporated into carbonate sediments as one of the primary sinks in the surface uranium budget. The other major sink in the ocean is strongly reducing sediment, where soluble U(VI) species are reduced to insoluble U(IV) species. The cycling of uranium in Earth's surface environments through time is of interest to geoscientists, including as a potential paleo-fO_2 proxy. Geochemical fractionation of uranium isotopes is a potential tool for understanding this cycling.

2.1.1. Early measurements of uranium isotope fractionation

All uranium isotopes are radioactive, but three isotopes (^{238}U – $t_{1/2}$=4.5 Gyr, ^{235}U – $t_{1/2}$=704 Myr, and ^{234}U – $t_{1/2}$=246 kyr) are long-lived and abundant enough to be routinely measured in the environment. They are important in U-Pb and U-series dating. Uranium isotope ratios vary with time due to the isotopes each having different half-lives. ^{234}U/^{238}U abundance variations primarily reflect radioactive decay processes and decay-enhanced dissolution, and will not be considered further in this study. In the absence of chemical fractionation and stimulated nuclear reactions, naturally occurring uranium will have a uniform ^{238}U/^{235}U at any particular time. However, chemical fractionation does occur in nature. The possibility for non-radiogenic, non-radioactive fractionation was recognized when chemists began to take an interest in processes that enrich ^{235}U for the purposes of nuclear technology, and observed in early chromatographic uranium isotope separation experiments a tendency for the more massive ^{238}U isotope to be incorporated into the species with the lowest oxidation state (Shimokaua and Kobayashi, 1970; Florence et al. 1975; Fukuda et al. 1983; Fujii et al., 1989ab). The first modern, high precision ^{238}U/^{235}U isotope measurements (Stirling et al. 2005, 2006, 2007; Weyer et al. 2008) discovered significant variability in natural samples and laboratory partitioning experiments that can only be explained through chemical fractionation processes, analogous to previously known fractionations of stable isotopes of other elements (Figure 2-1). The underlying theory and methodology of stable isotope geochemistry can be used to examine the uranium isotope system, and in this sense ‘chemically fractionating’ is a more accurate term than ‘stable isotope fractionation’. The early observations that the more reduced phases of uranium, typically U(IV), tended to be enriched in ^{238}U relative to oxidized U(VI) phases goes in the opposite direction of typical stable isotopic systems, where more oxidized species are usually isotopically heavier (e.g., O'Neil, 1986).

2.1.2. Nuclear field shift effect

^{238}U/^{235}U enrichment in U(IV) species is a consequence of the nuclear field shift effect. The term 'field shift' comes from observed isotope shifts in atomic spectra, and field shift effects have been observed in vapor-phase atomic and ionic spectra for decades (Van Vleck, 1936; King, 1984). Bigeleisen (1996) and Nomura et al. (1996) were the first to show that chemical uranium isotope separation in laboratory experiments with ion-exchange resins tracked nuclear charge radii rather than mass, and had the same physical cause as spectroscopic field shifts. Bigeleisen proposed a semi-quantitative model using spectroscopically determined isotope shifts in uranium vapor and predicted equilibrium shifts of up to several per mil from the nuclear field shift effect.

The nuclear field shift effect is an equilibrium thermodynamic phenomenon that results from the finite size and non-spherical shape of atomic nuclei (Figure 2-2). Nuclear sizes and shapes differ among the isotopes of a given element and affect the Coulomb potential felt by the atom's bound electrons, which in turn impacts their electronic structures and energies. Electrons with high probability densities near the nucleus are bound less strongly to nuclei with greater volumes (^{238}U in this system). A higher electron density at the nucleus will result in a greater energy difference between large and small nuclei. The *s*-electrons are directly sensitive to nuclear size and shape because their maximal density is inside the nucleus. In contrast, electrons in *p*, *d*, and *f*-orbitals have mainly indirect effects by partially screening *s*-electrons. In oxidized uranium species, i.e., U(VI) species, the 5*f* shell is nominally empty, and the absence of 5*f* electrons results in less screening of s-electrons, and thus a higher s-electron density in the region inside the uranium nucleus. Reduced uranium species, primarily U(IV) – $5f^2$ and to a lesser extent U(V) – $5f^1$, will have a lower s-electron density inside the nucleus and are expected to have higher ^{238}U/^{235}U as a result. An approximate equation relating the field shift effect to electron densities and nuclear charge radii can be adapted from the theory of Mössbauer isomer shifts, adapted here from Blanchard et al., (2017):

$$\ln \alpha_{\mathrm{fs}} \approx \frac{2\pi Z e^2}{3\mathrm{k}T} \left(|\psi(0)_{\mathrm{AX}}|^2 - |\psi(0)_{\mathrm{BX}}|^2 \right) \Delta\langle \mathrm{r}^2_{\mathrm{isotopes}} \rangle$$

Where α_{fs} is the field shift fractionation factor, Z is the atomic number, e is the charge of an electron, k is the Boltzmann constant, $|\psi(0)_{AX}|^2$ and $|\psi(0)_{BX}|^2$ are the electron probability densities at the nucleus for the species AX and BX, and $\Delta\langle r^2 \rangle$ is the difference in the mean squared charge radius between the nuclei of interest. Of note is that contrary to the mass dependent component of fractionation, which varies according to $1/T^2$, the field shift varies according to 1/T so long as the fractionating species are in their electronic ground states.

2.1.3 Previous studies

Abe et al. (2008ab) and Schauble (2006) performed all-electron relativistic calculations on simple uranium species using Dirac-Fock theory. They showed that the observed ^{238}U enrichment in reduced uranium species can be modeled qualitatively and quantitatively using the volume component of the nuclear field shift effect, confirming the Bigeleisen (1996) and Nomura et al. (1996) model. They determined that the field shift effect between U(VI) and U(IV) species was approximately twice the magnitude of the mass dependent component of fractionation, and that it goes in the opposite direction. Subsequently, Abe et al. (2010) examined speciation effects using all-electron calculations, focusing on Cl-, F-, and Br-bearing species. They determined that it was important to consider the presence and identity of ligands when examining reactions between U(VI) and U(IV), though speciation effects within a single oxidation state were minor. However, these studies were limited to modeling simple species *in vacuo* due to the computational difficulty of all-electron calculations. Recent studies have expanded the all-electron model to more complex molecules (Sato et al., 2021) but this method remains computationally intensive, and is not compatible with periodic boundary condition model boundaries that are useful for investigating solid species.

Experiments have confirmed the reversed oxidation state dependence observed in early measurements and theoretical calculations. Isotopic fractionation during microbial reduction has been examined in several experiments, finding values an increase in $^{238}U/^{235}U$ of approximately 1‰ for reduction of U(VI) to solid U(IV) (Basu et al., 2014; Stirling et al., 2015; Stylo et al., 2015ab). Abiotic reduction has also been examined, and the experiments of Wang et al. (2015ab) are particularly relevant to the present study. Wang et al. (2015a) examined the oxidation of solid U(IV) into aqueous U(VI) by dissolved oxygen, and also examined oxidation of aqueous U(IV). They measured a fractionation of 1.1-1.6 ‰ between aqueous U(IV) and U(VI), with the U(IV) species having higher $^{238}U/^{235}U$, but were unable to achieve complete equilibration between aqueous U(VI) and solid U(IV) in their experimental conditions.

Where soluble U(VI) is partially reduced to insoluble U(IV) in the ocean, it is expected to impart a strong fractionation signature as ^{238}U is preferentially incorporated into the reduced sediment. This behavior makes both uranium abundance and isotopic composition promising candidates for paleoredox studies in anoxic sediments (Lau et al., 2019). This behavior also impacts the isotopic composition of uranium that is incorporated as U(VI) into carbonates. Due to the fact that uranium behaves conservatively in the ocean, the isotopic composition of U(VI)-bearing carbonates deposited in an open ocean setting is believed to reflect the isotopic composition of seawater at the time of deposition, which changes based on the amount of uranium sequestered into reducing sediments, making the uranium isotope system potentially useful for tracking the changing redox state of the ocean with time (Zhang et al., 2018; 2020).

However, fractionation resulting from speciation within a single oxidation state could complicated this seemingly simple relationship, and such non-redox fractionation has only been examined for relatively simple species (Abe et al., 2010). It is reasonable to expect that if different bonding environments have a strong impact on the electron density at the nucleus by changing the electronic structure of the valence orbitals, there may be measurable fractionations due to the field shift effect. Apparent non-redox effects have been detected: Brennecka et al. (2011) examined U(VI) absorption to birnessite and found a small fractionation of 0.2 ‰ consistent with the expected mass dependent fractionation. Chen et al. (2016) examined U incorporation into carbonate minerals at a variety of pH values and concentrations. They found that at high pH (8.5), there was measurable fractionation of ~0.13‰ in the incorporation of U into aragonite, which could complicate models of paleoredox that utilize U-bearing carbonates (Chen et al., 2017).

2.1.4. Motivation

Through more comprehensive theoretical modeling of dissolved and solid species, it is hoped that the present study will allow a direct comparison to previous uranium isotope measurements in experimental settings, modern environments, and samples representing deep time. We hope to also guide future studies to determine if the effects observed in computational studies can be seen elsewhere. We examine the relevant species in the systems studied by Wang et al. (2015ab) and Chen et al. (2016) to allow direct comparison of computational results to experimentally derived measurements. We also model complexes of uranium with various ligands. Uranium sulfate complexes are observed in sulfate-rich, low pH mine waters (Bernhard et al., 1998; Arnold et al., 2011) and phosphates are potentially relevant in microbial reduction, including in U(IV) species with phosphate coordination (Alessi et al., 2014) and so we model both uranyl phosphate and a solid U(IV) phosphate. Several studies have examined microbial reduction of uranium (Bosu et al. 2014; Stylo et al. 2015ab), where organic ligands are likely to play a significant role. Siderophore compounds scavenge uranium (Bouby et al. 1998; Mullen et al. 2007; Moll et al. 2008, Mo et al., 2016) and some fraction of uranium that is delivered to the seafloor is adsorbed to organic particulates (Andersen, 1982; Zheng et al., 2002). Therefore, we chose to model the siderophore functional groups from the study of Kirby et al. (2020) as simple analogs to these complex molecules. We have also included complexes of oxalate and catecholate, previously modeled by Kubicki et al. (2009). Those authors chose oxalate due to its relative simplicity as well as its common occurrence as an organic acid in natural environments. Catecholate is of interest due to observations that uranium interacts with catechol, a functional group common in humic substances (Shindo and Huang, 1992) and therefore these complexes may function as an analog for humic substances. A U(V) species UO_2-dpaea (an aminocarboxylate, dpaeaH_2 = bis(pyridyl-6-methyl-2-carboxylate)-ethylamine) has been stabilized at room temperature (Faizova et al., 2018) and allows us to examine the U(V) system in a way that may allow for direct experimental comparison in the future. Studies also indicate that U(V) intermediates may form during microbial reduction of U(VI) (Renshaw et al., 2005), though they are hard to detect due to the tendency for U(V) complexes to undergo disproportionation. Therefore we examine U(V) complexes and U(IV) complexes for the previously listed organic-bearing species, in addition to the *dpaea* species.

Uranium also readily substitutes into zircons as U(IV). Large $^{238}U/^{235}U$ fractionations of over 5‰ have been reported in one study (Hiess et al. 2012); however, a more recent study indicates smaller but still measurable fractionations of -0.60 to -0.12 ‰ (Tissot et al., 2019). We therefore model U-bearing solids for the three major oxidation states. These species will allow us to examine the role of the field shift in igneous fractionation, providing analogues for magmas of different fO_2. We can also examine the impact of bond type on U(VI) species in particular, as we can model both uranyl-type solid species as well as uranate (UO_4^{2-}) species. Table 2-1 lists all species used in this study.

2.2 Methods

Equilibrium uranium isotope ($^{238}U/^{235}U$) are estimated as the sum of mass dependent and field shift components of fractionation, derived from *ab initio* electronic structure calculations. In the present study, the DFT-PAW method of Schauble (2007; 2013) is primarily used for estimating field shift fractionation, while the equation of Urey (1947) or the force constant method of Bigeleisen and Mayer (1947) are used to determine the mass dependent component of fractionation. Field shift fractionation is assumed to be dominated by changes in the nuclear charge volume, and other shape effects are neglected.

2.2.1. Determination of mass dependent component of fractionation and DFT-PAW electron density

For each molecular species studied, optimized geometries are determined using the Perdew, Burke, and Ernzerhof (PBE) functional (Perdew et al., 1996), a gradient corrected density functional that has been commonly used for calculating isotope fractionations (e.g., Schauble et al., 2006; Meheut et al. 2007). The def2-TZVPP family of basis sets is used for all light elements (Weigend and Ahlrichs, 2005), chosen because of its balanced design across a wide range of elements and availability via the https://www.basissetexchange.org/ Basis Set Exchange (Feller, 1996; Schuchardt et al., 2007; Pritchard et al., 2019). The def2-TZVPP basis set family does not include uranium, so the slightly older def-TZVP basis set is used instead (Cao et al., 2002). Because we are mainly interested in aqueous environments we used an implicit solvation model, CPCM, the conductor-like polarizable continuum model from Barrone and Cossi (1998), to approximate molecule-water interactions. For each molecular species, vibrational frequencies are calculated at the optimized geometry, and the mass dependent component of fractionation is estimated using the equation of Urey (1947). All molecular geometry optimizations are performed with the Gaussian09 software package (Frisch et al., 2009) on the UCLA Hoffman2 computing cluster.

The PBE functional is known to underestimate vibrational frequencies (Schauble, 2004; Mehuet et al., 2007). Our calculations use raw, unscaled frequencies, but it is possible to estimate a best-fit vibrational frequency scale factor in order to quantify the potential significance of this mismatch by comparing our ab initio frequencies to experimental Raman or infrared vibrational frequencies. We examined experimental frequencies for UF_6, UF_4, UO_2F_2, and $UO_2(CO_3)_3^{4-}$ (McDowell et al., 1973; Souter and Andrews, 1997; Paine et al., 2009; Hunt et al., 1993; Lu et al., 2018; Austin et al., 2009; Wacker et al., 2017) and determined a scale factor of 2% (Figure 2-3). The standard error of the linear regression slope is 0.8%. Using $UO_2(H_2O)_5^{2+}$ versus $U(H_2O)_9^{4+}$ as a typical example of how this impacts isotopic fractionation, we find that the mass dependent component of fractionation between these species changes from 0.75‰ to 0.77‰ (i.e., ± 0.01‰) when adjusting vibrational frequencies with this 2% scale factor. Therefore, our choice to use unscaled frequencies is unlikely to be significant for this system.

The Projector Augmented Wave (PAW) method (Blöchl, 1994), with plane wave basis sets, is used for geometry and unit cell optimization of crystals, and for the DFT-PAW estimation of the field shift fractionation component. PAW datasets for non-uranium elements are taken from the AbInit JTH library (https://www.abinit.org/psp-tables) (Jollet et al., 2014). A PAW dataset for uranium was constructed and tested at UCLA using the AtomPAW software (Holzwarth et al., 2001); it is based on the $6s^2 6p^6 7s^2 6d^1 5f^3 7p^0$ valence electron configuration, and assumes a finite (non-zero), spherically symmetric nuclear charge volume. All calculations used a plane wave cutoff of 40 Hartree (1088 eV) with a Hubbard U parameter of 4.5 eV and J of 0.51 eV for the *f*-electron-derived bands of U-bearing crystals, to correct systematic errors underestimating band gaps with DFT. These DFT-U correction parameters are consistent with previous work on uraninite (Dudarev et al., 1997; Dorado et al., 2009; Dorado et al., 2010; Devey, 2011). All PAW calculations are made using the AbInit software package (Torrent et al, 2008; Gonze et al., 2009). For vapor phase species, a unit cell of ~12 Å is used in order to minimize effects on the electron density from adjacent cells.

Crystalline species are optimized under periodic boundary conditions, allowing the positions of the atoms and volumes of the unit cell to fully relax to nearest local energy minimum to the guess structure. The mass dependent component of fractionation for crystalline species is determined from PAW calculations with displaced uranium atoms, using the force constant method of Widanagamage et al. (2014), adapted from the original formulation by Bigeleisen and Mayer (1947). Formally, this method assumes that a single atom is perturbed, but in the present periodic boundary condition simulations there will be one atom moving in each unit cell. It has been found that sufficiently large unit cells, in which the perturbed atom is distant from its periodic images, yield reasonably accurate force constant results, with a trade off in larger cells between accuracy and computational complexity. As an example, in the case of uraninite ($UO_{2\,(s)}$), we were constricted to a system with 12 atoms (four UO_2 formulas) and minimum unit cell length 5.51 Å, because larger supercells of 24 and 48 atoms did not converge successfully in the DFT iteration process. Structural parameters for each solid are included in Table 2-7. All U(IV) and U(V) solids were modeled as antiferromagnetic. The actual magnetic structure of $UO_{2(s)}$ is complex, and previous studies indicate that a reasonably accurate simplified model treats $UO_{2(s)}$ as an antiferromagnet at the temperatures of interest in our study (Frazer et al., 1964; Lander and Caciuffo, 2020). We assumed this behavior to hold true for the remaining open shell species. Choosing to model the species $UO_{2(s)}$ as ferromagnetic impacts field shift components of fractionation by less than 0.1‰ in general, and impacts mass dependent fractionation similarly.

Calculations of force constant methods via the perturbation method tend to overestimate ln β for solid species at low temperatures, because ln β increasingly deviates from T^{-2} proportionality (Bigeleisen and Mayer, 1947) as temperature decreases. In order to account for this effect we adapt the method of Dauphas et al. (2017) to generate higher order correction terms. The β-factor of a given substance can be approximated by a series expansion of the reduced partition function ratio (Dauphas et al., 2012), according to the following equation:

$$1000 \ln \beta = A_1/T^2 + B\, A_1^2/T^4 + C\, A_1^3/T^6$$

Where A_1 is proportional to the total force constant, and the coefficients B and C are obtained by regressing A_2 vs. A_1^2 and A_3 vs. A_1^3, respectively, in a polynomial fit of ln β (determined via vibrational analyses of test species) vs. T^{-2}. As an initial check we first used the perturbation method of Bigeleisen and Mayer (1947) to directly determine the force constants term (A_1), and compared those with the first term in the fits obtained via the vibrational frequency method of Urey (1947). The correspondence is generally good, with a slope of 1.02 and $R^2 = 0.999$, with the mean A_1 within 2%, allowing us to make direct comparisons (Figure 2-4). We then use the fitted relationships between A_1^2 and A_2, and A_1^3 and A_3, obtained via fitting of ln β determined by the vibrational frequency method, seen in (Figure 2-5), to approximate A_2 and A_3 for ln β determined by the perturbation method. The species used for this calculation are indicated in Table 2-1. We can thus approximate the β-factor of solids at low temperatures to a reasonable degree of accuracy.

2.2.2. All-electron relativistic calculations and field shift component of fractionation

The DFT-PAW method for estimating field shift fractionation factors (Schauble, 2013) requires calibration via all-electron calculations to relate isotopic energy differences from changing nuclear charge radii to the electron density at the uranium nucleus determined by DFT-PAW calculations. Total DFT-PAW electron densities at the uranium nucleus in each species are determined using the method of Zwanziger (2009), as a post-processing step at the optimized (relaxed) geometry. Of note is that, while we calculate geometries using an implicit solvation model, we cannot include implicit solvation in the relativistic all-electron and DFT-PAW calculations – so the molecular geometries determined with implicit solvation are treated *in vacuo* in these steps. Relativistic all-electron calculations are performed at the coupled-cluster level using the eXact 2-Component Hamiltonian (X2C), as implemented in the DIRAC software package (Saue et al., 2011). The X2C method is convenient for our calculations, given that it is much faster computationally, and less demanding of memory, than true four-component methods, and because only two components are required in the Hamiltonian to determine spin-orbit coupling (Saue, 2011). Although spin-orbit coupling is not included in the plane-wave uranium DFT-PAW calibration calculations, it was necessary for preliminary comparisons between all-electron relativistic models and atomic spectroscopy measurements at the beginning of this study. All-electron calculations use uncontracted double-zeta quality relativistic Gaussian basis set for uranium (Dyall, 2007), and correlation-consistent non-relativistic basis sets (cc-pVDZ) for other elements (Dunning et al., 1989; Woon et al., 1993). The species used for this calibration are indicated in Table 2-1. Nuclear radii for the uranium atoms in these calculations are from the tabulation of Angeli (2004). Other possible sources for nuclear charge radii include Fricke and Heilig (2004), Nadjakov et al. (2008), Angeli and Marinova (2013), and Angeli (2008). The choice of nuclear charge radii impacts estimates of the field shift, due to differences in the mean squared charge radius between each tabulation. In each all-electron calibration calculation, the charge radius of the uranium nucleus is adjusted to match radii for the ^{238}U and ^{235}U isotopes, and the resulting difference in electronic energy is the field shift. Linear regression of the energy difference from all-electron calculations against DFT-PAW nuclear electron densities at the nucleus for the same species (Figure 2-6) is used to calibrate the relationship between the all-electron model equilibrium constant and the DFT-PAW electron density. The equilibrium constant is determined from the isotopic energy difference using $\Delta G = -RT\ln K$.

In order to test that our method is robust with regards to determining the field shift, we can examine the changes in electron density for the optimized structures of 3 solid species: UO_2CO_3, KUO_3, and UO_2. At 298 K, the DFT-PAW electron density for the initial guess structure of each species, respectively, is 2617 e^-/a_0^3, 2615 e^-/a_0^3, and 2533 e^-/a_0^3. For the fully optimized structures, the DFT-PAW electron density of each species, respectively, is 2611 e^-/a_0^3, 2611 e^-/a_0^3, and 2533 e^-/a_0^3. Each of these differences in electron density impact the field shift by less than 0.1‰. We therefore conclude that relatively small changes in geometry, such as those that might result from different methods of optimization for either our solid or vapor phase species, will tend to drive insignificant changes in the field shift effect.

2.2.3. Solvation model

We tested the effects of solvation on nuclear field shifts for the species $UO_2(H_2O)_5^{2+}$, $UO_2(H_2O)_5^{+}$, $UO_2(CO_3)_3^{4-}$, and $Ca_2UO_2(CO_3)_3$ using implicit solvation models, as well as the effects of inner shell hydration for UO_2CO_3 and $UO_2(CO_3)_2^{2-}$ (Table 2-2).

We determined that for $UO_2(CO_3)_3^{4-}$ and $Ca_2UO_2(CO_3)_3$ there was a small difference in electron density between structures optimized with implicit solvation models and *in vacuo* calculations, which produces minimal effects on estimated isotopic fractionations. The implicitly solvated model most closely matches known bond lengths for uranium-carbonate species, with $U\text{-}OCO_2 = 2.46$ Å for $UO_2(CO_3)_3^{4-}$ vs. measurements of 2.44 - 2.46 Å (Bargar et al., 1999; Docrat, 1999; Bernhard et al., 2001; Elzinga et al., 2004; Ikeda et al., 2007) while the unsolvated *in vacuo* model produces a bond length of 2.53 Å. Similarly, our implicitly solvated model for the species $Ca_2UO_2(CO_3)_3$ yields bond lengths of 2.46 Å - comparing favorably to the experimental range of 2.44 – 2.45 Å (Bernhard et al., 2001; Kelly et al., 2007) while the *in vacuo* model produces a bond length of 2.43 Å.

Correct treatment of inner-shell coordination of water molecules is expected to be important, in order to achieve a reasonable simulation of relevant natural (and lab-generated) complexes. For complexes where the inner-shell coordination is uncertain, we added water molecules *ad hoc* to achieve a total $CN > 6$ (e.g., with at least four equatorial U-L bonds for uranyl species). Additional waters were added past this point as well, as a rough test of the inner-shell coordination structure. If the extra water molecules did not coordinate around the central uranium atom when optimizing molecular geometries, they were removed from the model. For the main results on molecular and dissolved species presented below, we report estimates for models optimized with implicit solvation only, because this method closely reproduces experimental bond lengths while being less computationally intensive than explicit solvation. Some initial tests of explicit solvation gave conflicting results, and were not pursued further given their computationally demanding nature.

2.3. Results

Calculated field shift and mass dependent fractionations are shown in Tables 2-3 to 2-6 and Figures 2-7 to 2-12. We group species together as analogs to the experimental systems of Wang et al. (2015ab) in Table 2-3 and Figure 2-7, and Chen et al. (2016) in Table 2-4 and Figure 2-8. For the remaining species, we group according to chemical similarity, e.g., U(VI) oxyanions for Table 2-5 and Figure 2-9, organic ligands for Table 2-6 and Figures 2-10 and 2-11, and solid species in Figure 2-12 and Table 2-7. Finally, we examine select species from each of these categories in Figure 2-13. All fractionations are reported relative to the species $Ca_2UO_2(CO_3)_3$, which we chose as a common reference because it may be the most common species in seawater (Endrizzi and Rao, 2014). Finally we include Table 2-8 which displays polynomial fits up to 4000 K for all species modeled.

A general observation is that predicted fractionations usually decrease with increasing temperature, and depend primarily on the oxidation state of uranium, with $^{238}U/^{235}U$ in U(IV) ≥ U(V) > U(VI) at ~25ºC. In general U(IV) species have 1-2‰ higher $^{238}U/^{235}U$ than U(VI) species, while U(V) species have approximately 1-1.5‰ higher $^{238}U/^{235}U$ than U(VI) species. The field shift component of fractionation ranges from approximately 2-2.5‰ for U(IV) species and 1.5-2.0‰ for U(V) species, relative to U(VI) species. Estimated fractionations between species sharing the same oxidation state are much smaller, e.g. 0-0.2‰ among most U(VI) species, with a few exceptions. Speciation effects may be more pronounced for U(IV) and to a lesser extent U(V) species compared to U(VI) species, as seen in Figures 2-10 and 2-11 and Table 2-6. The presence of multiple catecholate or oxalate groups can apparently impact the field shift effect by over 1‰, with a second ligand tending to result in a lower $^{238}U/^{235}U$ for most species, while different siderophore ligands for U(V) species show a range of 1.14 ‰ for UO_2(V)-dpa to 1.56 ‰ for UO_2(V)-aminocarboxylate. Within the crystals studied, we expect U(VI) species to be approximately 0.4-1‰ lighter than $Ca_2UO_2(CO_3)_3$. The U(V)-bearing crystal studied, KUO_3, is predicted to be 0.3‰ lighter than $Ca_2UO_2(CO_3)$. U(IV)-bearing crystals will generally have 1.3-1.4‰ higher $^{238}U/^{235}U$ than $Ca_2UO_2(CO_3)_3$.

2.4. Discussion

2.4.1. Sources of uncertainty

Uncertainty in estimated field shift fractionation factors likely arises from several factors. The first is the use of implicit solvation models for geometry optimization, because calculated electron densities vary depending on the type of solvation model used (Table 2-2), and because the DFT-PAW calculations used for electron density determination do not incorporate implicit solvation directly. Rather, they are periodic boundary condition calculations in a large box (mostly vacuum) made using molecular geometries which were first relaxed within an implicit solvent model. It is unclear what impact the lack of an implicit solvation model in the DFT-PAW calculations has on electron density, but we can quantify the difference in electron density that arises due to differences in the geometries of solvated and unsolvated molecules. A variation of ~10 e^-/a_0^3, which appears reasonably likely, will alter the calculated fractionation factor by ~0.2-0.3‰ at 25°C. For example, an offset of 11 e^-/a_0^3 can be seen for the species $UO_2(CO_3)_3^{4-}$

between the *in vacuo* model and the implicitly solvated model, with the *in vacuo* model estimate approximately 0.3‰ heavier than the implicitly solvated model. Implicit solvation's impact on electron density does not appear to vary in a predictable manner, however. Implicitly solvated model geometries reproduce measured bond lengths for carbonate species well, and this is the basis for using them as the default method of calculation. However, uncertainty about the impact of solvation on electron density remains.

Another potential source of uncertainty is the fixed value of 4.5 eV chosen for the Hubbard U parameter in this study, based mainly on previous work on uraninite (UO_2). The correct value for U likely varies to some degree when examining other U(IV) species as well as U(V) and U(VI) species (Beridze and Kowalski, 2014; Beridze et al., 2016). We tested the effect of varying the Hubbard U parameter by 3.0 eV in either direction for the species UF_6, UF_5, and UF_4. For the U(VI) species UF_6, the electron density differed by ~3 e^-/a_0^3, increasing with the lower U and decreasing with the higher U. For both UF_5 and UF_4 differed by less than 1 e^-/a_0^3. Assuming that the value of the Hubbard U impacts U(VI) species by 3 e^-/a_0^3 but leaves U(IV) and U(V) species relatively unchanged, this results in an error of <0.1‰ when calculating field shifts between species of different oxidation states. We therefore do not regard the Hubbard U parameter as a likely source of significant error in estimated fractionations.

The use of finite basis sets and approximate model chemistries introduces uncertainty into any electronic structure calculation. To test this effect for fractionation factor estimates, we made analogous models calculations with a smaller (presumably less accurate) basis set family, the LANL2-DZ series of basis sets (Hay, 1983), versus the preferred def2/def-TZVP family of basis sets (Table 2-9). Model geometries optimized using the smaller basis sets appear to result in the carbonate complexes $Ca_2(UO_2CO_3)_3$ and $UO_2(CO_3)_3^{4-}$ having a lower DFT-PAW electron density than the def2/def-TZVP basis sets by ~10 e^{-}/a_0^3, but they do not appear to change the results for the species $UO_2(H_2O)_5^{2+}$ and $U(H_2O)_9^{4+}$ significantly. Similarly, optimizing molecular geometries using the hybrid functional B3LYP (Becke, 1993) or Restricted or Unrestricted Hartree-Fock methods (RHF for closed shell species and UHF for open-shell species) in Gaussian do not appear to change calculated DFT-PAW electron densities (still calculated with the PBE functional) significantly for any of the species we examined.

Uncertainties in nuclear charge radii could significantly affect estimated field shift fractionation factors. Relative to the radii we used (Angeli, 2004), the compilation of Fricke and Helig (2004) indicates an 18% larger difference in mean square charge radius difference between ^{238}U and ^{235}U; the Angeli and Marinova (2013) & Nadjakov et al. (2008) compilations indicate 6-7% larger differences, and the Angeli (2008) tabulation suggests a 4% larger difference in mean square charge radius. As an example of how this would impact our results, the present result for $UO_2(H_2O)_5^{2+}$ versus $U(H_2O)_9^{4+}$ fractionation at 25ºC, 1.34 ‰, will increase by 0.05 - 0.24 ‰ using the other charge radius compilations.

The calibration between all-electron model isotopic energy differences and DFT-PAW electron densities has significant uncertainties that impact on estimated field shift fractionations. In particular, the highly charged atomic ion U^{6+} is an outlier relative to more chemically realistic molecular species. We have found similar disagreements between atomic ions and molecules for at least some other elements, possibly indicating a limit to consistency between all-electron and projector-augmented wave models of electronic structure (and ultimately the DFT-PAW method). For an example as to how these species impact the field shift effect, if the species U^{6+} is included, the slope of the line in Figure 2-6 becomes 19 $(e^{-}/a_0^3)/(J/mol)$, with $R^2=0.957$. For $UO_2(H_2O)_5^{2+}$ versus UO_2-$U(H_2O)_9^{4+}$ fractionation, the resulting overall fractionation would be

0.98‰, versus the reported value of 1.24‰. Because molecular species are relevant to geochemistry, we have omitted atoms and atomic ions (e.g. U^{6+}, U^{5+}, U^{4+}) from the calibration. The slope of the calibration line omitting atoms and atomic ions in Figure 2-6 is approximately 16 (e^-/a_0^3)/(J/mol), with a standard error of ~1 (e^-/a_0^3)/(J/mol). Examining $UO_2(H_2O)_5^{2+}$ versus UO_2-$U(H_2O)_9^{4+}$ overall fractionation again, this standard error gives a range of 1.23‰-1.40‰.

As previously discussed we also examined potential errors in the mass dependent component of fractionation caused by uncertainties in model vibrational frequencies through determination of a scale factor. The PBE-based methods used in this study systematically underestimate vibrational frequencies by about 2% (Figure 2-3). We determined that for a sample fractionation between $UO_2(H_2O)_5^{2+}$ versus $U(H_2O)_9^{4+}$ the result of the scale factor results in an uncertainty of ± 0.01‰ (0.76‰ for the unscaled model, 0.75-0.77‰ using the scale factors. The force constant method that we used for solids tends to systematically overestimate mass dependent fractionations at low temperature (Bigeleisen and Mayer, 1947; Criss, 1991) and so we used the method of Dauphas et al. (2017) to more accurately approximate mass dependent components of fractionation for solids. We can approximate the potential error in these calculations by comparing the β-factor obtained using this correction to the β-factor obtained via vibrational frequencies for vapor phase species. For the species used in the correlation in Figure 2-5, we find that corrected force-constant models deviate from the vibrational frequency method by an average of 0.02‰, with a standard deviation of 0.07‰ at 298 K.

Solvation models also impact estimates of the mass dependent component of fractionation. For example, comparing solvated models versus in vacuo calculations, respectively, the species $UO_2(H_2O)_5^{2+}$ (1.49‰ vs. 1.64‰), $U(H_2O)_9^{4+}$ (0.74‰ vs. 0.70‰), and $Ca_2(UO_2CO_3)_3$ (1.49‰ vs. 1.54‰) each displays some degree of variation in calculated fractionation. As in the case of DFT-PAW electron density, there does not appear to be a systematic way in which the mass dependent component of fractionation is impacted by implicit solvation.

In summary, the largest source of uncertainty is in the choice of the nuclear charge radii. The Angeli (2004) radius compilation used here produces the lowest estimates of the field shift compared to other recent sources. In contrast, the value of the Hubbard U does not impact the electron density to a significant degree and therefore doesn't impact estimated field shift effects significantly. Uncertainty resulting from the choice of solvation model is significant, and does not vary in a predictable manner. We justify the choice to use implicit solvation due to its ability to reproduce measured bond lengths well, while having greater computational efficiency relative to explicit solvation. The choice of which species to include in the calibration line for the DFT-PAW method impacts the field shift effect substantially, by up to 0.3‰ in the case of the apparent U^{6+}(v) outlier. Errors in the mass dependent component of fractionation calculated via the equation of Urey (1947) are likely to be small, on the order of 0.1‰, mainly because the mass-dependent component of fractionation is itself smaller than the field shift component. However, at present we cannot directly compare solids to other species due to the force constant method's tendency to overestimate fractionations at low temperature.

2.4.2. Geochemical systematics of equilibrium $^{238}U/^{235}U$ fractionation

Our results confirm that - to first order - the most important determining factor of equilibrium isotope fractionation in uranium is its oxidation state. At 298 K, the field shift component of fractionation is always larger than the mass dependent component of fractionation between U(VI) and U(IV) species. This is also true for most U(V) species, when compared to U(VI) species, with the only exception being the U(V) dicatecholate species, which has an electron density similar to that of U(VI) species. The field shift component of fractionation for U(IV) vs. U(VI) species is typically on the order of ~1.5-2‰ while the field shift for U(V) vs. U(VI) species is ~1.5‰. Due to the difference in the mass dependent components of fractionation, however, U(V) species may have $^{238}U/^{235}U$ comparable to U(IV) species at Earth surface temperatures in some cases, as seen in Table 2-6 and Figures 2-9 and 2-10. Indeed, we find that the U(V) species $UO_2(H_2O)_5^+$ will have slightly higher $^{38}U/^{235}U$ than some U(IV) species. Sato et al. (2021) also performed *ab initio* calculations on U(V) species, allowing us to make a direct comparison with their results. They examined a multi-step reaction of U(VI) binding to a cytochrome analog, then being reduced from U(VI) to U(V) and subsequently from U(V) to U(IV). They determined that the fractionation associated with the initial reduction step to U(V) (1.44-1.60‰) was much larger than the second step from U(V) to U(IV) (0.76-0.79‰). Sato et al. hypothesize that the first electron added to the 5*f* orbital produces a larger screening effect on the 6*s* electrons than the second electron. Calculated field shifts for U(V) species, as compared to U(IV) species, appear to support their hypothesis.

For species in the same physical state, with uranium in the same oxidation state, isotope shifts tend to be small. Mass dependent components of fractionation tend to vary by approximately 0-0.1‰ while field shift fractionations are typically on the order of 0-0.3‰. However, some non-redox fractionations among U(VI) species can be as large as 0.6-1.0‰. Such shifts are large enough to be measurable. Sato et al. (2021) find that the binding of their initial U(VI) $UO_2(CO_3)_3^{4-}$ molecule to a cytochrome analog resulted in a calculated fractionation of 0.6‰, which is comparable to the present results for some organic ligands such as hydroxamate (0.55‰), as well as in $UO_2NO_3(H_2O)_3^+$ (0.49‰) relative to $Ca_2UO_2(CO_3)_3$.

Solid species with U(VI) and U(V) are predicted to have lower $^{238}U/^{235}U$ than vapor phase or aqueous species of the same oxidation state at 298 K, owing primarily to the field shift component of fractionation. An exception is the solid species UO_2CO_3, which is predicted to be 0.42‰ heavier than seawater at 298 K, and 1.0-1.6‰ heavier than other U(VI) solids. This species is an outlier and due to its sheetlike structure, we will regard it separately from other U(VI) solids. U(IV) species are predicted to be isotopically similar in most solid, aqueous, and vapor phases. Within the category of U(VI)-bearing solid species, uranate-type structures are predicted to have lower $^{238}U/^{235}U$ than uranyl-type structures on average, by approximately 0.4-0.6‰ at 298 K. While only one crystalline U(V)-bearing species was modeled, KUO_3, it is predicted to be approximately 0.2-0.8‰ heavier than solid U(VI) species at 298 K. There is little variation amongst U(IV) species, within ±0.1‰ at 298 K, suggesting that the limited variety of species studied here may still be representative of more complex and diverse natural materials. They are predicted to be 2.0-2.6‰ heavier than solid U(VI) species. At 500 K, U(IV) species are 1.3-1.7‰ heavier than U(VI) species while U(V)-bearing KUO_3 is 0.3-0.6‰ heavier than solid U(VI) species. At 1000 K, U(IV) species are still 0.8-0.9‰ heavier than solid U(VI) species, while the single U(V) species studied is 0.2-0.3‰ heavier than solid U(VI) species. Owing to the field shift decreasing according to $1/T$ as opposed to $1/T^2$ for the mass dependent component of fractionation, we are able to see that the field shift effect still produces significant isotopic differences for solids between different oxidation states up to metamorphic and igneous temperatures. If we take solids as being roughly analogous to U-bearing melts, then melts of different oxidation states should also be isotopically distinct across a wide range of temperatures.

Structural parameters such as the uranyl U=O bond length or average U-ligand bond length do not appear to systematically correlate with field shift fractionation (beyond their correlation with oxidation state). A possible exception is U(V) uranyl species. As seen in Figure 2-14, there is no clear trend for U=O bond length versus electron density with U(VI) species, but there is a correlation for U(V) species. The ligand bond length does not appear to have any clear relationship with the electron density of any of the oxidation states studied (Figure 2-15). Similarly, the ligands themselves do not show a simple universal relationship with the electron density. We can make some qualitative observations, however. U(VI) species with small N-bearing ligands such as NO_3^+ (Table 2-5) and hydroxamate (Table 2-6) appear to have lower electron densities than otherwise comparable U(VI) species, resulting in field shifts of ~0.5-0.6‰ favoring high $^{238}U/^{235}U$ in the former. U(VI) species with higher charged (-2 or -3) ligands such as phosphate, carbonate, and aromatic compounds (e.g. catecholate) (Figures 2-8 to 2-10 and Tables 2-5 and 2-6) appear to have higher electron densities. Additional ligands tend to result in a higher electron density in most U(VI) and U(V) uranyl-type species, but this effect is not significant in U(IV) species.

2.4.3. Comparison with measurements

The present results are compared to the experiments of Wang et al. (2015ab) in Table 2-3 and Figure 2-7. We can also compare these results to microbial reduction studies, which typically find the reduced phase of uranium to be enriched by approximately 1‰ (Basu et al. 2014; Stirling et al. 2015; Stylo et al. 2015ab). In the experiments Wang et al. (2015ab), U(IV) was oxidized by dissolved oxygen under acidic conditions, with either solid UO_2 or aqueous U(IV) as the starting material. We therefore compare the models for these U(IV) species with models for aqueous U(VI) phases likely to be present as products in the experimental system. Wang et al. (2015ab) determine fractionations of 1.1 - 1.6‰ between aqueous U(VI) (likely $UO_2(H_2O)_5^{2+}$) and U(IV) (likely $U(H_2O)_9^{4+}$) species, and argue that 1.6‰ is more representative of a reaction progressing toward equilibrium exchange. They determined that it was difficult to achieve equilibrium with the bulk solid U(IV) due to kinetic effects, and did not regard their results in that experiment as approaching equilibrium. We estimate that $UO_{2(s)}$ and U(IV) $_{(aq)}$ have very similar isotopic compositions, with $^{238}U/^{235}U$ 1.24‰ and 1.26‰ higher, respectively, compared to $UO_2(H_2O)_5^{2+}$. We also observe that chloride-bearing U(VI) species, expected in chloride-rich aqueous solutions, will become isotopically lighter with an increasing number of chlorides; the species $UO_2Cl_3(H_2O)_2^-$ being 0.2‰ lighter than $UO_2(H_2O)_5^{2+}$. The U(V) species $UO_2(H_2O)_5^+$, which was not directly observed in the experiments, may nonetheless play a role as a reaction intermediate. We estimate that this species will have higher $^{238}U/^{235}U$ than both the aqueous and solid U(IV) species by ~0.3‰, and be 1.6‰ heavier than its U(VI) counterpart. Similarly, solid U(IV) species $CaU(PO_4)_2$, modeled because uranium-phosphate bonds have been detected as the product of microbial reduction, also falls within a similar range, being 1.39‰ higher than the seawater U(VI) species studied. Organic U(IV) species which are aqueous also fall within this range of 1-2‰.

Non-redox fractionation was studied in Chen et al. (2016), who examined uranium isotope fractionation for uranium(VI) incorporated from aqueous solution into calcite and aragonite during precipitation at 7.5 pH and 8.5 pH at 298 K. They detected no fractionation for calcite precipitation at either pH, but determined a 0.13‰ fractionation during aragonite precipitation at pH 8.5, with the precipitated aragonite having higher $^{238}U/^{235}U$. In a subsequent study Chen et al. (2017) modeled changes in uranium carbonate speciation throughout the Phanerozoic, and using the results of their previous experiment estimated that the fractionation between carbonate sediments and seawater may have varied from 0.11-0.23‰ across the Phanerozoic as a consequence of changes in seawater chemistry. They calculate a sediment-seawater fractionation of approximately 0.18‰ at the Permian-Triassic boundary, which could impact estimates of seafloor anoxia by as much as 32%. Studies of uranium in carbonate sediments have assumed no fractionation for uranium bound within carbonate sediments (Weyer et al., 2008; Brennecka et al., 2011), so it is important to determine potential seawater-carbonate mineral fractionations and to compare them to the results of Chen et al. (2016). The results indicate that the field shift effect rather than mass dependent fractionation is most likely to drive differences in isotopic composition under these conditions. The relevant species with the highest predicted $^{238}U/^{235}U$ species is $UO_2CO_3(H_2O)_3$. $UO_2(CO_3)_3^{4-}$, in contrast, has the lowest predicted $^{238}U/^{235}U$. The difference between the two is approximately 0.4‰. All other species fall between these two values. Another common species, $Ca_2UO_2(CO_3)_3$, is 0.2‰ lighter than $UO_2CO_3(H_2O)_3$ (aq) and 0.2‰ heavier than $UO_2(CO_3)_3^{4-}$. The solid species UO_2CO_3 is predicted to have the highest $^{238}U/^{235}U$, being 0.4‰ heavier than seawater. Chen et al. (2016) posited that negatively charged species would be heavier than neutral species, but we instead find that they seem to have lower $^{238}U/^{235}U$ in equilibrium with neutral species. Previous studies indicate that uncharged species tend to incorporate more readily into calcite, while uranyl within aragonite has a coordination number consistent with a tris-carbonato species (Reeder et al., 2000; 2001). While it is unclear which species drive the effects of Chen et al. (2016), speciation effects appear to be significant enough to drive fractionations of a similar magnitude to what was found in that experiment, and therefore may warrant careful consideration in paleo-redox studies using the $^{238}U/^{235}U$ proxy.

2.5. Conclusions

The field shift component of fractionation is the main driver of uranium isotope fractionation within the uranium system. We determine that equilibrium reduction of U(VI) to

U(IV) results in the U(IV) species having 1-2‰ higher $^{238}U/^{235}U$ than oxidized species. We also find that reduction of U(VI) to U(V) results in the U(V) species having approximately 1-1.5‰ higher $^{238}U/^{235}U$. The overlap between U(IV) and U(V) is likely a result of the initial addition of the first 5*f* electron having a larger impact on the electron density than the second, and the weaker mass dependent fractionation between U(VI)-U(V) when compared to U(VI)-U(IV). Within the same oxidation state, mass dependent components of fractionation are expected to be insignificant in determining the overall isotopic fractionation. Speciation effects tend to be minor as well, compared to reduction or oxidation. However, they still may warrant careful consideration in the case of the uranium carbonate system, as they may be large enough to impact paleoredox estimates (Chen et al., 2017). Organic ligands may also impart measurable isotope fractionations, as seen in some siderophore ligands; these substances may play a role in controlling fractionations during microbial reduction. The most accurate and efficient treatment of solvation for fractionation estimates is not yet resolved, but implicit solvation closely reproduces bond lengths for select species.

Tables

Table 2-1: All species analyzed are displayed below alongside the reference for the initial guess structure and the method of structural optimization. Species with * symbol are used for the DFT-PAW calibration line while species with ‡ symbol are used to calibrate the perturbation method by the method of Dauphas et al. (2012). Abbreviations: ox – oxalate, cat = catecholate, dpa = dipicolinate, carb = α-hydroxycarboxylate, amino = α-aminocarboxylate, phenyl = hydroxy-phenyloxazalone, amate = hydroxamate, imid = α-hydroxyimidazolate.

Species	Structure reference	Method of optimization
US_3*	Adapted from Liang et al. (2002)	Unoptimized
UOF_4^{2-} *, UO_2F_2 *	Adapted from Kovács and Konings (2006)	Unoptimized
UO_3 *	Zhou et al. (2000)	Unoptimized
UN_2 *	Tecmer et al. (2011)	Unoptimized
UF_6 *‡	Privalov et al. (2002)	PBE-def-TZVP/def2-TZVPP
UF_4	Shamov et al. (2007)	PBE-def-TZVP/def2-TZVPP
UCl_6 *‡	Malli (2002)	PBE-def-TZVP/def2-TZVPP
UOS *	Wang et al. (2009)	Unoptimized
UO_2^{2+} *	Zhou et al. (2000)	Unoptimized
UO_2Cl_2 *	Adapted from Su et al. (2011)	Unoptimized
UO_4^{2-} ‡	Bolvin et al. (2001)	PBE-def-TZVP/def2-TZVPP
$UO_2(H_2O)_5^{2+}$ *, $UO_2(H_2O)_5^{+}$	Gutowkski and Dixon (2006)	PBE-def-TZVP/def2-TZVPP
$U(H_2O)_9^{4+}$, $UO_2SO_4(H_2O)_3$, $UO_2(SO_4)_2(H_2O)_3^{2-}$	Adapted from Hennig et al. (2007)	PBE-def-TZVP/def2-TZVPP
$UO_2Cl(H_2O)_4^{+}$ ‡, $UO_2Cl_2(H_2O)_3$ ‡, $UO_2Cl_3(H_2O)_2^{-}$‡	Adapted from Soderholm et al. (2011)	PBE-def-TZVP/def2-TZVPP
$UO_2CO_3(H_2O)_3$ ‡	Adapted from Vasquez et al. (2003)	PBE-def-TZVP/def2-TZVPP
$UO_2(CO_3)_2H_2O^{2-}$ ‡, $CaUO_2(CO_3)_3^{2-}$ ‡, $MgUO_2(CO_3)_3^{2-}$ ‡	Adapted from Kerisit and Liu (2010)	PBE-def-TZVP/def2-TZVPP
$UO_2(CO_3)_3^{4-}$ ‡	Adapted from Li and Burns (2001)	PBE-def-TZVP/def2-TZVPP
$Ca_2UO_2(CO_3)_3$ ‡, $Mg_2UO_2(CO_3)_3$ ‡	Adapted from Bernhard et al. (2001)	PBE-def-TZVP/def2-TZVPP
$UO_2NO_3(H_2O)_3^{+}$, $UO_2(NO_3)_2(H_2O)_2$	Adapted from Rodriguez-Jeangros and Seminario (2014)	PBE-def-TZVP/def2-TZVPP
$UO_2PO_4(H_2O)_3^{-}$, $UO_2(PO_4)_2H_2O^{4-}$, UO_2(VI)-ox$(H_2O)_3$, UO_2(VI)-cat$(H_2O)_3$, UO_2(V)-ox$(H_2O)_3^{-}$, UO_2(V)-cat$(H_2O)_3^{-}$	Adapted from Kubicki et al. (2009)	PBE-def-TZVP/def2-TZVPP
UO_2(VI)-ox$_2$H2O^{2-}, UO_2(VI)-cat$_2H_2O^{2-}$, UO_2(V)-ox$_2$H2O^{3-}, UO_2(V)-cat$_2H_2O^{3-}$, U(IV)-ox$(H_2O)_7^{2+}$, U(IV)-ox$_2(H_2O)_4$, U(IV)-cat$(H_2O)_7^{2+}$, U(IV)-cat$_2(H_2O)_4$, U(IV)-carb$(H_2O)_7^{2+}$, $U(OH)_6$, $U(OH)_5$, $U(OH)_4$	Created *ad hoc*	PBE-def-TZVP/def2-TZVPP
UO2(VI)-dpaH2O, UO_2(V)-dpa^{-}	Faizova et al. (2018)	PBE-def-TZVP/def2-TZVPP
UO_2(VI)-carb$(H_2O)_4$, UO_2(VI)-amino$(H_2O)_3^{2+}$, UO_2(VI)-phenyl$(H_2O)_3^{+}$, UO_2(VI)-amate$(H_2O)_4^{+}$, UO_2(VI)-imid$(H_2O)_3$, UO_2(V)-carb$(H_2O)_4^{-}$, UO_2(V)-amino$(H_2O)_3^{+}$, UO_2(V)-phenyl$(H_2O)_3$, UO_2(V)-amate$(H_2O)_4$, UO_2(V)-imid$(H_2O)_3^{-}$	Adapted from Kirby et al. (2020)	PBE-def-TZVP/def2-TZVPP
$UO_2CO_{3\,(s)}$	Finch et al. (1999)	PBE-PAW
$BaUO_2Si_2O_{6\,(s)}$	Plaisier et al. (1995)	PBE-PAW
$Li_4UO_{5\,(s)}$	Hoekstra and Siegel (1964)	PBE-PAW
$BaUO_{4\,(s)}$	Loopstra and Rietveld (1969)	PBE-PAW
$KUO_{3\,(s)}$	Rudorff et al. (1962)	PBE-PAW
$UO_{2\,(s)}$	Wyckoff (1963)	PBE-PAW
$UTi_2O_{6\,(s)}$	Szymanski and Scott (1982)	PBE-PAW
$CaU(PO_4)_{2\,(s)}$	Dusausoy et al. (1996)	PBE-PAW

Table 2-2: The effects of solvation on molecular structures and calculated field shift fractionation factors. For each species, fractionations are given relative to an otherwise equivalent model of that species with no solvation (i.e., *in vacuo*).

Species	Solvation model	U=O bond length (Å)	U-ligand bond length (Å)	H_2O bond length (Å)	DFT-PAW electron density (e^-/a_0^3)	Field shift produced by solvation model (‰)
$UO_2(H_2O)_5^{2+}$	*In vacuo*	1.76	-	2.48	2609	-
	Implicit	1.77	-	2.46	2615	-0.15
$UO_2CO_3(H_2O)_3$	*In vacuo*	1.81	2.27	2.59	2614	-
	Implicit	1.80	2.33	2.57	2609	0.13
$UO_2(CO_3)_2H_2O^{2-}$	*In vacuo*	1.84	2.35	2.93	2617	-
	Implicit	1.83	2.38	2.60	2617	0
$UO_2(CO_3)_3^{4-}$	*In vacuo*	1.85	2.54	-	2617	-
	Implicit	1.85	2.46	-	2628	-0.28
$Ca_2UO_2(CO_3)_3$	*In vacuo*	1.83	2.43	-	2622	-
	Implicit	1.83	2.46	-	2619	0.08
$UO_2(H_2O)_5^+$	*In vacuo*	1.81	-	2.59	2541	-
	Implicit	1.83	-	2.57	2540	-0.03

Table 2-3: Estimated fractionation factors relevant to redox experiments reported in Wang et al. (2015ab). All fractionations are reported relative to $Ca_2UO_2(CO_3)_3$ at 298 K (ln β = 1.49‰ and DFT-PAW electron density = 2619 e^-/a_0^3). We have included the U(V) species $UO_2(H_2O)_5^+$, which was not discussed or found in the original experimental system.

	U=O bond length (Å)	U-ligand bond length (Å)	U-OH_2 bond length (Å)	DFT-PAW electron density (e^-/a_0^3)	$^{238}U/^{235}U$ mass dependent (ln α_{md}) component of fractionation (‰)	$^{238}U/^{235}U$ field shift relative to $Ca_2UO_2(CO_3)_3$ (‰)	$^{238}U/^{235}U$ total fractionation relative to $Ca_2UO_2(CO_3)_3$ (‰)
$UO_2(H_2O)_5^{2+}$	1.77	-	2.46	2615	0.00	0.12	0.12
$U(H_2O)_9^{4+}$	-	-	2.44	2533	-0.75	2.09	1.34
$UO_{2\ (s)}$	-	2.39	-	2533	-0.81	2.20	1.38
$UO_2Cl(H_2O)_4^+$	1.78	2.62	2.50	2612	0.10	0.20	0.30
$UO_2Cl_2(H_2O)_3$	1.79	2.67	2.56	2615	-0.07	0.11	0.04
$UO_2Cl_3(H_2O)_2^-$	1.80	2.71	2.58	2618	-0.11	0.03	-0.08
$UO_2(H_2O)_5^+$	1.83	-	2.57	2540	-0.32	2.04	1.72

Table 2-4: Calculated molecular structures and estimated $^{238}U/^{235}U$ fractionation factors in uranium carbonate species relevant to the experiments of Chen et al. (2016). Fractionations are reported relative to the species $Ca_2UO_2(CO_3)_3$ at 298 K (ln β = 1.49‰ and DFT-PAW electron density = 2619 e^-/a_0^3). The mineral rutherfordine, $UO_2CO_{3(s)}$, is also included.

		U=O bond length (Å)	U-ligand bond length (Å)	H_2O bond length (Å)	DFT-PAW electron density (e^-/a_0^3)	$^{238}U/^{235}U$ mass dependent (ln α_{md}) component of fractionation (‰)	$^{238}U/^{235}U$ field shift relative to $Ca_2UO_2(CO_3)_3$ (‰)	$^{238}U/^{235}U$ total fractionation relative to $Ca_2UO_2(CO_3)_3$ (‰)
$UO_2CO_3(H_2O)_3$		1.80	2.33	2.57	2609	-0.06	0.26	0.20
$UO_2(CO_3)_2H_2O^{2-}$		1.83	2.38	2.60	2617	-0.03	0.07	0.04
$UO_2(CO_3)_3^{4-}$		1.85	2.46	-	2628	-0.05	-0.23	-0.28
$CaUO_2(CO_3)_3^{2-}$		1.83	2.40	-	2626	-0.05	-0.16	-0.21
$Ca_2UO_2(CO_3)_3$		1.83	2.46	-	2619	-	-	-
$MgUO_2(CO_3)_3^{2-}$		1.83	2.40	-	2624	-0.03	-0.11	-0.14
$Mg_2UO_2(CO_3)_3$		1.82	2.46	-	2619	0.01	0.01	0.02
$UO_2CO_{3\ (s)}$		1.77	2.51	-	2611	0.21	0.22	0.43

Table 2-5: Uranyl complexes with oxyanions. All fractionations are reported relative to $Ca_2UO_2(CO_3)_3$ at 298 K (ln β = 1.49‰ and DFT-PAW electron density = 2619 e^-/a_0^3).

	U=O bond length (Å)	U-ligand bond length (Å)	H_2O bond length (Å)	DFT-PAW electron density (e^-/a_0^3)	$^{238}U/^{235}U$ mass dependent (ln α_{md}) component of fractionation (‰)	$^{238}U/^{235}U$ field shift relative to $Ca_2UO_2(CO_3)_3$ (‰)	$^{238}U/^{235}U$ total fractionation relative to $Ca_2UO_2(CO_3)_3$ (‰)
$UO_2CO_3(H_2O)_3$	1.80	2.33	2.57	2609	-0.06	0.26	0.20
$UO_2(CO_3)_2H_2O^{2-}$	1.83	2.38	2.60	2617	-0.03	0.07	0.04
$UO_2(CO_3)_3^{4-}$	1.85	2.46	-	2628	-0.05	-0.23	-0.28
$UO_2SO_4(H_2O)_3$	1.79	2.35	2.55	2607	0.01	0.33	0.34
$UO_2(SO_4)_2(H_2O)_3^{2-}$	1.81	2.26	2.55	2591	-0.01	0.74	0.73
$UO_2NO_3(H_2O)_3^+$	1.78	2.45	2.44	2598	-0.05	0.54	0.49
$UO_2(NO_3)_2(H_2O)_2$	1.79	2.48	2.53	2612	0.04	0.19	0.23
$UO_2PO_4(H_2O)_3^-$	1.82	2.27	2.60	2612	0.00	0.19	0.19
$UO_2(PO_4)_2H_2O^{4-}$	1.85	2.29	2.31	2633	-0.04	-0.33	-0.37

Table 2-6: Complexes of uranium with organic ligands. Geometries for siderophore functional groups are taken from Kirby et al. (2020), the dpa (dipicolinate) structure is taken from Faizova et al. (2019). All fractionations are reported relative to $Ca_2UO_2(CO_3)_3$ at 298 K (ln β = 1.49‰ and DFT-PAW electron density = 2619 e^-/a_0^3). Also included is a solid U(IV) phosphate species $CaU(PO_4)_2$. Abbreviations: ox – oxalate, cat = catecholate, dpa = dipicolinate, carb = α-hydroxycarboxylate, amino = α-aminocarboxylate, phenyl = hydroxy-phenyloxazalone, amate = hydroxamate, imid = α-hydroxyimidazolate

	U=O bond length (Å)	U-ligand bond length (Å)	H_2O bond length (Å)	DFT-PAW electron density (e^-/a_0^3)	$^{238}U/^{235}U$ mass dependent (ln α_{md}) component of fractionation (‰)	$^{238}U/^{235}U$ field shift relative to $Ca_2UO_2(CO_3)_3$ (‰)	$^{238}U/^{235}U$ total fractionation relative to $Ca_2UO_2(CO_3)_3$ (‰)
UO_2(VI)-ox$(H_2O)_3$	1.80	2.29	2.53	2614	-0.03	0.13	0.10
UO_2(VI)-ox_2H2O^{2-}	1.82	2.35	2.59	2623	-0.02	-0.09	-0.11
UO_2(V)-ox$(H_2O)_3^-$	1.85	2.41	2.62	2555	-0.31	1.66	1.35
UO_2(V)-$ox_2H_2O^{3-}$	1.87	2.46	2.70	2602	-0.33	0.45	0.12
U(IV)-ox$(H_2O)_7^{2+}$	-	2.12	2.61	2520	-0.72	2.54	1.82
U(IV)-$ox_2(H_2O)_4$	-	2.24	2.61	2523	-0.76	2.47	1.89
UO_2(VI)-cat$(H_2O)_3$	1.82	2.28	2.57	2613	-0.08	0.17	0.09
UO_2(VI)-$cat_2H_2O^{2-}$	1.84	2.35	2.68	2629	-0.11	-0.24	-0.35
UO_2(V)-cat$(H_2O)_3^-$	1.86	2.41	2.70	2554	-0.34	1.66	1.32
UO_2(V)-$cat_2H_2O^{3-}$	1.90	2.44	2.78	2604	-0.38	0.39	0.01
U(IV)-cat$(H_2O)_7^{2+}$	-	2.20	2.57	2520	-0.72	2.53	1.74
U(IV)-$cat_2(H_2O)_4$	-	2.28	2.69	2514	-0.76	2.70	1.94
UO_2(VI)-dpaH_2O	1.81	2.48	2.89	2617	-0.01	0.07	0.06
UO_2(V)-dpa^-	1.85	2.50	-	2563	-0.24	1.45	1.21
UO_2(VI)-carb$(H_2O)_4$	1.81	2.16	2.55	2625	0.01	-0.14	-0.13
UO_2(V)-carb$(H_2O)_4^-$	1.86	2.34	2.61	2557	-0.36	1.59	1.23
U(IV)-carb$(H_2O)_7^{2+}$	-	2.48	2.43	2535	-0.57	2.16	1.59
UO_2(VI)-amino$(H_2O)_3^{2+}$	1.78	2.31	2.48	2616	-0.03	0.09	0.06
UO_2(V)-amino$(H_2O)_3^+$	1.84	2.46	2.58	2543	-0.32	1.94	1.62
UO_2(VI)-phenyl$(H_2O)_3^+$	1.80	2.36	2.59	2613	-0.03	0.16	0.13
UO_2(V)-phenyl$(H_2O)_3$	1.84	2.45	2.66	2551	-0.29	1.76	1.47
UO_2(VI)-amate$(H_2O)_4^+$	1.80	2.15	2.54	2595	-0.01	0.62	0.61
UO_2(V)-amate$(H_2O)_4$	1.85	2.26	2.64	2549	-0.34	1.79	1.45
UO_2(VI)-imid$(H_2O)_3$	1.82	2.17	2.53	2626	0.01	-0.17	-0.16
UO_2(V)-imid$(H_2O)_3^-$	1.87	2.34	2.65	2565	-0.35	1.39	1.04
$CaU(PO_4)_{2\ (s)}$	-	2.46	-	2531	-0.81	2.25	1.39

Table 2-7: Structural parameters, electron density, and isotope fractionations for solids species relative to $Ca_2UO_2(CO_3)_3$ at 298 K (ln β = 1.49‰ and DFT-PAW electron density = 2619 e^-/a_0^3). Additional isotopic fractionations listed at 500 K (ln β = 0.58‰) and 1000 K respectively (lnβ = 0.15‰).

Species	Structural parameters	Average U-O bond length (Å)	DFT-PAW electron density (e^-/a_0^3)	Total uranium coordination number	Mass dependent component (ln α_{md}) of fractionation at 298 K, 500 K, and 1000 K (‰)	Field shift component of fractionation relative to $Ca_2UO_2(CO_3)_3$ at 298 K, 500 K, and 1000 K (‰)	Total fractionation relative to $Ca_2UO_2(CO_3)_3$ at 298 K, 500 K, and 1000 K (‰)
UO_2CO_3 - ruthorfordine	N = 28 A =9.81 Å, B = 10.04 Å, and C = 4.37 Å	2.33	2611	8	0.21 0.08 0.02	0.22 0.13 0.07	0.43 0.22 0.09
$BaUO_2Si_2O_6$	N = 48 A = 5.72 Å; B = 16.89 Å; C = 7.74 Å	2.13	2648	6	0.12 0.05 0.01	-0.74 -0.44 -0.22	-0.62 -0.39 -0.21
Li_4UO_5	N = 20 A = 6.77 Å; B = 6.77 Å; C = 4.49 Å	2.10	2665	6	-0.04 -0.02 0.00	-1.17 -0.70 -0.35	-1.21 -0.71 -0.35
$BaUO_4$	N = 24 A = 5.84 Å; B = 8.24 Å; C = 8.32 Å	2.12	2658	6	-0.07 -0.03 -0.01	-0.97 -0.58 -0.29	-1.05 -0.61 -0.30
KUO_3	N = 20 A = 8.68 Å; B = 8.68 Å; C = 4.34 Å	2.17	2611	6	-0.63 -0.26 -0.07	0.22 0.13 0.07	-0.41 -0.12 0.00
UO_2 – uraninite	N = 12 A = 5.51 Å; B = 5.51 Å; C = 5.51 Å	2.39	2533	8	-0.81 -0.33 -0.09	2.20 1.31 0.66	1.39 0.98 0.57
UTi_2O_6 - brannerite	N = 18 A = 9.99 Å; B = 3.77 Å; C = 7.11 Å	2.45	2531	8	-0.96 -0.38 -0.10	2.25 1.36 0.67	1.30 0.96 0.55
$CaU(PO_4)_2$	N = 48 A = 14.10 Å, B = 7.04 Å, C = 6.20 Å	2.46	2531	8	-0.85 -0.34 -0.09	2.25 1.34 0.67	1.39 1.00 0.57

Table 2-8: Polynomial fits of the fractionations relative to the species $Ca_2UO_2(CO_3)_3$, in the form 1000 ln $\alpha_{total} = A_1/T^2 + A_2T^4 + C/T$, with the first two constants corresponding to the mass dependent component of fractionation and the last constant corresponding to the nuclear field shift. Fits are constrained at temperatures from 250 K to 4000 K.

	A_1	A_2	C
$UO_2(H_2O)_5^{2+}$	$5.83x10^{3}$	$-5.05x10^{8}$	36.74
$U(H_2O)_9^{4+}$	$-7.30x10^{4}$	$6.07x10^{8}$	660.44
$UO_{2\ (s)}$	$-8.56x10^{4}$	$1.09x10^{9}$	655.55
$UO_2Cl(H_2O)_4^{+}$	$-4.94x10^{2}$	$-3.23x10^{8}$	58.15
$UO_2Cl_2(H_2O)_3$	$-3.46x10^{3}$	$-2.62x10^{8}$	31.94
$UO_2Cl_3(H_2O)_2^{-}$	$-7.67x10^{3}$	$-1.60x10^{8}$	9.48
$UO_2(H_2O)_5^{+}$	$-3.07x10^{4}$	$1.87x10^{8}$	607.40
$UO_2CO_3(H_2O)_3$	$-4.09x10^{3}$	$-9.88x10^{7}$	76.05
$UO_2(CO_3)_2H_2O^{2-}$	$-2.40x10^{3}$	$-9.56x10^{6}$	20.96
$UO_2(CO_3)_3^{4-}$	$-6.80x10^{3}$	$1.89x10^{8}$	-68.33
$CaUO_2(CO_3)_3^{2-}$	$-4.70x10^{3}$	$3.57x10^{7}$	-47.22
$MgUO_2(CO_3)_3^{2-}$	$-2.78x10^{3}$	$-2.58x10^{7}$	-33.56
$Mg_2UO_2(CO_3)_3$	$1.29x10^{3}$	$-5.59x10^{7}$	2.79
$UO_2CO_{3\ (s)}$	$2.33x10^{4}$	$-4.05x10^{8}$	66.35
$UO_2SO_4(H_2O)_3$	$3.92x10^{3}$	$-2.87x10^{8}$	97.01
$UO_2(SO_4)_2(H_2O)_3^{2-}$	$6.52x10^{2}$	$-1.58x10^{8}$	219.72
$UO_2NO_3(H_2O)_3^{+}$	$-3.25x10^{3}$	$-1.34x10^{8}$	161.03
$UO_2(NO_3)_2(H_2O)_2$	$6.99x10^{3}$	$-3.20x10^{8}$	56.39
$UO_2PO_4(H_2O)_3^{-}$	$9.21x10^{2}$	$-1.11x10^{8}$	56.96
$UO_2(PO_4)_2H_2O^{4-}$	$-4.78x10^{3}$	$8.02x10^{7}$	-99.81
UO_2(VI)-ox$(H_2O)_3$	$4.30x10^{2}$	$-2.42x10^{8}$	40.04
UO_2(VI)-ox$_2H_2O^{2-}$	$9.74x10^{2}$	$-2.06x10^{8}$	-27.53
UO_2(V)-ox$(H_2O)_3^{-}$	$-2.97x10^{4}$	$1.91x10^{8}$	493.52
UO_2(V)-ox$_2$H2O^{3-}	$-3.57x10^{4}$	$5.12x10^{8}$	132.69
U(IV)-ox$(H_2O)_7^{2+}$	$-7.84x10^{4}$	$1.16x10^{9}$	765.78
U(IV)-ox$_2(H_2O)_4$	$-6.47x10^{4}$	$1.06x10^{9}$	737.42
UO_2(VI)-cat$(H_2O)_3$	$-6.97x10^{3}$	$-6.21x10^{7}$	51.70
UO_2(VI)-cat$_2H_2O^{2-}$	$-1.21x10^{4}$	$1.67x10^{8}$	-70.91
UO_2(V)-cat$(H_2O)_3^{-}$	$-3.64x10^{4}$	$4.95x10^{8}$	495.62
UO_2(V)-cat$_2H_2O^{3-}$	$-4.07x10^{4}$	$5.85x10^{8}$	115.58
U(IV)-cat$(H_2O)_7^{2+}$	$-8.50x10^{4}$	$1.19x10^{9}$	755.81
U(IV)-cat$_2(H_2O)_4$	$-8.20x10^{4}$	$1.18x10^{9}$	804.56
UO_2(VI)-dpaH_2O	$2.57x10^{3}$	$-3.05x10^{8}$	22.17
UO_2(V)-dpa^{-}	$-2.29x10^{4}$	$1.37x10^{8}$	431.95
UO_2(VI)-carb$(H_2O)_4$	$-1.03x10^{3}$	$9.84x10^{7}$	-43.08
UO_2(V)-carb$(H_2O)_4^{-}$	$-3.67x10^{4}$	$3.98x10^{8}$	473.48
U(IV)-carb$(H_2O)_7^{2+}$	$-5.85x10^{4}$	$6.75x10^{8}$	643.20
UO_2(VI)-amino$(H_2O)_3^{2+}$	$-2.89x10^{3}$	$-6.22x10^{7}$	26.60
UO_2(V)-amino$(H_2O)_3^{+}$	$-3.14x10^{4}$	$2.38x10^{8}$	579.64
UO_2(VI)-phenyl$(H_2O)_3^{+}$	$5.70x10^{2}$	$-2.60x10^{8}$	47.63
UO_2(V)-phenyl$(H_2O)_3$	$-2.86x10^{4}$	$2.50x10^{8}$	524.37
UO_2(VI)-amate$(H_2O)_4^{+}$	$-1.11x10^{3}$	$-4.24x10^{7}$	184.68
UO_2(V)-amate$(H_2O)_4$	$3.45x10^{4}$	$3.42x10^{8}$	534.28
UO_2(VI)-imid$(H_2O)_3$	$5.94x10^{2}$	$-3.52x10^{7}$	-50.38
UO_2(V)-imid$(H_2O)_3^{-}$	$-3.62x10^{4}$	$4.03x10^{8}$	413.32
$CaU(PO_4)_{2\ (s)}$	$-8.95x10^{4}$	$1.13x10^{9}$	669.62
$BaUO_2Si_2O_6$	$1.35x10^{4}$	$-2.53x10^{8}$	-221.36
Li_4UO_5	$-4.16x10^{3}$	$2.21x10^{7}$	-347.83
$BaUO_4$	$-7.54x10^{3}$	$7.39x10^{7}$	-290.33
KUO_3	$-6.69x10^{4}$	$8.92x10^{8}$	65.95
UTi_2O_6	$-9.98x10^{4}$	$1.21x10^{9}$	671.61

Table 2-9: Test of the effect of structures optimized with different functionals and basis sets on calculated DFT-PAW electron densities. The PBE functional and def-TZVP and def2-TZVPP family of basis sets (first column) are the main optimization method used for molecules and molecular complexes in this study. Species were optimized with the functional and basis set listed, and then electron densities were calculated using the PBE functional in the DFT-PAW method.

	DFT-PAW electron density (e^-/a_0^3)			
	PBEPBE, def2TZVPP and def-TZVP	HF, def2TZVPP and def-TZVP	B3LYP, def2TZVPP and def-TZVP	PBEPBE, LANLDZ
$UO_2(H_2O)_5^{2+}$	2609	2604	2609	2605
$U(H_2O)_9^{4+}$	2532	2531	2532	2531
$UO_2(CO_3)_3^{4-}$	2617	2620	2618	2610
$Ca_2UO_2(CO_3)_3$	2622	2619	2622	2609

Figures

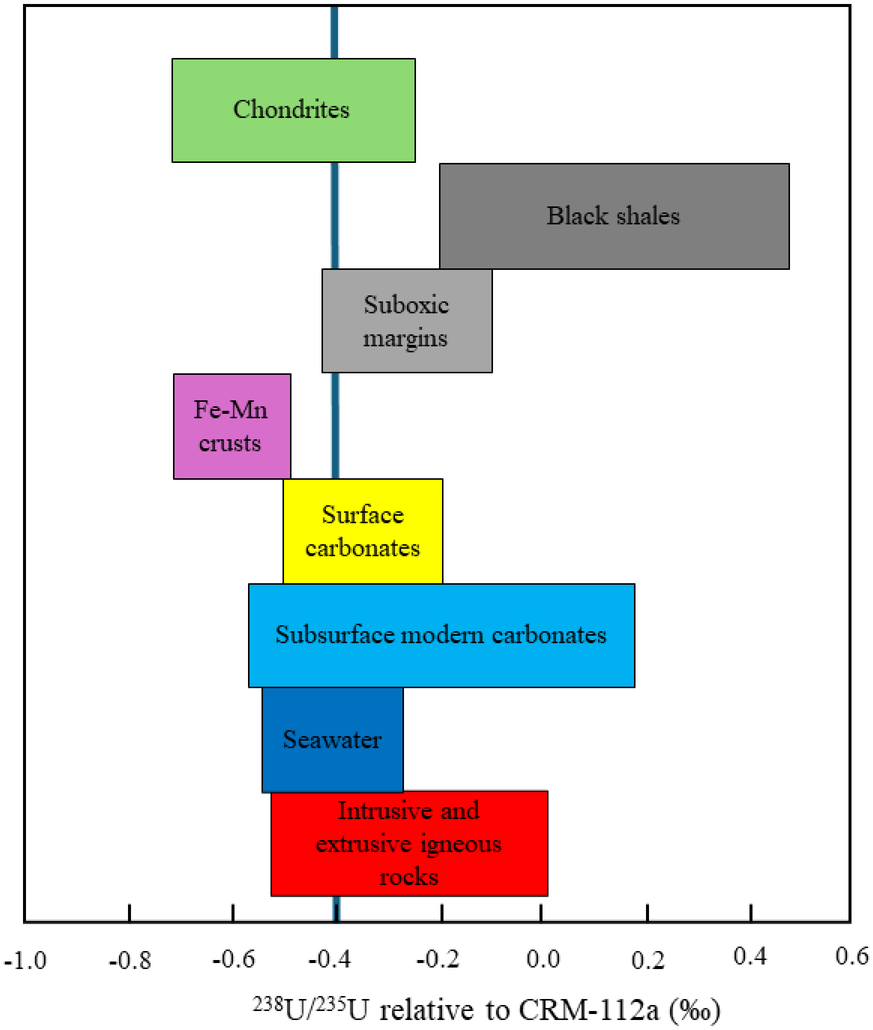

Figure 2-1: Overview of measurements of $^{238}U/^{235}U$ isotopic ratios for a select group of materials (adapted from Tissot and Dauphas, 2015). The blue line at approximately -0.4‰ represents the average value of seawater. Reducing sediments such as black shales have higher $^{238}U/^{235}U$ than oxidizing sediments such as Fe-Mn crusts and pelagic clay. The difference in the modern environment between seawater and the heaviest black shales is approximately 1‰. Black shales can be even heavier, up to ~ +2‰, though most tend to remain at around 1‰ heavier than seawater. Subsurface modern carbonates include carbonates down to 40 cm below sediment-water interface.

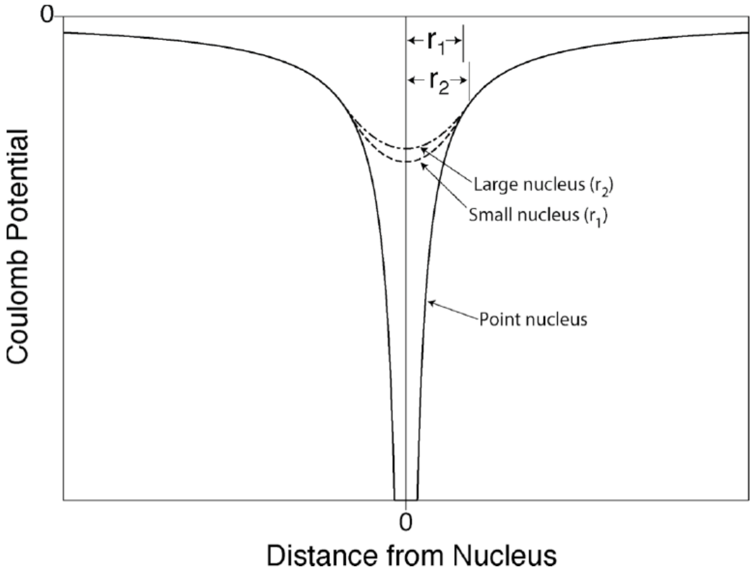

Figure 2-2: The impact of a finite nucleus can be seen in the way that the Coulomb potential at the nucleus does not go to negative infinity, but instead reaches a finite value in contrast to the point nucleus model. Further, it can be seen that a smaller nucleus will have a slightly lower Coulomb potential compared to a larger nucleus. Figure from Schauble (2007).

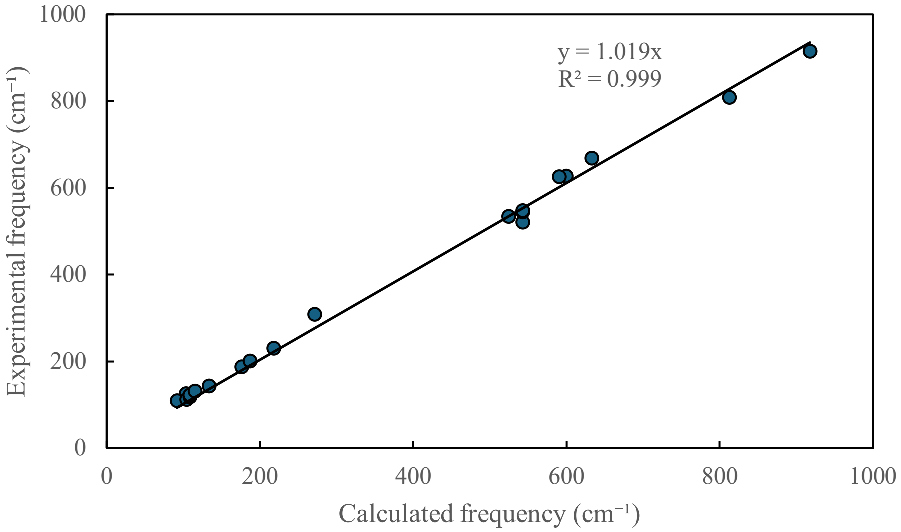

Figure 2-3: Measured vibrational frequencies from Raman & infrared spectroscopy vs. model frequencies for UF_6, UF_4, UO_2F_2, and $UO_2(CO_3)_3^{4-}$ (McDowell et al., 1973; Souter and Andrews, 1997; Paine et al., 2009; Hunt et al., 1993; Lu et al., 2018; Austin et al., 2009; Wacker et al., 2017). All model frequencies are calculated with the PBE functional and def-TZVP & def2-TZVPP basis sets.

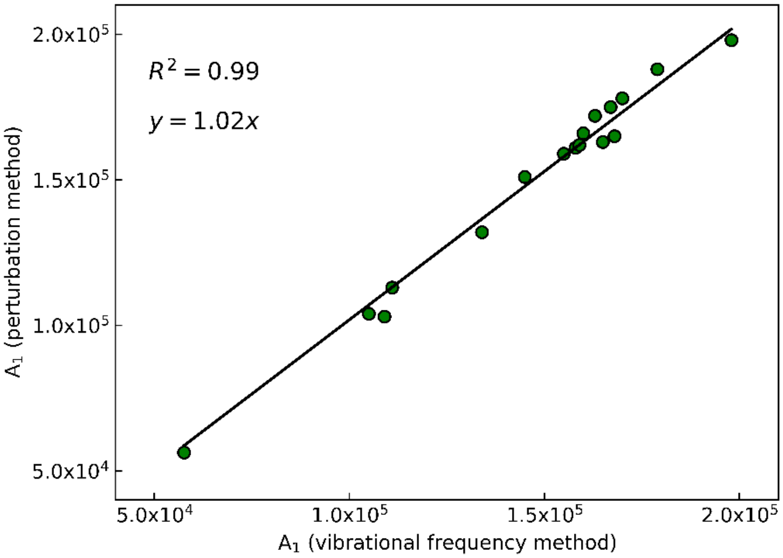

Figure 2-4: Relationship between A_1 values obtained via the perturbation method vs A_1 values obtained via the vibrational frequency method. Species analyzed include *in vacuo* geometries for $Ca_2UO_2(CO_3)_3$, $CaUO_2(CO_3)_3^{2-}$, $Mg_2UO_2(CO_3)_3$, $MgUO_2(CO_3)_3^{2-}$, $UO_2(CO_3)_3^{4-}$, $UO_2(CO_3)_2(H_2O)^{2-}$, $UO_2CO_3(H_2O)_3$, $UO_2(H_2O)_5^{2+}$, $UO_2Cl(H_2O)_4^{+}$, $UO_2Cl_2(H_2O)_3$, $UO_2Cl_3(H_2O)_2^{-}$, UF_6, UCl_6, UO_4^{2-}, $U(OH)_5$, $U(OH)_4$, and UCl_6^{2-}. Species which were attempted but excluded from analysis due to anomalous results are *in vacuo* geometries for UCl_4, UF_4, $U(H_2O)_9^{4+}$, UCl_5, UF_5, and $UO_2(H_2O)_5^{+}$

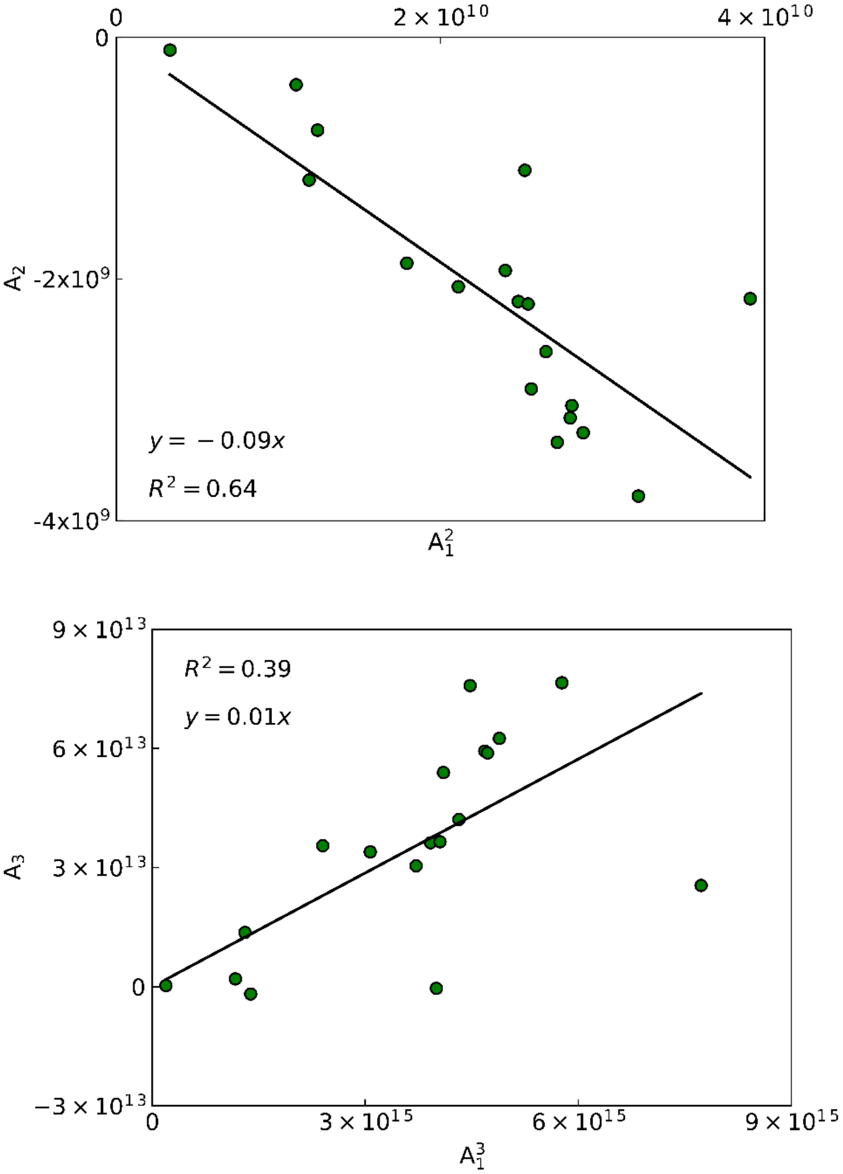

Figure 2-5: Correlation between coefficients of the polynomial expansion of the mass dependent component (natural logarithm of the β-factor) vs. T^{-2}, as detailed in Dauphas et al. (2012). β-factors for each datum are calculated via the vibrational frequency method. Species analyzed are the same as in figure 3.

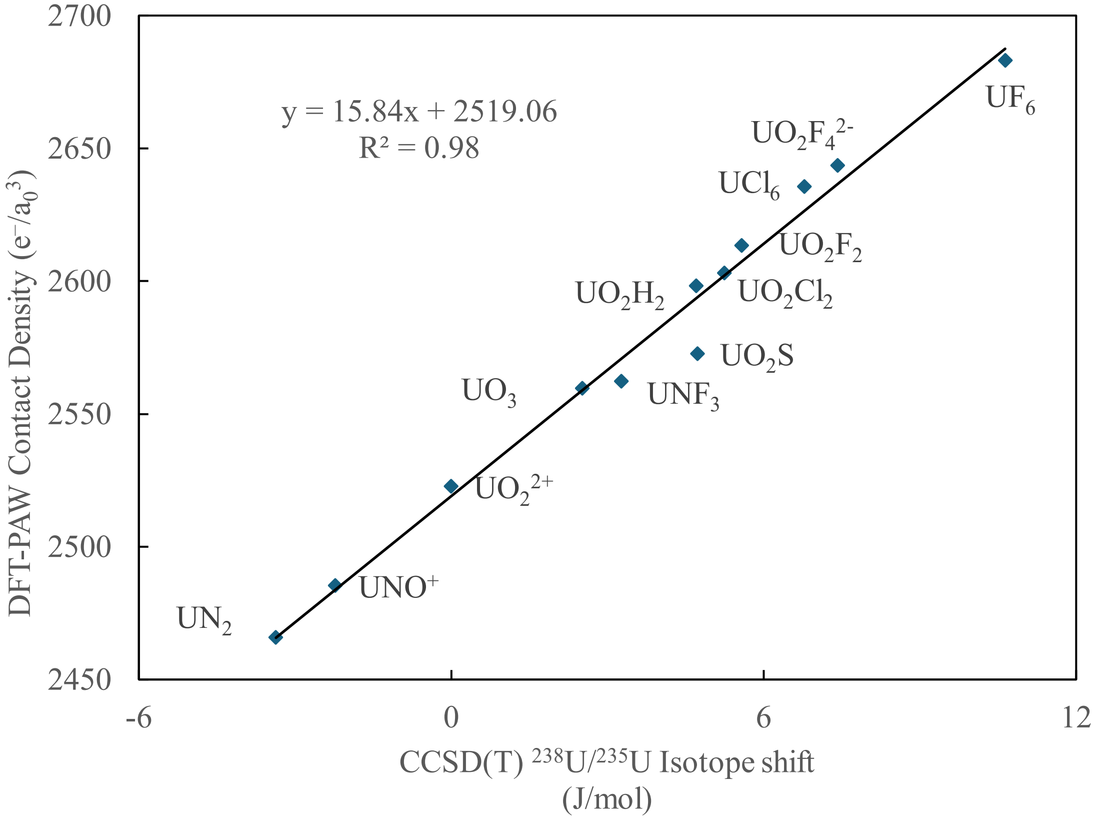

Figure 2-6: Calibration of DFT-PAW electron densities at uranium nuclei vs. all-electron relativistic calculations of the ^{238}U-^{235}U field shift for closed shell U-bearing molecules. The slope of this line calculated using least-squares regression is 15.84 ± 0.65 e^-/a_0^3 per J/mol. This slope makes it possible to estimate the field shift component of fractionation from DFT-PAW electron density. Note that field shifts are calculated relative to a reference species, in this case UO_2^{2+}-vapor.

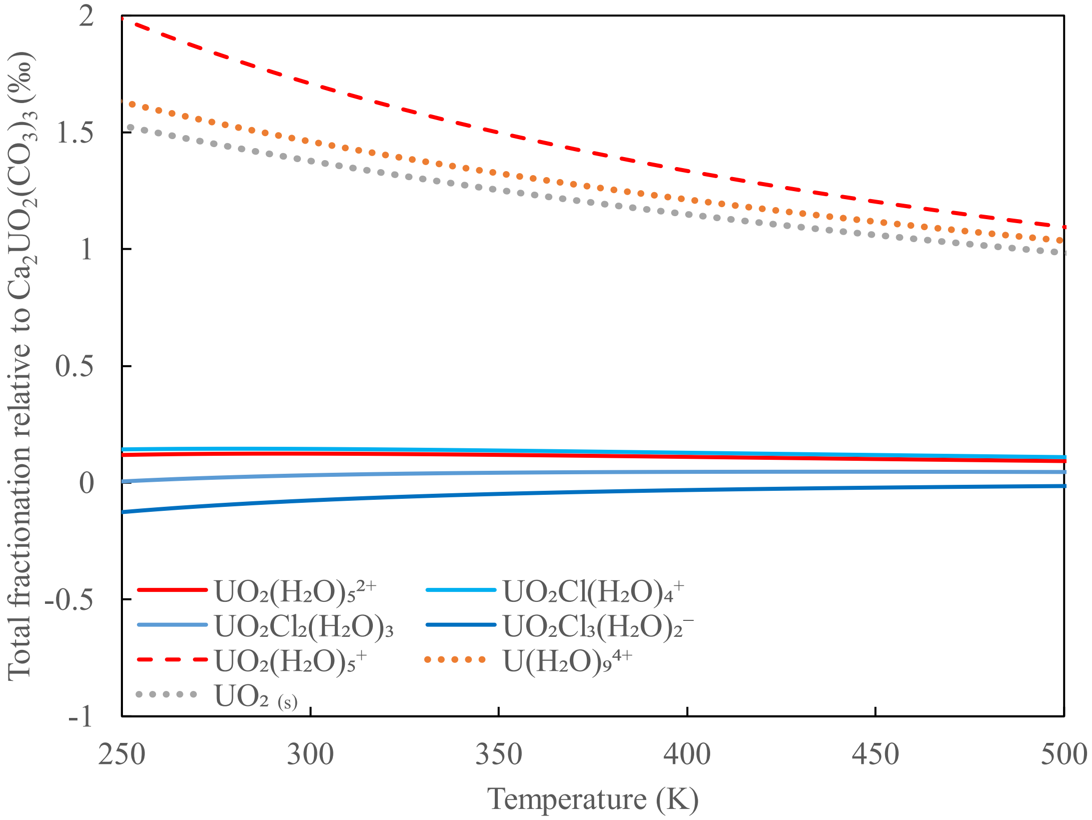

Figure 2-7: Total equilibrium fractionation factors (including nuclear field shift and mass-dependent components) versus temperature, relative to the species $Ca_2UO_2(CO_3)_3$ for species described in the experiments of Wang et al. (2015ab), as well as the species $UO_2(H_2O)_5^+$. Solid lines indicate U(VI) species, the dashed lines indicates the U(V) species $UO_2(H_2O)_5^+$, and dotted lines indicate U(IV) species.

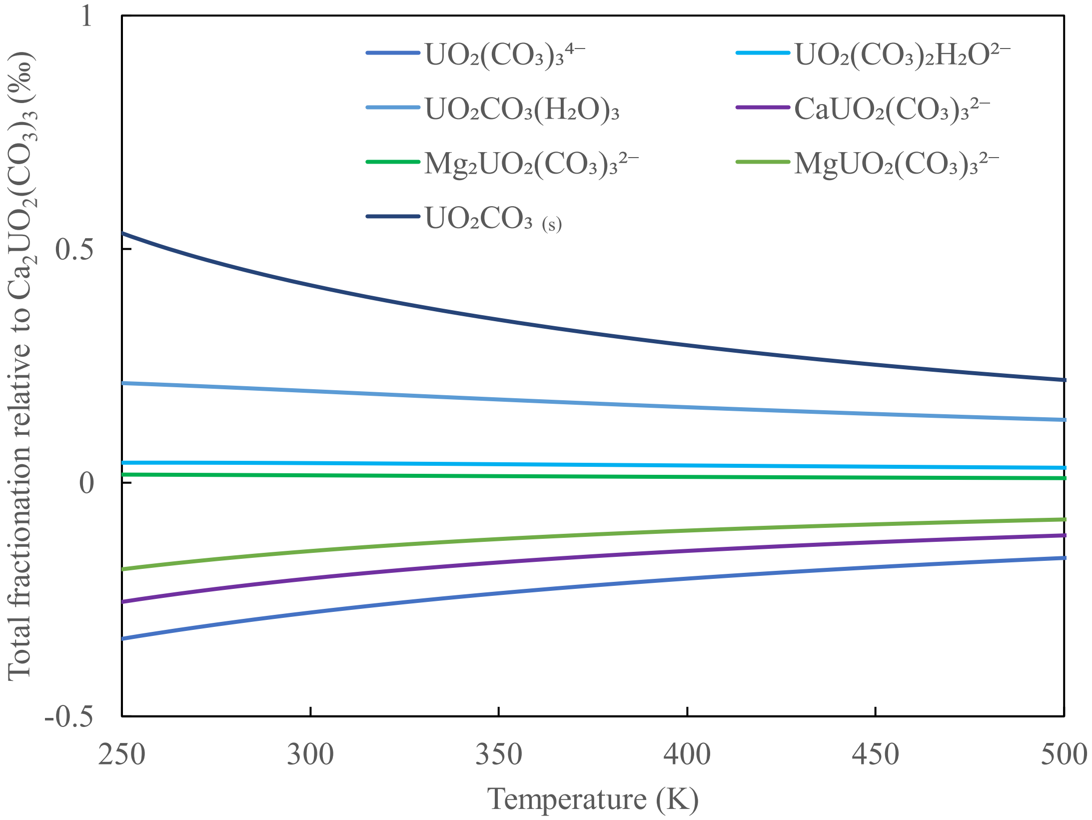

Figure 2-8: Total equilibrium fractionation factors (including nuclear field shift and mass-dependent components) relative to temperature for the uranium carbonate system, including the species examined in Chen et al. (2016), relative to $Ca_2UO_2(CO_3)_3$.

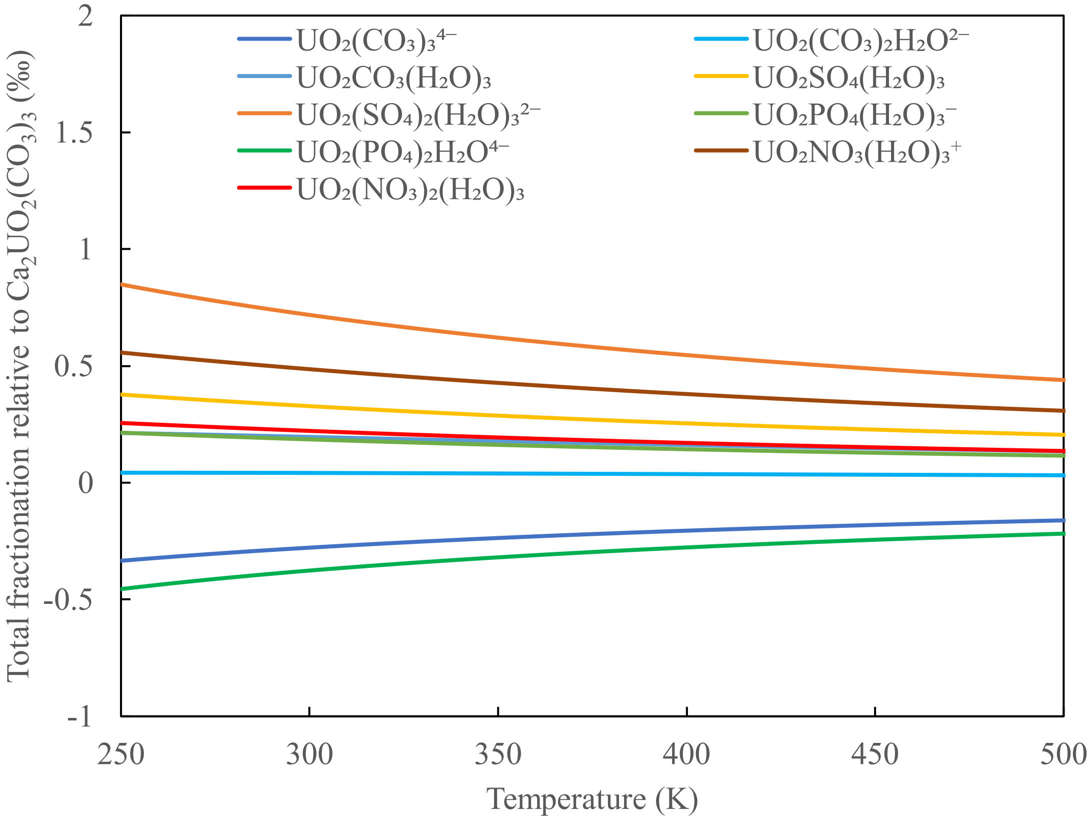

Figure 2-9: Total equilibrium fractionation factors versus temperature for uranyl-type oxyanion compounds, relative to $Ca_2UO_2(CO_3)_3$.

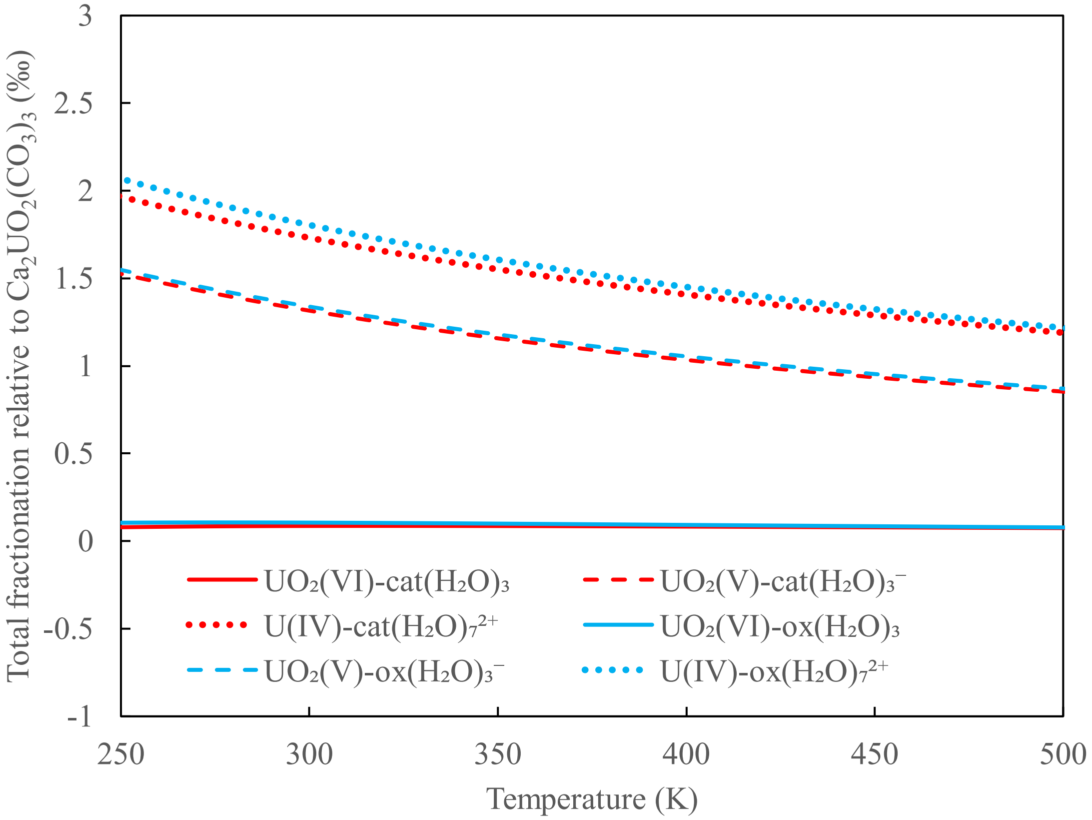

Figure 2-10: Total equilibrium fractionation factors versus temperature for select oxalate (ox) and catecholate (cat) compounds relative to $Ca_2UO_2(CO_3)_3$. Solid lines indicate U(VI) species, dashed lines indicate U(V) species and dotted lines indicate U(IV) species.

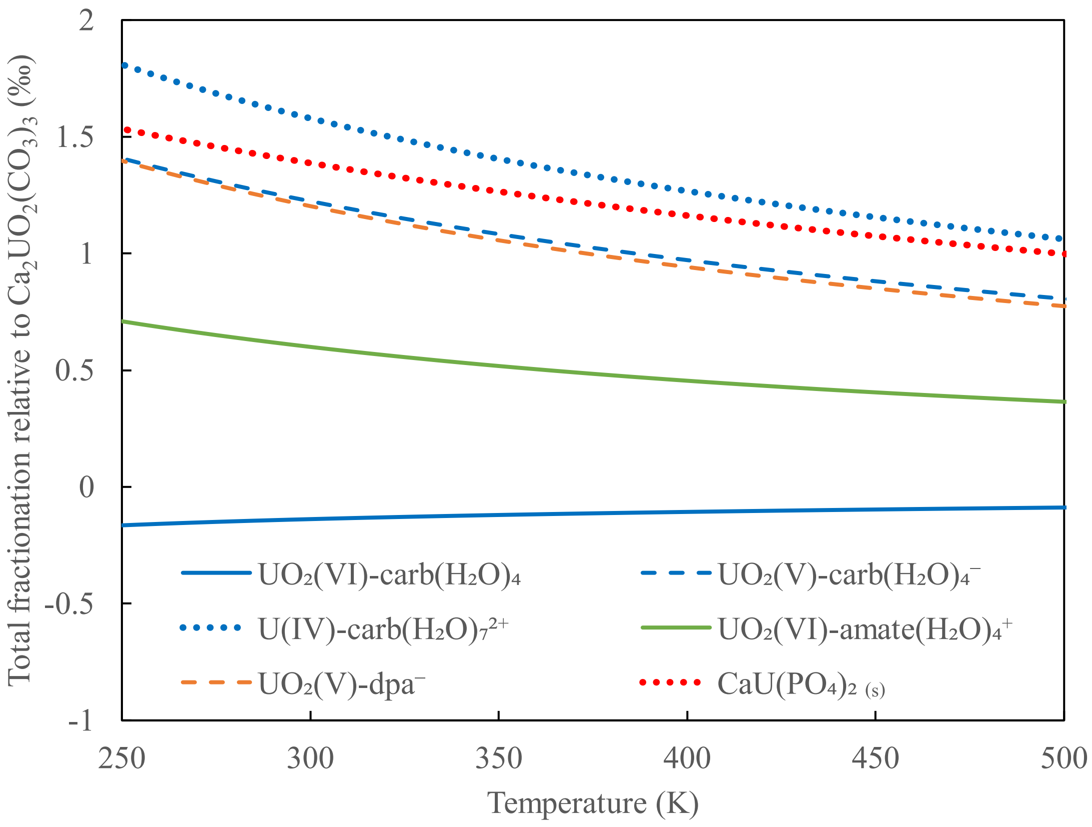

Figure 2-11: Total fractionation factors for select organic complexes relative to the species $Ca_2UO_2(CO_3)_3$. Solid lines indicate U(VI) species, dashed lines indicate U(V) species and dotted lines indicate U(IV) species. Carb = α-hydroxycarboxylate, amate = hydroxamate, dpa = dipicolinate.

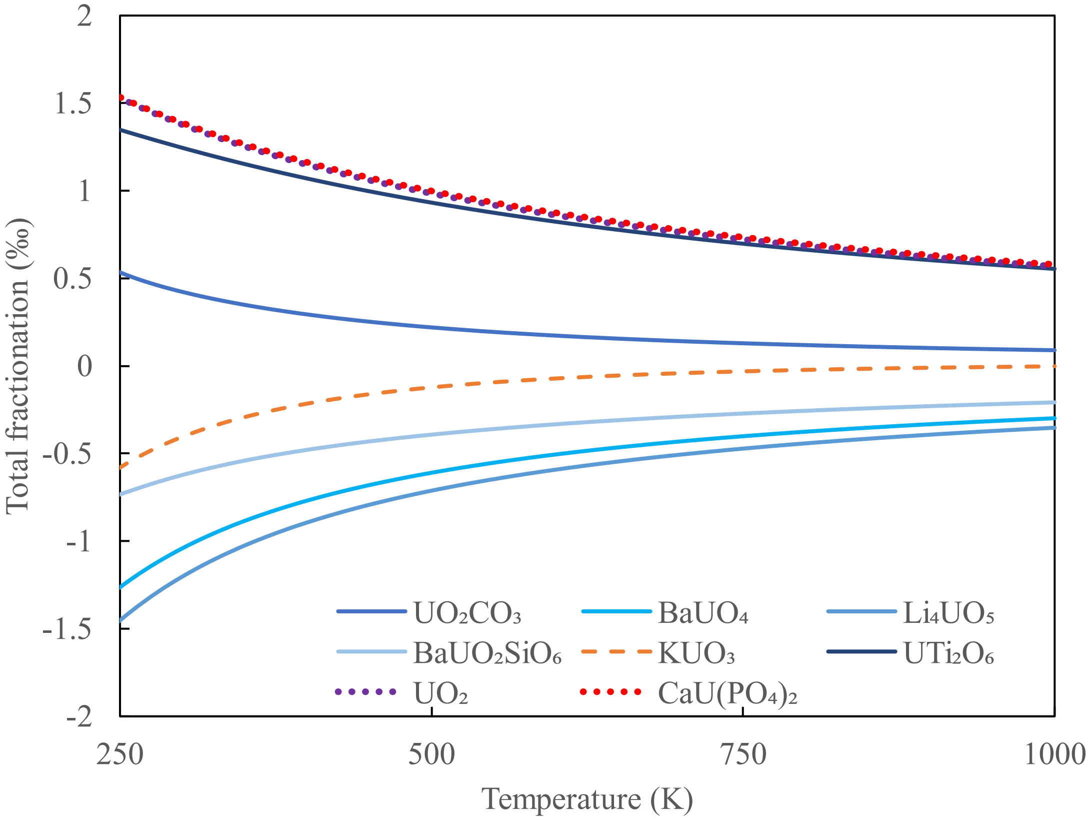

Figure 2-12: Total equilibrium fractionation factors for all solid species modeled relative to $Ca_2UO_2(CO_3)_3$. Solid lines indicate U(VI) species, dashed lines indicate U(V) species, and dotted lines indicate U(IV) species.

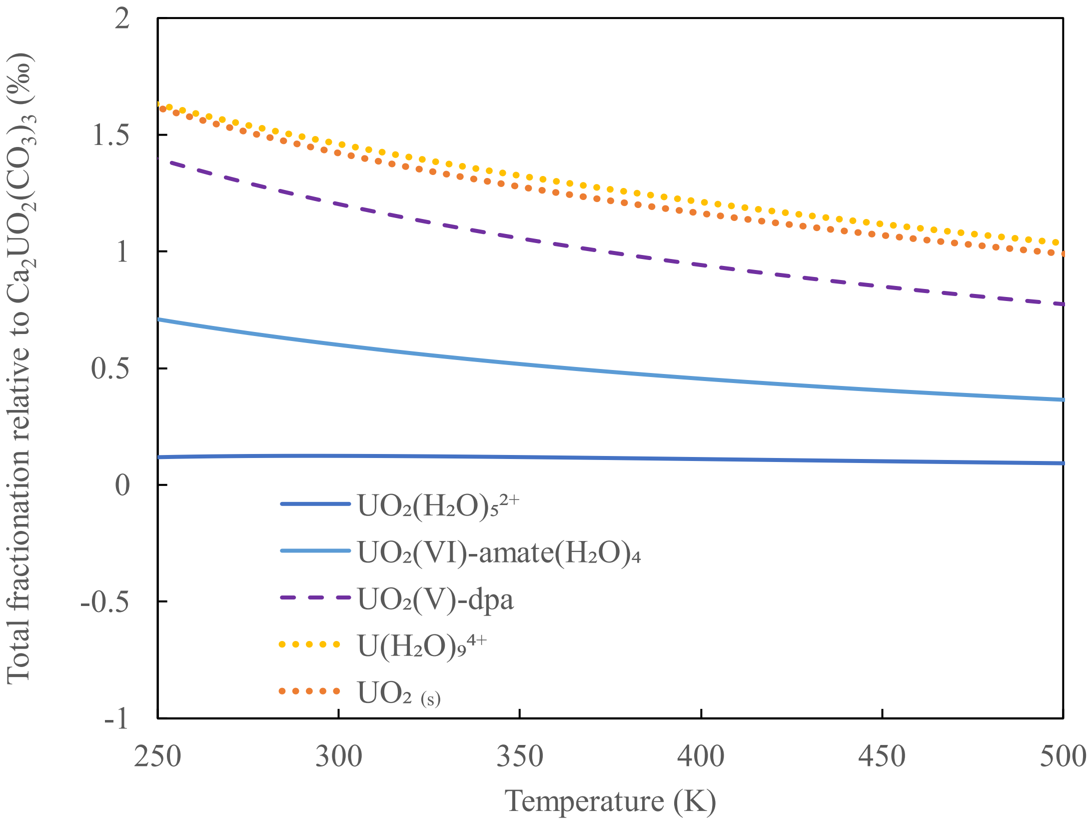

Figure 2-13: Total equilibrium fractionation factors for select species versus temperature, relative to $Ca_2UO_2(CO_3)_3$. Solid lines indicate U(VI) species, dashed lines indicate U(V) species, and dotted lines indicate U(IV) species. Species displayed include those from the experiments of Wang et al. (2015ab) and Faizova et al. (2018) as well as the siderophore complex from Kirby et al. (2020) and display the significance of oxidation state and speciation effects on uranium isotope fractionation.

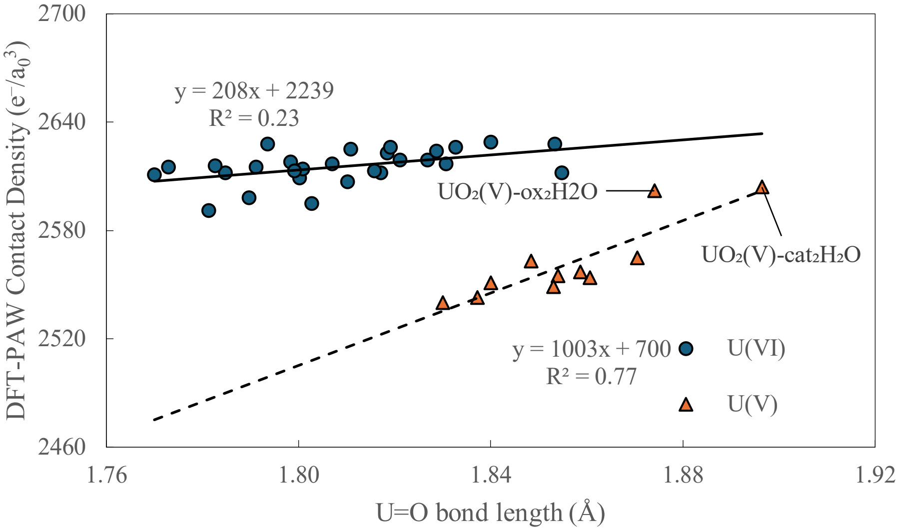

Figure 2-14: Electron density at the uranium nucleus vs. uranyl U=O bond length (Å) for U(VI) and U(V) species. It can be seen that for U(VI) species there is at best a weak trend ($R^2 = 0.23$), but for U(V) the correlation with bond length is moderately strong ($R^2 = 0.77$). Removing the two labeled U(V) data points results in $R^2 = 0.64$ and equation DFT-PAW Contact Density = 522(bond length) + 1587.

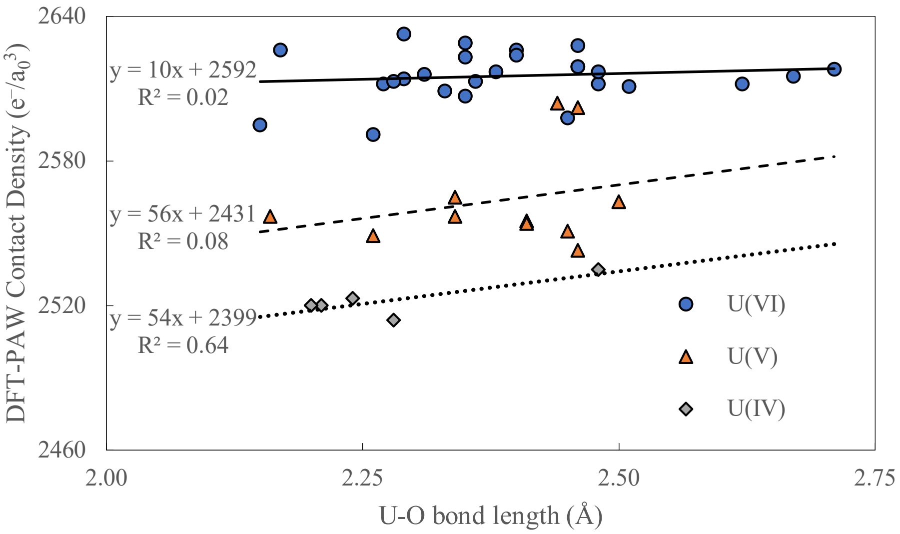

Figure 2-15: Electron density at the uranium nucleus vs. ligand (non-uranyl U-O) bond lengths. While there are notable differences in the bond lengths between the oxidation states, there is only a well-defined trend within U(IV)-bearing species.

References

Abe M, Suzuki T, Fujii Y, et al (2008a) An ab initio molecular orbital study of the nuclear volume effects in uranium isotope fractionations. The Journal of Chemical Physics 129:164309. https://doi.org/10.1063/1.2992616

Abe M, Suzuki T, Fujii Y, et al (2010) Ligand effect on uranium isotope fractionations caused by nuclear volume effects: An ab initio relativistic molecular orbital study. The Journal of Chemical Physics 133:044309. https://doi.org/10.1063/1.3463797

Abe M, Suzuki T, Fujii Y, Hada M (2008b) An ab initio study based on a finite nucleus model for isotope fractionation in the U(III)–U(IV) exchange reaction system. The Journal of Chemical Physics 128:144309. https://doi.org/10.1063/1.2898541

Alessi DS, Lezama-Pacheco JS, Stubbs JE, et al (2014) The product of microbial uranium reduction includes multiple species with U(IV)–phosphate coordination. Geochimica et Cosmochimica Acta 131:115–127. https://doi.org/10.1016/j.gca.2014.01.005

Andersen MB, Elliott T, Freymuth H, et al (2015) The terrestrial uranium isotope cycle. Nature 517:356–359. https://doi.org/10.1038/nature14062

Andersen MB, Stirling CH, Weyer S (2017) Uranium Isotope Fractionation. Reviews in Mineralogy and Geochemistry 82:799–850. https://doi.org/10.2138/rmg.2017.82.19

Anderson RF (1982) Concentration, vertical flux, and remineralization of particulate uranium in seawater. Geochimica et Cosmochimica Acta 46:1293–1299. https://doi.org/10.1016/0016-7037(82)90013-8

Angeli I (2004) A consistent set of nuclear rms charge radii: properties of the radius surface R(N,Z). Atomic Data and Nuclear Data Tables 87:185–206. https://doi.org/10.1016/j.adt.2004.04.002

Angeli I, Marinova KP (2013) Table of experimental nuclear ground state charge radii: An update. Atomic Data and Nuclear Data Tables 99:69–95. https://doi.org/10.1016/j.adt.2011.12.006

Arnold T, Baumann N, Krawczyk-Bärsch E, et al (2011) Identification of the uranium speciation in an underground acid mine drainage environment. Geochimica et Cosmochimica Acta 75:2200–2212. https://doi.org/10.1016/j.gca.2011.01.037

Austin JP, Sundararajan M, Vincent MA, Hillier IH (2009) The geometric structures, vibrational frequencies and redox properties of the actinyl coordination complexes ([AnO_2(L)n]m; An = U, Pu, Np; L = H_2O, Cl^-, CO_3^{2-}, $CH_3CO_2^-$, OH^-) in aqueous solution, studied by density functional theory methods. Dalton Trans 5902–5909. https://doi.org/10.1039/B901724K

Barone V, Cossi M (1998) Quantum Calculation of Molecular Energies and Energy Gradients in Solution by a Conductor Solvent Model. J Phys Chem A 102:1995–2001. https://doi.org/10.1021/jp9716997

Basu A, Sanford RA, Johnson TM, et al (2014) Uranium isotopic fractionation factors during U(VI) reduction by bacterial isolates. Geochimica et Cosmochimica Acta 136:100–113. https://doi.org/10.1016/j.gca.2014.02.041

Becke AD (1993) A new mixing of Hartree–Fock and local density-functional theories. The Journal of Chemical Physics 98:1372–1377. https://doi.org/10.1063/1.464304

Beridze G, Birnie A, Koniski S, et al (2016) DFT + U as a reliable method for efficient ab initio calculations of nuclear materials. Progress in Nuclear Energy 92:142–146. https://doi.org/10.1016/j.pnucene.2016.07.012

Beridze G, Kowalski PM (2014) Benchmarking the DFT+U Method for Thermochemical Calculations of Uranium Molecular Compounds and Solids. J Phys Chem A 118:11797–11810. https://doi.org/10.1021/jp5101126

Bernhard G, Geipel G, Brendler V, Nitsche H (1998) Uranium speciation in waters of different uranium mining areas. Journal of Alloys and Compounds 271–273:201–205. https://doi.org/10.1016/S0925-8388(98)00054-1

Bernhard G, Geipel G, Reich T, et al (2001) Uranyl(VI) carbonate complex formation: Validation of the Ca2UO2(CO3)3(aq.) species. Radiochimica Acta 89:511–518. https://doi.org/10.1524/ract.2001.89.8.511

Bigeleisen J (1996) Nuclear Size and Shape Effects in Chemical Reactions. Isotope Chemistry of the Heavy Elements. J Am Chem Soc 118:3676–3680. https://doi.org/10.1021/ja954076k

Bigeleisen J, Mayer MG (1947) Calculation of Equilibrium Constants for Isotopic Exchange Reactions. The Journal of Chemical Physics 15:261–267. https://doi.org/10.1063/1.1746492

Blöchl PE (1994) Projector augmented-wave method. Phys Rev B 50:17953–17979. https://doi.org/10.1103/PhysRevB.50.17953

Bolvin H, Wahlgren U, Gropen O, Marsden C (2001) Ab Initio Study of the Two Iso-electronic Molecules NpO_4^- and UO_4^{2-}. J Phys Chem A 105:10570–10576. https://doi.org/10.1021/jp011240j

Bouby M, Billard I, MacCordick J, Rossini I (1998) Complexation of Uranium VI with the Siderophore Pyoverdine. Radiochimica Acta 80:95–112. https://doi.org/10.1524/ract.1998.80.2.95

Brennecka GA, Herrmann AD, Algeo TJ, Anbar AD (2011) Rapid expansion of oceanic anoxia immediately before the end-Permian mass extinction. PNAS 108:17631–17634. https://doi.org/10.1073/pnas.1106039108

Cao X, Dolg M, Stoll H (2002) Valence basis sets for relativistic energy-consistent small-core actinide pseudopotentials. J Chem Phys 118:487–496. https://doi.org/10.1063/1.1521431

Chen X, Romaniello SJ, Anbar AD (2017) Uranium isotope fractionation induced by aqueous speciation: Implications for U isotopes in marine $CaCO_3$ as a paleoredox proxy. Geochimica et Cosmochimica Acta 215:162–172. https://doi.org/10.1016/j.gca.2017.08.006

Chen X, Romaniello SJ, Herrmann AD, et al (2016) Uranium isotope fractionation during coprecipitation with aragonite and calcite. Geochimica et Cosmochimica Acta 188:189–207. https://doi.org/10.1016/j.gca.2016.05.022

Clark DL, Conradson SD, Donohoe RJ, et al (1999) Chemical speciation of the uranyl ion under highly alkaline conditions. Synthesis, structures, and oxo ligand exchange dynamics. Inorganic Chemistry 38:1456–1466. https://doi.org/10.1021/ic981137h

Dauphas N, John SG, Rouxel O (2017) Iron Isotope Systematics. Reviews in Mineralogy and Geochemistry 82:415–510. https://doi.org/10.2138/rmg.2017.82.11

Dauphas N, Roskosz M, Alp EE, et al (2012) A general moment NRIXS approach to the determination of equilibrium Fe isotopic fractionation factors: Application to goethite and jarosite. Geochimica et Cosmochimica Acta 94:254–275. https://doi.org/10.1016/j.gca.2012.06.013

Docrat TI Electrochemical and Spectroscopic Studies of the Actinyl Ions in Aqueous Solutions. Ph.D., The University of Manchester (United Kingdom)

Dorado B, Amadon B, Freyss M, Bertolus M (2009) DFT+U calculations of the ground state and metastable states of uranium dioxide. Physical Review B 79:235125. https://doi.org/10.1103/PhysRevB.79.235125

Dorado B, Jomard G, Freyss M, Bertolus M (2010) Stability of oxygen point defects in UO_2 by first-principles DFT+U calculations: Occupation matrix control and Jahn-Teller distortion. Physical Review B 82:035114. https://doi.org/10.1103/PhysRevB.82.035114

Dudarev SL, Manh DN, Sutton AP (1997) Effect of Mott-Hubbard correlations on the electronic structure and structural stability of uranium dioxide. Philosophical Magazine B 75:613–628. https://doi.org/10.1080/13642819708202343

Dunning TH Jr (1989) Gaussian basis sets for use in correlated molecular calculations. I. The atoms boron through neon and hydrogen. The Journal of Chemical Physics 90:1007–1023. https://doi.org/10.1063/1.456153

Dusausoy Y, Ghermani N-E, Podor R, Cuney M (1996) Low-temperature ordered phase of CaU (PO4) 2: synthesis and crystal structure. European Journal of Mineralogy-Ohne Beihefte 8:667–674. https://doi.org/10.1127/ejm/8/4/0667

Dyall KG (2007) Relativistic double-zeta, triple-zeta, and quadruple-zeta basis sets for the actinides Ac–Lr. Theor Chem Acc 117:491–500. https://doi.org/10.1007/s00214-006-0175-4

Eichkorn K, Weigend F, Treutler O, Ahlrichs R (1997) Auxiliary basis sets for main row atoms and transition metals and their use to approximate Coulomb potentials. Theor Chem Acta 97:119–124. https://doi.org/10.1007/s002140050244

Elzinga EJ, Tait CD, Reeder RJ, et al (2004) Spectroscopic investigation of U(VI) sorption at the calcite-water interface. Geochimica et Cosmochimica Acta 68:2437–2448. https://doi.org/10.1016/j.gca.2003.09.023

Endrizzi F, Rao L (2014) Chemical Speciation of Uranium(VI) in Marine Environments: Complexation of Calcium and Magnesium Ions with [(UO2)(CO3)3]4− and the Effect on the

Extraction of Uranium from Seawater. Chemistry – A European Journal 20:14499–14506. https://doi.org/10.1002/chem.201403262

Faizova R, Scopelliti R, Chauvin A-S, Mazzanti M (2018) Synthesis and Characterization of a Water Stable Uranyl(V) Complex. J Am Chem Soc 140:13554–13557. https://doi.org/10.1021/jacs.8b07885

Feller D (1996) The role of databases in support of computational chemistry calculations. Journal of Computational Chemistry 17:1571–1586. https://doi.org/10.1002/(SICI)1096-987X(199610)17:13<1571::AID-JCC9>3.0.CO;2-P

Finch RJ, Cooper MA, Hawthorne FC, Ewing RC (1999) Refinement of the crystal structure of rutherfordine. The Canadian Mineralogist 37:929–938

Florence TM, Batley GE, Ekstrom A, et al (1975) Separation of uranium isotopes by uranium(IV)-uranium(VI) chemical exchange. Journal of Inorganic and Nuclear Chemistry 37:1961–1966. https://doi.org/10.1016/0022-1902(75)80925-0

Frazer BC, Shirane G, Cox DE, Olsen CE (1965) Neutron-Diffraction Study of Antiferromagnetism in U O 2. Physical Review 140:A1448. https://doi.org/10.1103/physrev.140.a1448

Fricke G, Heilig K (2004) 92-U Uranium. In: Schopper H (ed) Nuclear Charge Radii. Springer-Verlag, Berlin/Heidelberg, pp 1–5

Frisch MJ, Trucks GW, Schlegel HB, et al (2009) Gaussian 09: Programmer's Reference. Gaussian Inc., Wallingford, CT

Fujii Y, Nomura M, Okamoto M, et al (1989a) An Anomalous Isotope Effect of ^{235}U in U(IV)-U(VI) Chemical Exchange. Zeitschrift für Naturforschung A 44:395–398. https://doi.org/10.1515/zna-1989-0507

Fujii Y, Nomura M, Onitsuka H, Takeda K (1989b) Anomalous Isotope Fractionation in Uranium Enrichment Process. Journal of Nuclear Science and Technology 26:1061–1064. https://doi.org/10.1080/18811248.1989.9734427

Fukuda J, Fujii Y, Okamoto M (1983) A Fundamental Study on Uranium Isotope Separation Using U(IV)—U(VI) Electron Exchange Reaction. Zeitschrift für Naturforschung A 38:1072–1077. https://doi.org/10.1515/zna-1983-1005

Gonze X, Amadon B, Anglade P-M, et al (2009) ABINIT: First-principles approach to material and nanosystem properties. Computer Physics Communications 180:2582–2615. https://doi.org/10.1016/j.cpc.2009.07.007

Gutowski KE, Dixon DA (2006) Predicting the energy of the water exchange reaction and free energy of solvation for the uranyl ion in aqueous solution. The Journal of Physical Chemistry A 110:8840–8856. https://doi.org/10.1021/jp061851h

Hay PJ (1983) Ab initio studies of excited states of polyatomic molecules including spin-orbit and multiplet effects: The electronic states of UF6. The Journal of Chemical Physics 79:5469–5482. https://doi.org/10.1063/1.445665

Hennig C, Schmeide K, Brendler V, et al (2007) EXAFS Investigation of U(VI), U(IV), and Th(IV) Sulfato Complexes in Aqueous Solution. Inorg Chem 46:5882–5892. https://doi.org/10.1021/ic0619759

Hiess J, Condon DJ, McLean N, Noble SR (2012) 238U/235U Systematics in Terrestrial Uranium-Bearing Minerals. Science 335:1610–1614. https://doi.org/10.1126/science.1215507

Hoekstra H, Siegel S (1964) Structural studies on Li_4UO_5 and Na_4UO_5. Journal of Inorganic and Nuclear Chemistry 26:693–700. https://doi.org/10.1016/0022-1902(64)80311-0

Holzwarth NAW, Tackett AR, Matthews GE (2001) A Projector Augmented Wave (PAW) code for electronic structure calculations, Part I: atompaw for generating atom-centered functions. Computer Physics Communications 135:329–347. https://doi.org/10.1016/S0010-4655(00)00244-7

Ikeda A, Hennig C, Tsushima S, et al (2007) Comparative Study of Uranyl(VI) and -(V) Carbonato Complexes in an Aqueous Solution. Inorg Chem 46:4212–4219. https://doi.org/10.1021/ic070051y

Jollet F, Torrent M, Holzwarth N (2014) Generation of Projector Augmented-Wave atomic data: A 71 element validated table in the XML format. Computer Physics Communications 185:1246–1254. https://doi.org/10.1016/j.cpc.2013.12.023

Kelly SD, Kemner KM, Brooks SC (2007) X-ray absorption spectroscopy identifies calcium-uranyl-carbonate complexes at environmental concentrations. Geochimica et Cosmochimica Acta 71:821–834. https://doi.org/10.1016/j.gca.2006.10.013

King WH (1984) Isotope shifts in atomic spectra. Springer New York, New York

Kirby ME, Sonnenberg JL, Simperler A, Weiss DJ (2020) Stability Series for the Complexation of Six Key Siderophore Functional Groups with Uranyl Using Density Functional Theory. J Phys Chem A 124:2460–2472. https://doi.org/10.1021/acs.jpca.9b10649

Knyazev DA, Myasoedov NF (2001) Specific Effects of Heavy Nuclei in Chemical Equilibrium. Separation Science and Technology 36:1677–1696. https://doi.org/10.1081/SS-100104758

Kovács A, Konings RJM (2006) A Theoretical Study of the Structure and Bonding of UOX_4 (X=F, Cl, Br, I) Molecules: The Importance of Inverse Trans Influence. ChemPhysChem 7:455–462. https://doi.org/10.1002/cphc.200500324

Kubicki JD, Halada GP, Jha P, Phillips BL (2009) Quantum mechanical calculation of aqueuous uranium complexes: carbonate, phosphate, organic and biomolecular species. Chemistry Central Journal 3:10. https://doi.org/10.1186/1752-153X-3-10

Lander GH, Caciuffo R (2020) The fifty years it has taken to understand the dynamics of UO_2 in its ordered state. J Phys: Condens Matter 32:374001. https://doi.org/10.1088/1361-648X/ab1dc5

Lau KV, Romaniello SJ, Zhang F (2019) The Uranium Isotope Paleoredox Proxy. Elements in Geochemical Tracers in Earth System Science. https://doi.org/10.1017/9781108584142

Liang B, Andrews L, Ismail N, Marsden CJ (2002) The First Infrared Spectra and Quasirelativistic DFT Studies of the US, US2, and US3 Molecules. Inorg Chem 41:2811–2813. https://doi.org/10.1021/ic0255407

Loopstra BO, Rietveld HM (1969) The structure of some alkaline-earth metal uranates. Acta Crystallographica Section B: Structural Crystallography and Crystal Chemistry 25:787–791. https://doi.org/10.1107/S0567740869002974

Malli GL (2003) Ab initio all-electron fully relativistic Dirac—Fock self-consistent field calculations for UCl6. Molecular Physics 101:287–294. https://doi.org/10.1080/00268970210162790

McDowell RS, Asprey LB, Paine RT (1974) Vibrational spectrum and force field of uranium hexafluoride. The Journal of Chemical Physics 61:3571–3580. https://doi.org/10.1063/1.1682537

McManus J, Berelson WM, Klinkhammer GP, et al (2005) Authigenic uranium: Relationship to oxygen penetration depth and organic carbon rain. Geochimica et Cosmochimica Acta 69:95–108. https://doi.org/10.1016/j.gca.2004.06.023

Méheut M, Lazzeri M, Balan E, Mauri F (2007) Equilibrium isotopic fractionation in the kaolinite, quartz, water system: Prediction from first-principles density-functional theory. Geochimica et Cosmochimica Acta 71:3170–3181. https://doi.org/10.1016/j.gca.2007.04.012

Meinrath G (1996) Coordination of uranyl (VI) carbonate species in aqueous solutions. Journal of radioanalytical and nuclear chemistry 211:349–362. https://doi.org/10.1007/BF02039703

Mo K-F, Dai Z, Wunschel DS (2016) Production and Characterization of Desmalonichrome Relative Binding Affinity for Uranyl Ions in Relation to Other Siderophores. J Nat Prod 79:1492–1499. https://doi.org/10.1021/acs.jnatprod.5b00933

Moll H, Glorius M, Bernhard G, et al (2008) Characterization of Pyoverdins Secreted by a Subsurface Strain of Pseudomonas fluorescens and Their Interactions with Uranium(VI). Geomicrobiology Journal 25:157–166. https://doi.org/10.1080/01490450802006850

Mullen L, Gong C, Czerwinski K (2007) Complexation of uranium (VI) with the siderophore desferrioxamine B. Journal of Radioanalytical and Nuclear Chemistry 273:683–688. https://doi.org/10.1007/s10967-007-0931-5

Nadjakov EG, Marinova KP, Gangrsky YP (1994) Systematics of Nuclear Charge Radii. Atomic Data and Nuclear Data Tables 56:133–157. https://doi.org/10.1006/adnd.1994.1004

Nomura M, Higuchi N, Fujii Y (1996) Mass Dependence of Uranium Isotope Effects in the U(IV)−U(VI) Exchange Reaction. J Am Chem Soc 118:9127–9130. https://doi.org/10.1021/ja954075s

O’Neil JR (1986) Theoretical and Experimental Aspects of Isotopic Fractionation. Reviews in Mineralogy 16:1–40 https://doi.org/10.1515/9781501508936-006

Paine RT, McDowell RS, Asprey LB, Jones LH (2008) Vibrational spectroscopy of matrix-isolated UF_6 and UF_5. The Journal of Chemical Physics 64:3081–3083. https://doi.org/10.1063/1.432574

Perdew JP, Burke K, Ernzerhof M (1996) Generalized Gradient Approximation Made Simple. Phys Rev Lett 77:3865–3868. https://doi.org/10.1103/PhysRevLett.77.3865

Plaisier JR, Ijdo DJW, de Mello Donega C, Blasse G (1995) Structure and luminescence of barium uranium disilicate (BaUO2Si2O6). Chemistry of materials 7:738–743. https://doi.org/10.1021/cm00052a020

Pritchard BP, Altarawy D, Didier B, et al (2019) New Basis Set Exchange: An Open, Up-to-Date Resource for the Molecular Sciences Community. J Chem Inf Model 59:4814–4820. https://doi.org/10.1021/acs.jcim.9b00725

Privalov T, Schimmelpfennig B, Wahlgren U, Grenthe I (2002) Structure and Thermodynamics of Uranium(VI) Complexes in the Gas Phase: A Comparison of Experimental and ab Initio Data. J Phys Chem A 106:11277–11282. https://doi.org/10.1021/jp0260402

Rademacher LK, Lundstrom CC, Johnson TM, et al (2006) Experimentally Determined Uranium Isotope Fractionation During Reduction of Hexavalent U by Bacteria and Zero Valent Iron. Environ Sci Technol 40:6943–6948. https://doi.org/10.1021/es0604360

Reeder RJ, Elzinga EJ, Tait CD, et al (2004) Site-specific incorporation of uranyl carbonate species at the calcite surface. Geochimica et Cosmochimica Acta 68:4799–4808. https://doi.org/10.1016/j.gca.2004.05.031

Reeder RJ, Nugent M, Lamble GM, et al (2000) Uranyl Incorporation into Calcite and Aragonite: XAFS and Luminescence Studies. Environ Sci Technol 34:638–644. https://doi.org/10.1021/es990981j

Renshaw JC, Butchins LJC, Livens FR, et al (2005) Bioreduction of Uranium: Environmental Implications of a Pentavalent Intermediate. Environ Sci Technol 39:5657–5660. https://doi.org/10.1021/es048232b

Rodríguez-Jeangros N, Seminario JM (2014) Density functional theory and molecular dynamics study of the uranyl ion $(UO_2)^{2+}$. J Mol Model 20:2150. https://doi.org/10.1007/s00894-014-2150-7

Rüdorff W, Kemmler S, Leutner H (1962) Ternary Uranium (V) Oxides. Angewandte Chemie International Edition in English 1:329–330. https://doi.org/10.1002/anie.196203292

Sato A, Bernier-Latmani R, Hada M, Abe M (2021) Ab initio and steady-state models for uranium isotope fractionation in multi-step biotic and abiotic reduction. Geochimica et Cosmochimica Acta 307:212–227. https://doi.org/10.1016/j.gca.2021.05.044

Saue T, Visscher L, Jensen HA, et al (2011) DIRAC, a relativistic ab initio electronic structure program, release DIRAC10

Schauble EA (2006) Equilibrium uranium isotope fractionation by nuclear volume and mass-dependent processes. AGU Fall Meeting Abstracts 21:V21B-0570

Schauble EA (2004) Applying Stable Isotope Fractionation Theory to New Systems. Reviews in Mineralogy and Geochemistry 55:65–111. https://doi.org/10.2138/gsrmg.55.1.65

Schauble EA (2007) Role of nuclear volume in driving equilibrium stable isotope fractionation of mercury, thallium, and other very heavy elements. Geochimica et Cosmochimica Acta 71:2170–2189. https://doi.org/10.1016/j.gca.2007.02.004

Schauble EA (2013) Modeling nuclear volume isotope effects in crystals. PNAS 110:17714–17719. https://doi.org/10.1073/pnas.1216216110

Schuchardt KL, Didier BT, Elsethagen T, et al (2007) Basis Set Exchange: A Community Database for Computational Sciences. J Chem Inf Model 47:1045–1052. https://doi.org/10.1021/ci600510j

Shamir J, Silberstein A (1975) Laser raman spectra of the uranium hexachloride molecule and anions (UCl_6, UCl_6^{-1} and UCl_6^{-2}). Journal of Inorganic and Nuclear Chemistry 37:1173–1175. https://doi.org/10.1016/0022-1902(75)80464-7

Shamov GA, Schreckenbach G, Vo TN (2007) A Comparative Relativistic DFT and Ab Initio Study on the Structure and Thermodynamics of the Oxofluorides of Uranium(IV), (V) and (VI). Chemistry – A European Journal 13:4932–4947. https://doi.org/10.1002/chem.200601244

Shen C-C, Lin H-T, Chu M-F, et al (2006) Measurements of natural uranium concentration and isotopic composition with permil-level precision by inductively coupled plasma–quadrupole mass spectrometry. Geochemistry, Geophysics, Geosystems 7:. https://doi.org/10.1029/2006GC001303

Shimokaua J, Kobayashi F (1970) Separation of Uranium Isotopes by Chemical Exchange. Isotopenpraxis Isotopes in Environmental and Health Studies 6:170–176. https://doi.org/10.1080/10256017008621706

Shindo H, Huang PM (1992) Comparison of the influence of Mn(IV) oxide and tyrosinase on the formation of humic substances in the environment. Science of The Total Environment 117–118:103–110. https://doi.org/10.1016/0048-9697(92)90078-7

Soderholm L, Skanthakumar S, Wilson RE (2011) Structural correspondence between uranyl chloride complexes in solution and their stability constants. The Journal of Physical Chemistry A 115:4959–4967. https://doi.org/10.1021/jp111551

Souter PF, Andrews L (1997) Infrared spectra of some uranium oxyfluoride molecules isolated in solid argon. Journal of Molecular Structure 412:161–167. https://doi.org/10.1016/S0022-2860(97)00068-9

Stirling CH, Andersen MB, Potter E-K, Halliday AN (2007) Low-temperature isotopic fractionation of uranium. Earth and Planetary Science Letters 264:208–225. https://doi.org/10.1016/j.epsl.2007.09.019

Stirling CH, Andersen MB, Warthmann R, Halliday AN (2015) Isotope fractionation of ^{238}U and ^{235}U during biologically-mediated uranium reduction. Geochimica et Cosmochimica Acta 163:200–218. https://doi.org/10.1016/j.gca.2015.03.017

Stirling CH, Halliday AN, Porcelli D (2005) In search of live ^{247}Cm in the early solar system. Geochimica et Cosmochimica Acta 69:1059–1071. https://doi.org/10.1016/j.gca.2004.06.034

Stirling CH, Halliday AN, Potter E-K, et al (2006) A low initial abundance of ^{247}Cm in the early solar system and implications for r-process nucleosynthesis. Earth and Planetary Science Letters 251:386–397. https://doi.org/10.1016/j.epsl.2006.09.023

Stylo M, Neubert N, Roebbert Y, et al (2015a) Mechanism of Uranium Reduction and Immobilization in Desulfovibrio vulgaris Biofilms. Environ Sci Technol 49:10553–10561. https://doi.org/10.1021/acs.est.5b01769

Stylo M, Neubert N, Wang Y, et al (2015b) Uranium isotopes fingerprint biotic reduction. Proceedings of the National Academy of Sciences 112:5619–5624. https://doi.org/10.1073/pnas.1421841112

Su J, Wang Y-L, Wei F, et al (2011) Theoretical study of the luminescent states and electronic spectra of UO_2Cl_2 in an argon matrix. Journal of Chemical Theory and Computation 7:3293–3303. https://doi.org/10.1021/ct200419x

Szymanski JT, Scott JD (1982) A crystal-structure refinement of synthetic brannerite, UTi2O6, and its bearing on rate of alkaline-carbonate leaching of brannerite in ore. Canadian Mineralogist 20:271–279

Tecmer P, Gomes ASP, Ekström U, Visscher L (2011) Electronic spectroscopy of UO_2^{2+}, NUO^+ and NUN: an evaluation of time-dependent density functional theory for actinides. Phys Chem Chem Phys 13:6249–6259. https://doi.org/10.1039/C0CP02534H

Tissot FLH, Dauphas N (2015) Uranium isotopic compositions of the crust and ocean: Age corrections, U budget and global extent of modern anoxia. Geochimica et Cosmochimica Acta 167:113–143. https://doi.org/10.1016/j.gca.2015.06.034

Tissot FLH, Ibanez-Mejia M, Boehnke P, et al (2019) ^{238} U/ ^{235} U measurement in single-zircon crystals: implications for the Hadean environment, magmatic differentiation and geochronology. Journal of Analytical Atomic Spectrometry 34:2035–2052. https://doi.org/10.1039/C9JA00205G

Torrent M, Jollet F, Bottin F, et al (2008) Implementation of the projector augmented-wave method in the ABINIT code: Application to the study of iron under pressure. Computational Materials Science 42:337–351. https://doi.org/10.1016/j.commatsci.2007.07.020

Urey H (1947) The thermodynamic properties of isotopic substances. J Chem Soc 562–581. https://doi.org/10.1039/JR9470000562

Vallet V, Wahlgren U, Schimmelpfennig B, et al (2001) The Mechanism for Water Exchange in [UO2(H2O)5]2+ and [UO2(oxalate)2(H2O)]2-, as Studied by Quantum Chemical Methods. J Am Chem Soc 123:11999–12008. https://doi.org/10.1021/ja015935+

Van Vleck JH (1936) On the Isotope Corrections in Molecular Spectra. The Journal of Chemical Physics 4:327–338. https://doi.org/10.1063/1.1749853

Wacker JN, Vasiliu M, Huang K, et al (2017) Uranium(IV) Chloride Complexes: UCl_6^{2-} and an Unprecedented $U(H_2O)_4Cl_4$ Structural Unit. Inorg Chem 56:9772–9780. https://doi.org/10.1021/acs.inorgchem.7b01293

Wang X, Andrews L, Marsden CJ (2009) Infrared Spectra and Density Functional Calculations of the SUO_2 Molecule. Inorg Chem 48:6888–6895. https://doi.org/10.1021/ic900869f

Wang X, Johnson TM, Lundstrom CC (2015a) Isotope fractionation during oxidation of tetravalent uranium by dissolved oxygen. Geochimica et Cosmochimica Acta 150:160–170. https://doi.org/10.1016/j.gca.2014.12.007

Wang X, Johnson TM, Lundstrom CC (2015b) Low temperature equilibrium isotope fractionation and isotope exchange kinetics between U(IV) and U(VI). Geochimica et Cosmochimica Acta 158:262–275. https://doi.org/10.1016/j.gca.2015.03.006

Weigend F, Ahlrichs R (2005) Balanced basis sets of split valence, triple zeta valence and quadruple zeta valence quality for H to Rn: Design and assessment of accuracy. Phys Chem Chem Phys 7:3297–3305. https://doi.org/10.1039/B508541A

Weyer S, Anbar AD, Gerdes A, et al (2008) Natural fractionation of $^{238}U/^{235}U$. Geochimica et Cosmochimica Acta 72:345–359. https://doi.org/10.1016/j.gca.2007.11.012

Widanagamage IH, Schauble EA, Scher HD, Griffith EM (2014) Stable strontium isotope fractionation in synthetic barite. Geochimica et Cosmochimica Acta 147:58–75. https://doi.org/10.1016/j.gca.2014.10.004

Woon DE, Dunning TH Jr (1993) Gaussian basis sets for use in correlated molecular calculations. III. The atoms aluminum through argon. The Journal of Chemical Physics 98:1358–1371. https://doi.org/10.1063/1.464303

Wyckoff RWG (1963) Fluorite structure. In: Crystal Structures, 2nd edn. Interscience Publishers, New York, pp 239–444

Zhang F, Algeo TJ, Romaniello SJ, et al (2018) Congruent Permian-Triassic $\delta^{238}U$ records at Panthalassic and Tethyan sites: Confirmation of global-oceanic anoxia and validation of the U-isotope paleoredox proxy. Geology 46:327–330. https://doi.org/10.1130/G39695.1

Zhang F, Lenton TM, del Rey Á, et al (2020) Uranium isotopes in marine carbonates as a global ocean paleoredox proxy: A critical review. Geochimica et Cosmochimica Acta 287:27–49. https://doi.org/10.1016/j.gca.2020.05.011

Zheng Y, Anderson RF, van Geen A, Fleisher MQ (2002) Preservation of particulate non-lithogenic uranium in marine sediments. Geochimica et Cosmochimica Acta 66:3085–3092. https://doi.org/10.1016/S0016-7037(01)00632-9

Zhou M, Andrews L, Ismail N, Marsden C (2000) Infrared Spectra of UO_2, UO_2^+, and UO_2^- in Solid Neon. J Phys Chem A 104:5495–5502. https://doi.org/10.1021/jp000292q

Zwanziger JW (2009) Computation of Mössbauer isomer shifts from first principles. J Phys: Condens Matter 21:195501. https://doi.org/10.1088/0953-8984/21/19/195501

Chapter 3

Field shift isotopic fractionations in the transuranic elements plutonium and neptunium

Abstract

In this study we examine the field shift effect in equilibrium isotope fractionation of Pu and Np using the DFT-PAW method (Schauble, 2013). We then estimate total (mass dependent and field shift) isotopic fractionations across species with different oxidation states, as well as species that are potentially significant in the natural environment. We determine that the presence of the +3 or +6 oxidation state in redox reactions tends to drive the largest fractionations. At ambient temperatures, ^{242}Pu/^{239}Pu will be 5‰ higher in Pu(III)-bearing species than Pu(V), 3.5‰ higher than Pu(V), and 3.0‰ higher than Pu(IV). It is expected that Pu(V) and Pu(IV) species will only differ from each other by up to 0.5‰, but may overlap in composition. Other plausibly measurable isotope pairs in the Pu system produce fractionations that go in the same direction relative to the neutron numbers, for the most part, with the pair ^{241}Pu/^{238}Pu being essentially identical in total isotopic fractionation to ^{242}Pu/^{239}Pu. For the ^{237}Np/^{235}Np system, unknown neptunium nuclear charge radii required us to extrapolate from the measured charge radius systematics of nearby actinide elements (Ferro et al., 2010). Using these model radii, we estimate that the Np(III) oxidation state will have ~1.3‰ higher ^{237}Np/^{235}Np than Np(VI) species, and 0.6‰ higher ^{237}Np/^{235}Np than either Np(V) or Np(IV). Np(V) and Np(IV) will be approximately 0.7‰ higher than Np(VI) However, estimated Np isotope fractionations reported here are less precise because the nuclear charge radii are as yet unmeasured. To the best of our knowledge, this is the first detailed study of potential equilibrium field shift isotope fractionation in the transuranic elements. The potential for non-radiogenic or radioactive fractionation of transuranic elements is of interest due to their presence as toxins in the environment as a

consequence of nuclear fallout from weapons tests, nuclear disasters, and potential leaks due to storage of nuclear waste.

3.1. Introduction

3.1.1 Plutonium and neptunium presence in the environment

Since the advent of nuclear weapons and nuclear energy, plutonium and neptunium have been released into the environment on a global scale. As toxic, radioactive elements, their behavior in the environment is of great interest in order to assess and mitigate risks associated with their presence in the environment. Detectable quantities have been found in water, vegetation, soils, sediments, and ice as a consequence of anthropogenic release (Holm et al., 1986; Cooper et al., 2000; Olivier et al., 2004; Child and Hotchkis, 2013; Bu et al., 2014ab; Hirose and Povinec, 2015; Cao et al., 2021; Lopez-Lora et al., 2023), reflecting a variety of possible sources. Nuclear waste is typically stored in the vadose zone with the goal of containment. Notably, there have been incidents in which material has been released more widely into the environment; lawsuits over their presence are common, with one settlement of $1 billion over the release of a small quantity of plutonium to the atmosphere at the Waste Isolation Pilot Plant (Klaus, 2019). Nuclear weapons tests occasionally still happen in countries such as North Korea, and proliferation remains a contentious geopolitical issue. Nuclear disasters have released large quantities of radioactive elements in places such as Fukushima (Bu et al., 2015; Evrvard et al., 2014; Jaegler et al., 2019), Three Mile Island, and Chernobyl (Mietelski and Was, 1995; Jakopic et al., 2010), the effects of which may persist generations after the event. In the case of plutonium, isotopic ratios differ spatially due to the nuclear histories of particular regions, with areas such as Bikini Atoll having markedly different isotopic ratios than areas for which the only significant input of Pu is stratospheric fallout (Table 3-1). Depleted uranium ammunition, which still sees combat use today, can also release small quantities of transuranic elements (Desideri et al., 2004). Nuclear disarmament requires the safe storage of nuclear weapons so as to mitigate the release of radioactive elements into the environment. Certain environments also tend to concentrate plutonium at higher rates, for example Mono Lake in California has a higher-than-average concentration of plutonium owing primarily to its high alkalinity (Anderson et al., 1982; Simpson et al., 1982; Nelson et al., 1989).

While there is strong evidence for extinct naturally-formed ^{239}Pu in places such as the Oklo natural reactor, which was produced during the reactor phase due to neutron capture by uranium and subsequently decayed to ^{235}U (Horie et al., 2004), as well as evidence of primordial ^{244}Pu formed during the Big Bang (Hoffman et al., 1971; Wallner et al., 2004), essentially all present day Pu and Np in the Earth surface environment is a consequence of human activity, with the exception of the small quantity of ^{239}Pu that is present in uranium ores. Anthropogenic release has increased the abundance of plutonium by approximately 10^6 (Geckeis et al., 2016). It can be assumed that essentially all environmental Pu and Np was released after the first nuclear detonations in 1945, with over 2400 nuclear tests overall, including over 500 stratospheric tests that impacted the radioisotope signal globally (Beck and Bennett, 2002). This also makes neptunium and plutonium isotopes good case studies and stratigraphic markers for anthropogenic and natural changes to the Earth's environment that have occurred since 1945 (Waters et al. 2015, 2016) as they do not appear in sediments prior to 1945 and therefore can mark the start of the nuclear age in recent sediments. It is also possible to use these radioactive isotopes as proxies for recent erosion (Hoo et al., 2011; Alewell et al., 2017).

3.1.2 Actinide behavior in the environment

Plutonium and neptunium exhibit qualitatively similar behaviors in the environment to uranium, which has been extensively studied in both natural and anthropogenic occurrences. For each of these actinides, oxidation state is a primary control over their solubility in the environment, in addition to pH and availability of certain ligands. Pentavalent and hexavalent species tend to form highly soluble, linear actinyl type molecules (AnO_2^{n+}) complexed equatorially by various ligands (Choppin, 2006). Common ligands include CO_3^{2-}, OH^-, carboxylic acids, and other organic ligands. Organic ligands may also play a role in oxidation/reduction reactions involving U, Np and Pu, and likely play a role in their microbial reduction as well (Neu et al., 2009, 2011; Law et al., 2010). Tetravalent An(IV) species tend to be insoluble, forming oxides, hydroxides, and colloids. The solubility of the An(III) trivalent species are comparatively poorly understood. The oxidation state and mobility of these elements is in turn influenced by pH, Eh, and the presence of complexing ligands (Nitsche, 1990; Hirose & Sugimora 1993). As a general rule for solubility, $AnO_2^+ < AnO_2^{2+} \leq An^{3+} < An^{4+}$ (Maher et al., 2013). The Pourbaix diagrams in Figure 3-1, 3-2, and 3-3 demonstrate the speciation of each actinide at a variety of environmental conditions.

Uranium occurs primarily in the hexavalent and tetravalent oxidation states. Hexavalent uranium will tend to occur in aqueous, oxygenated settings as U(VI)-bearing uranyl type species (UO_2^{2+}). The uranyl ion is highly mobile and soluble. At neutral-to-alkaline pH, U(VI) will tend to be bound to carbonate ligands, forming species such as $Ca_2UO_2(CO_3)_3$ and $UO_2(CO_3)_3^{4-}$. Under reducing conditions, uranium occurs primarily in the U(IV) oxidation state. U(IV) tends to be insoluble, forming oxides or adsorbing to mineral surfaces. While U(V) has been stabilized in experimental settings (Faizova et al., 2019) in uranyl-type compounds, it does not tend to be stable in nature.

Plutonium displays the most variation in redox states among the actinides, being found as Pu(VI), Pu(V), Pu(IV), and Pu(III) in natural environments (Keeney-Kennicut & Morse, 1984; Fukai et al., 1987; Choppin & Kobashi, 1988; Morse & Choppin 1986; Nelson et al. 1987; Nash et al., 1988; Mitchell et al., 1991; Sanchez et al., 1994). The variation in redox states of plutonium observed at surface conditions arises both from the difference in the stability of these phases at environmentally relevant Eh and pH, as well as from its tendency to undergo disproportionation reactions (Silver, 2014), which are most likely to occur at $pH < 1.5$ or $pH > 7$ (Choppin and Jensen, 2006). Pu(VI) and Pu(V) species occur as plutonyl-type compounds (PuO_2^{2+} and PuO_2^{+} respectively). Similar to U(IV), Pu(IV) occurs primarily as refractory solid oxides such as PuO_2, or hydrated species bound to hydroxyl groups. Pu(IV) is also likely to sorb to mineral surfaces and colloids. Pu(III) species are poorly understood compared to those in other oxidation states. It is believed they also have an affinity for hydroxyl groups. However, they may be more similar in solubility to PuO_2^{2+} species, owing to the effective equatorial charge of the PuO_2^{2+} ion being 2.9 (Choppin and Rao, 1984). All 4 of these oxidation states may be present simultaneously in acidic solutions due to disproportionation reactions, owing to the relatively low potentials for all common redox couples (Table 3-2), with the redox couples of Pu(III)/Pu(IV) and $Pu(V)O_2^{+}/Pu(VI)O_2^{2+}$ also being less negative than the $Pu(IV)/Pu(VI)O_2^{+}$ couple (Clark et al. 2006). At higher pH, it is believed that Pu(III) is unlikely to remain stable. In neutral conditions, Pu(IV), Pu(V), and Pu(VI) may be present, while more alkaline environments favor the Pu(V) and Pu(VI) oxidation states.

Neptunium redox chemistry is less variable relative to plutonium redox chemistry. Pentavalent NpO_2^{+} species are stable under oxic to moderately suboxic conditions, binding to carbonate ligands at higher pH (Degueldre et al., 2010). Tetravalent neptunium occurs primarily in poorly crystalline $Np(OH)_4$ solids or sorbs to form complexes with minerals or other solids (Runde et al., 2010). The solid NpO_2 is thermodynamically favored but has not been precipitated in experiments involving waters of natural composition (Kaszuba and Runde, 1999).

Uranium and plutonium released to the environment during nuclear weapon detonations mainly distributes refractory, tetravalent, insoluble -O_2 oxide particles (Choppin, 2006). However, it has been observed in the Rocky Flats Environmental Technology Site that the presence of organic matter stabilized colloidal plutonium, and that colloidal plutonium was responsible for elevated concentrations observed in storm runoff, rather than dissolved plutonium (Santschi et al., 2002). Additionally, plutonium at this site was preferentially associated with organic molecules rather than clay particles. Neptunium is of great concern with respect to nuclear waste storage owing to NpO_2^+ species being stable under suboxic conditions and being highly mobile (Maher et al., 2013).

3.1.3 Motivation

Uranium, plutonium, and neptunium have no stable isotopes. However, within the uranium system, it is possible to observe the chemical fractionation effects analogous to those found in stable isotopic systems (Stirling et al. 2005, 2006, 2007; Weyer et al. 2008; Wang et al., 2015ab). Both ^{238}U and ^{235}U are long-lived, dominantly primordial to the solar system, and the isotopes are well mixed in planetary materials. This allows researchers to assign a “canonical” ratio for $^{238}U/^{235}U$ of 137.88 as a reference for geochronology, and for evaluating fractionation processes. In the case of U, chemically induced deviations from the canonical $^{238}U/^{235}U$ ratio can be measured in natural, contaminated, and synthetic samples. These deviations are most systematic when U(IV) species are compared to U(VI) species, the reduced species tending to have higher $^{238}U/^{235}U$, by approximately 1-2‰ in materials reacting at Earth surface conditions (Wang et al., 2015; Weyer et al., 2008). The observed enrichment of ^{238}U in reduced uranium is in the opposite direction from what would be predicted from mass dependent fractionation, where oxidized species tend to be enriched in the more massive isotopes at equilibrium. The magnitude of the fractionation is also larger than predicted for a mass-dependent equilibrium at such high atomic numbers. Instead, uranium isotope fractionation is believed to be driven mainly by the field shift effect (Bigeleisen et al., 1996; Nomura et al. 1996). Subsequent experimental and theoretical studies have confirmed this result, finding that the field shift effect is approximately twice the magnitude of the mass-dependent component of fractionation $^{238}U/^{235}U$ fractionation, with field shift and mass-dependent effects going the opposite direction (Schauble, 2006; Abe et al., 2008 ab; Wang et al., 2015).

We are interested in determining whether the field shift effect observed in uranium also occurs to a significant degree in environmentally relevant contexts for plutonium and neptunium. This seems likely: the isotopic difference in the nuclear charge radii of Np and Pu isotopes may equal or exceed that between the major U isotopes, while differences in electron density between different oxidation states appear to increase with increasing atomic number. This can be seen in the following equation for the field shift effect, taken from Blanchard et al., (2017):

$$\ln \alpha_{\mathrm{fs}} \approx \frac{2\pi Z e^2}{3\mathrm{k}T} \left(|\psi(0)_{\mathrm{A}}|^2 - |\psi(0)_{\mathrm{B}}|^2\right) \Delta\langle \mathrm{r}^2_{\mathrm{isotopes}}\rangle$$

Where α_{fs} is the field shift fractionation factor, Z is the atomic number, e is the charge of an electron, k is the Boltzmann constant, $|\psi(0)AX|$ and $|\psi(0)BX|$ are the electron density at the nucleus for the species AX and BX, and $\Delta\langle \mathrm{r}^2\rangle$ is the difference in the mean squared charge radius between the nuclei of interest. We therefore expect the possibility of field shift effects comparable to or possibly even larger than those seen in the uranium system, particularly when more than one oxidation state or Np or Pu is present.

A further motivation for investigating transuranic elements is as a test of theoretical methods for estimating field shift effects against independently measured isomer shifts from ^{237}Np-Mössbauer spectroscopy. In Mössbauer spectroscopy, based on isotope-specific gamma ray absorption, very high spectral resolution allows for the determination of small energy shifts between various solids. What is important for our study is that the absorption of gamma radiation produces an excited nuclear state in the target isotope in a solid that slightly changes the volume of the nucleus. This process can be thought of as the reverse of the field shift effect, with the transition energy between two nuclear states depending on the volume change of the nucleus in those states, as well as the electron density at its crystallographic site in the solid. We have compared DFT calculations of electron densities at Np sites in solids to their Mössbauer shifts (Figure 3-4 and Table 3-3). The linearity of the comparison suggests that an analogous phenomenon such as the field shift can be modeled for neptunium using the same *ab initio* methods. Owing to the chemical similarities among U, Np, and Pu, this suggests that the same method may be extended to uranium and plutonium as well.

It is important to emphasize that Pu and Np isotopes are relatively short-lived compared to ^{238}U and ^{235}U, and are not primordial in the surface environment of the Earth, so there are large radiogenic variations in their isotopic compositions. However, non-radiogenic isotope variability may still be of interest, both as a possible confounding factor in assigning sources and as a potential tracer of post-radiogenic processes. So long as 1) the isotope ratio of the Pu or Np source is known, 2) there is sufficient instrumental precision to measure per mil level fractionations, and 3) the radioactive lifetimes for the relevant isotopes are well-constrained (or much longer than the time scale of interest), it may be possible to measure isotopic fractionation. The half-lives of the major Pu and Np isotopes are displayed in Table 3-4. We expect that the greatest fractionations will be observed in environments in which reduction or oxidation is taking place, and so these environments should be the focus of any future study.

Isotope ratios of plutonium are used to determine the sources of plutonium in the environment (Varga, 2007). For example, ^{242}Pu is present in higher abundances in nuclear waste than from nuclear detonations, and therefore can be used to determine if the Pu found in a given environment is a product of nuclear testing or a leak from fuel disposal, for example. Similarly, plutonium generated from a reactor after a sufficiently long irradiation time and high neutron flux will have an abundance of ^{238}Pu, and high ^{241}Pu/^{239}Pu ratio. The potential heterogeneities that result due to the scatter in material sources may render per mil level measurement of limited value in many contexts. In contrast, nuclear waste may consist of material for which the isotope ratios are well-constrained. It is also in the public interest to monitor if nuclear materials stored in the vadose zone are mobilized via redox reactions, which can perhaps be done through monitoring their isotope ratios over time and determining if there are any deviations that can be explained through field shift effects.

For plutonium, the primary isotope ratio we have chosen to study is ^{242}Pu/^{239}Pu. The isotopic difference of 3 amu between these isotopes is convenient for qualitative comparison to ^{238}U/^{235}U. It is also difficult to separate ^{238}Pu from ^{238}U in mass spectrometry (Steier et al., 2013) and so the ratio ^{241}Pu/^{238}Pu, while having the same difference in neutron numbers, may be less promising to measure. We anticipate that the fractionations would be quite similar ^{242}Pu/^{239}Pu. ^{242}Pu and ^{239}Pu are also long-lived enough to persist in the environment with little decay for the entire duration of the nuclear era (Table 3-4). A primary motivation of the present study is to examine the consequences of nuclear waste disposal, and ^{242}Pu is a potential tool for such analysis owing to its enrichment in nuclear waste relative to its occurrence in nuclear fallout. In the case of Np, it does not appear that environmental ratios are considered often in environmental studies, likely owing to the short half-lives of many isotopes (Table 3-4) and the rarity of neptunium in the environment compared to plutonium or uranium. We have therefore somewhat arbitrarily chosen to examine the ratio ^{237}Np/^{235}Np, as ^{237}Np is the primary isotope of interest to environmental geochemists as well as in Mössbauer spectroscopy.^{235}Np has a large enough difference in neutron number to potentially display meaningful fractionation, as well as a half-life that is significant on human timescales.

3.2. Method

Equilibrium chemical fractionations of Np and Pu isotopes are estimated by using the DFT-PAW method of Schauble (2013) to determine the field shift component of fractionation, and the equations of Urey (1947) and Bigeleisen and Mayer (1947) to determine the mass dependent components of fractionation. These are summed to produce an estimate of the overall, or net, fractionation. The DFT-PAW method requires calibration to all-electron calculations to relate electron density at the actinide nucleus to an energy shift caused by isotope substitution.

The Pourbaix diagrams of Figures 3-2 and 3-3 provided the basis for choosing geochemically relevant species to model, encompassing a variety of carbonate, hydroxide, and aqueous compounds, as shown in Table 3-5 and 3-6. Recent studies suggest the presence of Ca atoms in many carbonate complexes of Pu and Np (Reiller, 2024). Our previous work in the U isotope system suggests that any differences in the isotopic composition of Ca-bearing complexes vs. complexes without Ca will be insignificant. We also included α-hydroxycarboxylate as a sample organic ligand. There is limited data on the exact speciation of plutonium and neptunium species in natural systems, especially with regards to inner sphere hydration. For species with analogous uranium compounds that may be more well studied, we used these as initial guesses. For the hydroxide species, we modeled them with additional solvating waters at this step in order to more accurately represent their speciation in the environment. For all other natural species in which inner shell solvation may be significant, we removed any water molecules which did not coordinate around the central actinide atom.

Owing to the intensive nature of all-electron calculations, it is necessary to pick relatively simple species for calibration before being able to analyze more complex species. We choose to model small fluorides, chlorides, and hydroxide molecules and complex ions in oxidation states ranging from +3 to +6. We used 11 Pu species and 12 Np species for calibration.

3.2.1. Determining optimized geometries and mass dependent fractionations

Initial guess geometries for each molecule were obtained from previous calculations of analogous U-bearing species, as described in Chapter 2. For each molecule or molecular complex studied, the geometry is relaxed to the minimum-energy configuration within DFT theory, and vibrational frequencies are then calculated. The sensitivity of vibrational frequencies to isotope substitution determines the mass dependent component of fractionation, determined using the method of Urey (1947). For Pu and Np, we use the def-TZVP basis sets (Cao et al. 2002) while for all other elements we use def2-TZVPP basis set family (Weigend and Alrichs, 2005) obtained via the Basis Set Exchange (Feller, 1996; Schuchardt et al., 2007; Pritchard et al., 2019). This choice of basis set allows us to have related basis sets for both the central actinide as well as the smaller atoms that coordinate it. This family of basis sets was also used to model uranium species in Chapter 2, allowing us to compare the present results to those from the uranium system. We use the Perdew, Burke, and Ernzerhof (PBE) functional (Perdew et al., 1996) for all calculations. Geometry optimization and vibrational analyses for molecules and molecular complexes are performed using the software Gaussian09 (Frisch et al. 2009), on the Hoffman2 cluster at UCLA.

We also examined crystalline solid uraninite-like structures for PuO_2 and NpO_2 (Wyckoff, 1963) due to their potential significance in the environment as a consequence of nuclear detonations. In order to obtain optimized geometries for these solids we use periodic boundary conditions and projector-augmented-waves in the software AbInit. Projector-augmented-wave (PAW) datasets generated using the software AtomPAW (Holzwarth et al., 2001) were utilized for these calculations. PAW datasets for Np and Pu were generated for this study. For Np the PAW dataset is generated using a valence and semicore electronic configuration of $6s^2\ 7s^2\ 6p^6\ 7p^0\ 6d^1\ 5f^4$. For Pu the valence used is $6s^2\ 7s^2\ 6p^6\ 7p^0\ 5f^6$. It should be noted that the Np PAW dataset is constructed with a finite nuclear charge radius, whereas the Pu PAW assumes a point nucleus. As a result, raw electron densities at the Pu vs. Np nuclei from the two PAW datasets are not directly comparable. PAW datasets for all other elements are taken from the AbInit JTH library (https://www.abinit.org/psp-tables) (Jollet et al., 2014). For all PAW calculations, we use a Hubbard U parameter (not to be confused with the atomic symbol for uranium) to correct systematic errors that arise due to the *f*-electron bands of actinide-bearing crystals; the choice of U is based on previous DFT studies. For Pu, U is set to 4.0 eV and a J of 0.75 eV (Sun et al., 2008). For Np we use a U of 4.0 eV and a J of 0.6 eV (Maldonado et al., 2016). For both PuO_2 and NpO_2, we examined a 12-atom cell (with 4 formula units) and allowed each crystal to fully relax both its atomic positions and unit cell volumes. PuO_2 relaxed to unit cell length A=5.42Å, B = 5.42Å, and C = 5.47Å. NpO_2 relaxed to A=5.48Å, B=5.48Å, and C=5.42Å. Both species were modeled as antiferromagnetic (Pegg et al., 2019) but it was determined that there was minimal change in electron density for a ferromagnetic structure ($\leq$0.1‰).

The vibrational frequencies from the optimized geometries of aqueous species allow us to determine the mass dependent component of fractionation via the equation of Urey (1947). To obtain the mass dependent component of fractionation for the solid dioxide species we use the force constant method of Widanagamage et al. (2014), adapted from the original formulation by Bigeleisen and Mayer (1947). Formally, in this method a single Pu or Np atom from the fully optimized geometry is perturbed in the x, y, and z-directions to obtain the force constant, though due to the periodic boundary conditions of this model, a single atom is perturbed in each unit cell.

The PBE functional tends to underestimate vibrational frequencies (Schauble, 2004; Meheut et al., 2007). In order to estimate uncertainties caused by this underestimation, a frequency scale factor is fitted via comparison of ab initio vibrational frequencies versus experimental values. There are limited vibrational frequency data for plutonium and neptunium species, though molecular PuF_6 and NpF_6 have been carefully measured (McDowell et al., 1974) We compared the measured and calculated frequencies for these, as well as the analogous species UF_6. All three appear to show similar systematic underestimation, i.e., scale factors that are approximately equal to one another. Therefore, we use the scale factor from our previous study of uranium in Chapter 2 to examine the potential error in mass dependent components of fractionation. In that study we found the PBE-based calculations underestimated vibrational frequencies by ~2.0 ± 0.1%. We determined for the $^{238}U/^{235}U$ system that this results in an uncertainty of 0.01‰, and infer that the error is of a similar magnitude for plutonium and neptunium.

3.2.2. Determining the field shift component of fractionation

After optimizing molecular geometries, electronic energies for the calibration species are determined using all-electron relativistic methods, via eXact 2-Component Hamiltonian (X2C) theory (Liu and Peng, 2009). Density functional theory with projector-augmented-waves (PAWs) and plane-wave basis sets is then used to determine the electron density at the nucleus for each species. For all-electron relativistic models of Np and Pu species, double-zeta quality basis sets are used (Dyall, 2007), while cc-pVDZ (Dunning, 1989; Woon and Dunning, 1993) is used for all other elements. These are relatively small basis sets, chosen to keep the computational complexity reasonable. The field shift is directly estimated in the all-electron calculations by varying the mean squared charge radius of the Pu or Np atom in each species. For Pu, isotopic charge radii are tabulated from Fricke and Heilig (2004). For Np, there is limited data available so we instead calculate the radius for each isotope approximately via the method of Ferro et al. (2010), using uranium nuclear charge radii from Fricke and Heilig (2004) as input data. This allows us to give an initial estimate of the field shift fractionation for neptunium until more data becomes available, but clearly these estimates should be updated when charge radius measurements become available. Because the field shift effect is an equilibrium effect, we can use energies of isotope substitution from this step to determine the equilibrium constant using the equation $\Delta G = -RT\ln K$. All-electron calculations at this step are performed with the software DIRAC (Saue et al., 2011).

Once field shift energy differences have been determined via the all-electron method, corresponding DFT-PAW electron densities are calculated in order to generate the calibration line. Optimized vapor phase species are modeled as-is under periodic boundary conditions in a cube with a side length of ~12 Å to minimize inter-molecular interactions. Projector-augmented-wave data sets are utilized for all elements as discussed previously. DFT-PAW models are generated with the AbInit package (Torrent et al, 2008; Gonze et al., 2009). DFT-PAW electron densities at the nucleus are calculated using the method of Zwanziger (2009).

Calibration lines for isotope pairs of Pu and Np are plotted in Figures 3-5 and 3-6, displaying DFT-PAW electron density vs. isotopic energy shift. If these relationships hold for other species, the slope of the calibration lines allow estimation of field shift energy differences from DFT-PAW calculations on more complex species relevant to natural systems that would be impractical to model with all-electron methods.

It is most convenient to report the field shift effect relative to other species. This requires consideration of both the most relevant oxidation state and most relevant species for comparison. For both Pu and Np, the most relevant oxidation state at surface conditions is the pentavalent state. Using the Pourbaix diagrams of Figures 3-2 and 3-3, we also chose the species which is likely to occur in seawater as well as circumneutral pH. For Pu we chose the species $PuO_2CO_3(H_2O)_2^-$. For Np we chose the species $NpO_2CO_3(H_2O)_2^-$. All fractionations in this study are reported relative to this pair of species.

As a test on the influence of structure optimization on estimated field shift effects, Table 3-3 includes the DFT-PAW electron densities for Np-bearing experimental structures, structures in which the unit cell parameters remain unchanged from the experimental values while the atomic positions are allowed to optimize, and structures in which both the unit cell volume, angles, and atomic positions are allowed to optimize freely. It can be seen that the electron densities vary by 1-9 e^-/a_0^3 between these methods, suggesting that the differences in electron density that result from these different methods of structural optimization are unlikely to be significant. It can be inferred from this data that differences in electron density between the optimized structures of the plane wave method and the method of the linear combination of atom-centered basis sets that we use for most species in this study are similarly unlikely to impact estimates of electron density significantly; oxidation state and bond partner are likely more important than atomic position.

3.3.4 Scale factors

Fractionations for other isotopic ratios are obtained by multiplying field shift and mass dependent scale factors times the $^{242}Pu/^{239}Pu$ or $^{237}Np/^{235}Np$ fractionation for any pair of species (Tables 3-7 and 3-8). The field shift component of fractionation's scale factor is dependent on the difference in the mean squared nuclear charge radii. The mass dependent component of fractionation's scale factor derives from the equation of Young et al. (2002):

$$\alpha_{2-1}^{A-B}=(\alpha_{3-1}^{A-B})^{\beta}$$

where A and B are the substances of interest for isotopes 1, 2, and 3. Note that this β is distinct from the β for the fractionation factor for a species versus atomic vapor as defined in chapter 1. We derive β according to the equation

$$\beta = \frac{\frac{1}{m_1}-\frac{1}{m_2}}{\frac{1}{m_1}-\frac{1}{m_3}}$$

where m_1, m_2, and m_3 refer to the masses of three isotopes, and use this value as a scale factor to switch between isotopic ratios. It is possible to determine a scale factor for isotope pairs that have no isotope in common, e.g. of mass m_4 and m_5, by multiplying by an intermediate β which contains one of the new isotopes, resulting in the formula below:

$$\beta = \frac{\frac{1}{m_2}-\frac{1}{m_4}}{\frac{1}{m_1}-\frac{1}{m_2}} \text{ x } \frac{\frac{1}{m_4}-\frac{1}{m_5}}{\frac{1}{m_2}-\frac{1}{m_4}}$$

3.3. Results

Estimated $^{242}Pu/^{239}Pu$ fractionations at 298 K and 500 K are shown in Table 3-9. $^{237}Np/^{235}Np$ fractionations are shown in Table 3-10. Total fractionations versus temperature are displayed in Figure 3-7 for Pu and Figure 3-8 for Np. Polynomial fits for each Pu species from 250 K to 4000 K are shown in Table 3-11, and for each Np species in Table 3-12.

3.3.1 Plutonium

Consistent with previous studies of uranium, the field shift effect for the $^{242}Pu/^{239}Pu$ isotopic ratio is larger than the mass dependent component of fractionation between species of different oxidation states, by a factor of ~2-10 times at 298 K. Field shift and mass dependent components of fractionation oppose each other for these redox reactions. Pu(VI) species are predicted have 0.9-1.9‰ lower $^{242}Pu/^{239}Pu$ than the reference Pu(V) species $PuO_2CO_3(H_2O)_2^-$. Pu(IV) species are predicted to be only 0.1-0.8‰ higher in $^{242}Pu/^{239}Pu$ than the Pu(V) reference. Pu(III) species are predicted to be approximately 3.3-3.5‰ higher than the Pu(V) reference species. At 500 K, Pu(VI) species are predicted have 0.6-1.2‰ lower $^{242}Pu/^{239}Pu$ than the reference Pu(V) species $PuO_2CO_3(H_2O)_2^-$. Pu(IV) species are predicted to be only 0.1-0.5‰ higher in $^{242}Pu/^{239}Pu$ than the Pu(V) reference. Pu(III) species are predicted to be approximately 2‰ higher than the Pu(V) reference species.

3.3.2 Neptunium

At 298 K, Np(VI)-bearing compounds are expected to have approximately 0.4-0.7‰ lower $^{237}Np/^{235}Np$ than the Np(V) reference species $NpO_2CO_3(H_2O)_2^-$. Np(IV)-species are expected to differ very little from Np(V) compounds, with $^{237}Np/^{235}Np$ only 0.1‰ higher than $NpO_2CO_3(H_2O)_2^-$ on average. Np(III) species are expected to have 0.7-1.2‰ higher $^{237}Np/^{235}Np$

than Np(V)-bearing $NpO_2CO_3(H_2O)_2^-$. At 500 K, Np(VI)-bearing compounds are expected to have approximately 0.3-0.4‰ lower $^{237}Np/^{235}Np$ than the Np(V) reference species $NpO_2CO_3(H_2O)_2^-$. Np(IV)-species are expected to differ very little from Np(V) compounds, with $^{237}Np/^{235}Np$ 0.0-0.1‰ higher in these species than the Np(V) reference species. Np(III) species are expected to have 0.4-0.8‰ higher $^{237}Np/^{235}Np$ at this temperature.

3.4 Discussion

3.4.1 Sources of uncertainty

As previously indicated, published speciation data for the actinide elements in this study are not as detailed as in the uranium system, nor are the molecular structures of as many relevant species available. A few species studied here have notably distinct DFT-PAW electron densities, which may reflect speciation effects, but it is also possible that they are unrealistic species, or have optimized geometries that are not reflective of their actual structures. For instance, $PuO_2(CO_3)_3^{4-}$ is predicted to be 1‰ higher in $^{242}Pu/^{239}Pu$ than other Pu(VI) species, while the structurally similar species $PuO_2(CO_3)_3^{5-}$ is predicted to be 1‰ lower in $^{242}Pu/^{239}Pu$ than other Pu(V) species. Finally, we did not model solvation for the present study, beyond the addition of inner sphere water molecules. Implicit solvation models can impact structures and bond lengths as observed for uranium species in Chapter 2, potentially changing the inner sphere coordination for some molecules. This concern is particularly relevant because water molecules were added to the central actinide in some species in an *ad hoc* fashion due to the limited data on speciation and structure. These factors could change the calculated electron densities. Indeed, previous calculations for uranium suggest that changes in electron density due to solvation models don’t necessarily vary in a predictable manner.

The slope of the DFT-PAW calibration line (Figure 3-5) for ^{242}Pu/^{239}Pu is 101 +/- 5 (1 s.e.) e^{-}/a_0^3 per J/mol. Using the standard error, we can estimate calibration errors between the test species $PuO_2CO_3(H_2O)_3$ and $PuCO_3(H_2O)_5^+$ and their effects on estimated fractionation. A ±1 s.e. change in the slope leads to a change of ±0.3‰ out of an estimated fractionation of 6.3‰. The slope of the calibration line is also impacted in by the choice of nuclear charge radii. We can determine the impact the choice in nuclear charge radius has on the electron density by comparing the difference in the square of the charge radii for the isotopes in question from other sources, using equation 1. In the case of ^{242}Pu vs. ^{239}Pu, the tabulation of Nadjakov et al. (2015) indicates an 11% larger difference in mean squared charge radii. For $PuO_2CO_3(H_2O)_2$ vs. $PuCO_3(H_2O)_5^+$ the estimated field shift component of fractionation would increase by 0.7‰, to 7.0‰, with the 11% larger radius difference. If we use the nuclear charge radii tabulated in Angeli et al. (2008) instead, the difference 17% larger, and the resulting field shift component of fractionation would be 7.3‰ vs. 6.3‰.

The standard error of the slope of the calibration line for ^{237}Np/^{235}Np (Figure 3-6) is 1 e^{-}/a_0^3 per J/mol. Examining a sample fractionation between the species $NpO_2CO_3(H_2O)_3$ and $NpCO_3(H_2O)_5^+$ we find a range of field shift fractionations between 2.24 and 2.42‰ – suggesting uncertainty of ±0.09‰. However, in the case of neptunium the radii are estimated roughly, and the uncertainty associated with this estimation almost certainly dominates the overall uncertainty in field shift isotope fractionation factors. We are not able to quantify this source of error. If measurements of neptunium charge radii are eventually made, the field shift results can easily be scaled so as to be consistent with them. Mass dependent fractionation results are not impacted by the nuclear charge radius.

Uncertainty in vibrational frequencies and their sensitivities to isotope substitution control the accuracy of the estimated mass dependent component of fractionation. Because the PBE functional typically underestimates vibrational frequencies and force constants (Schauble, 2004; Meheut at al., 2007), we determined the magnitude of this systematic underestimation using measurements of vibrational frequencies within the uranium system, and applied the same scale factor to the Pu and Np systems. It turns out that the scale factor effect is limited relative to other likely sources of error. For instance, on the isotopic fractionation between the species $PuO_2CO_3(H_2O)_3$ and $PuCO_3(H_2O)_5^+$ we determine the mass dependent component of fractionation to be -0.97‰ for this pair, compared to the scaled result of -0.98 to -1.01‰. For the neptunium species $NpO_2CO_3(H_2O)_3$ and $NpCO_3(H_2O)_5^+$we determine the mass dependent component of fractionation using this scale factor to be 0.57 to 0.59‰, versus the initial result of 0.56‰. Of course, the assumption that uranium species show the same frequency scaling as neptunium and plutonium-bearing molecules and solids introduces additional uncertainty. Random scatter is also not accounted for. Calculations of force constants via the perturbation method (used for solid species in the present study) tend to overestimate β at low temperatures because of their implicit assumption that lnβ is proportional to $1/T^2$. Previous study of the uranium system determined that this method overestimated the mass dependent component of fractionation for $UO_{2(s)}$ by approximately 0.05‰. It is likely that the Np and Pu equivalents have a similar offset, though we do not make any correction for this effect in the tabulated data. At higher temperatures, the offset will be minimal because $1/T^2$ proportionality is more closely followed.

3.4.2. Systematics of plutonium equilibrium isotope fractionation

^{242}Pu/^{239}Pu fractionation appears to be comparable to what is seen in the ^{238}U/^{235}U system, with fractionations of up to several per mil that are largest between species with plutonium in different oxidation states. The net fractionation for these reactions is dominated by field shift effects that go in the opposite direction of the predicted mass dependent component and are 2-10X as large. As in uranium, more reduced species will tend to be enriched in the larger (heavier) plutonium isotope and more oxidized species will be enriched in the smaller (lighter) isotope. It does not appear that the electron density (and therefore the field shift) scale linearly with the change in oxidation state, however. The magnitude of the field shift component of fractionation between Pu(VI) and Pu(V) is ~2‰, between Pu(V) and Pu(IV) it is 0.8‰, and between Pu(V) and Pu(III) it is ~4‰. As a consequence of the smaller field shift component of fractionation between Pu(V) and Pu(IV) species, overall fractionations between species in these intermediate oxidation states are expected to be minimal, as the mass dependent component of fractionation partially offsets the smaller field shift between these two species. Large fractionations are mainly expected when either Pu(VI) or Pu(III) species are present along with any other oxidation states, because in these cases the field shift components of fractionation are much larger than the mass dependent component of fractionation.

Because the field shift component of fractionation varies according to 1/T rather than $1/T^2$, it is likely to be of more relative importance with increasing temperature. The different temperature sensitivity, combined with the opposition of mass dependent and field shift components, means that overall fractionation will decline more slowly with increasing temperature than would be expected for mass dependent equilibrium fractionation alone. This can result in significant equilibrium isotopic differences persisting even at high temperatures

(Figure 3-7). For instance, the studied Pu(III) species are each predicted to be 2-2.5‰ higher in $^{242}Pu/^{239}Pu$ than Pu(V)-bearing $PuO_2CO_3(H_2O)_2^-$ at 500 K while Pu(VI) species are predicted to remain approximately 1‰ lower than Pu(V)-bearing $PuO_2CO_3(H_2O)_2^-$. In contrast to the gradual decline in the fractionation at increasing temperature that is observed for other oxidation states, Pu(IV) vs. Pu(V) fractionation factors remain relatively unchanged up to 500 K, with Pu(IV) species ranging from 0.1-0.5‰ higher than $PuO_2CO_3(H_2O)_2^-$.

Given the limited number of species studied, it is not entirely clear which chemical systematics control non-redox fractionations between different species. It is noteworthy that $PuO_2(CO_3)_3^{4-}$ [Pu(VI)], $PuO_2(CO_3)_3^{5-}$ [Pu(V)], and $PuO_2(H_2O)_5^+$ [Pu(V)] are predicted to have higher $^{242}Pu/^{239}Pu$ than other species sharing the same oxidation states, by ~1-2‰ at 298 K. Additional study is warranted to examine these species in particular.

3.4.3. Systematics of equilibrium neptunium isotopic fractionation

Species in the Np(VI) oxidation state are predicted to have 0.4-0.7‰ lower $^{237}Np/^{235}Np$ than the reference Np(V) standard species $NpO_2CO_3(H_2O)_2^-$. Np(IV) species are predicted to have only 0.1‰ higher $^{237}Np/^{235}Np$ than $NpO_2CO_3(H_2O)_2^-$. Np(III) species are predicted to have 0.7-1.2‰ higher $^{237}Np/^{235}Np$ than $NpO_2CO_3(H_2O)_2^-$ owing to a large field shift fractionation. This is of course dependent on the caveat that the charge radii of the neptunium isotopes are not known, and are being roughly estimated for this study. The DFT-PAW electron density and mass dependent component of fractionation are not impacted by this uncertainty in the model, however, and therefore we can still qualitatively compare the observed patterns between different isotopic systems. Pairs containing either Np(III) or Np(VI) species display the largest isotopic fractionations owing primarily to the nuclear field shift. This observation is consistent with what is seen in the Pu system. There is also minimal isotopic fractionation predicted between Np(V) and Np(IV) species, owing to the lower electron density difference between Np(V) and Np(IV) species than between pairs of Np(VI)-Np(V) or Np(IV)-Np(III) species, as well as the mass dependent component of fractionation partially offsetting the field shift. The observation that the successive removal/addition of electrons changes the electron density nonlinearly is also consistent with what we see in the plutonium and uranium systems (Sato et al., 2021).

Non-redox speciation effects can be seen within the results as well. Among the Np(V) species modeled, $NpO_2(H_2O)_5^+$ has 0.36‰ higher $^{237}Np/^{235}Np$ than $NpO_2CO_3(H_2O)_2^-$ and in fact overlaps with Np(IV) species, while the Np(V) species $NpO_2C_2H_2O_3(H_2O)_4$ has 0.21‰ lower $^{237}Np/^{235}Np$ than $NpO_2CO_3(H_2O)_2^-$. The Np(III) species $Np(OH)_3(H_2O)_4$ has 0.5-0.6‰ lower $^{237}Np/^{235}Np$ than the other Np(III) species modeled as well. As in the case of plutonium, it is unclear what controls these non-redox fractionations, or whether similar effects are likely to be observable in environmental samples. Significant isotopic fractionations persist to 500 K for redox pairs involving either the Np(III) or Np(VI) oxidation states (Figure 3-8). Np(III) species are predicted to have 0.4 - 0.8‰ higher $^{237}Np/^{235}Np$ than $NpO_2CO_3(H_2O)_2^-$, while Np(VI) species are predicted to have 0.3 - 0.4‰ lower $^{237}Np/^{235}Np$. Np(IV) species are predicted to have 0.03 - 0.1‰ higher $^{237}Np/^{235}Np$ than $NpO_2CO_3(H_2O)_2^-$ at 500 K.

3.4.4. Potential applications

As previously discussed, plutonium waste is primarily stored in the solid state as Pu(IV)-bearing species. The Pu(V) and Pu(VI) states are highly mobile in solution, while species with the less studied Pu(III) state are believed likely more soluble than Pu(IV) species. The largest possible isotope fractionations within the plutonium isotope system are likely to be observed under conditions in which Pu(VI) or Pu(III) are present. These species are most common under either oxidizing, alkaline conditions [Pu(VI)], or reducing, acidic conditions [Pu(III)], and therefore we expect stored plutonium waste that is mobilized in these environments to have the largest potential for isotopic fractionation. If the nuclear fallout signature over an area is well-characterized, it may also be possible to observe isotopic fractionation in naturally alkaline, oxidizing environments such as Mono Lake, or in other arid-climate surface and ground waters, provided they reach conditions such that Pu(VI) is the predominant form of Pu. Alternatively, large fractionations are possible in areas of acidic mine waste if conditions are such that Pu(III) species are present. Isotopic fractionation between the most common oxidation states, Pu(V) and Pu(IV), is likely to be subtle, which may make detection of mobilized Pu in many environments more challenging. It is hoped that the present results can guide the design of experiments to determine conditions in which significant fractionations might develop, and to characterize the species expected to be present in the mobilization of plutonium waste. The present results suggest that it is possible for experiments examining plutonium isotope fractionation to be carried out to relatively high temperatures and still produce large isotopic fractionations, owing to the field shift effect.

Although we selected the isotope ratios we believe to be most practical to measure, other isotope ratios are also expected to display significant isotope fractionations. Table 3-7 is intended to facilitate conversions to fractionations for other ratios. For example, the ratio ^{241}Pu/^{238}Pu will display fractionations similar to ^{242}Pu/^{239}Pu in both magnitude and direction. The largest fractionations would be seen with ratios including ^{244}Pu, so if this relatively understudied isotope becomes viable to measure to a high degree of accuracy, it would be the strongest candidate for measuring isotopic fractionation in the Pu system when measured against ^{240}Pu, ^{239}Pu, or ^{238}Pu. Detection of ^{244}Pu in the environment is of interest due to its high cost and the depletion in the stock of ^{244}Pu standard for laboratory analysis (Armstrong et al., 2016), but measurements remain relatively rare.

In the case of neptunium, there are likely to be fewer settings in which large isotopic fractionations are expected. Isotopic fractionation between the two most likely oxidation states Np(V) and Np(IV) is predicted to be on the order of 0.1‰ at surface relevant temperatures. Similar to Pu, the largest isotopic fractionations are expected for the trivalent and hexavalent oxidation states, but both Np(VI) and Np(III) are apparently not as common as the charge equivalent states in Pu in natural environments.

The choice of isotope ratio for neptunium was based in part on the observation that ^{237}Np is the primary isotope that is measured in environmental studies, and that the isotope ^{235}Np is one of the few longer-lived isotopes for Np. However, if the shorter-lived ^{239}Np isotope is measured, then the ratio ^{239}Np/^{235}Np will display more pronounced isotope fractionations, and this ratio can be obtained via the scale factors in Table 3-8.

3.5. Conclusion

The field shift fractionation first observed in the uranium system is modeled for both neptunium- and plutonium-bearing species using first principles methods. Fractionations of up to several per mil in redox reactions are predicted. The ^{242}Pu/^{239}Pu isotope system displays large fractionations, especially in redox reactions when either the Pu(VI) or Pu(III) oxidation state is present. We therefore expect environments in which these phases are stable to display the largest isotopic fractionations. Fractionations between the two most common oxidation states Pu(V) and Pu(IV) are significantly smaller, but may still be useful if measurable. Neptunium isotope fractionations for the ^{237}Np/^{235}Np system are generally more muted because of the apparent predominance of N(V) and Np(IV) in natural environments, but display similar behaviors to the

Pu system, where the presence of the hexavalent or trivalent oxidation state in redox equilibria between aqueous species produces the largest isotopic fractionations. Exchanges between N(V) and Np(IV) species are predicted to have small fractionations on the order of 0.1‰ at ambient surface temperatures.

Tables

Table 3-1: Ratios of Pu isotopes from different sources, taken from Geckeis et al. (2016) and references therein.

	$^{240}Pu/^{239}Pu$	$^{241}Pu/^{239}Pu$	$^{242}Pu/^{239}Pu$
Undetonated plutonium weapons	0.01 - 0.07	-	-
Low-yield detonations, U-based	0.00015-0.053	$(0.2 - 2.3) \times 10^{-4}$	-
Low-yield detonations, Pu-based	0.01 - 0.08	$(0.2 - 6.7) \times 10^{-4}$	-
Low-yield detonations, Ground Zero Semipalatinsk	0.0438 ± 0.0001	$(2.21 \pm 0.035) \times 10^{-4}$	$(7.89 \pm 0.26) \times 10^{-5}$
Global fallout, Northern Hemisphere	0.182 ± 0.005	$(1.12 \pm 0.85) \times 10^{-3}$	$(3.71 \pm 0.3) \times 10^{-3}$
Bikini Atoll, Ivy Mike	0.363 ± 0.004	$(2.27 \pm 0.29) \times 10^{-3}$	0.019 ± 0.003
Reactor debris, Chernobyl	0.13 - 0.53	0.12 - 0.13	0.034 – 0.048
Gas-cooled reactor, fuel burnup 3.6 GWd/t	0.23	0.045	0.006
Pressurized heavy water reactor, fuel burnup 7.5 GWd/t	0.41	0.077	0.023
Advanced gas-cooled reactor, fuel burnup 18GWd/t	0.57	0.184	0.093
RMBK reactor, fuel burnup 27.5 GWd/t	0.67	0.203	0.108
Pressurized water reactor, fuel burnup 33GWd/t	0.43	0.229	0.096

Table 3-2: Electrochemical potentials (V) for redox couples relating the Pu ions in acidic (1 M $HClO_4$), neutral/slightly alkaline (pH 8), and basic (1 M NaOH) aqueous solutions versus the standard hydrogen electrode. Taken from Hixon and Powell (2018), which was adapted from Clark et al. (2006).

Redox reaction	Acidic	Neutral	Basic
$Pu(III) \leftrightarrow Pu(IV) + e^-$	+0.982	−0.39	−0.96
$Pu(IV) + 2H_2O \leftrightarrow Pu(V) + 4H^+ + e^-$	+1.170	+0.70	−0.67
$Pu(V) \leftrightarrow Pu(VI) + e^-$	+0.913	+0.60	+0.12
$Pu(IV) + 2H_2O \leftrightarrow Pu(V) + 4H^+ + 2e^-$	+1.043	+0.65	+0.34
$Pu(III) + 2H_2O \leftrightarrow Pu(V) + 4H^+ + 2e^-$	-	+1.076	-

Table 3-3: Mössbauer isomer shifts and DFT-PAW electron densities for Np solids, relative to the Mössbauer standard species $NpAl_2$.

	^{237}Np isomer shift vs. $NpAl_2$ (mm/sec)	DFT-PAW electron density of literature structure (e^-/a_0^3)	DFT-PAW electron density of literature structure with atomic positions optimized (e^-/a_0^3)	DFT-PAW electron density of fully relaxed structure (e^-/a_0^3)	Structure reference	Mössbauer isomer reference
$Na_3NpO_4(OH)_2$	-66.1	3001	2996	2993	Grigoreiv et al. (2007)	Ilyatov et al. (1975)
NpF_6	-63	2969	2960	-	Weinstock and Goodman (1965)	Ionova et al. (1998)
Li_4NpO_5	-58.9	2957	2955	2954	Morss et al. (1994)	Ionova et al. (1998)
NpO_2CO_3	-35.5	2905	2904	-	Thevenin et al. (1986)	Ionova et al. (1998)
NpO_2F_2	-32	2870	-	-	Zachariasen (1949)	Ionova et al. (1998)
NpF_5	-37	2893	2891	-	Malm et al. (1993)	Ionova et al. (1998)
NpO_2	-6.1	2817	2817	2818	Wang et al. (2010)	Gal et al. (1973)
NpF_3	39.65	2717	-	-	Zalkin and Templeton (1985)	Jove et al. (1988)
$NpSi_2$	7.9	2808	2808	-	Zachariasen (1949)	Yaar et al. (1991)
$NpAl_2$	0	2846	2846	-	Borin et al. (1985)	0 by definition (reference material)

Table 3-4: Half-lives of the common Pu and Np isotopes (Kondev et al., 2021).

Isotope	$t_{1/2}$
^{244}Pu	8.13×10^{7} yrs
^{242}Pu	3.75×10^{5} yrs
^{241}Pu	14.33 yrs
^{240}Pu	6.56×10^{3} yrs
^{239}Pu	2.41×10^{4} yrs
^{238}Pu	87.7 yrs
^{239}Np	2.36 days
^{238}Np	87.7 yrs
^{237}Np	2.14×10^{6} yrs
^{236}Np	1.53×10^{3} yrs
^{235}Np	396.1 days

Table 3-5: Initial guess structure methods for modeled plutonium-bearing species modeled. All U-bearing analog structures are adapted from Chapter 2.

Species	Structure source	Method
PuF_3	Adapted from NpF_3 structure from Beridze et al. (2016) with substitution of Np	PBE-def-TZVP/def2-TZVPP
PuF_4	Adapted from NpF_4 structure from Beridze et al. (2016) with substitution of Np	PBE-def-TZVP/def2-TZVPP
PuF_5	Adapted from NpF_5 structure from Marsh and Albrecht-Schmitt (2018) with replacement by Pu	PBE-def-TZVP/def2-TZVPP
PuF_6	Adapted from Schimmelpfennig et al. (2003)	PBE-def-TZVP/def2-TZVPP
$PuCl_3$	Adapted from Surbella et al. (2022)	PBE-def-TZVP/def2-TZVPP
$PuCl_4$	Adapted from Kumar and Seminario (2015)	PBE-def-TZVP/def2-TZVPP
$PuCl_6$	Adapted from Govid and de Jong (2013) with change of oxidation state	PBE-def-TZVP/def2-TZVPP
$Pu(OH)_3$	Constructed *ad hoc*	PBE-def-TZVP/def2-TZVPP
$Pu(OH)_4$	Constructed *ad hoc*	PBE-def-TZVP/def2-TZVPP
$Pu(OH)_5$	Constructed *ad hoc*	PBE-def-TZVP/def2-TZVPP
$Pu(OH)_6$	Constructed *ad hoc*	PBE-def-TZVP/def2-TZVPP
$PuO_2(CO_3)_3^{4-}$	U-bearing analog	PBE-def-TZVP/def2-TZVPP
$PuO_2(CO_3)_2H_2O^{2-}$	U-bearing analog	PBE-def-TZVP/def2-TZVPP
$PuO_2CO_3(H_2O)_3$	U-bearing analog	PBE-def-TZVP/def2-TZVPP
$PuO_2(H_2O)_5^{2+}$	U-bearing analog	PBE-def-TZVP/def2-TZVPP
$PuO_2C_2H_2O_3(H_2O)_4$	U-bearing analog	PBE-def-TZVP/def2-TZVPP
$PuO_2(CO_3)_3^{5-}$	U-bearing analog	PBE-def-TZVP/def2-TZVPP
$PuO_2(CO_3)_2H_2O^{3-}$	U-bearing analog	PBE-def-TZVP/def2-TZVPP
$PuO_2CO_3(H_2O)_3^-$	U-bearing analog	PBE-def-TZVP/def2-TZVPP
$PuO_2(H_2O)_5^+$	U-bearing analog	PBE-def-TZVP/def2-TZVPP
$PuO_2C_2H_2O_3(H_2O)_4^-$	U-bearing analog	PBE-def-TZVP/def2-TZVPP
$PuO_{2(s)}$	Wyckoff (1963)	PBE-PAW
$Pu(OH)_4(H_2O)_2$	Adapted from $Pu(H_2O)_8^{4+}$ structure from Ryzhkov et al. (2021) via removal of H atoms and noncoordinating water molecules	PBE-def-TZVP/def2-TZVPP
$Pu(IV)C_2H_2O_3(H_2O)_6^{2+}$	U-bearing analog	PBE-def-TZVP/def2-TZVPP
$Pu(OH)_3(H_2O)_3^+$	Adapted from $Pu(H_2O)_8^{4+}$ structure from Ryzhkov et al. (2021) via removal of H atoms and noncoordinating water molecules	PBE-def-TZVP/def2-TZVPP
$Pu(CO_3)_4^{4-}$	Adapted from Bruno et al. (1989)	PBE-def-TZVP/def2-TZVPP
$Pu(III)C_2H_2O_3(H_2O)_5^+$	U-bearing analog	PBE-def-TZVP/def2-TZVPP
$Pu(OH)_3(H_2O)_3$	Adapted from $Pu(H_2O)_8^{4+}$ structure from Ryzhkov et al. (2021) via removal of H atoms and noncoordinating water molecules	PBE-def-TZVP/def2-TZVPP
$PuCO_3(H_2O)_5^+$	Adapted from $Pu(H_2O)_8^{4+}$ structure from Ryzhkov et al. (2021) via addition of CO_3^{2-} anion and removal of water molecules	PBE-def-TZVP/def2-TZVPP
PuO_4^-	Huang et al. (2013)	PBE-def-TZVP/def2-TZVPP
PuO_4	Gibson et al. (2019)	PBE-def-TZVP/def2-TZVPP

Table 3-6: Initial guess structure methods for modeled neptunium-bearing species modeled. All U-bearing analog structures are adapted from Chapter 2.

Species	Structure source	Method of optimization
NpF_3	Adapted from Beridze et al. (2016)	PBE-def-TZVP/def2-TZVPP
NpF_4	Adapted from Beridze et al. (2016)	PBE-def-TZVP/def2-TZVPP
NpF_5	Adapted from Marsh and Albrecht-Schmitt (2018)	PBE-def-TZVP/def2-TZVPP
NpF_6	Adapted from Schimmelpfennig et al. (2003)	PBE-def-TZVP/def2-TZVPP
$NpCl_3$	Adapted from Pu equivalent via replacement of Np	PBE-def-TZVP/def2-TZVPP
$NpCl_4$	Adapted from Pu equivalent via replacement of Np	PBE-def-TZVP/def2-TZVPP
$NpCl_5$	Adapted from Su et al. (2013) with substitution of U	PBE-def-TZVP/def2-TZVPP
$NpCl_6$	Adapted from Govid and de Jong (2013) with change of oxidation state	PBE-def-TZVP/def2-TZVPP
$Np(OH)_3$	Constructed *ad hoc*	PBE-def-TZVP/def2-TZVPP
$Np(OH)_4$	Constructed *ad hoc*	PBE-def-TZVP/def2-TZVPP
$Np(OH)_5$	Constructed *ad hoc*	PBE-def-TZVP/def2-TZVPP
$Np(OH)_6$	Constructed *ad hoc*	PBE-def-TZVP/def2-TZVPP
$NpO_2(CO_3)_3^{4-}$	U-bearing analog	PBE-def-TZVP/def2-TZVPP
$NpO_2(CO_3)_2H_2O^{2-}$	U-bearing analog	PBE-def-TZVP/def2-TZVPP
$NpO_2CO_3(H_2O)_3$	U-bearing analog	PBE-def-TZVP/def2-TZVPP
$NpO_2(H_2O)_5^{2+}$	U-bearing analog	PBE-def-TZVP/def2-TZVPP
$Np^{VI}O_2C_2H_2O_3(H_2O)_4$	U-bearing analog	PBE-def-TZVP/def2-TZVPP
$NpO_2(CO_3)_3^{5-}$	U-bearing analog	PBE-def-TZVP/def2-TZVPP
$NpO_2(CO_3)_2H_2O^{3-}$	U-bearing analog	PBE-def-TZVP/def2-TZVPP
$NpO_2CO_3(H_2O)_3^-$	U-bearing analog	PBE-def-TZVP/def2-TZVPP
$NpO_2(H_2O)_5^+$	U-bearing analog	PBE-def-TZVP/def2-TZVPP
$Np^VO_2C_2H_2O_3(H_2O)_4$	U-bearing analog	PBE-def-TZVP/def2-TZVPP
$NpO_{2\ (s)}$	Wyckoff (1963)	PBE-PAW
$Np(OH)_4(H_2O)_2$	Adapted from $Pu(H_2O)_8^{4+}$ structure from Ryzhkov et al. (2021) via replacement by Np and removal of H atoms and noncoordinating water molecules	PBE-def-TZVP/def2-TZVPP
$Np(OH)_3(H_2O)_4^+$	Adapted from $Pu(H_2O)_8^{4+}$ structure from Ryzhkov et al. (2021) via replacement by Np and removal of H atoms and noncoordinating water molecules	PBE-def-TZVP/def2-TZVPP
Np^{IV}-$C_2H_2O_3(H_2O)_7$	U-bearing analog	PBE-def-TZVP/def2-TZVPP
$Np(OH)_3(H_2O)_4$	Adapted from $Pu(H_2O)_8^{4+}$ structure from Ryzhkov et al. (2021) via replacement by Np and removal of H atoms and noncoordinating water molecules	PBE-def-TZVP/def2-TZVPP
$Np(OH)_2(H_2O)_7^+$	Adapted from $Pu(H_2O)_8^{4+}$ structure from Ryzhkov et al. (2021) via replacement by Np and removal of H atoms and noncoordinating water molecules	PBE-def-TZVP/def2-TZVPP
$NpCO_3(H_2O)_5^+$	Adapted from $Pu(H_2O)_8^{4+}$ structure from Ryzhkov et al. (2021) via replacement by Np and addition of CO_3^{2-} anion and removal of water molecules	PBE-def-TZVP/def2-TZVPP
$NpO_2(OH)_4^-$	Constructed *ad hoc*	PBE-def-TZVP/def2-TZVPP

Table 3-7: Fractionation scale factors for different plutonium isotope ratios, relative to ^{242}Pu/^{239}Pu. Mass dependent scale factors are determined using equilibrium mass law expression of Young et al. (2002). Field shift scale factors are proportional to the isotopic difference in mean squared nuclear charge radii (Fricke and Heilig, 2004).

	Mass dependent component of fractionation scale factor	Field shift component of fractionation scale factor
^{244}Pu /^{238}Pu	1.99	1.95
^{244}Pu /^{239}Pu	1.65	1.58
^{244}Pu /^{240}Pu	1.32	1.11
^{244}Pu/^{241}Pu	0.98	0.95
^{244}Pu/^{242}Pu	0.65	0.58
^{242}Pu/^{238}Pu	1.34	1.37
^{242}Pu/^{240}Pu	0.66	0.53
^{242}Pu/^{241}Pu	0.33	0.37
^{241}Pu/^{238}Pu	1.01	1.00
^{241}Pu/^{239}Pu	0.67	0.63
^{241}Pu/^{240}Pu	0.33	0.16
^{240}Pu/^{238}Pu	0.68	0.84
^{240}Pu/^{239}Pu	0.34	0.47
^{239}Pu/^{238}Pu	0.34	0.37

Table 3-8: Fractionation scale factors for different neptunium isotopes ratios, relative to ^{237}Np/^{235}Np. Mass dependent scale factors are determined using equilibrium mass law expression of Young et al. (2002). Field shift scale factors are proportional to the isotopic difference in mean squared nuclear charge radii, which have been estimated.

	Mass dependent component of fractionation scale factor	Field shift component of fractionation scale factor
^{239}Np/^{235}Np	1.98	2.00
^{239}Np/^{236}Np	1.48	1.51
^{239}Np/^{237}Np	0.98	1.00
^{239}Np/^{238}Np	0.49	0.50
^{238}Np/^{235}Np	1.54	1.50
^{238}Np/^{236}Np	1.02	1.01
^{238}Np/^{237}Np	0.51	0.50
^{237}Np/^{236}Np	0.50	0.50
^{236}Np/^{235}Np	0.50	0.50

Table 3-9: Equilibrium ^{242}Pu/^{239}Pu fractionations at 298 K and 500 K, along with the DFT-PAW electron density used to calculate the field shift component of fractionation. Mass dependent components of fractionation (ln α_{md}), field shift component and total fractionation are reported relative to the species $PuO_2CO_3(H_2O)_2^-$. Total fractionations are obtained by adding the field shift and the difference in the mass dependent component of fractionation. For the species $PuO_2CO_3(H_2O)_2^-$, ln β = 1.29‰ at 298 K and ln β = 0.52‰, and DFT=PAW electron density = 28356 e^-/a_0^3.

	ln α_{md} (‰) for ^{242}Pu/^{239}Pu relative to $PuO_2CO_3(H_2O)_2^-$ at 298 K and 500 K		Field shift component of fractionation (‰) at 298 K relative to $PuO_2CO_3(H_2O)_2^-$ at 298 K and 500 K		Total fractionation (‰) relative to $PuO_2CO_3(H_2O)_2^-$ at 298 K and 500 K		DFT-PAW electron density (e^-/a_0^3)
$PuO_2(CO_3)_3^{4-}$	0.02	0.01	-0.40	-0.25	-0.37	-0.24	28456
$PuO_2(CO_3)_2H_2O^{2-}$	0.25	0.10	-2.25	-1.35	-1.99	-1.25	28919
$PuO_2CO_3(H_2O)_3$	0.23	0.09	-2.10	-1.26	-1.88	-1.25	28880
$PuO_2(H_2O)_5^{2+}$	0.34	0.15	-2.18	-1.31	-1.83	-1.16	28902
$Pu^{VI}O_2C_2H_2O_3(H_2O)_4$	0.28	0.11	-1.18	-0.71	-0.89	-0.60	28650
$PuO_2(CO_3)_3^{5-}$	-0.17	-0.07	-1.80	-1.08	-1.95	-1.15	28805
$PuO_2(CO_3)_2H_2O^{3-}$	-0.07	-0.03	-0.03	0.01	-0.09	-0.02	28363
$PuO_2CO_3(H_2O)_3^-$	1.29	0.52	-	-	-	-	28356
$PuO_2(H_2O)_5^+$	0.04	0.02	0.74	0.43	0.79	0.45	28171
$Pu^VO_2C_2H_2O_3(H_2O)_4^-$	0.00	0.01	0.07	0.04	0.09	0.04	28337
$PuO_{2(s)}$	-0.62	-0.26	0.65	0.38	0.02	0.12	28205
$Pu(OH)_4(H_2O)_2$	-0.27	-0.11	0.40	0.23	0.14	0.12	28256
$Pu^{IV}C_2H_2O_3(H_2O)_6^{2+}$	-0.43	-0.18	0.84	0.49	0.43	0.31	28145
$Pu(OH)_3(H_2O)_3^+$	-0.28	-0.11	0.37	0.21	0.10	0.10	28263
$Pu(CO_3)_4^{4-}$	-0.55	-0.26	1.30	0.77	0.77	0.51	28030
$Pu^{III}C_2H_2O_3(H_2O)_5^+$	-0.70	-0.28	4.22	2.51	3.53	2.23	27300
$Pu(OH)_3(H_2O)_3$	-0.67	-0.27	3.93	2.34	3.28	2.07	27371
$PuCO_3(H_2O)_5^+$	-0.73	-0.26	4.17	2.48	3.45	2.22	27312
PuO_4^-	0.54	0.22	-2.53	-1.52	-1.97	-1.30	28989
PuO_4	0.72	0.33	-3.95	-2.36	-3.22	-2.06	29344

Table 3-10: Equilibrium $^{237}Np/^{235}Np$ fractionations at 298 K, along with the DFT-PAW electron density used to calculate the field shift component of fractionation. Mass dependent components of fractionation (ln α_{md}), field shift component and total fractionation are relative to the species $NpO_2CO_3(H_2O)_2^-$. Total fractionations are obtained by adding the field shift and the difference in the mass dependent component of fractionation. For the species $NpO_2CO_3(H_2O)_2^-$, ln β = 0.84‰ at 298 K and ln β = 0.33‰ at 500 K, and DFT=PAW electron density = 2847 e^-/a_0^3.

	ln α_{md} (‰) for $^{237}Np/^{235}Np$ relative to $NpO_2CO_3(H_2O)_2^-$ at 298 K and 500 K		Field shift component of fractionation (‰) for $^{237}Np/^{235}Np$ relative to $NpO_2CO_3(H_2O)_2^-$ at 298 K and 500 K		Total fractionation for $^{237}Np/^{235}Np$ (‰) relative to $NpO_2CO_3(H_2O)_2^-$ at 298 K and 500 K		DFT-PAW electron density (e^-/a_0^3)
$NpO_2(CO_3)_3^{4-}$	0.10	0.04	-0.79	-0.47	-0.69	-0.43	2908
$NpO_2(CO_3)_2H_2O^{2-}$	0.19	0.08	-0.68	-0.41	-0.48	-0.33	2899
$NpO_2CO_3(H_2O)_3$	0.19	0.08	-0.78	-0.46	-0.59	-0.39	2907
$NpO_2(H_2O)_5^{2+}$	0.26	0.12	-0.68	-0.40	-0.41	-0.29	2899
$Np^{VI}O_2C_2H_2O_3(H_2O)_4$	0.26	0.11	-0.84	-0.50	-0.58	-0.39	2911
$NpO_2(CO_3)_3^{5-}$	-0.08	-0.03	0.21	0.12	0.12	0.09	2830
$NpO_2(CO_3)_2H_2O^{3-}$	-0.03	-0.02	0.00	0.00	-0.03	-0.01	2846
$NpO_2(H_2O)_5^{+}$	0.05	0.02	0.31	0.19	0.36	0.21	2822
$Np^{V}O_2C_2H_2O_3(H_2O)_4$	0.02	0.01	-0.23	-0.14	-0.21	-0.13	2864
$NpO_{2\ (s)}$	0.15	0.02	0.36	0.21	0.02	0.06	2819
$Np(OH)_4(H_2O)_2$	-0.08	-0.07	0.17	0.10	0.09	0.03	2833
$Np(OH)_3(H_2O)_4^{+}$	-0.17	-0.07	0.26	0.16	0.09	0.08	2826
Np^{IV}-$C_2H_2O_3(H_2O)_7$	-0.20	-0.08	0.33	0.20	0.13	0.12	2821
$Np(OH)_3(H_2O)_4$	-0.31	-0.16	0.97	0.58	0.66	0.42	2772
$Np(OH)_2(H_2O)_7^{+}$	-0.45	-0.18	1.70	1.01	1.25	0.83	2715
$NpCO_3(H_2O)_5^{+}$	-0.39	-0.16	1.54	0.92	1.14	0.76	2728
$NpO_2(OH)_4^-$	0.43	0.17	-1.86	-1.11	-1.81	-0.94	2990

Table 3-11: Polynomial fits of the fractionations relative to $PuO_2CO_3(H_2O)_2^-$ are shown below with the form $1000 \ln \alpha_{total} = A_1/T^2 + A_2/T^4 + C/T$, with the first two constants corresponding to the mass dependent component of fractionation and the last constant corresponding to the nuclear field shift. Fits are constrained at temperatures from 250 K to 4000 K.

	A_1	A_2	C
$PuO_2(CO_3)_3^{4-}$	$5.18\text{x}10^4$	$-3.16\text{x}10^9$	-123.41
$PuO_2(CO_3)_2H_2O^{2-}$	$7.40\text{x}10^4$	$-3.31\text{x}10^9$	-674.06
$PuO_2CO_3(H_2O)_3$	$7.43\text{x}10^4$	$-3.59\text{x}10^9$	-629.00
$PuO_2(H_2O)_5^{2+}$	$9.01\text{x}10^4$	$-3.94\text{x}10^9$	-654.41
$Pu^{VI}O_2C_2H_2O_3(H_2O)_4$	$7.82.10^4$	$-3.45\text{x}10^9$	-354.93
$PuO_2(CO_3)_3^{5-}$	$3.12\text{x}10^4$	$-2.85\text{x}10^9$	-539.64
$PuO_2(CO_3)_2H_2O^{3-}$	$3.92\text{x}10^4$	$-2.80\text{x}10^9$	3.68
$PuO_2(H_2O)_5^+$	$5.58\text{x}10^4$	$-3.31\text{x}10^9$	215.48
$Pu^VO_2C_2H_2O_3(H_2O)_4^-$	$5.13\text{x}10^4$	$-3.24\text{x}10^9$	17.71
$PuO_{2(s)}$	$2.20\text{x}10^4$	$-1.76\text{x}10^9$	192.43
$Pu(OH)_4(H_2O)_2$	$2.08\text{x}10^4$	$-2.68\text{x}10^9$	114.56
$Pu^{IV}C_2H_2O_3(H_2O)_6^{2+}$	$-6.48\text{x}10^2$	$-2.12\text{x}10^9$	246.71
$Pu(OH)_3(H_2O)_3^+$	$1.86\text{x}10^4$	$-2.59\text{x}10^9$	105.60
$Pu(CO_3)_4^{4-}$	$-1.99\text{x}10^4$	$-1.93\text{x}10^9$	383.76
$Pu^{III}C_2H_2O_3(H_2O)_5^+$	$-2.51\text{x}10^4$	$-2.06\text{x}10^9$	1253.33
$Pu(OH)_3(H_2O)_3$	$-6.84\text{x}10^4$	$8.43\text{x}10^8$	1168.71
$PuCO_3(H_2O)_5^+$	$-3.20\text{x}10^4$	$-1.78\text{x}10^9$	1238.74
PuO_4^-	$1.07\text{x}10^5$	$-3.86\text{x}10^9$	-758.05
PuO_4	$1.29\text{x}10^5$	$-4.43\text{x}10^9$	-1181.01

Table 3-12: Polynomial fits of the fractionations relative to $NpO_2CO_3(H_2O)_2^-$ are shown below with the form 1000 ln $\alpha_{total} = A_1/T^2 + A_1/T^4 + C/T$, with the first two constants corresponding to the mass dependent component of fractionation and the last constant corresponding to the nuclear field shift. Fits are constrained at temperatures from 250 K – 4000 K.

	A_1	A_2	C
$NpO_2(CO_3)_3^{4-}$	$1.00x10^4$	$-9.11x10^7$	-235.83
$NpO_2(CO_3)_2H_2O^{2-}$	$2.00x10^4$	$-2.00x10^8$	-202.99
$NpO_2CO_3(H_2O)_3$	$1.97x10^4$	$-2.25x10^8$	-232.25
$NpO_2(H_2O)_5^{2+}$	$3.18x10^4$	$-6.30x10^8$	-202.47
$Np^{VI}O_2C_2H_2O_3(H_2O)_4$	$2.77x10^4$	$-3.71x10^8$	-249.29
$NpO_2(CO_3)_3^{5-}$	$-9.13x10^3$	$1.26x10^8$	62.01
$NpO_2(CO_3)_2H_2O^{3-}$	$-4.55x10^3$	$1.54x10^8$	0.63
$NpO_2(H_2O)_5^+$	$6.70x10^3$	$-1.99x10^8$	93.25
$Np^VO_2C_2H_2O_3(H_2O)_4$	$2.13x10^3$	$-4.08x10^7$	-68.62
$NpO_{2\ (s)}$	$1.97x10^3$	$8.76x10^8$	106.94
$Np(OH)_4(H_2O)_2$	$-4.46x10^4$	$1.96x10^9$	51.23
$Np(OH)_3(H_2O)_4^+$	$-1.98x10^4$	$3.92x10^8$	77.53
Np^{IV}-$C_2H_2O_3(H_2O)_7$	$-2.08x10^4$	$2.49x10^8$	98.93
$Np(OH)_3(H_2O)_4$	$-4.14x10^4$	$6.47x10^8$	288.16
$Np(OH)_2(H_2O)_7^+$	$-4.68x10^4$	$5.27x10^8$	505.95
$NpCO_3(H_2O)_5^+$	$-4.19x10^4$	$5.42x10^8$	458.31
$NpO_2(OH)_4^-$	$4.44x10^4$	$-4.75x10^8$	-553.97

Figures

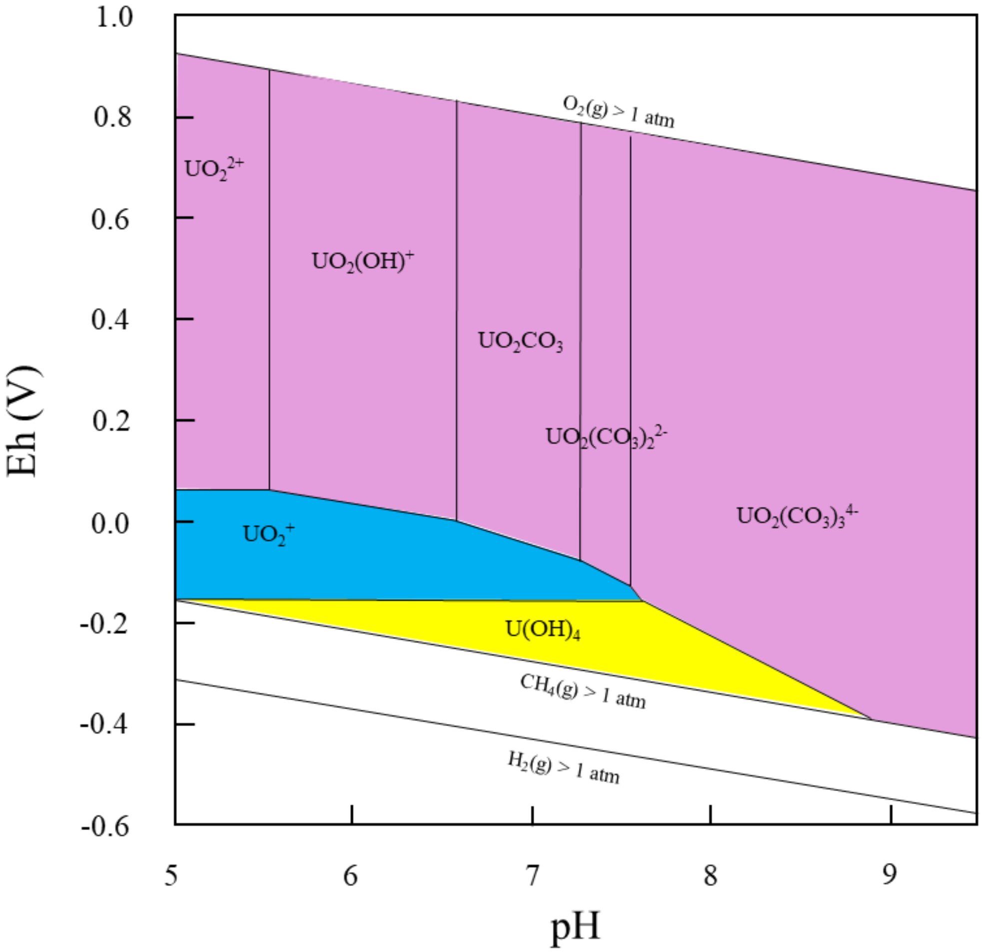

Figure 3-1: Pourbaix diagram for uranium adapted from Reiller (2024), at 298 K with [U] = 0.1 nmol kg_w^{-1}, I_m = 0.1 mol kg^{-1} NaCl, and $P(CO_2) = 10^{-3.5}$ atm. Purple indicates the +6 oxidation state, blue indicates the +5 oxidation state, and yellow indicates the +4 oxidation state.

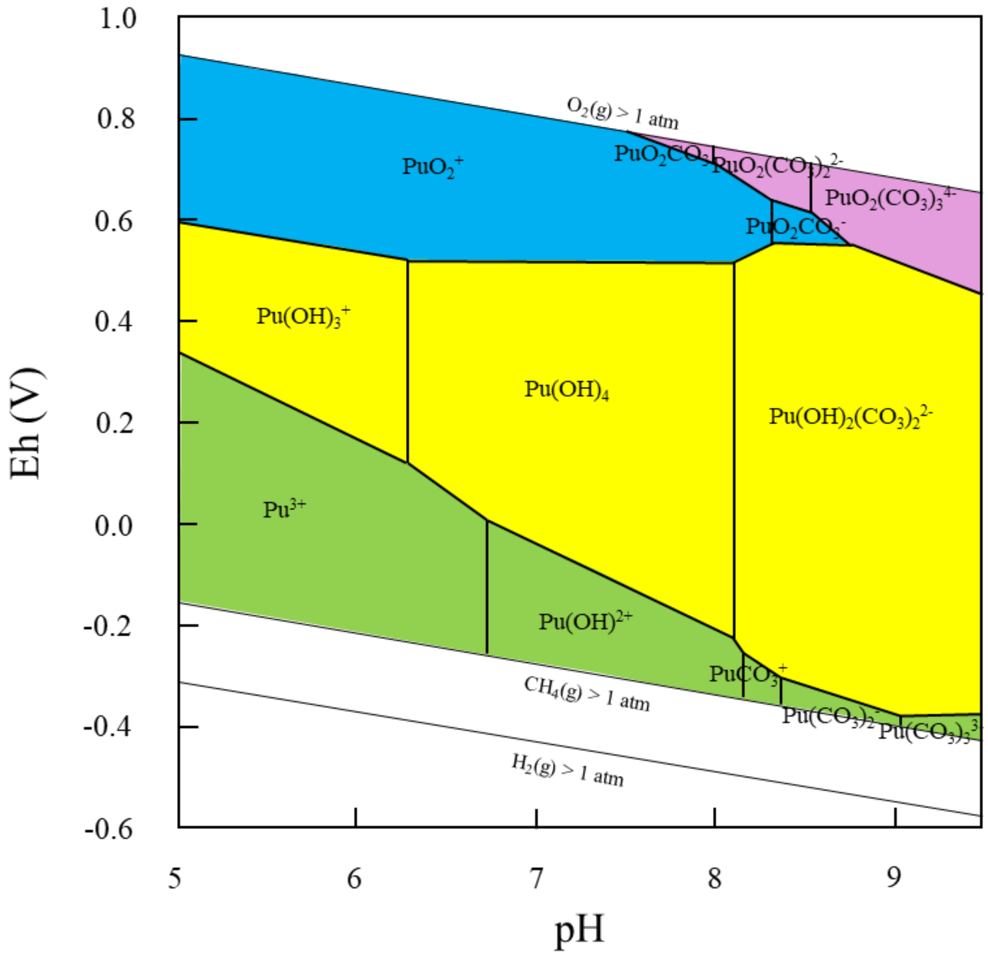

Figure 3-2: Pourbaix diagram for plutonium adapted from Reiller (2024), at 298 K with [Pu] = 0.1 nmol kg_w^{-1}, I_m = 0.1 mol kg^{-1} NaCl, and $P(CO_2) = 10^{-3.5}$ atm. Purple indicates the +6 oxidation state, blue indicates the +5 oxidation state, yellow indicates the +4 oxidation state, and green indicates the +3 oxidation state.

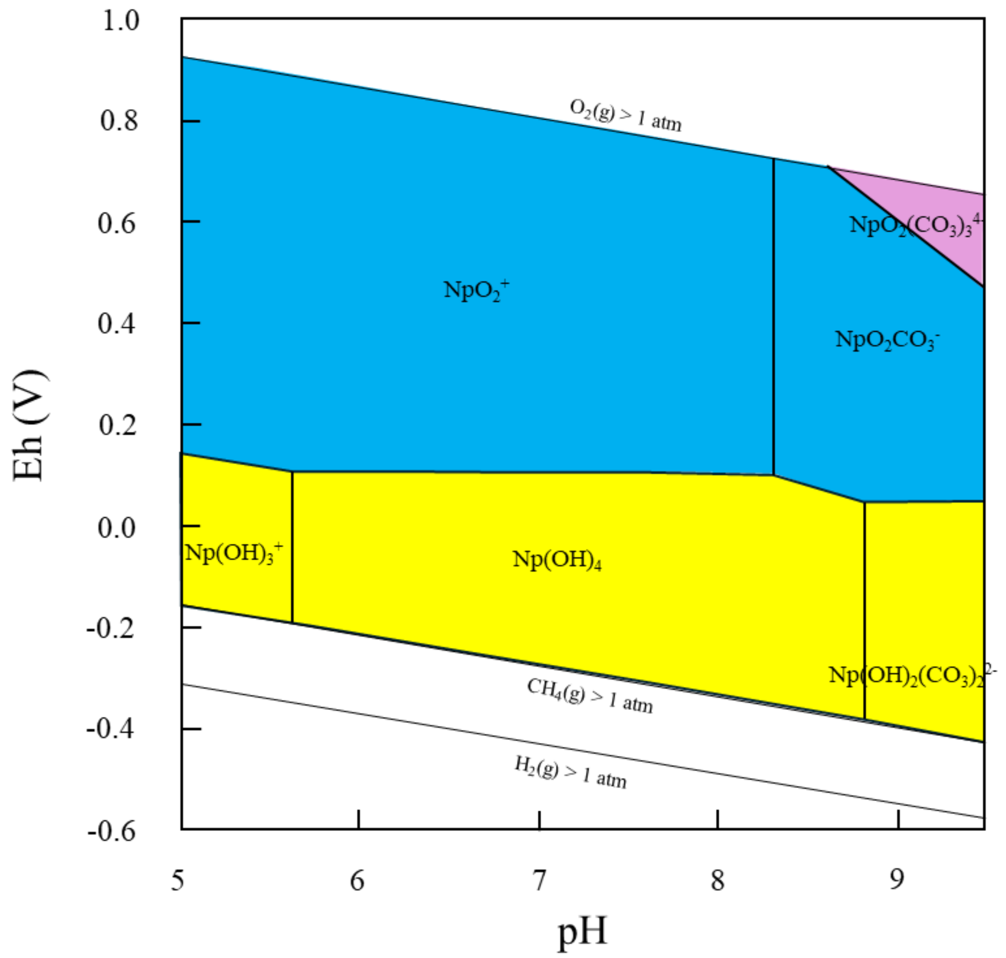

Figure 3-3: Pourbaix diagram for neptunium adapted from Reiller (2024), at 298 K with [Np] = 0.1 nmol kg_w^{-1}, I_m = 0.1 mol kg^{-1} NaCl, and $P(CO_2) = 10^{-3.5}$ atm. Purple indicates the +6 oxidation state, blue indicates the +5 oxidation state, and yellow indicates the +4 oxidation state.

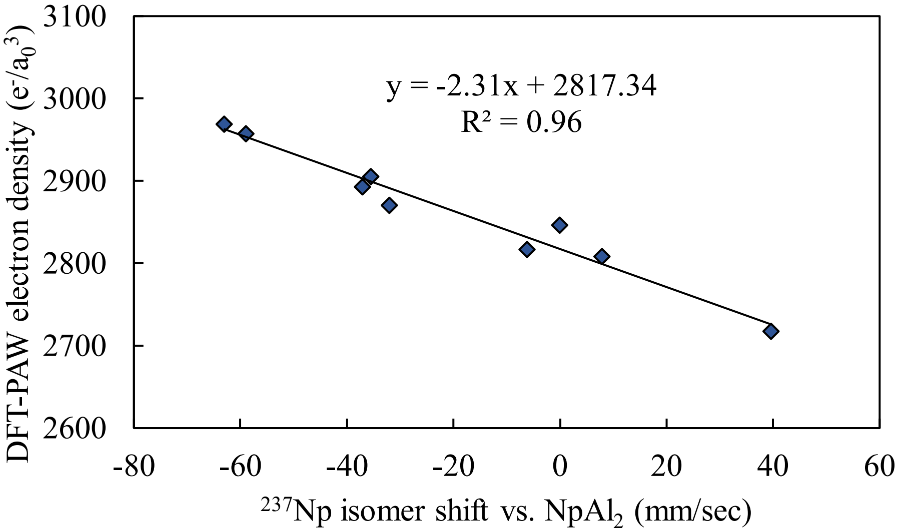

Figure 3-4: DFT-PAW electron density of vs. ^{237}Np Mössbauer isomer shifts. Electron densities are calculated on measured (unoptimized) crystal structures (Table 3-3).

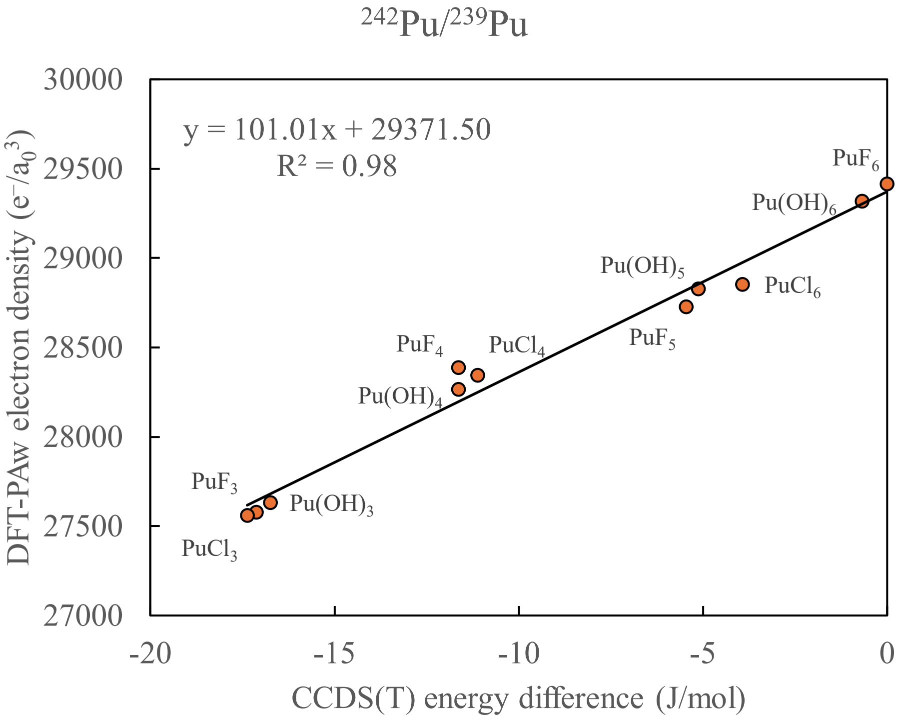

Figure 3-5: Calibration of DFT-PAW electron densities vs. all electron model field shifts for ^{242}Pu - ^{239}Pu substitution relative to PuF$_6$. The standard error of the slope regression is 4.79 e^-/a_0^3 per J/mol.

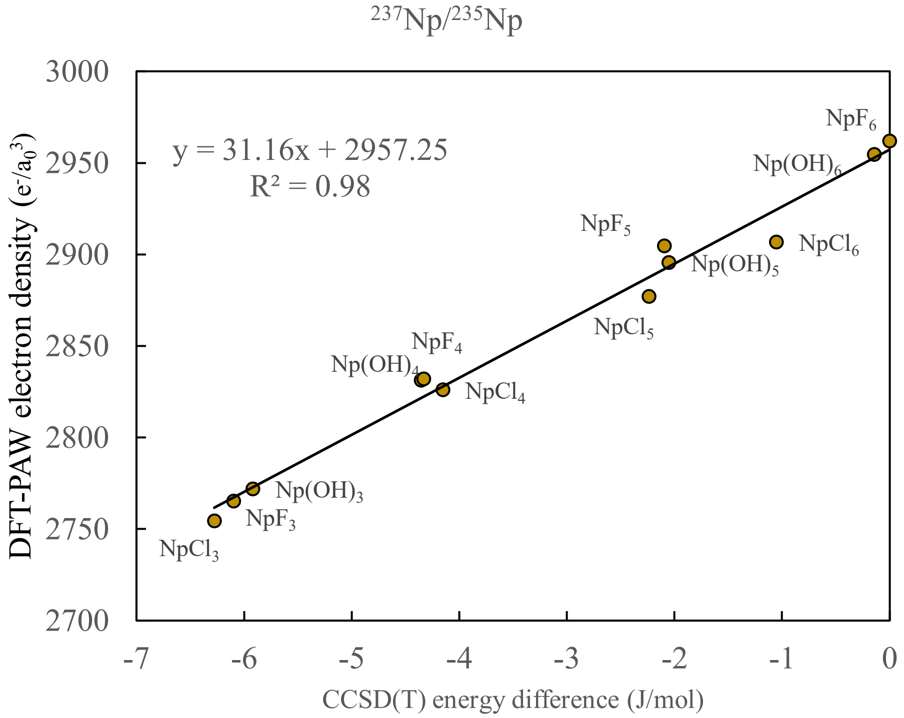

-

Figure 3-6: Calibration of DFT-PAW electron densities vs. all electron model field shifts for ^{237}Np – ^{239}Np substitution relative to NpF6. The standard error of the slope regression is 1.24 e^{-} /a$_0^3$ per J/mol.

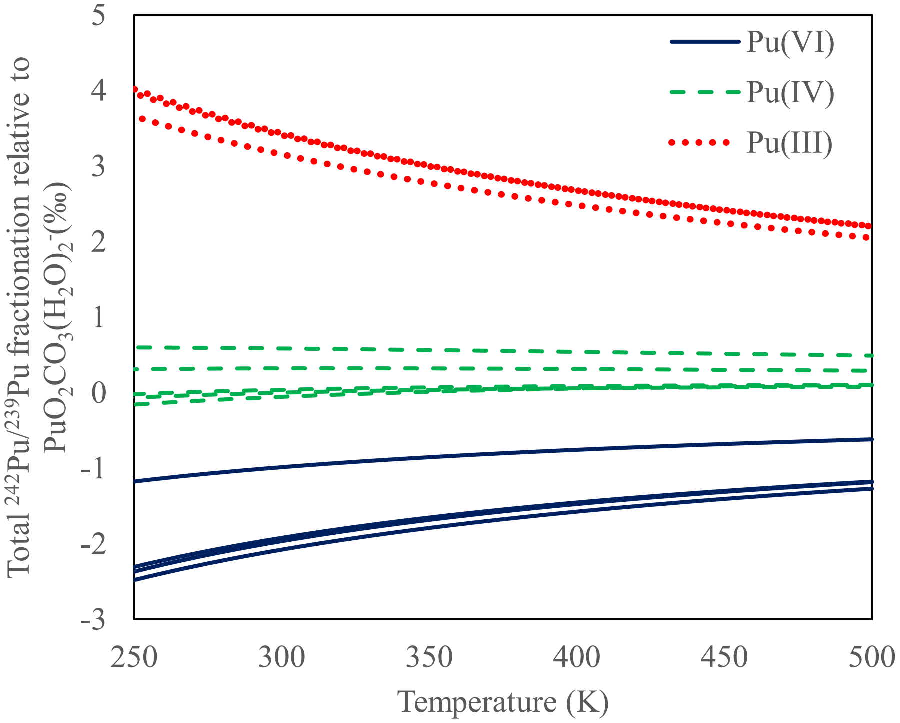

Figure 3-7: Total ^{242}Pu/^{239}Pu isotopic fractionation versus temperature for select species. All are reported relative to $PuO_2CO_3(H_2O)_2^-$.

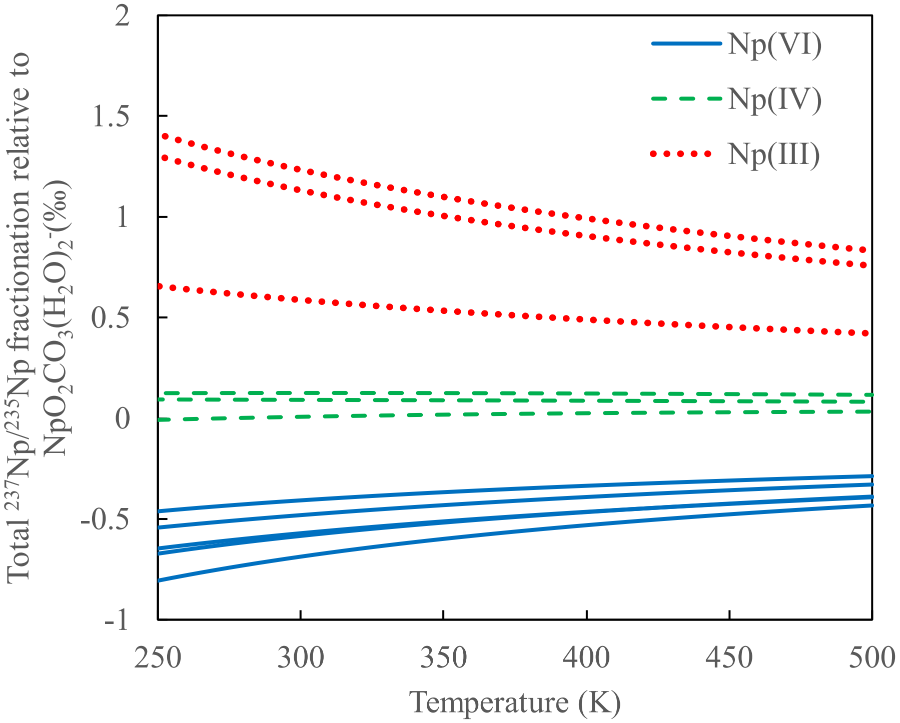

Figure 3-8: Total ^{237}Np/^{235}Np isotopic fractionation versus temperature for select species. All fractionations are reported relative to $NpO_2CO_3(H_2O)_2^-$.

References

Abe M, Suzuki T, Fujii Y, et al (2008a) An ab initio molecular orbital study of the nuclear volume effects in uranium isotope fractionations. The Journal of Chemical Physics 129:164309. https://doi.org/10.1063/1.2992616

Abe M, Suzuki T, Fujii Y, Hada M (2008b) An ab initio study based on a finite nucleus model for isotope fractionation in the U(III)–U(IV) exchange reaction system. The Journal of Chemical Physics 128:144309. https://doi.org/10.1063/1.2898541

Alewell C, Pitois A, Meusburger K, et al (2017) 239+240Pu from "contaminant" to soil erosion tracer: Where do we stand? Earth-Science Reviews 172:107–123. https://doi.org/10.1016/j.earscirev.2017.07.009

Anderson RF, Bacon MP, Brewer PG (1982) Elevated Concentrations of Actinides in Mono Lake. Science 216:514–516. https://doi.org/10.1126/science.216.4545.514

Armstrong CR, Brant HA, Nuessle PR, et al (2016) Anthropogenic plutonium-244 in the environment: Insights into plutonium's longest-lived isotope. Sci Rep 6:21512. https://doi.org/10.1038/srep21512

Beck HL, Bennett BG (2002) Historical Overview of Atmospheric Nuclear Weapons Testing and Estimates of Fallout in the Continental United States. Health Physics 82:591. https://doi.org/10.1097/00004032-200205000-00007

Bigeleisen J (1996) Nuclear Size and Shape Effects in Chemical Reactions. Isotope Chemistry of the Heavy Elements. J Am Chem Soc 118:3676–3680. https://doi.org/10.1021/ja954076k

Bigeleisen J, Mayer MG (1947) Calculation of Equilibrium Constants for Isotopic Exchange Reactions. The Journal of Chemical Physics 15:261–267. https://doi.org/10.1063/1.1746492

Blanchard M, Balan E, Schauble EA (2017) Equilibrium Fractionation of Non-traditional Isotopes: a Molecular Modeling Perspective. Reviews in Mineralogy and Geochemistry 82:27–63. https://doi.org/10.2138/rmg.2017.82.2

Boring AM, Albers RC, Stewart GR, Koelling DD (1985) Electronic structure and anomalous properties of UAl_2, $NpAl_2$, and $PuAl_2$. Physical Review B 31:3251. https://doi.org/10.1103/physrevb.31.3251

Bruno J, Grenthe I, Robouch P (1989) Studies of metal carbonate equilibria. 20. Formation of tetra(carbonato)uranium(IV) ion, $U(CO_3)_4^{4-}$, in hydrogen carbonate solutions. Inorganica Chimica Acta 158:221–226. https://doi.org/10.1016/S0020-1693(00)80837-3

Bu W, Zheng J, Guo Q, et al (2014a) Ultra-trace plutonium determination in small volume seawater by sector field inductively coupled plasma mass spectrometry with application to Fukushima seawater samples. Journal of Chromatography A 1337:171–178. https://doi.org/10.1016/j.chroma.2014.02.066

Bu W, Zheng J, Guo Q, et al (2015) Temporal distribution of plutonium isotopes in marine sediments off Fukushima after the Fukushima Dai-ichi Nuclear Power Plant accident. J Radioanal Nucl Chem 303:1151–1154. https://doi.org/10.1007/s10967-014-3437-y

Bu W, Zheng J, Guo Q, Uchida S (2014b) Vertical distribution and migration of global fallout Pu in forest soils in southwestern China. Journal of Environmental Radioactivity 136:174–180. https://doi.org/10.1016/j.jenvrad.2014.06.010

Cao L, Zheng J, Zhou Z, et al (2021) Distribution and behavior of plutonium isotopes in Western Pacific marginal seas. CATENA 198:105023. https://doi.org/10.1016/j.catena.2020.105023

Cao X, Dolg M, Stoll H (2002) Valence basis sets for relativistic energy-consistent small-core actinide pseudopotentials. J Chem Phys 118:487–496. https://doi.org/10.1063/1.1521431

Child DP, Hotchkis MAC (2013) Plutonium and uranium contamination in soils from former nuclear weapon test sites in Australia. Nuclear Instruments and Methods in Physics Research Section B: Beam Interactions with Materials and Atoms 294:642–646. https://doi.org/10.1016/j.nimb.2012.05.018

Choppin G (2007) Actinide speciation in the environment. Journal of Radioanalytical and Nuclear Chemistry 273:695–703. https://doi.org/10.1007/s10967-007-0933-3

Choppin GR, Jensen MP (2006) Actinides in solution: complexation and kinetics. In: The chemistry of the actinide and transactinide elements. Springer Netherlands, Dordrecht, pp 2524–2621. https://doi.org/10.1007/1-4020-3598-5_23

Choppin GR, Kobashi A (1990) Distribution of Pu(V) and Pu(VI) in seawater. Marine Chemistry 30:241–247. https://doi.org/10.1016/0304-4203(90)90073-L

Choppin GR, Rao LF (1984) Complexation of Pentavalent and Hexavalent Actinides by Fluoride. Radiochimica Acta 37:143–146. https://doi.org/10.1524/ract.1984.37.3.143

Clark DL, Hecker SS, Jarvinen GD, Neu MP (2006) Plutonium. In: Morss LR, Edelstein NM, Fuger J (eds) The Chemistry of the Actinide and Transactinide Elements. Springer Netherlands, Dordrecht, pp 813–1264

Cooper LW, Kelley JM, Bond LA, et al (2000) Sources of the transuranic elements plutonium and neptunium in arctic marine sediments. Marine Chemistry 69:253–276. https://doi.org/10.1016/S0304-4203(99)00109-7

Degueldre C (2006) Identification and Speciation of Actinides in the Environment. In: The chemistry of the actinide and transactinide elements. Springer Netherlands, Dordrecht, pp 3013–3085

Desideri D, Meli MA, Roselli C, Testa C (2004) Analytical techniques for the separation and determination of transuranium element ultratraces in depleted uranium ammunitions. International Journal of Environmental Analytical Chemistry 84:331–339. https://doi.org/10.1080/03067310001640410

Dunning TH Jr (1989) Gaussian basis sets for use in correlated molecular calculations. I. The atoms boron through neon and hydrogen. The Journal of Chemical Physics 90:1007–1023. https://doi.org/10.1063/1.456153

Dyall KG (2007) Relativistic double-zeta, triple-zeta, and quadruple-zeta basis sets for the actinides Ac–Lr. Theor Chem Acc 117:491–500. https://doi.org/10.1007/s00214-006-0175-4

Evrard O, Pointurier F, Onda Y, et al (2014) Novel Insights into Fukushima Nuclear Accident from Isotopic Evidence of Plutonium Spread along Coastal Rivers. Environ Sci Technol 48:9334–9340. https://doi.org/10.1021/es501890n

Faizova R, Scopelliti R, Chauvin A-S, Mazzanti M (2018) Synthesis and Characterization of a Water Stable Uranyl(V) Complex. J Am Chem Soc 140:13554–13557. https://doi.org/10.1021/jacs.8b07885

Ferro F, Artemyev A, Stöhlker T, Surzhykov A (2010) Isotope shift of the $1s2p\ ^3P_0$–$1s2s\ ^1S_0$ level splitting in heavy He-like ions: Implications for atomic parity-nonconservation studies. Physical Review A 81:062503. https://doi.org/10.1103/PhysRevA.81.062503

Fricke G, Heilig K (2004) 94-Pu Plutonium. In: Schopper H (ed) Nuclear Charge Radii. Springer-Verlag, Berlin/Heidelberg, pp 1–5

Frisch MJ, Trucks GW, Schlegel HB, et al (2009) Gaussian 09: Programmer's Reference. Gaussian Inc., Wallingford, CT

Fukai R, Yamato A, Thein M, Bilinski H (1987) Oxidation states of fallout plutonium in Mediterranean rain and seawater. Geochemical Journal 21:51–57. https://doi.org/10.2343/geochemj.21.51

Gal J, Hadari Z, Atzmony U, et al (1973) Hyperfine Interactions and Relaxation Effects in Laves-Phase Intermetallic Compounds of Neptunium. Physical Review B 8:1901. https://doi.org/10.1103/physrevb.8.1901

Geckeis H, Salbu B, Schafer T, Zavarin M (2019) Environmental chemistry of plutonium. Lawrence Livermore National Lab, Livermore, CA

Gibson JK, de Jong WA, Dau PD, Gong Y (2017) Heptavalent Actinide Tetroxides NpO_4^- and PuO_4^-: Oxidation of Pu(V) to Pu(VII) by Adding an Electron to PuO_4. J Phys Chem A 121:9156–9162. https://doi.org/10.1021/acs.jpca.7b09721

Gonze X, Amadon B, Anglade P-M, et al (2009) ABINIT: First-principles approach to material and nanosystem properties. Computer Physics Communications 180:2582–2615. https://doi.org/10.1016/j.cpc.2009.07.007

Govind N, de Jong WA (2014) Simulating Cl K-edge X-ray absorption spectroscopy in MCl_6^{2-} (M = U, Np, Pu) complexes and $UOCl_5^-$ using time-dependent density functional theory. Theor Chem Acc 133:1463. https://doi.org/10.1007/s00214-014-1463-z

Grigoriev MS, Krot NN (2007) Reinvestigation of trisodium dihydroxidotetraoxidoneptunate (VII). Acta Crystallographica Section E: Structure Reports Online 63:i176–i176. https://doi.org/10.1107/S1600536807039025

Hirose K, Povinec PP (2015) Sources of plutonium in the atmosphere and stratosphere-troposphere mixing. Sci Rep 5:15707. https://doi.org/10.1038/srep15707

Hirose K, Sugimura Y (1993) Chemical speciation of particulate ^{238}U, ^{239,240}Pu and Th isotopes in seawater. Science of The Total Environment 130–131:517–524. https://doi.org/10.1016/0048-9697(93)90106-G

Hoffman DC, Lawrence FO, Mewherter JL, Rourke FM (1971) Detection of Plutonium-244 in Nature. Nature 234:132–134. https://doi.org/10.1038/234132a0

Holm E, Aarkrog A, Ballestra S, Dahlgaard H (1986) Origin and isotopic ratios of plutonium in the Barents and Greenland Seas. Earth and Planetary Science Letters 79:27–32. https://doi.org/10.1016/0012-821X(86)90037-3

Holzwarth NAW, Tackett AR, Matthews GE (2001) A Projector Augmented Wave (PAW) code for electronic structure calculations, Part I: atompaw for generating atom-centered functions. Computer Physics Communications 135:329–347. https://doi.org/10.1016/S0010-4655(00)00244-7

Hoo WT, Fifield LK, Tims SG, et al (2011) Using fallout plutonium as a probe for erosion assessment. Journal of Environmental Radioactivity 102:937–942. https://doi.org/10.1016/j.jenvrad.2010.06.010

Horie K, Hidaka H, Gauthier-Lafaye F (2004) Isotopic evidence for trapped fissiogenic REE and nucleogenic Pu in apatite and Pb evolution at the Oklo natural reactor. Geochimica et Cosmochimica Acta 68:115–125. https://doi.org/10.1016/S0016-7037(03)00415-0

Huang W, Xu W-H, Su J, et al (2013) Oxidation States, Geometries, and Electronic Structures of Plutonium Tetroxide PuO4 Isomers: Is Octavalent Pu Viable? Inorg Chem 52:14237–14245. https://doi.org/10.1021/ic402170q

Ilyatov KV, Matuzenko MY, Krizhanskii LM, Chai WP (1975) Investigation of Certain Heptavalent Neptunium Compounds by the Method of Mössbauer. Radiokhimiya 17:905

Ionova GV, Mikhalko VK, Zhoveh Z (1998) Charge distribution in neptunium compounds calculated from Mössbauer spectroscopy data. Zhurnal Neorganicheskoj Khimii 43:592–597

Jaegler H, Pointurier F, Diez-Fernández S, et al (2019) Reconstruction of uranium and plutonium isotopic signatures in sediment accumulated in the Mano Dam reservoir, Japan, before and after the Fukushima nuclear accident. Chemosphere 225:849–858. https://doi.org/10.1016/j.chemosphere.2019.03.064

Jakopič R, Richter S, Kühn H, Aregbe Y (2010) Determination of ^{240}Pu/^{239}Pu, ^{241}Pu/^{239}Pu and ^{242}Pu/^{239}Pu isotope ratios in environmental reference materials and samples from Chernobyl by thermal ionization mass spectrometry (TIMS) and filament carburization. J Anal At Spectrom 25:815–821. https://doi.org/10.1039/B925918J

Jollet F, Torrent M, Holzwarth N (2014) Generation of Projector Augmented-Wave atomic data: A 71 element validated table in the XML format. Computer Physics Communications 185:1246–1254. https://doi.org/10.1016/j.cpc.2013.12.023

Jové J, Cousson A, Abazli H, et al (1988) Systematic trends in the ^{237}neptunium Mössbauer isomer shift: Overlap of IV, V and VI neptunium oxidation states and correlation between isomer shift and crystal structure. Hyperfine Interactions 39:1–16. https://doi.org/10.1007/bf02394642

Kaszuba JP, Runde WH (1999) The aqueous geochemistry of neptunium: Dynamic control of soluble concentrations with applications to nuclear waste disposal. Environmental Science & Technology 33:4427–4433. https://doi.org/10.1021/es990470x

Keeney-Kennicutt WL, Morse JW (1984) The interaction of $Np(V)O_2^+$ with common mineral surfaces in dilute aqueous solutions and seawater. Marine Chemistry 15:133–150. https://doi.org/10.1016/0304-4203(84)90012-4

Klaus DM (2019) What really went wrong at WIPP: An insider's view of two accidents at the only US underground nuclear waste repository. Bulletin of the Atomic Scientists 75:197–204. https://doi.org/10.1080/00963402.2019.1628516

Kondev FG, Wang M, Huang WJ, et al (2021) The NUBASE2020 evaluation of nuclear physics properties. Chinese Phys C 45:030001. https://doi.org/10.1088/1674-1137/abddae

Kumar N, Seminario JM (2015) Solvation of Actinide Salts in Water Using a Polarizable Continuum Model. J Phys Chem A 119:689–703. https://doi.org/10.1021/jp507613a

Law GTW, Geissler A, Lloyd JR, et al (2010) Geomicrobiological Redox Cycling of the Transuranic Element Neptunium. Environ Sci Technol 44:8924–8929. https://doi.org/10.1021/es101911v

Liu W, Peng D (2009) Exact two-component Hamiltonians revisited. The Journal of Chemical Physics 131:031104. https://doi.org/10.1063/1.3159445

López-Lora M, Olszewski G, Chamizo E, et al (2023) Plutonium Signatures in a Dated Sediment Core as a Tool to Reveal Nuclear Sources in the Baltic Sea. Environ Sci Technol 57:1959–1969. https://doi.org/10.1021/acs.est.2c07437

Maher K, Bargar JR, Brown GEJr (2013) Environmental Speciation of Actinides. Inorg Chem 52:3510–3532. https://doi.org/10.1021/ic301686d

Maldonado P, Paolasini L, Oppeneer PM, et al (2016) Crystal dynamics and thermal properties of neptunium dioxide. Phys Rev B 93:144301. https://doi.org/10.1103/PhysRevB.93.144301

Malm JG, Williams CW, Soderholm L, Morss LR (1993) Preparation, chemical reactions, and some physical properties of neptunium pentafluoride. Journal of alloys and compounds 194:133–137. https://doi.org/10.1016/0925-8388(93)90658-A

McDowell RS, Asprey LB, Paine RT (1974) Vibrational spectrum and force field of uranium hexafluoride. The Journal of Chemical Physics 61:3571–3580. https://doi.org/10.1063/1.1682537

Méheut M, Lazzeri M, Balan E, Mauri F (2007) Equilibrium isotopic fractionation in the kaolinite, quartz, water system: Prediction from first-principles density-functional theory. Geochimica et Cosmochimica Acta 71:3170–3181. https://doi.org/10.1016/j.gca.2007.04.012

Mietelski JW, Was B (1995) Plutonium from Chernobyl in Poland. Applied Radiation and Isotopes 46:1203–1211. https://doi.org/10.1016/0969-8043(95)00162-7

Mitchell PI, Batlle JV, Ryan TP, et al (1991) Studies on the Speciation of Plutonium and Americium in the Western Irish Sea. In: Kershaw PJ, Woodhead DS (eds) Radionuclides in the Study of Marine Processes. Springer Netherlands, Dordrecht, pp 37–51

Morse JW, Choppin GR (1986) Laboratory studies of plutonium in marine systems. Marine Chemistry 20:73–89. https://doi.org/10.1016/0304-4203(86)90067-8

Morss LR, Appelman EH, Gerz RR, Martin-Rovet D (1994) Structural studies of Li_5ReO_6, Li_4NpO_5 and Li_5NpO_6 by neutron and X-ray powder diffraction. Journal of alloys and compounds 203:289–295. https://doi.org/10.1016/0925-8388(94)90748-X

Nadjakov EG, Marinova KP, Gangrsky YP (1994) Systematics of Nuclear Charge Radii. Atomic Data and Nuclear Data Tables 56:133–157. https://doi.org/10.1006/adnd.1994.1004

Nash KL, Cleveland JM, Rees TF (1988) Speciation patterns of actinides in natural waters: a laboratory investigation. Journal of Environmental Radioactivity 7:131–157. https://doi.org/10.1016/0265-931X(88)90004-5

Nelson DM, Larsen RP, Penrose WR (1987) Chemical speciation of plutonium in natural waters. Argonne National Lab, Lemont, IL

Nelson DM, Orlandini KA, Penrose WR (1989) Oxidation states of plutonium in carbonate-rich natural waters. Journal of Environmental Radioactivity 9:189–198. https://doi.org/10.1016/0265-931X(89)90043-X

Neu MP, Boukhalfa H, Merroun ML (2010) Biomineralization and biotransformations of actinide materials. MRS Bulletin 35:849–857. https://doi.org/10.1557/mrs2010.711

Neu MP, Icopini GA, Boukhalfa H (2005) Plutonium speciation affected by environmental bacteria. Radiochimica Acta 93:705–714. https://doi.org/10.1524/ract.2005.93.11.705

Nitsche H (1990) Basic Research for Assessment of Geologic Nuclear Waste Repositories: What Solubility and Speciation Studies of Transuranium Elements Can Tell US. MRS Online Proceedings Library (OPL) 212:517. https://doi.org/10.1557/PROC-212-517

Nomura M, Higuchi N, Fujii Y (1996) Mass Dependence of Uranium Isotope Effects in the U(IV)−U(VI) Exchange Reaction. J Am Chem Soc 118:9127–9130. https://doi.org/10.1021/ja954075s

Olivier S, Bajo S, Fifield LK, et al (2004) Plutonium from Global Fallout Recorded in an Ice Core from the Belukha Glacier, Siberian Altai. Environ Sci Technol 38:6507–6512. https://doi.org/10.1021/es0492900

Pegg JT, Shields AE, Storr MT, et al (2019) Noncollinear Relativistic DFT + U Calculations of Actinide Dioxide Surfaces. J Phys Chem C 123:356–366. https://doi.org/10.1021/acs.jpcc.8b07823

Perdew JP, Burke K, Ernzerhof M (1996) Generalized Gradient Approximation Made Simple. Phys Rev Lett 77:3865–3868. https://doi.org/10.1103/PhysRevLett.77.3865

Pritchard BP, Altarawy D, Didier B, et al (2019) New Basis Set Exchange: An Open, Up-to-Date Resource for the Molecular Sciences Community. J Chem Inf Model 59:4814–4820. https://doi.org/10.1021/acs.jcim.9b00725

Reiller PE (2024) Predominance of the alkaline earth(II) triscarbonatoactinyl(VI) complexes in different geochemical contexts: Review of existing data and estimation of potentially unidentified species. Chemosphere 350:141049. https://doi.org/10.1016/j.chemosphere.2023.141049

Runde W, Neu MP (2010) Actinides in the Geosphere. In: The chemistry of the actinide and transactinide elements. Springer Netherlands, Dordrecht, pp 3475–3593

Ryzhkov MV, Enyashin AN, Delley B (2021) Plutonium complexes in water: new approach to ab initio modeling. Radiochimica Acta 109:327–342. https://doi.org/10.1515/ract-2020-0091

Sanchez AL, Gastaud J, Holm E, Roos P (1994) Distribution of Plutonium and its oxidation states in Framvaren and Hellvik fjords, Norway. Journal of Environmental Radioactivity 22:205–217. https://doi.org/10.1016/0265-931X(94)90082-5

Santschi PH, Roberts KA, Guo L (2002) Organic Nature of Colloidal Actinides Transported in Surface Water Environments. Environ Sci Technol 36:3711–3719. https://doi.org/10.1021/es0112588

Sato A, Bernier-Latmani R, Hada M, Abe M (2021) Ab initio and steady-state models for uranium isotope fractionation in multi-step biotic and abiotic reduction. Geochimica et Cosmochimica Acta 307:212–227. https://doi.org/10.1016/j.gca.2021.05.044

Saue T, Visscher L, Jensen HA, et al (2011) DIRAC, a relativistic ab initio electronic structure program, release DIRAC10

Schauble EA (2006) Equilibrium uranium isotope fractionation by nuclear volume and mass-dependent processes. AGU Fall Meeting Abstracts 21:V21B-0570

Schauble EA (2004) Applying Stable Isotope Fractionation Theory to New Systems. Reviews in Mineralogy and Geochemistry 55:65–111. https://doi.org/10.2138/gsrmg.55.1.65

Schauble EA (2013) Modeling nuclear volume isotope effects in crystals. PNAS 110:17714–17719. https://doi.org/10.1073/pnas.1216216110

Schimmelpfennig B, Privalov T, Wahlgren U, Grenthe I (2003) Ab Initio Studies of Np and Pu Complexes and Reactions in the Gas Phase: Structures and Thermodynamics. J Phys Chem A 107:9705–9711. https://doi.org/10.1021/jp035683u

Schuchardt KL, Didier BT, Elsethagen T, et al (2007) Basis Set Exchange: A Community Database for Computational Sciences. J Chem Inf Model 47:1045–1052. https://doi.org/10.1021/ci600510j

Silver GL (2014) Plutonium: verification of comprehensive disproportionation equations. J Radioanal Nucl Chem 301:905–908. https://doi.org/10.1007/s10967-014-3217-8

Simpson HJ, Trier RM, Toggweiler JR, et al (1982) Radionuclides in Mono Lake, California. Science 216:512–514. https://doi.org/10.1126/science.216.4545.512

Steier P, Dellinger F, Forstner O, et al (2010) Analysis and application of heavy isotopes in the environment. Nuclear Instruments and Methods in Physics Research Section B: Beam Interactions with Materials and Atoms 268:1045–1049. https://doi.org/10.1016/j.nimb.2009.10.094

Stirling CH, Andersen MB, Potter E-K, Halliday AN (2007) Low-temperature isotopic fractionation of uranium. Earth and Planetary Science Letters 264:208–225. https://doi.org/10.1016/j.epsl.2007.09.019

Stirling CH, Halliday AN, Porcelli D (2005) In search of live ^{247}Cm in the early solar system. Geochimica et Cosmochimica Acta 69:1059–1071. https://doi.org/10.1016/j.gca.2004.06.034

Stirling CH, Halliday AN, Potter E-K, et al (2006) A low initial abundance of ^{247}Cm in the early solar system and implications for r-process nucleosynthesis. Earth and Planetary Science Letters 251:386–397. https://doi.org/10.1016/j.epsl.2006.09.023

Sun B, Zhang P, Zhao X-G (2008) First-principles local density approximation+U and generalized gradient approximation+U study of plutonium oxides. The Journal of Chemical Physics 128:084705. https://doi.org/10.1063/1.2833553

Surbella RGI, Ducati LC, Schofield MH, et al (2022) Plutonium Hybrid Materials: A Platform to Explore Assembly and Metal–Ligand Bonding. Inorg Chem 61:17963–17971. https://doi.org/10.1021/acs.inorgchem.2c02084

Thevenin T, Jove J, Madic C (1986) Crystal chemistry and ^{237}Np mössbauer investigations of neptunyl (vi) carbonate NpO2CO3. Journal of the Less Common Metals 121:477–481. https://doi.org/10.1016/0022-5088(86)90565-5

Torrent M, Jollet F, Bottin F, et al (2008) Implementation of the projector augmented-wave method in the ABINIT code: Application to the study of iron under pressure. Computational Materials Science 42:337–351. https://doi.org/10.1016/j.commatsci.2007.07.020

Urey H (1947) The thermodynamic properties of isotopic substances. J Chem Soc 562–581. https://doi.org/10.1039/JR9470000562

Varga Z (2007) Origin and release date assessment of environmental plutonium by isotopic composition. Anal Bioanal Chem 389:725–732. https://doi.org/10.1007/s00216-007-1371-3

Wallner C, Faestermann T, Gerstmann U, et al (2004) Supernova produced and anthropogenic 244Pu in deep sea manganese encrustations. New Astronomy Reviews 48:145–150. https://doi.org/10.1016/j.newar.2003.11.020

Wang B-T, Shi H, Li W, Zhang P (2010) First-principles LDA+ U and GGA+ U study of neptunium dioxide. Physical Review B 81:045119. https://doi.org/10.1103/PhysRevB.81.045119

Wang X, Johnson TM, Lundstrom CC (2015a) Isotope fractionation during oxidation of tetravalent uranium by dissolved oxygen. Geochimica et Cosmochimica Acta 150:160–170. https://doi.org/10.1016/j.gca.2014.12.007

Wang X, Johnson TM, Lundstrom CC (2015b) Low temperature equilibrium isotope fractionation and isotope exchange kinetics between U(IV) and U(VI). Geochimica et Cosmochimica Acta 158:262–275. https://doi.org/10.1016/j.gca.2015.03.006

Waters CN, Syvitski JPM, Gałuszka A, et al (2015) Can nuclear weapons fallout mark the beginning of the Anthropocene Epoch? Bulletin of the Atomic Scientists 71:46–57. https://doi.org/10.1177/0096340215581357

Waters CN, Zalasiewicz J, Summerhayes C, et al (2016) The Anthropocene is functionally and stratigraphically distinct from the Holocene. Science 351:aad2622. https://doi.org/10.1126/science.aad2622

Weigend F, Ahlrichs R (2005) Balanced basis sets of split valence, triple zeta valence and quadruple zeta valence quality for H to Rn: Design and assessment of accuracy. Phys Chem Chem Phys 7:3297–3305. https://doi.org/10.1039/B508541A

Weinstock B, Goodman GL (1965) Vibrational properties of hexafluoride molecules. Advances in Chemical Physics 9:169–319. https://doi.org/10.1002/9780470143551.ch3

Weyer S, Anbar AD, Gerdes A, et al (2008) Natural fractionation of $^{238}U/^{235}U$. Geochimica et Cosmochimica Acta 72:345–359. https://doi.org/10.1016/j.gca.2007.11.012

Widanagamage IH, Schauble EA, Scher HD, Griffith EM (2014) Stable strontium isotope fractionation in synthetic barite. Geochimica et Cosmochimica Acta 147:58–75. https://doi.org/10.1016/j.gca.2014.10.004

Woon DE, Dunning TH Jr (1993) Gaussian basis sets for use in correlated molecular calculations. III. The atoms aluminum through argon. The Journal of Chemical Physics 98:1358–1371. https://doi.org/10.1063/1.464303

Wyckoff RWG (1963) Fluorite structure. In: Crystal Structures, 2nd edn. Interscience Publishers, New York, pp 239–444

Yaar I, Fredo S, Gal J, et al (1992) Magnetic properties of $NpGa_2$ and $NpSi_2$. Physical Review B 45:9765. https://doi.org/10.1103/physrevb.45.9765

Young ED, Galy A, Nagahara H (2002) Kinetic and equilibrium mass-dependent isotope fractionation laws in nature and their geochemical and cosmochemical significance. Geochimica et Cosmochimica Acta 66:1095–1104. https://doi.org/10.1016/S0016-7037(01)00832-8

Zachariasen WH (1949) Crystal chemical studies of the 5*f*-series of elements. XII. New compounds representing known structure types. Acta Crystallographica 2:388–390. https://doi.org/10.1107/s0365110x49001016

Zalkin A, Templeton DH (1985) Refinement of the trigonal crystal structure of lanthanum trifluoride with neutron diffraction data. Acta Crystallographica Section B: Structural Science 41:91–93. https://doi.org/10.1107/s0108768185001689

Zwanziger JW (2009) Computation of Mössbauer isomer shifts from first principles. J Phys: Condens Matter 21:195501. https://doi.org/10.1088/0953-8984/21/19/195501

Chapter 4

Field shift fractionation in the platinum group elements: a preliminary study

Abstract

We performed a pilot study of equilibrium platinum-isotope ($^{198}Pt/^{194}Pt$) fractionation including both field shift and mass dependent components of fractionation. We find that for most species, the field shift component of fractionation relative to native Pt at 300 K is small, and in fact falls within the reported analytical error of ±0.08‰ given by a recent measurement study (Creech et al., 2014). Fractionations are expected to be even more subdued at higher temperatures. Exceptions include the solid species PtS (cooperite) and $PtAs_2$ (sperrylite), which display potentially measurable field shift effects relative to native Pt (~-0.1‰) in the opposite direction of the mass dependent component of fractionation at temperatures up to 500 K, as well as Pt substituted into the olivine structure. Pt-substituted olivine displays a total equilibrium $^{198}Pt/^{194}Pt$ fractionation (field shift plus mass fractionation) of approximately +0.1‰ relative to an iron-platinum alloy Fe_7Pt at core-mantle differentiation temperatures of 3000 K (Wood et al., 2006). We examined the isotope fractionations during core-mantle differentiation between the iron-platinum alloy and a variety of potential species that may be present in reduced silicate melts using a Rayleigh fractionation process under the end-member assumption of equilibrium partitioning in a closed system. While it is unclear which species is the best analog for platinum in a silicate melt, Pt-substituted olivine, native Pt, and solid PtS are all capable of reproducing the isotopically heavy primitive mantle of Creech et al., (2017), who determined the unmixed Archean mantle to be 0.4-0.6‰ heavier than chondrites. An additional pilot study of iridium isotope fractionation was performed using Mössbauer isomer shifts and DFT-PAW electron density for a select group of species. We find comparable field shifts between different oxidation

states among Cl-bearing species in this system, with an estimated field shift fractionation of 0.08‰ expected between K_2IrCl_4 and K_3IrCl_4, with the reduced species being enriched in the larger, more massive isotope (i.e., having higher $^{193}Ir/^{191}Ir$) as in the case of platinum.

4.1. Introduction

The platinum group elements (PGEs: Pt, Pd, Rh, Ir, Ru, and Os) are a loose grouping of transition metals that display a somewhat coherent pattern of behavior that is distinct from other nearby elements in the periodic table (e.g., Fe, Ni, and Co). The PGEs are siderophile (Chou, 1978), meaning they favor forming compounds with iron rather than with silicates. Experiments have confirmed this behavior, finding that PGEs have more than 10^5 times greater preference for liquid metal than silicate melt (Righter, 2003). The PGEs are also chalcophilic within the range of oxygen and sulfur fugacities believed to be of significance in the mantle. In a sample of fertile orogenic lherzolites, they were found to be concentrated primarily in "nuggets" rich in Pt-Ir-Os alloys, S-bearing phases such as laurite and ehrlichmanite, and Pt-Pd-Bi-Te phases such as moncheite (Lorand et al., 2010). The PGEs also tend to be refractory in cosmochemical environments. Platinum itself has an estimated 50% condensation temperature of 1410K, while the rest of the PGEs fall between 1360 and 1800 K (Taylor, 2001). In resource exploration they tend to be found together in minerals and ore deposits (Clarke, 1920).

The PGEs can be found in nature as various native metal alloys, tellurides, arsenides, selenides, antimonides, oxides, and most significantly base metal sulfides, especially in mafic and ultramafic rocks (McDonough, 2003). Several minerals of significance are listed in Table 4-1. PGEs are generally rare as trace-element substitutions in silicate minerals, and don't readily form their own silicate mineral structures (Hagen, 1954). Most economically significant deposits of PGEs are primary igneous bodies, though the Witwatersrand is an exception as the only known paleoplacer (clastic sedimentary) deposit with an economically significant proportion of PGEs (MacDonald, 1987). PGEs are also abundant in both undifferentiated and (even more so) iron meteorites (D’Orazio and Folco, 2003; Petaev and Jacobson, 2004) relative to Earth rocks, owing to their highly siderophile behavior during the formation of metallic cores.

4.1.1. Uses of PGEs in geoscience

Some of the most fundamental questions still outstanding in the geosciences pertain to the processes by which the Earth accreted and the core and mantle differentiated. The nature of the material from which the Earth accreted is still an open question, with chondrites being the closest analog (Anders and Grevesse, 1989; Grevesse and Sauval, 1998). However, there is no single group of chondrites that precisely matches measurements from the Earth and Moon, with particular groups matching better geochemically in some ways, but not necessarily in others; this likely reflects an origin from a variety of materials (Albarede, 2003). The physical processes and constraints (such as pressure, temperature, oxygen fugacity, and water) by which the core and mantle formed are another important question pertaining to the early stages of the Earth. Finally, it is important to determine to what extent the differentiation process can be explained by equilibrium processes.

The geochemically distinct behavior of the PGEs has historically made them useful for addressing these questions. Their siderophile behavior has been confirmed experimentally (Capobiano, 1995; Borisov et al., 1994; Ohtani et al., 1997; Holzheid et al., 2000; Fortenfant et al., 2003; Righter et al., 2003; Cottrell and Walker, 2006; Ertel et al., 2006; Righter et al., 2008; Brenan and McDonough, 2009; Cottrell et al., 2009). However, although the Earth’s primitive upper mantle is observed to be strongly depleted in these elements, the observed concentration of PGEs in the mantle and crust is much, much higher than predicted from silicate-metal partitioning at equilibrium at low to moderate pressures (Ringwood, 1966; Chou, 1978; Jagoutz, 1979; Righter, 2003; Day et al., 2016). Therefore, any model of the differentiation of the core and mantle must account for the anomalously high concentration of siderophile elements in the mantle. The two primary hypotheses are a late addition of meteoric material in the form of chondrites (Kimura et al., 1974; Chou, 1978; Morgan, 1985; Morgan et al., 2001), known as the "late veneer" hypothesis, or equilibrium core formation deep within a magma ocean (Cottrell and Walker, 2006; Righter et al., 2008; Mann et al., 2012). It should be noted that these theories are not mutually exclusive (Brenan and McDonough, 2009; Mann et al., 2012).

The late veneer hypothesis (Figure 4-1) states that the last ~0.1-1.0% of the Earth's mass was accreted after core formation (Kimura et al., 1974; Chou et al., 1978; Holzeid et al., 2000; Dauphas and Marty, 2002). The exact composition of this added material is unknown, but likely reflects a variety of sources, including carbonaceous chondrites, enstatite chondrites, and ordinary chondrites. Studies have indicated that the mantle concentration of siderophile elements increased throughout Earth's early history, up until about 2.9 Ga (Maier et al, 2009), which is believed to be indicative of progressive mixing of the late veneer into the mantle. Meteorites provide evidence that other planetary bodies that underwent differentiation may have undergone a similar process (Walker et al., 2004; Day et al., 2012). The late veneer hypothesis is linked to another hypothesis known as the Late Heavy Bombardment. The Late Heavy Bombardment is typically linked to the cratering history of the moon. Many lunar craters have been constrained to form during a narrow period of time (Tera et al., 1974; Wetherill, 1975; Hartmann et al., 2000), implying a short interval of intense impacts. However, questions remain regarding whether such a period of impact could have delivered a sufficient quantity of material to account for the observed siderophilic abundances in the mantle (Kleine, 2011).

Initial models of equilibrium core formation relied on partition coefficients obtained in experiments at low pressures and moderate temperatures, none of which could reproduce the observed abundance of Highly Siderophile Elements (HSEs) in the mantle. However, experiments performed at higher pressures, higher temperatures, and different oxygen fugacities (Brett, 1971; Ringwood, 1977; Brett, 1984; Murthy, 1991; Capobianco et al., 1993; Righter and Drake, 1997; Li and Agee, 2001), predicted less removal of siderophile elements from the mantle into the core, potentially explaining the conflict between initial partitioning experiments and the bulk silicate Earth composition. For example, initial low pressure and low temperature experiments resulted in a partition coefficient $D(Pt)_{metal/silicate} = 10^8–10^{12}$, while later high pressure, high temperature experiments obtained results of 10^3-10^5 (Righter, 2003; Cotrell and Walker, 2006; Walker, 2009). Models emerged of a hydrous magma ocean, of varying depth and oxygen fugacity. Such models can reproduce the observed abundances of several HSEs, including Pd and W. However, these newer models are not without their own problems. Even experiments at >60 GPa still do not yield partition coefficients that can fully explain all HSE anomalies, achieving partition coefficients of 10^2-10^4 (Ertel et al., 2006; Mann et al., 2012). Additionally, Mann et al. (2012) point out that at high pressures the partition coefficients of the highly siderophile elements differ from one another by ~0.5-3 orders of magnitude, in contrast to the relatively constant depletions observed across all of the HSEs in the mantle. They conclude that the entire suite of HSEs in the mantle cannot be reproduced in such models (Figure 4-1).

Stable isotope geochemistry is one potential tool to better understand the HSE anomaly. In the case of the magma ocean hypothesis, the partitioning of PGEs takes place at high temperature and pressure, conditions where mass dependent isotopic fractionations are expected to be small. However, measurement precisions have advanced to the point that the isotopes of Cr, Si, Mo, and S appear to show detectable fractionations at similar temperatures (Georg et al., 2007; Fitoussi et al., 2009; Shahar et al., 2009, 2011; Armytage et al., 2011; Moynier et al., 2011; Labidi et al., 2013; Hin et al., 2013). The isotopic fractionation related to metal-silicate differentiation specifically has also been examined for Si (Young et al., 2015), Mo (Hin et al., 2013; Burkhardt et al., 2014), and Zn (Mahan et al., 2017). However, the PGEs partition into metal to an even greater extent than these elements. Therefore, we might expect to see slightly different PGE isotopic compositions for chondrites versus the primitive upper mantle for PGEs in the magma ocean scenario. Alternately, if there is little to no isotopic difference between chondrites and the post-Archean primitive upper mantle, this would support the post-core addition of PGE-rich chondritic material, e.g. a late veneer. A major caveat, however, is that very little unequilibrated material would be required to overprint the equilibrium isotope signature of a highly PGE-depleted silicate magma ocean after core formation.

4.1.2. Platinum

The present study focuses primarily on the platinum system, in order to establish the significance of the field shift effect within the PGEs and open up study of additional elements. The platinum isotope system itself is relatively little studied. Modern high-precision measurements were first developed by Creech et al., (2013; 2014). We will focus on one recent study examining the ^{198}Pt/^{194}Pt system as a basis for evaluating the present models and calculations. Creech et al. (2017) examined the platinum isotope composition of a variety of meteorites and both Archean and post-Archean mantle rocks, and determined that the $\delta^{198/194}$Pt of multiple varieties of chondrites aren't significantly different from the post-Archean upper mantle (-0.14‰ and -0.11‰), respectively. The Archean mantle was observed to range from 0.21-0.46‰. This was interpreted as an isotopic signal resulting from metal-silicate differentiation, which was later overprinted by the addition of chondritic material (Figure 4-2).

Platinum's stable isotopes include ^{198}Pt, ^{196}Pt, ^{195}Pt, ^{194}Pt, ^{192}Pt, and ^{190}Pt, the last of which is nominally radioactive with a half-life of 4.83×10^{11} years. We aim to determine the magnitude of the field shift component of fractionation for the ^{198}Pt/^{194}Pt system in order to determine if it this component is important for platinum isotope studies, and more generally whether the field shift is likely to be measurable and significant for other PGEs. We mainly investigate ^{198}Pt and ^{194}Pt in this study, but other stable isotope ratios can be calculated from these results via the use of scale factors based on nuclear charge radii. Recent ^{198}Pt/^{194}Pt measurements report a reproducibility of ~0.08‰ (Creech et al., 2014, 2017) which we can use as a rough threshold to determine if a predicted field shift effect is likely to be measurable under current analytical precision.

Platinum group isotopes have been examined in other contexts as well. While platinum is known as a refractory element, it can still be mobilized to a limited extent at surface conditions and is present in small quantities in the ocean. Platinum occurs primarily in the divalent state in solution, forming chloro and bromo-complexes, with the most important being $PtCl_4^{2-}$ (Azaroual et al., 2001), but experiments indicate platinum may be oxidized to the +4 state when adsorbed to Fe-Mn crusts (Corcoran, 2016). It has been found in laboratory experiments that ^{198}Pt/^{194}Pt in these crusts is ~1.0‰ higher than other crustal and mantle samples (Corcoran, 2016).

4.1.3. Iridium

Iridium's stable isotopes are ^{193}Ir and ^{191}Ir. Approximately 63% of iridium consists of ^{193}Ir, and 37% of ^{191}Ir. Measurements of ^{193}Ir/^{191}Ir have been performed and a certified reference material has been developed (Zhu et al., 2017), but this system has not seen extensive use in stable isotope geochemistry to date. We aim to estimate the magnitude of the field shift effect for iridium using ab initio methods and measured Mössbauer isomer shifts – which should track the field shift effect (Schauble, 2013). Through the use of the DFT-PAW method and Mössbauer isomer shifts for the platinum group elements iridium and platinum, this study will provide a framework for future *ab initio* studies of the PGEs as well as future measurements of PGE stable isotopes.

4.1.4. Nuclear field shift effect and Mössbauer isomer shifts

The field shift effect is now known to be the dominant component of chemical isotope fractionation in uranium (Bigeleisen, 1996; Nomura et al., 1996), causing ^{238}U to be enriched in reduced species (Shimokaua and Kobayashi, 1970; Florence et al. 1975; Fujii et al., 1989ab; Fukuda et al. 1983). Mass dependent components of fractionation usually go the opposite direction (e.g., Schauble, 2004), and in the case of uranium are expected to be relatively muted because of the very high masses of the ^{238}U/^{235}U system.

The field shift effect is an equilibrium thermodynamic phenomenon caused by the finite volumes and nonspherical shapes of atomic nuclei. The physical origin of the effect is closely related to the Mössbauer isomer shift, seen in high-resolution gamma-ray absorption spectroscopy (Mössbauer 1958ab; 1959). Both effects can be described approximately by a relation adapted from the Mössbauer spectroscopy literature (e.g., Schauble (2017):

$$\ln \alpha_{fs} \approx \frac{2\pi Z e^2}{3kT} \left(|\psi(0)_{AX}|^2 - |\psi(0)_{BX}|^2 \right) \Delta\langle r^2_{isotopes} \rangle$$

Here α_{fs} is the field shift fractionation factor, Z is the atomic number, e is the charge of an electron, k is the Boltzmann constant, $|\psi(0)_{AX}|^2$ and $|\psi(0)_{BX}|^2$ are the electron density at the nucleus for the species AX and BX, and $\Delta\langle r^2 \rangle$ is the difference in the mean squared charge radius between the nuclei of interest (for Mössbauer spectroscopy the radius difference corresponds to upper and lower energy states of the Mössbauer isotope nucleus).

It is noteworthy that Mössbauer isomer shifts have been measured for platinum group elements, among them Ir (Mössbauer, 1958ab, 1959), Pt (Harris et al., 1965), and Os (Morrison et al., 1964). These measurements give access to the critical electron-density parameters that control the field shift:

$$\delta(\nu)\text{isomer} = \frac{c}{E_\gamma}\frac{2\pi Ze^2}{3}\left(|\psi(0)_{AX}|^2 - |\psi(0)_{BX}|^2\right)\Delta\langle r^2_{\text{isomer}}\rangle$$

Where δ(v)isomer is the isomer shift in units of velocity, Z is the atomic number of the nucleus, e is the charge of an electron, $|\Psi(0)|^2_{AX,BX}$ are the contact densities at the nucleus in substances A and B (for Mössbauer studies these would be the source and absorber materials), $\Delta<r^2>$ is the change in root-mean-squared (rms) nuclear charge radius between the initial and final states of the Mössbauer isotope, c is the speed of light, and E_γ is the energy of the Mössbauer gamma ray. Therefore, since Mössbauer isomer shifts depend on the two primary variables for the nuclear field shift, i.e., nuclear volume and electron density, we can estimate the nuclear field shift effect by calculating the electron density for that species and multiplying the isomer shift by the ratio of $\Delta\langle r^2\rangle$ between the measured nuclear charge radii used for this study, and the Mössbauer data. Previous studies have confirmed an excellent agreement between DFT-PAW electron densities and isomer shifts (Zwanziger, 2009). However, the range of substances with measured isomer shifts is limited, particularly with respect to geochemically-relevant materials, and $\Delta\left\langle r^2_{\text{isomer}}\right\rangle$may have large uncertainties for PGE Mössbauer isotopes.

Unlike equilibrium mass dependent fractionation, which typically varies according to $1/T^2$ for high atomic number elements, the field shift varies scales with 1/T so long as the fractionating species are mainly in their electronic ground states. The nuclear charge radius varies with different isotopes of a given element, while the electron density at the nucleus may vary depending on the oxidation state, state of matter, and other chemical speciation effects such as the identity of ligands bound to that central atom of interest. The weaker temperature sensitivity of the field shift is important to the study of the PGE isotope fractionations. During higher temperature processes such as core-mantle differentiation, the field shift component of fractionation is likely to exceed the mass dependent component of fractionation, or at least significantly impact estimates of the final isotopic composition, even if it is less important than mass-dependent effects at room temperatures. This strongly affects the potential to examine core-mantle differentiation using PGE isotope fractionations.

Field shift effects have been predicted and measured in both the Tl and Hg stable isotope systems (Schauble, 2007; 2013). These elements are of particular interest to us, as their atomic numbers (Z=81 and Z=80) are close to Pt (Z=78), and it is therefore worth examining whether transition metals of a similar atomic number might display comparable fractionation. In the case of thallium and mercury, the oxidized species (Tl^{3+} and Hg^{2+}) are enriched in the heavier isotope relative to the reduced species (Tl^{+} and Hg^{0}). This contrasts with the U-isotope system. Hg- and Tl-isotope fractionations can be as great as 3‰ at 298 K. Field shifts in Eu (Z=63) have also been examined (Schauble, 2023). It was determined that at 298 K, Eu^{2+} species will have 0.4-1.0‰ higher $^{153}Eu/^{151}Eu$ than Eu^{3+} species, and 0.3‰ higher $^{153}Eu/^{151}Eu$ at 973K. The Re (Z=75) isotope system has also been examined, where it was predicted that Re(IV) species will display a field shift of approximately 0.5‰ in the direction of high $^{187}Re/^{185}Re$ in reduced species relative to the Re(VIII) species ReO_4^-, an effect approximately 25-50% as large as the mass dependent fractionation between these species at ambient temperatures (Miller et al., 2015). Based on these other elements, is unclear in which direction Pt isotopes would be enriched as a consequence of the field shift, but the U, Tl, Hg, Re, and Eu systems all show that this effect can have large, measurable effects on equilibrium isotope fractionation that should be accounted for when interpreting isotopic ratios measurements in the high-Z part of the periodic table.

4.2. Methods

Equilibrium fractionations for platinum group elements are estimated as the sum of mass dependent and field shift components of fractionation, each calculated via *ab initio* electronic structure methods. The mass dependent component of fractionation for vapor phase and aqueous species is determined from vibrational frequencies of isotopically substituted species (Urey, 1946), and for solids via the force constant method of Widanagamage et al. (2014), adapted from Bigeleisen and Mayer (1947). The field shift component of fractionation is estimated via the DFT-PAW (Density Functional Theory-Projector Augmented Wave) method of Schauble (2013).

The DFT-PAW method requires first generating a calibration line using relatively simple species. We chose the following vapor phase Pt^{II} and Pt^{IV} species: $PtCl_2$, $Pt(OH)_2$, cisplatin, transplatin, PtC, PtO_2, and $PtCl_6^{2-}$. This calibration line makes it possible to determine the field shift effect for more complex molecules. As previously discussed, the primary platinum species in the ocean are halogen complexes. We therefore chose to model additional chlorine-bearing complexes. We chose structures for Pt-bearing solids that are relatively simple and common, such as native Pt, $PtAs_2$, and PtS), as well as the crystalline PtO_2 and $CaPtO_3$ in order to examine Pt^{IV}-bearing solids. Two hypothetical trace Pt^{II}-bearing species were modeled by substituting Pt atoms into literature structures of pure (non-Pt-bearing) solids. The first species was chosen as a potential analog for Pt^{II} within a silicate melt at the time of core-mantle differentiation. Olivine was chosen to be crudely representative the mantle. Pt-substituted olivine was modeled by replacing a single Mg cation in the M2 site in the forsterite, yielding a $Mg_4(PtMg_3)Si_4O_{16}$ unit cell. Pt-substituted fayalite was also modeled, as well as placing the platinum substitution at an M1 site instead of at M2, but no significant differences were found for these variations, and they were therefore omitted from further analysis. An Fe-rich alloy, Fe_7Pt, was modeled by substituting a single Pt atom into an 8 atom 2x2x2 supercell of the BCC Fe^0 structure. This structure is taken to be an approximate analog to platinum in the metallic core and antecedent metallic melts. We also examined the alloys PtFe and PtNi in order to examine the impact of the Pt/Fe ratio as well as the impact of Ni versus Fe, as both are present in the core. Table 4-2 lists all species examined, the source for the initial structure, and the method of optimization.

4.2.1. Determination of mass dependent component of fractionation

The first step in *ab initio* calculations is to determine optimized (relaxed) molecular and crystal structures. We used the Perdew, Burke, and Ernzerhof (PBE) functional (Perdew et al., 1996), a commonly used gradient corrected density functional that has been successfully used to calculate equilibrium isotope fractionations and isotope ordering phenomena (e.g., Schauble et al., 2006; Meheut et al. 2007).

The def2-TZVPP family of basis sets is used for all elements in vapor phase optimizations (Weigend and Alrichs, 2005); this family of basis sets is designed to yield approximately similar accuracies across a wide range of elements. This family of basis sets is available platinum group elements as well as lighter elements, making it possible to use the same family of basis sets as in Chapters 2 and 3 without having to substitute the older def-TZVP basis sets, as was the case for actinide elements. Basis sets were obtained via the Basis Set Exchange (https://www.basissetexchange.org) (Feller, 1996; Schuchardt et al., 2007; Pritchard et al., 2019). After optimizing the geometry of each molecule, vibrational frequencies are obtained by differentiation to determine the dynamical matrix, which can then be reused for isotopically substituted molecules. These isotopic frequencies are then used in the equation of Urey (1947) to obtain mass dependent fractionations for each species. Calculations were performed in the software Gaussian09 (Frisch, 2009) on the Hoffman2 cluster at UCLA.

For each Pt-bearing crystal, an initial guess structure is taken from literature x-ray diffraction studies (Table 4-2). Under periodic boundary conditions, the unit cell dimensions and atomic positions of each guess structure are allowed to vary within the model to reach the nearest local energy minimum. Projector Augmented Wave (Blöchl, 1994) basis sets with plane wave basis sets are used for all solids, as PAW data sets make it possible to simultaneously determine the electron density of each crystalline species via the method of Zwanziger (2009). PAW data sets are obtained from the AbInit JTH library (https://www.abinit.org/psp-tables) (Jollet et al., 2014). All calculations used a plane wave cutoff of 40 Hartree (1088 eV) and a Hubbard U parameter of 4.5 eV for Pt (Mkhonto and Ngoepe, 2021). These calculations are performed using the software AbInit (Torrent et al, 2008; Gonze et al., 2009).

The mass dependent component of fractionation for solids is determined using force constants acting on platinum in each structure, calculated directly via numerical differentiation following the method of Widanagamage et al. (2014), as adapted from Bigeleisen and Mayer (1947). In this formulation, one platinum atom is displaced slightly from its equilibrium position in each of three Cartesian directions. Due to the periodic boundary conditions, every atom of the same position in other unit cells is also perturbed. The Bigeleisen and Mayer (1947) derivation of this method formally assumes that only a single atom is perturbed in the entire solid, so high accuracy may require supercells for species with few atoms in their unit cells in order to more closely approximate the ideal single-atom displacement assumption. We use N=8 for native Pt and Pt-Fe alloys (i.e., 2x2x2 FCC or BCC supercells), N=12 for $PtAs_2$ and PtO_2, N=16 for PtS, N=20 for $CaPtO_3$, and N=28 for Pt-substituted olivine.

Although we use unscaled vibrational frequencies for the present calculations, the PBE functional is known to underestimate vibrational frequencies (Schauble, 2004; Mehuet et al., 2007). In order to estimate the likely errors associated with this systematic underestimation, a corrective scale factor was fitted via correlation of *ab initio* vibrational frequencies with infrared (IR) and Raman spectroscopy measurements of $PtCl_4^{2-}$ (Parker and Forsyth, 1998) and $PtCl_6^{2-}$ (Bridgeman, 2008) (Figure 4-3). The correlation indicates that the *in vacuo* PBE-based models underestimate measured (fundamental) vibrational frequencies by approximately 18 ± 2%. However, reconnaissance correlations of Raman spectra suggest the scale factor may be closer to unity for condensed or uncharged species, suggesting that 18% is conservative. At 300 K the expected fractionation between the species $PtCl_4^{2-}$ and $PtCl_6^{2-}$ is 0.72‰ using raw model vibrational frequencies, whereas 18% scaled frequencies yield 0.99 +/- 0.03‰. At 500 K, unscaled vibrational frequencies yield an estimated fractionation of 0.27‰, and scaled frequencies yield 0.37 +/- 0.01‰. At 1000 K, the calculated frequencies produce a fractionation of 0.07‰ while the scale factor-corrected frequencies produce a fractionation of 0.09‰. For the sake of simplicity, we will assume that errors of a similar magnitude could be present in the solid-state calculations as are present in the molecules modeled (Schauble and Young, 2021).

4.2.2 All-electron relativistic calculations and field shift component of fractionation

Field shift isotopic energy differences in vapor phase species are determined using all-electron relativistic calculations. These are performed at the coupled cluster level using the eXact 2-Component Hamiltonian (X2C) (Liu and Peng, 2009), which is an order of magnitude more computationally efficient than available 4-component Hamiltonian methods; a 2-component

Hamiltonian is sufficiently flexible that it can treat spin-orbit coupling (Saue, 2011), which has been important for comparisons to atomic spectra in pilot studies of the DFT-PAW method. All-electron calculations use uncontracted double-zeta quality relativistic Gaussian basis set for the central platinum atom (Dyall, 2007), and correlation-consistent non-relativistic basis sets (cc-pVDZ) for all other elements (Dunning et al., 1989; Woon and Dunning, 1993). Nuclear radii for Pt isotopes are tabulated from Angeli and Marinova (2013). The radii of platinum vary monotonically, with $\Delta\langle r^2\rangle$ increasing approximately 0.3-0.4 fm^2 per amu. By varying the nuclear charge radii for each isotope in an all-electron model, we can directly estimate the effects of nuclear size on electronic energies. The electronic energy difference is related to the equilibrium constant between the two isotopes of interest by $\Delta G = -RT\ln K$. All-electron relativistic calculations were all performed in the DIRAC software package (Saue et al., 2011).

The DFT-PAW method requires calibration of electron densities and isotopic energy differences which arise from varying the nuclear charge radius of the platinum atom. Projector Augmented Wave (Blöchl, 1994) basis sets with plane wave basis sets are taken from the AbInit JTH library (https://www.abinit.org/psp-tables) (Jollet et al., 2014). Electron densities for the calibration species are then determined using the post-processing method of Zwanziger (2009). All calculations used a plane wave cutoff of 40 Hartree (1088 eV) and a Hubbard U parameter of 4.5 eV for Pt (Mkhonto and Ngoepe, 2021) as in the case of the solid species. All PAW calculations used the software package AbInit (Torrent et al, 2008; Gonze et al., 2009).

Energy differences from the all-electron calculations are fit against the DFT-PAW electron densities via least-squares linear regression, and this calibration is then used to relate DFT-PAW electron densities to field shift isotopic energy differences. The calibration line for the Pt system can be seen in Figure 4-4. Of note is that the distribution is rather narrow, with a few species mainly determining the trendline slope: PtC (v), PtO_2 (v), and $Pt(OH)_2$ (v). By assuming that this calibration is applicable generally across platinum-bearing species, DFT-PAW model electron densities of both solids or vapor phase molecules can be converted into expected field shift components of fractionation.

For vapor phase species, we use geometries relaxed with at the PBE/def2-TZVP level as previously described, and determined the DFT-PAW electron densities on these structures without further relaxation under periodic boundary conditions. Each vapor phase molecules is placed in a cubic cell of ~12 Å side length in order to minimize inter-molecular interactions. Crystalline species are intrinsically periodic, so structural relaxation within the DFT-PAW method is more appropriate, and the electron density may be determined at each step during structural optimization. As discussed in Chapter 2 and 3, it is unlikely that the DFT-PAW electron densities calculated using structures optimized with plane wave basis sets will be greatly different than the corresponding electron density in structures optimized with the same functional and atom-centered basis sets. The effects of small differences in bond lengths between optimization methods on estimated field shift fractionations are unlikely to be as significant as redox state and bonding environment.

Differences in field shift between species control isotopic fractionation, and atomic Pt^0 is not a convenient reference for field shift estimates. Instead, we use crystalline native Pt as the reference for reporting isotopic fractionations in this study.

4.2.3. Determination of field shift effects in iridium

In order to get a broader picture of potential PGE isotope fractionation, preliminary calculations were also performed to estimate $^{193}Ir/^{191}Ir$ fractionations among a select group of iridium species. The initial structures for these species as well as the method of optimization are listed in Table 4-3. Unlike platinum and actinide molecules, using the PBE/def2-TZVP electronic structure models for structural relaxation of gas-phase Ir-bearing species produced inconsistent results for reasons that are not clear. Instead, optimized geometries for a small number of vapor phase species were obtained using the DFT-PAW method. As with DFT-PAW models of Pt-bearing molecules, each Ir-bearing molecule was placed in an otherwise empty cubic 22 a_0 (~12 Å) unit cell. The size of the cell was held fixed. After optimization, electron densities and force constants were determined in the same way as for platinum-bearing species.

^{193}Ir-Mössbauer isomer shift data for iridium-bearing solids are compiled from the literature (Wagner and Zahn, 1969; Wagner, 1981; Sawicki et al., 2010). For the species IF_6 and IF_5, we paired vapor phase molecular results with solid-state Mössbauer data, owing to the difficulty of obtaining well-converged relaxed crystal structures for these crystals. However, we believe that these solids are likely to have similar electron densities to their molecular equivalents because Mössbauer isomer shifts in the system are strongly correlated to oxidation state (Atzmony et al., 1967). As a point of comparison, the solid species K_2IrCl_6 has a DFT-PAW electron density of 449 e^-/a_0^3 , while the analogous molecular species $IrCl_6^{2-}$ has a DFT-PAW electron density of 441 e^-/a_0^3, a difference of 8 e^-/a_0^3 compared to changes of approximately 30-90 e^-/a_0^3 for Ir species of different oxidation states. For this reconnaissance study we neglected the Hubbard parameter in order to simplify calculations; the online database from The Materials Project (Jain et al., 2013) reports a small Hubbard U value of approximately 2.0 or less for tabulated models of iridium-bearing species. Previous calculations with uranium further indicate that the Hubbard U does not impact the field shift by much (see Chapter 2). Mössbauer isomer shifts were scaled to estimated field shift isotope effects by the method of

Schauble (2013; 2023). Briefly, this involves first converting isomer shifts from velocity units to energies via the relation below:

$$\Delta \mathrm{E}_{\mathrm{Isomer}} = \frac{h\nu_{\gamma}}{c} \Delta \mathrm{IS}$$

Where h is Planck's constant, ν_{γ} is the energy of the gamma radiation source used in the Mössbauer transition, c is the speed of light, and ΔIS is the isomer shift. Once converted, we then can use the ratio of the isotopic difference in ground-state nuclear mean-squared charge radii to the isomeric change in the mean-squared ^{193}Ir radius to scale from the isomer shift to the field shift via the following relation:

$$\Delta \mathrm{E}_{\mathrm{fs}} = \Delta \mathrm{E}_{\mathrm{isomer}} \frac{\Delta < \mathrm{r}^2 >_{\mathrm{isotope}}}{\Delta < \mathrm{r}^2 >_{\mathrm{isomer}}}$$

using the ratio of the $\Delta\langle r^2\rangle$ of the isotope pair from the nuclear charge radius database of Angeli (2004) to the $\Delta\langle r^2\rangle$ of the Mössbauer isomer shift calculated by Wagner et al. (1967). These values are, respectively, 0.041 fm^2, and 0.006 fm^2, resulting in a scale factor between the energy shifts of 6.4.

4.3. Results

Estimated equilibrium fractionation factors relative at 300 K, 500 K, and 1000 K are shown in Table 4-4. Table 4-5 shows polynomial fits for each species. This allows for the calculation of fractionation factors above temperatures of 250 K. The mass dependent component of fractionation versus reciprocal temperature is shown in Figure 4-5. The field shift component of fractionation versus reciprocal temperature is shown in Figure 4-6. The total fractionation versus reciprocal temperature is shown in Figure 4-7. All fractionations are calculated relative to native platinum.

As expected, the mass dependent component of fractionation generally results in higher ^{198}Pt/^{194}Pt in more oxidized species (Pt^{IV} vs. Pt^{II} vs. Pt^{0}). For instance, the Pt^{IV} complex $PtCl_6^{2-}$ is expected to have 1‰ higher ^{198}Pt/^{194}Pt than native Pt at 300 K. The solid Pt^{IV} species $PtO_{2\,(s)}$ is expected to be 2.7‰ heavier than native Pt, while the Pt-bearing perovskite structure $CaPtO_3$ is expected to be 1.93‰ heavier. For Pt^{II} species, the mass dependent component of fractionation versus native Pt ranges considerably, from 0.1-0.8‰. For the solid species containing Pt^{0}, both PtFe and PtNi have a mass dependent component of fractionation less than 0.1‰ at 300 K, relative to pure platinum, but the species Fe_7Pt has a mass dependent component of fractionation of 0.6‰. Mass dependent fractionation decreases rapidly at higher temperatures, with most Pt^{II} species fractionating less than 0.5‰ at 500 K and less than 0.1‰ at 1000 K relative to solid Pt, whereas the Pt^{IV} species PtO_2 (s) is still predicted to be 0.2‰ heavier than native Pt at 1000 K. The species Fe_7Pt displays a mass dependent fractionation of 0.3‰ at 500 K, and only 0.05‰ at 1000 K, while the other Pt^{0}-bearing species display minimal mass dependent fractionation relative to solid Pt at these temperatures.

Field shift fractionations are generally predicted to be modest, with a few exceptions, and do not appear to vary systematically with oxidation state. Both Pt^{II} and Pt^{IV} species display field shift effects ranging from -0.2‰-0.1‰ at 300 K, relative to native Pt. The exceptions are the Pt^{II}-bearing crystals cooperite (PtS), sperrylite ($PtAs_2$), and Pt^{II}-substituted olivine, as well as the Pt-Fe alloys. For cooperite and sperrylite, the field shift component of fractionation results in a slightly lower ^{198}Pt/^{194}Pt than mass dependent fractionation alone would predict. The field shift effects are on the order of ~-0.2‰ at 300 K, ~-0.1‰ at 500 K, and less than -0.1‰ at 1000 K. However, these minerals are still predicted to have higher ^{198}Pt/^{194}Pt than native Pt throughout the temperature range modeled, owing to a much stronger mass dependent effect. Pt-substituted olivine displays the largest field shift effects of all: 0.5‰ at 300 K, 0.3‰ at 500 K, and 0.1‰ at 1000 K. Solid alloys containing Fe or Ni in addition to Pt^0 result in a field shift of -0.2 to -0.3‰ versus native Pt at 300 K, -0.1 to -0.2‰ at 500 K, and ~-0.1‰ at 1000 K.

Figure 4-8 shows DFT-PAW electron density versus the energy shift calculated via Mössbauer isomer shifts for ^{193}Ir. Isotope shifts estimated from scaled Mössbauer isomer shifts are shown in Table 4-6 and Figure 4-9. Isomer shifts are strongly correlated with DFT-PAW electron densities ($R^2 \approx 0.95$), indicating that both methods give a consistent picture of the relative sense of field shift fractionations among the species studied.

4.4. Discussion

4.4.1. Sources of uncertainty

The standard error for the slope of the ^{198}Pt/^{194}Pt calibration line in Figure 4-4 is 3 e^-/a_0^3 per J/mol, or about 8%. Examining a sample field shift component of fractionation between $PtCl_4^{2-}$ and $PtCl_6^{2-}$, we find that this propagates to an uncertainty in estimated fractionation at 300 K of +/- 0.01‰ out of a calculated 0.09‰ fractionation. Using this standard error to examine the field shift component of fractionation between the metallic core analog Fe_7Pt and possible silicate mantle analog Pt-substituted olivine at high temperature, we find the range of possible fractionation to be 0.57 +/- 0.04‰, 0.28 +/- 0.02‰, and 0.09-0.10‰ at temperatures of 500 K, 1000 K, and 3000 K, respectively. The slope of the calibration line is also impacted by the choice of nuclear charge radii. Using the radii of Nadjakov et al. (2015) or Fricke and Heilig (2004) instead of Angeli (2004), we find that the slope of the calibration line decreases by 10%. Using the radii of Angeli and Marinova (2013) we find that the slope decreases by 3% relative to Angeli (2004). For the field shift between $PtCl_4^{2-}$ and $PtCl_6^{2-}$ at 300 K, choosing the radii of

Nadjakov et al. (2015) or Fricke and Heilig (2004) instead of Angeli (2004) decreases the fractionation by 0.01‰, while choosing the radii of Angeli and Marinova (2013) results in a negligible change. Using the radii of Nadjakov et al. (2015) or Fricke and Heilig (2004) in place of Angeli (2004), the field shift fractionation between Fe_7Pt and Pt-substituted olivine decreases by 0.06‰ at 500 K, 0.03‰ at 1000 K, and 0.01‰ at 3000 K. Using the radii of Angeli and Marinova (2013) results in this field shift fractionation decreasing by 0.02‰ at 500 K, 0.01‰ at 1000 K, and < 0.01‰ change at 3000 K.

Obtaining a realistic structure for Pt within a silicate is another source of uncertainty. There are few platinum species in which platinum bonds to oxygen, and none for the Pt^{II} oxidation state. Platinum does not easily substitute for any of the common ions in mafic silicate minerals. This represents a challenge in obtaining a realistic coordination environment. Farges et al. (1996) studied synthetic glasses with XAFS spectroscopy, and found that Pt^{IV} was the primary oxidation state. Pt^{IV} was found to occur in an octahedral bonding environment under these conditions. This coordination also occurs in the solid Pt^{IV} species PtO_2 in the present study, for instance Muller and Roy (1968). However, Pt^{IV} is unlikely to be relevant at the oxygen fugacities expected during core-mantle differentiation (Li and Agee, 2001). We modeled Pt^{II} substitution into +2 cation (Mg) sites in multiple mafic silicate minerals, including multiple cation sites within the same minerals, but were unable to unambiguously achieve octahedral coordination within these structures. Instead, the coordination structures were distorted, with notably unequal bond lengths. This is consistent with the well-known square-planar coordination found in many Pt^{II}-species. However, we did observe that as substitution sites approaches a more regular 6-fold coordination, calculated electron density appears to decrease. The most octahedral-like coordination structures were obtained for forsterite and fayalite. In these models, four of the bonds were approximately 2.1 Å in length, while two other potential Pt-O bonds were approximately 2.5Å. This highly distorted geometry cannot unambiguously be categorized as either a 4-fold or 6-fold coordination and does not closely resemble a square planar or octahedral geometry. DFT-PAW calculations for Pt^{II}-substituted in Mg in diopside and clinoenstatite, and for Fe in ferrosilite all indicate an electron density of approximately 2630 e^{-}/a_0^3. For these structures, three bonds were approximately 2.1Å in length while two bonds were approximately 2.5Å. These highly distorted structures also do not closely resemble either octahedral or square planar geometries, and with these bond lengths it is not clear if the coordination is three-fold or five-fold. These structures, if they are more representative of silicate-hosted platinum than Pt-substituted olivine, would lower the overall equilibrium fractionation between the metallic core and the silicate mantle by 0.01-0.02‰ at 3000 K. Additional constraints on the speciation and coordination of platinum in melts may help to better predict the expected fractionation, as well as analysis of different melt or mantle analog structures.

4.4.2. Systematics of platinum isotope fractionation

Platinum isotope fractionation for geologically and environmentally relevant species is predicted to be dominantly mass dependent at all temperatures studied. This is true regardless of the state of matter being modeled or the oxidation state of platinum. This contrasts with U, Tl, Hg, and Eu, where the equilibrium field shift effect is usually greater than the mass dependent component of fractionation. It is broadly similar to the behavior of Re, however.

We find only small field shift fractionations in the Pt^{IV} solids PtO_2 and $CaPtO_3$ relative to native Pt at any temperature above 300 K, in contrast to significant mass dependent fractionation between these species. For the solid Pt^{II} species studied, the field shift component of fractionation versus native Pt is potentially significant between 300 and 500 K, and even to higher temperatures for Pt-substituted olivine species with silicate species having high $^{198}Pt/^{194}Pt$ due to the field shift effect, whereas the other Pt^{II} solids are predicted to be lower. For the solid Pt minerals cooperite and sperrylite, which are economically significant, the field shift component of fractionation relative to native Pt metal at 300 K is larger than current estimates of measurement uncertainty for the Pt system from Creech et al. (2014; 2017), suggesting potentially measurable non-mass dependent fractionations. Predicted $^{198}Pt/^{194}Pt$ fractionations are above 0.08‰ up to hydrothermal temperatures of 500 K, with the field shift component of fractionation making both species ~0.1‰ more depleted in $^{198}Pt/^{194}Pt$ than the purely mass dependent component of fractionation would predict. However, at the temperatures relevant for core-mantle equilibration, e.g. 1500-3000 K (Wood et al. 2006), these field shifts are likely to be modest, -0.04 to -0.03‰ at 1500 K and declining to -0.02 to -0.01‰ at 3000 K. Pt-substituted olivine, however, does display a markedly lower electron density than all other species modeled, and is therefore expected to be most enriched in larger, high-mass platinum isotopes in contrast to the other Pt^{II} solids, and thus in net heavier that native Pt at all temperatures. Relative to native Pt this species has field shift components of $^{198}Pt/^{194}Pt$ fractionation of 0.45‰, 0.27‰, and 0.13‰ at temperatures of 300 K, 500 K, and 1000 K. At 3000 K, Pt-substituted olivine retains a field shift effect of +0.04‰.

The highest electron densities at nuclei calculated among crystals in this study are found in metallic species with Pt^0 substituted into iron- or nickel-rich alloys. It appears that increasing the ratio of Fe to Pt in intermetallic structures results in a higher electron density and therefore a lower equilibrium $^{198}Pt/^{194}Pt$. For instance, the solid PtFe has a field shift component of $^{198}Pt/^{194}Pt$ fractionation of -0.30‰, -0.18‰, and -0.09‰ relative to native Pt. The species PtNi has field shift components of $^{198}Pt/^{194}Pt$ fractionation of -0.19‰, -0.11‰, and -0.06‰. The highest electron density, and therefore lightest isotopic composition, is expected for the solid Fe_7Pt. This species has a predicted field shift $^{198}Pt/^{194}Pt$ fractionation of -0.50‰, -0.30‰, and -0.15‰. This suggests that higher ratios of iron to platinum in a metallic solid will result in a more significant field shift effect relative to other likely coexisting species, and that nickel is likely to have a similar effect. We speculate that trace platinum in an iron-rich liquid metal, such as the material feeding into a growing planetary core, would behave similarly to Fe_7Pt.

This observation is analogous to the difference in the isomer shift that is seen in Mössbauer data of platinum impurities in solid iron, as well as for iron impurities in solid platinum (Benczer-Koller, 1971; Wolbeck and Zioutas, 1971; Dubiel, 1987). These studies indicate a more negative isomer shift in ^{195}Pt with an increasing ratio of Fe to Pt. Wolbeck and Zioutas (1971) report an ^{195}Pt 130keV-isomer shift of -2.37 mm/s in a Pt-Fe alloy of approximately 10% Pt. Benczer-Koller (1971) observed using 99 keV gamma radiation that an alloy of 3% platinum resulted in an isomer shift of approximately -2 mm/s, while the presence of Ni in place of Fe results in a similar shift relative to pure platinum. These differences are larger than redox-related variations between pure platinum, Pt^{II}, and Pt^{IV} species (Agresti et al., 1967), highlighting the strong effect of alloy composition on potential field shift fractionations.

Partial cancellation of opposing field shift and mass-dependent components of fractionation results in unusual temperature dependences of several species' overall fractionations. For instance, the Pt^0-bearing solid Fe_7Pt is expected to have higher $^{198}Pt/^{194}Pt$ than solid native Pt until the fractionation disappears at ~500 K; at higher temperatures the field shift component of fractionation dominates the mass dependent fractionation and results in this species having lower $^{198}Pt/^{194}Pt$ than native Pt by up to -0.1‰. The other Pt^0-bearing alloys PtFe and PtNi have almost no mass dependent fractionation relative to native Pt, but the field shift component of fractionation results in these species having lower $^{198}Pt/^{194}Pt$ at all temperatures. Pt-substituted olivine is similar to other Pt^{II}-bearing species with respect to the mass dependent component of fractionation, but its much greater field shift effect compared to other species results in this species having the highest $^{198}Pt/^{194}Pt$ of all species at temperatures exceeding 1500 K.

4.4.3. Applications of platinum isotope geochemistry

One potential use of platinum isotope measurements is testing different models for the PGE anomaly of Earth's silicate reservoir. We propose that the iron-rich species Fe_7Pt may be a reasonable analogue to the metallic liquid present during equilibration of metal and silicate as the Earth's core formed. This phase is predicted to have a strong field shift component of fractionation that will make it depleted in high-neutron number platinum isotopes (e.g., having low $^{198}Pt/^{194}Pt$), relative to other phases. While most Pt^{II} solids are predicted to display only slight field shift fractionation relative to Pt^0-bearing species at temperatures relevant to core-mantle equilibration, Pt-substituted olivine is predicted to have a larger (but still subtle) field shift fractionation versus Pt^0-bearing species, especially when compared to Fe_7Pt. It is not clear what drives this behavior, but it is possible that platinum bonded to the orthosilicate anion SiO_4^{4-} in particular tends to have lower electron densities. In contrast, the Pt^{IV} species PtO_2 has nearly the same electron density as native platinum while having a higher coordination number (CN=6) than Pt-substituted olivine, so it is not merely the presence of oxygen as a bonding partner or octahedral coordination that is driving the field shift effect. Furthermore, other Pt^{II}-bearing solids are predicted to have lower $^{198}Pt/^{194}Pt$ than native platinum, so this is not simply a redox effect. This observation, along with the observation of a higher electron density for Pt in Pt-Fe alloys, is consistent with Mössbauer data in suggesting that bonding environments for Pt, especially in alloys, can produce differences in electron density that are even larger than the difference observed between species of different oxidation states.

For an equilibrium fractionation at 3000 K, Pt-substituted olivine is predicted to have 0.09‰ higher ^{198}Pt/^{194}Pt than Fe_7Pt. However, it is uncertain at present if the Pt-substituted olivine species is a proper analog for the bonding environment of Pt during core-mantle differentiation, since it has been observed that Pt does not tend to incorporate into silicate structures at low temperatures (Hagen, 1954) and instead prefers sulfides or metallic phases (Lorand et al., 2010). In melts, it is expected that Pt will bond to ligands such as As, S, and Te, as well as platinum PGE alloys and nonbridging oxygens (Helmy et al., 2020). Studies of Pt in reduced melts have hypothesized that Pt^0, Pt-silicide, and even negatively charged Pt^- may exist (Amosse and Allibert, 1993; Bennett et al., 2014; Medard et al., 2015). Pt^- and Pt-silicide are beyond the scope of the present reconnaissance study. Pt^I has also been proposed to occur in silicate melts that have higher concentrations of S^{2-} (Wang and Li, 2023) though there is little to no data on analogous crystalline Pt^I species. In this study it was also posited that sulfide may have a greater effect on PGE partitioning than fO_2, which previous studies had not considered in detail. Therefore it seems reasonable that platinum sulfide species, as well as native Pt, are also potential analogs for the bonding environment of platinum in silicate melt during core-mantle differentiation. Cooperite (PtS) has an expected equilibrium ^{198}Pt/^{194}Pt fractionation versus Fe_7Pt of 0.03‰ at 3000 K, while native Pt has a very similar expected fractionation of 0.04‰ versus Fe_7Pt at 3000 K.

A Rayleigh distillation model can be applied to make a simplified estimate the expected isotopic composition of the silicate mantle under the end-member assumption of equilibrium partitioning in a system that is closed with respect to material addition. The fractionation between Fe_7Pt and Pt-substituted olivine is used to illustrate the most extreme variation possible driven by relevant species in this study (Figure 4-10). In this model we assume a homogeneous, initially chondritic mantle, from which Pt is fractionally and irreversibly removed into the core. By most estimates, >99% of the PGEs would be sequestered into the core during closed-system core-mantle differentiation, with metal-silicate partition coefficients of 10^2-10^4 at appropriate temperatures (1400-1600 ℃) and pressures (0.5-0.14 GPa) (Ertel et al., 2006). We can compare this model to the observations of Creech et al. (2017). They reported an average post-Archean mantle with $^{198}Pt/^{194}Pt$ of -0.11‰. The average chondrite value was -0.14‰. They find that the Archean mantle ranges from 0.27-0.46‰. The isotopic difference between the primitive mantle and the post-Archean mantle is therefore ~0.4-0.6‰. Assuming the largest predicted fractionation of 0.09‰ between an iron core and a Pt- substituted olivine as an analog for the silicate mantle at 3000 K, the residual mantle would have an isotopic composition between 0.4-0.6‰ when 0.1-1.0% chondritic Pt remains in the silicate mantle. If a 0.04‰ fractionation between native Pt and Fe_7Pt is assumed instead, the measured post-Archean mantle value is only achieved when 0.00003% to 0.004% of platinum remains in the silicate mantle. Finally, assuming fractionation of 0.03‰, as between cooperite and Fe_7Pt, the isotopic composition of the Archean mantle is achieved when 0.0000002% to 0.00003% of Pt is remaining. In the absence of a late veneer, approximately 99% depletion of Pt in the mantle during core formation is needed to explain the modern composition, which would be more consistent with the Pt-olivine analogue model than either the sulfide or native-Pt scenarios. It remains uncertain which species or combination of species would best reproduce the isotopic composition of the primitive mantle, but the present study provides evidence that primarily as a consequence of the nuclear field shift effect, it is possible to reproduce the fractionated Pt-isotope compositions of the mantle determined by Creech et al. (2017) with a closed-system Rayleigh fractionation model.

The field shift component appears unlikely to be a large contributor to the isotopic fractionation of dissolved platinum adsorbing on to Fe-Mn oxides, as investigated in the experiments of Corcoran (2016). At 300 K, the field shift may result in the Pt^{II} species $PtCl_4^{2-}$ having 0.1‰ higher $^{198}Pt/^{194}Pt$ than a purely mass dependent fractionation with the Pt^{IV} species $PtCl_6^{2-}$ would yield. The speciation of Pt^{IV} adsorbed on to the Fe-Mn hydroxides in the experiments of Corcoran (2016) is not clearly known, but neither the $PtCl_6^{2-}$ nor the solid species PtO_2 would be expected to have a strong field shift fractionation relative to $PtCl_4^{2-}$, the dominant species in seawater. Instead, mass dependent fractionation is expected to dominate in these environments. We predict an overall equilibrium fractionation of 0.64‰, while the experiments of Corcoran (2016) indicate a fractionation of 0.4‰ between seawater and adsorbed Pt, in qualitative agreement with the model results.

4.4.4. Systematics of iridium fractionation

Initial calculations for Ir-isotope ($^{193}Ir/^{191}Ir$) fractionation suggest that they are similar in magnitude to $^{198}Pt/^{194}Pt$. As analogues for chlorides of Ir^{III} and Ir^{IV} at ~298 K, the predominant species in natural waters (Anbar et al., 1996), we estimate field shift fractionations of ~0.06-0.08‰ between the solid species K_3IrCl_6 and K_2IrCl_6, with the Ir^{III}-bearing K_3IrCl_6 species having higher $^{193}Ir/^{191}Ir$. This is similar in magnitude to the field shift of 0.1‰ observed between $PtCl_4^{2-}$ and $PtCl_6^{2-}$. Relative to native Ir, the Ir^{III} species are expected to have a positive field shift fractionation, raising $^{193}Ir/^{191}Ir$ 0.12-0.14‰ higher, while Ir^{IV} species range from +0.06‰ - +0.08‰ relative to native Ir at 298 K. Though less significant in natural environments, the Ir^{V} oxidation state represented by the model species IrF_5 shows a negligible field shift isotope fractionation relative to native Ir. The Ir^{VI} species IrF_6 has a negative field shift fractionation of -0.09‰. The iridium system is particularly useful in that it is possible to examine a wider array of oxidation states than platinum. Here, species with low positive oxidation states are predicted to have lower electron densities than native Ir, and higher oxidation states may be more similar in electron density to native Ir. The present reconnaissance study suggests that successively higher oxidation states are characterized by higher electron densities, and native metals may be more similar in electron density to higher oxidation states. Again, platinum exhibits similar behavior, with Pt^{IV} solids having similar electron density to native Pt.

Based on Mössbauer data, it is possible to infer that Ir and Pt are also likely to behave similarly in metal alloys. Wagner et al. (1977) found a strong correlation in isomer shifts for multiple Mössbauer-active PGEs substituted into alloys, suggesting that the systematics of Ir, Pt, and periodic table-adjacent metals should be similar. An isomer shift occurs in Ir impurities located within a Fe-BCC solid (Mössbauer et al., 1971; Blachkowski et al., 2008) with a ^{193}Ir shift of 1.03 mm/s for and Fe-dominated Ir-Fe alloy consisting of 0.7% Ir, for example, but a smaller shift of 0.60 mm/s for an Ir-rich alloy consisting of 53.6% Ir (Mössbauer et al., 1971). These isomer shifts correspond to $^{193}Ir/^{191}Ir$ shifts of -0.16‰ and -0.09‰ relative to native Ir, respectively. Therefore a field shift effect for Ir isotopes within Fe-bearing alloys, similar to Pt isotopes in Pt-Fe alloys, is expected, and this fractionation appears to scale with a higher Fe/Ir to some extent. However, compared to the field shift effect for Fe_7Pt alloy relative to native Pt, this fractionation is less significant (-0.16‰ vs. -0.50‰). With further development of this isotope system, other similar patterns of isotope fractionation may be expected in the Ir system as in the Pt system.

4.5. Conclusion

For most species modeled, the field shift component of ^{198}Pt/^{194}Pt fractionation is modest or insignificant at temperatures between 300 and 3000 K. Pt^{0} and Pt^{IV} species are generally predicted to have similar electron densities and therefore minimal field shift fractionation effects, but Pt^{II} species may display modest field shift fractionation effects at a variety of temperatures. At hydrothermal temperatures up to 500 K, the minerals sperrylite and cooperite display field shifts of ~-0.1‰ versus native Pt in the opposite direction of their mass dependent components of fractionation. While it is currently unclear what species is relevant for modeling the platinum carrier within the silicate component during core-mantle differentiation, we find that a hypothetical Pt^{II}-substituted olivine as a possible analogue for a silicate bonding environment (olivine) would measurably fractionate to higher ^{198}Pt/^{194}Pt relative to a Pt-bearing iron core at equilibration temperatures up to 3000 K, owing to the field shift effect. We predict that a batch equilibration scenario at this temperature would leave the mantle isotopically heavier than the core by 0.09‰. In a Rayleigh fractionation model, using Pt-substituted olivine to represent the silicate relative with an iron-rich core yields a mantle vs. chondrite ^{198}Pt/^{194}Pt signature consistent with measurements of the Archean mantle by Creech et al. (2017). With native Pt, or PtS as the silicate analogue, fractionations would be smaller and appear unlikely to create the observed signature unless extreme PGE abundance depletions are achieved. The field shift is not expected to contribute significantly to isotopic fractionation between aqueous Pt in the oceans (dominated by Pt^{II} species) and Pt^{IV} adsorbed to Fe-Mn oxides. The Ir-isotope system appears to display generally similar systematics and fractionation magnitudes to the Pt system.

Tables

Table 4-1: Properties of the platinum group elements (PGEs), adapted from Mondal (2011). (Sources: Cabri, 1981; Buchanan, 1988; Cabri et al., 2002)

Element	Atomic number	Atomic weight	Melting temperature (K)	Density (g/cm^3)	Common minerals
Ru	44	101	2607	12.4	Laurite (RuS_2)
Rh	45	102	2239	12.4	Hollingworthite (RhAsS)
Pd	46	107	1825	12.0	Kotulskite (PdTe), Braggite (Pt,Pd)S, Merenskyite ($PdTe_2$)
Os	76	190	2973	22.7	Erlichmanite (OsS_2)
Ir	77	193	2727	22.6	Irarsite (IrAsS)
Pt	78	195	2042	21.5	Cooperite (PtS), Braggite (Pt,Pd)S, Sperrylite ($PtAs_2$), Moncheite ($PtTe_2$)

Table 4-2: Structure references and method of optimization for all Pt-bearing compounds studied. Vapor phase species were constructed manually using symmetries and bond lengths from cited studies. PBE-PAW method of structure optimization refers to use of PBE functional (Perdew et al., 1998) and projector-augmented-wave basis sets (Blöchl, 1994) with periodic boundary conditions as described in the methods section, while PBE-def2-TZVPP refers to use of PBE functional and Gaussian atom-centered basis sets (Weigend and Alrichs, 2005).

Species	Structure reference	Method of structure optimization
$Pt_{(s)}$	Wyckoff (1963)	PBE-PAW
BCC-$Fe_7Pt_{(s)}$	Adapted from Wilburn and Bassett (1978) as described in text	PBE-PAW
$PtFe_{(s)}$	Bayliss (1990)	PBE-PAW
$PtNi_{(s)}$	Bayliss (1990)	PBE-PAW
Pt-substituted olivine	Adapted from Bostrom (1987) as described in text	PBE-PAW
$PtS_{(s)}$ - cooperite	Rozhdestvina et al. (2008)	PBE-PAW
$PtAs_{2\,(s)}$ - sperrylite	Furuseth et al. (1965)	PBE-PAW
$CaPtO_{3\,(s)}$	Ohgushi et al. (2008)	PBE-PAW
$PtO_{2\,(s)}$	Muller and Roy (1968)	PBE-PAW
$PtCl_2(H_2O)_2$	Adapted from Deeth and Elding (1996)	PBE-def2-TZVPP
$PtCl_2$	Adapted from Deeth and Elding (1996) and Tagirov et al. (2019)	PBE-def2-TZVPP
$PtCl_4^{2-}$	Adapted from Trevino and Ermler (2023)	PBE-def2-TZVPP
$PtBr_4^{2-}$	Adapted from Kroening et al. (1974)	PBE-def2-TZVPP
$Pt(OH)_2$	Adapted from Li et al. (1992)	PBE-def2-TZVPP
cis-$PtCl_2(NH_3)_2$	Adapted Carloni et al., (1995)	PBE-def2-TZVPP
trans-$PtCl_2(NH_3)_2$	Adapted from Carloni et al. (1995)	PBE-def2-TZVPP
$PtCl_4$	Adapted from Chen et al. (2009)	PBE-def2-TZVPP
$PtCl_6^{2-}$	Adapted from Lienke et al. (2001)	PBE-def2-TZVPP
PtO_2	Adapted from Lu and Wang (2024)	PBE-def2-TZVPP
PtC	Adapted from Beaton and Steimle (1999)	PBE-def2-TZVPP

Table 4-3: Structure references and method of optimization for all Ir-bearing compounds studied. Vapor phase species were constructed manually using symmetries and bond lengths from cited studies. PBE-PAW method of structure optimization refers to use of PBE functional (Perdew et al., 1998), projector-augmented-wave basis sets (Blöchl, 1994) and periodic boundary conditions as described in methods; of note is that in contrast to Pt, the vapor phase species IrF_5 and IrF_6 were optimized using plane wave basis sets and allowing the atoms to move freely in a locked cubic unit cell with length of 12 Å.

	Structure reference	Method of structure optimization
K_3IrCl_6	Coll et al. (1987)	PBE-PAW
K_2IrCl_6	Griffiths et al. (1959)	PBE-PAW
IrO_2	Bolzan et al. (1997)	PBE-PAW
IrF_5	Adapted from Lu et al. (2022)	PBE-PAW
IrF_6	Adapted from Lu et al. (2022)	PBE-PAW

Table 4-4: ^{198}Pt/^{194}Pt fractionations relative to native Pt, alongside the electron density of each species. For native Pt, ln β_{300K} = 0.82‰, ln β_{500K} = 0.29‰, and ln β_{1000K} = 0.07‰, and the DFT-PAW electron density is 2553 e^-/a_0^3.

Species	Mass dependent component of ^{198}Pt/^{194}Pt fractionation (ln α_{md}) at 300 K, 500 K, and 1000 K (‰)	Field shift ^{198}Pt/^{194}Pt fractionation at 300 K, 500 K, and 1000 K (‰)	Total ^{198}Pt/^{194}Pt fractionation at 300 K, 500 K, and 1000 K (‰)	DFT-PAW electron density (e^-/a_0^3)
BCC-Fe_7Pt (s)	0.92	-0.50	0.42	2598
	0.33	-0.30	0.03	
	0.08	-0.15	-0.07	
PtFe (s)	0.08	-0.30	-0.22	2580
	0.03	-0.18	-0.15	
	0.01	-0.09	-0.08	
PtNi (s)	0.09	-0.19	-0.10	2570
	0.03	-0.11	-0.08	
	0.01	-0.06	-0.05	
Pt-substituted olivine	0.33	0.45	0.78	2513
	0.12	0.27	0.39	
	0.03	0.13	0.16	
Cooperite – PtS (s)	0.43	-0.15	0.29	2566
	0.16	-0.09	0.07	
	0.04	-0.04	0.00	
Sperrylite – $PtAs_2$ (s)	0.52	-0.22	0.30	2573
	0.19	-0.13	0.05	
	0.05	-0.07	-0.02	
$CaPtO_3$ (s)	1.96	-0.02	1.93	2555
	0.70	-0.01	0.69	
	0.18	-0.01	0.17	
PtO_2 (s)	2.70	0.00	2.70	2553
	0.97	0.00	0.97	
	0.24	0.00	0.24	
$PtCl_2(H_2O)_2$	0.85	0.07	0.92	2568
	0.33	0.04	0.37	
	0.09	0.02	0.11	
$PtCl_4^{2-}$	0.27	0.10	0.36	2544
	0.10	0.06	0.16	
	0.03	0.05	0.03	
cis-$PtCl_2(NH_3)_2$	0.80	-0.02	0.78	2555
	0.30	-0.01	0.29	
	0.08	0.00	0.07	
trans-$PtCl_2(NH_3)_2$	0.95	-0.03	0.91	2556
	0.38	-0.02	0.36	
	0.10	-0.01	0.09	
$PtCl_4$	0.46	-0.20	0.26	2571
	0.18	-0.12	0.06	
	0.05	-0.06	-0.01	
$PtCl_6^{2-}$	0.99	0.00	1.00	2553
	0.37	0.00	0.37	
	0.09	0.00	0.09	

Table 4-5: Polynomial fits of calculated $^{198}Pt/^{194}Pt$ fractionation factors relative to native Pt, in the form $1000\ln\alpha_{total} = A_1/T^2 + A_1/T^4 + C/T$, with the first two constants corresponding to the mass dependent component of fractionation and the last constant corresponding to the nuclear field shift. Fits are constrained at temperatures from 250 K-3000 K.

Species	A_1	A_2	C
BCC-$Fe_7Pt_{(s)}$	8.29×10^4	1.40×10^{-3}	-149.78
$PtFe_{(s)}$	7.22×10^3	7.47×10^{-4}	-90.00
$PtNi_{(s)}$	8.44×10^3	1.33×10^{-4}	-56.77
Pt-substituted olivine	3.01×10^4	6.26×10^{-4}	134.49
$PtS_{(s)}$ - cooperite	3.89×10^4	1.04×10^{-3}	-43.71
$PtAs_{2\ (s)}$ - sperrylite	4.69×10^4	8.13×10^{-4}	-66.93
$CaPtO_{3\ (s)}$	1.76×10^5	2.25×10^{-4}	-7.16
$PtO_{2\ (s)}$	2.43×10^5	1.05×10^{-3}	0.17
$PtCl_2(H_2O)_2$	8.62×10^4	-8.63×10^8	20.39
$PtCl_4^{2-}$	2.65×10^4	-2.00×10^8	28.60
cis-$PtCl_2(NH_3)_2$	7.81×10^4	-5.90×10^8	-4.73
trans-$PtCl_2(NH_3)_2$	9.86×10^4	-1.17×10^9	-10.19
$PtCl_4$	4.75×10^4	-5.19×10^8	-60.47
$PtCl_6^{2-}$	9.36×10^4	-3.87×10^8	1.47

Table 4-6: Mössbauer isomer data, isotope shifts, and DFT-PAW electron density for select Ir-bearing solids. Isotope shifts are calculated according to the method of Schauble (2013; 2023).

Species	Oxidation state	Isomer shift relative to native Ir (mm/s)	$^{193}Ir/^{191}Ir$ field shift relative to native Ir (‰)	$^{193}Ir/^{191}Ir$ field shift relative to native Ir, per fm^2 (‰)	DFT-PAW electron density (e^-/a_0^3)
K_3IrCl_6	+3	-2.26 (Wagner and Zahn, 1970)	0.14	3.35	386
K_2IrCl_6	+4	-0.95 (Wagner and Zahn, 1970)	0.06	1.41	449
IrO_2	+4	-0.84 (Sawicki et al., 2010)	0.05	1.24	460
IrF_5	+5	0.06 (Wagner and Zahn, 1970)	0.00	-0.09	543
IrF_6	+6	1.45 (Wagner and Zahn, 1970)	-0.09	-2.15	577

Figures

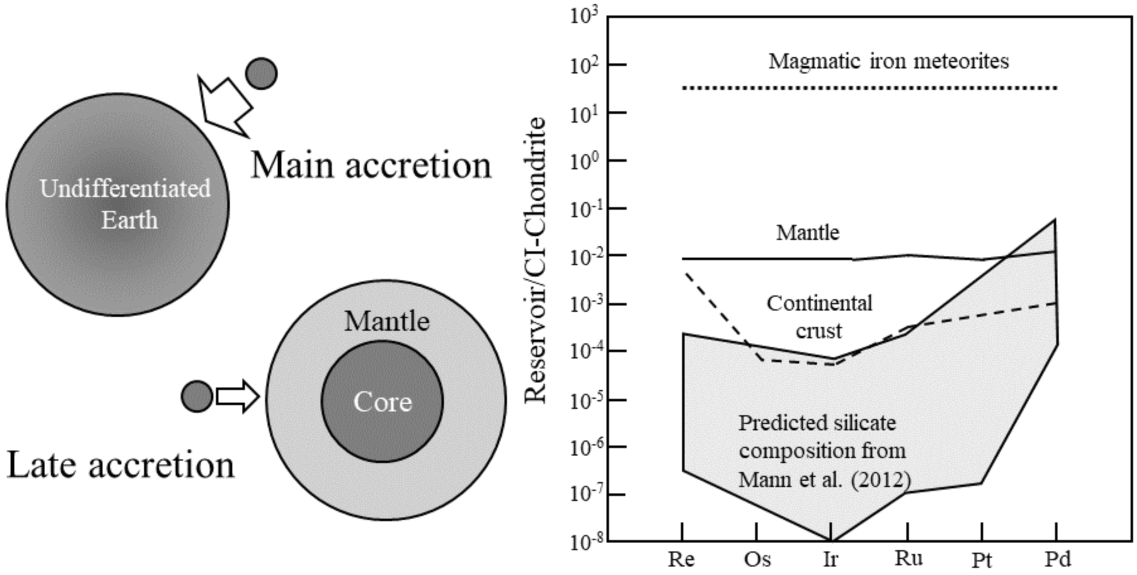

Figure 4-1: Schematic illustrating the late veneer theory, wherein after Earth's core-mantle differentiation is largely complete, additional chondritic material is added to the mass of the mantle. Also displayed are the observed and experimental abundances of the PGEs relative to CI-chondrites, indicating that experiments cannot reproduce mantle values. Adapted from Day et al. (2016)

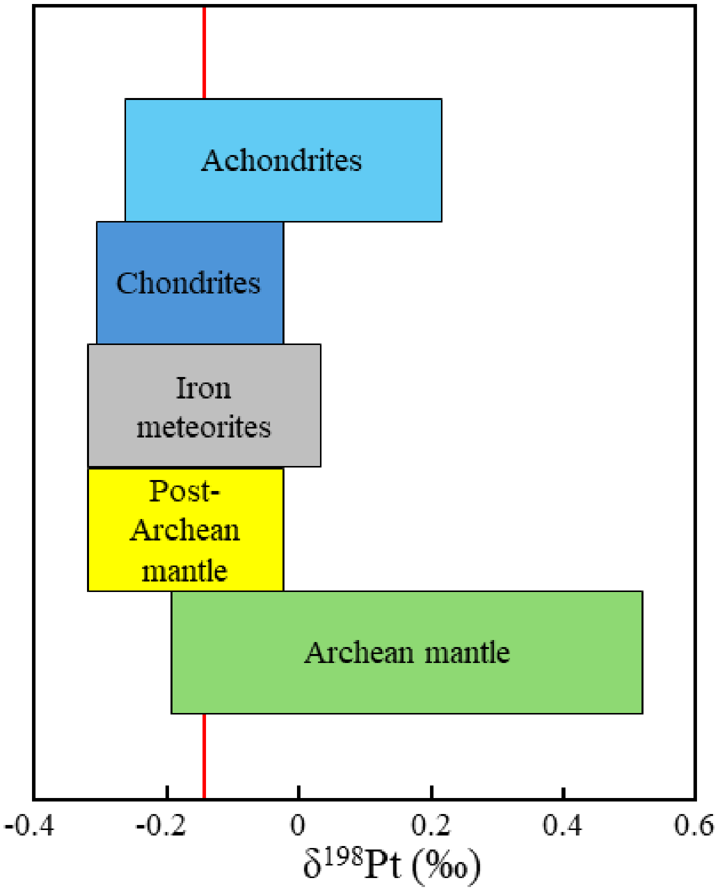

Figure 4-2: Adapted from Creech et al. (2017). $\delta^{198/194}$Pt is displayed for the Archean mantle, post-Archean mantle, iron meteorites, chondrites, and achondrites. The red line represents the mean chondritic value.

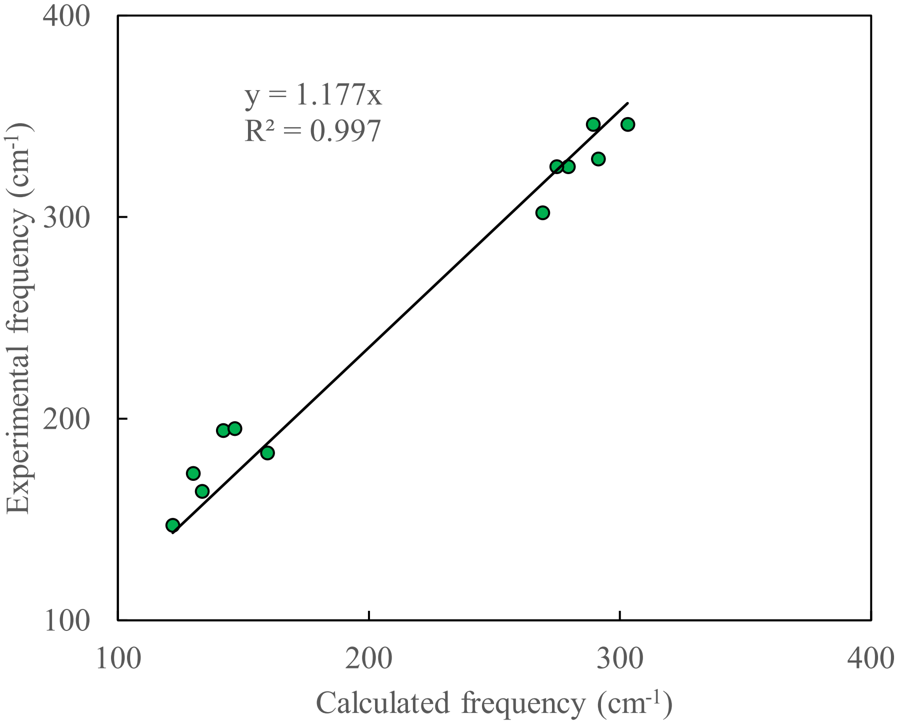

Figure 4-3: Measured vibrational frequencies from Raman and infrared spectroscopy vs. model frequencies for the species $PtCl_4^{2-}$ and $PtCl_6^{2-}$. Experimental data from Parker and Forsyth (1998) and Bridgeman (2008) respectively. All model frequencies are calculated at the PBE/def2-TZVPP level.

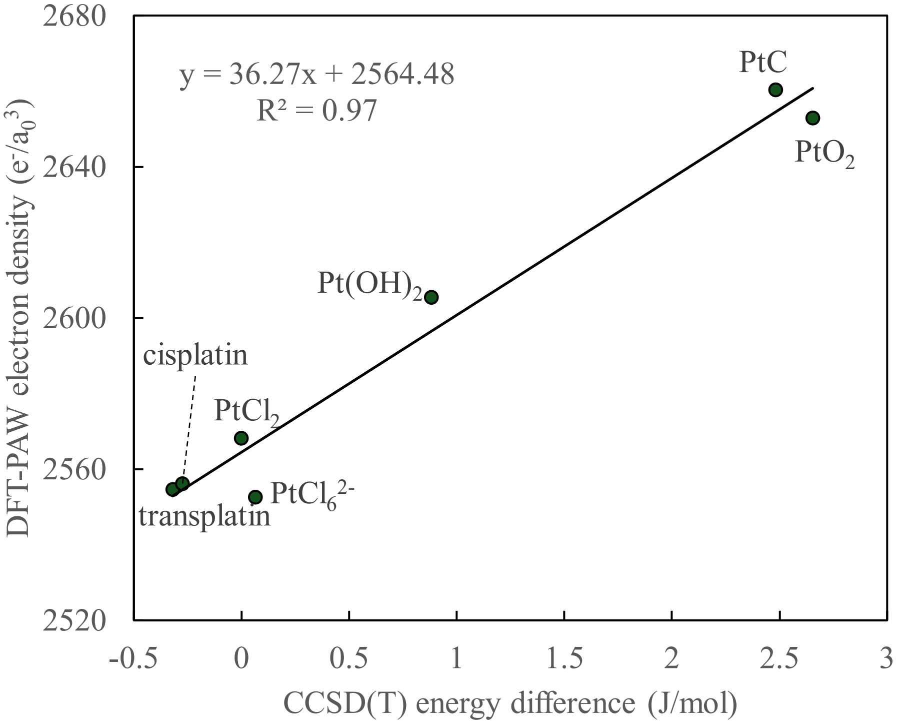

Figure 4-4: DFT-PAW electron density versus energy difference between ^{198}Pt and ^{194}Pt-bearing vapor-phase species, relative to $PtCl_2$ (v). This calibration line is used to estimate field shift energy differences for more complex molecular and crystalline species. The standard error of the slope is 2.83 e^-/a_0^3 per J/mol.

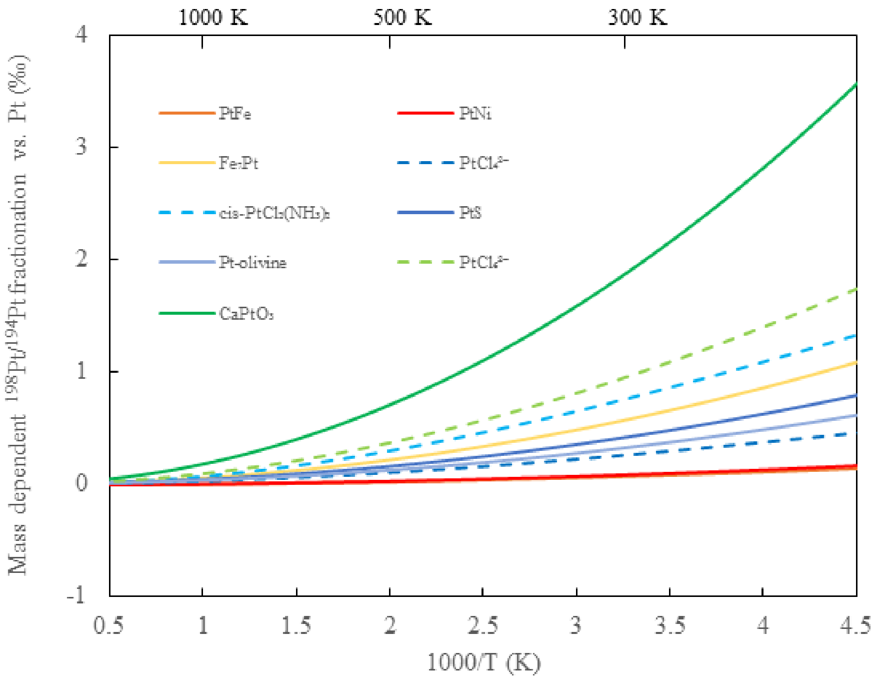

Figure 4-5: The mass dependent component of fractionation versus native Pt, plotted versus reciprocal temperature for select species from ~230 K to 2500 K. Solid lines indicate solid species, dashed lines indicate vapor phase models (including aqueous species). Green lines correspond to Pt^{4+}-bearing species, blue lines correspond to Pt^{2+}, and red/orange lines correspond to Pt^0.

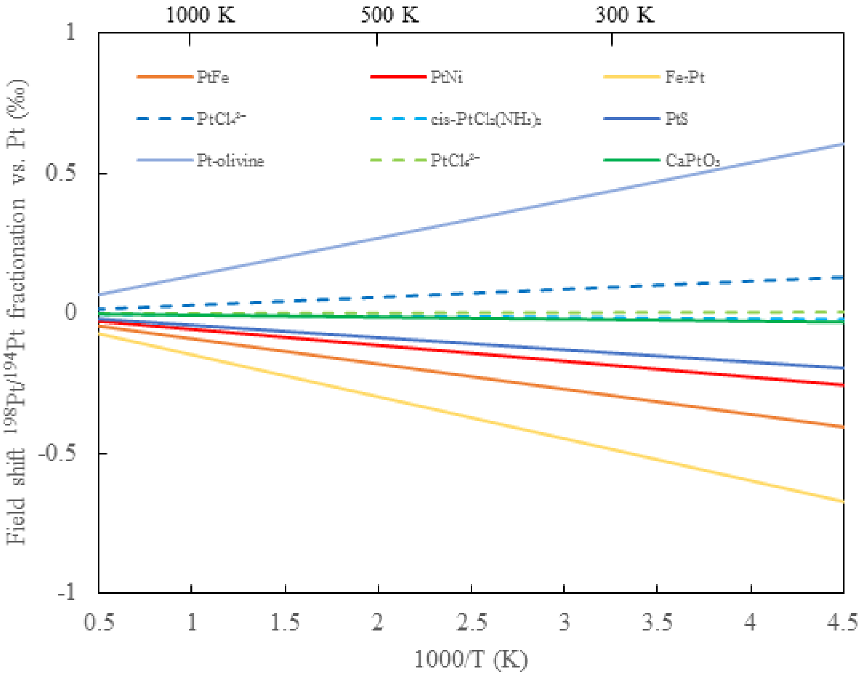

Figure 4-6: The field shift component of fractionation for select species versus native Pt versus reciprocal temperature, from ~230 K to 2500 K. Solid lines indicate solid species, dashed lines indicate vapor phase models (including aqueous species). Green lines correspond to Pt^{4+}-bearing species, blue lines correspond to Pt^{2+}, and red/orange lines correspond to Pt^0.

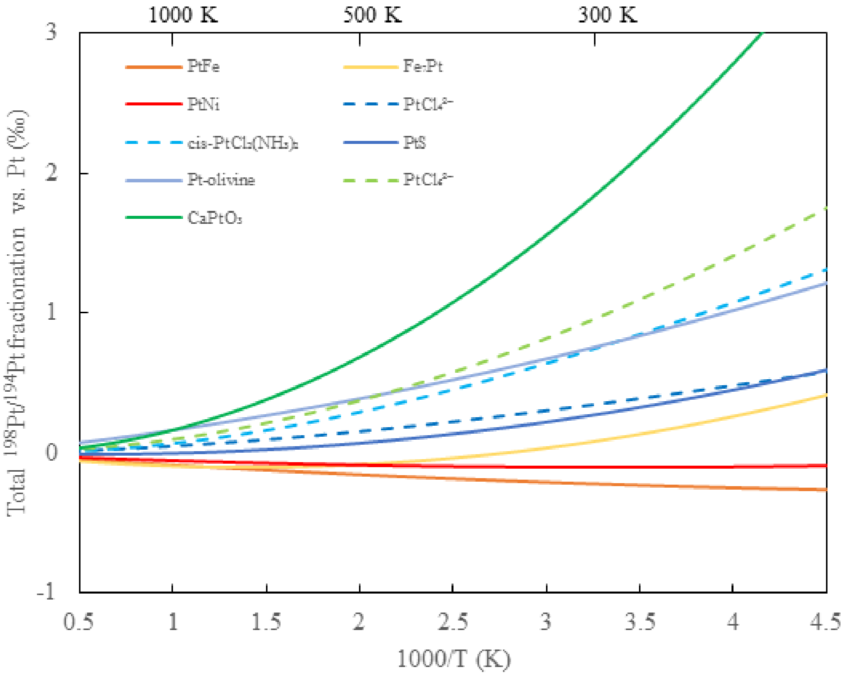

Figure 4-7: The total fractionation for select species versus native Pt versus reciprocal temperature, from ~230 K to 2500 K. Solid lines indicate solid species, dashed lines indicate vapor phase models (including aqueous species). Green lines correspond to Pt^{4+}-bearing species, blue lines correspond to Pt^{2+}, and red/orange lines correspond to Pt^0.

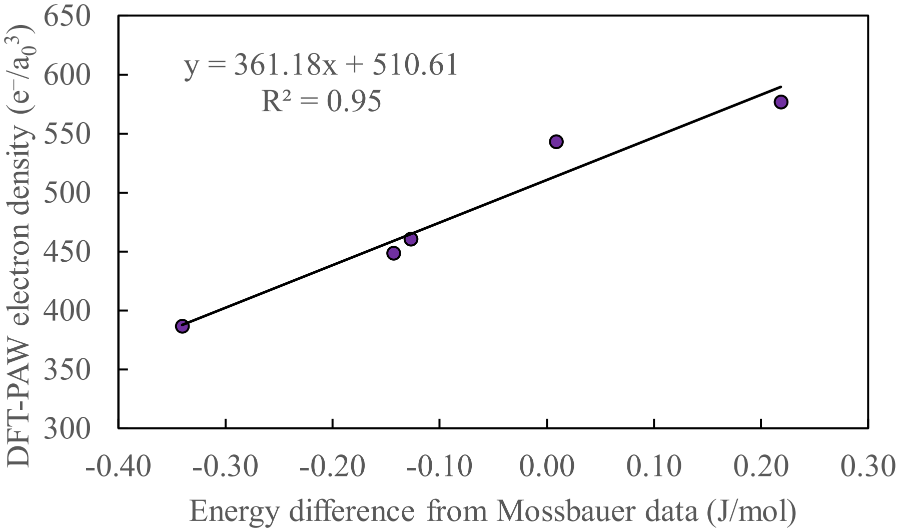

Figure 4-8: DFT-PAW electron densities versus the scaled ^{193}Ir/^{191}Ir energy difference relative to native Ir calculated via Mössbauer isomer shifts for iridium compounds as displayed in Table 4-6.

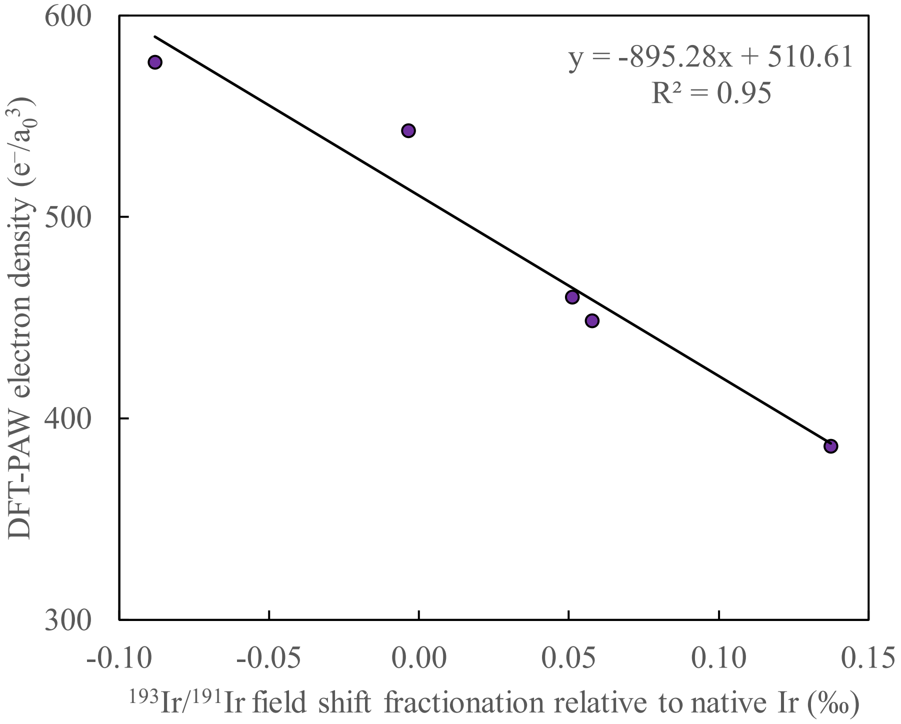

Figure 4-9: DFT-PAW electron densities versus field shift fractionations at 298 K for Ir-bearing solids as displayed in Table 4-6, calculated via Mössbauer isomer shifts according to the method of Schauble (2013; 2023).

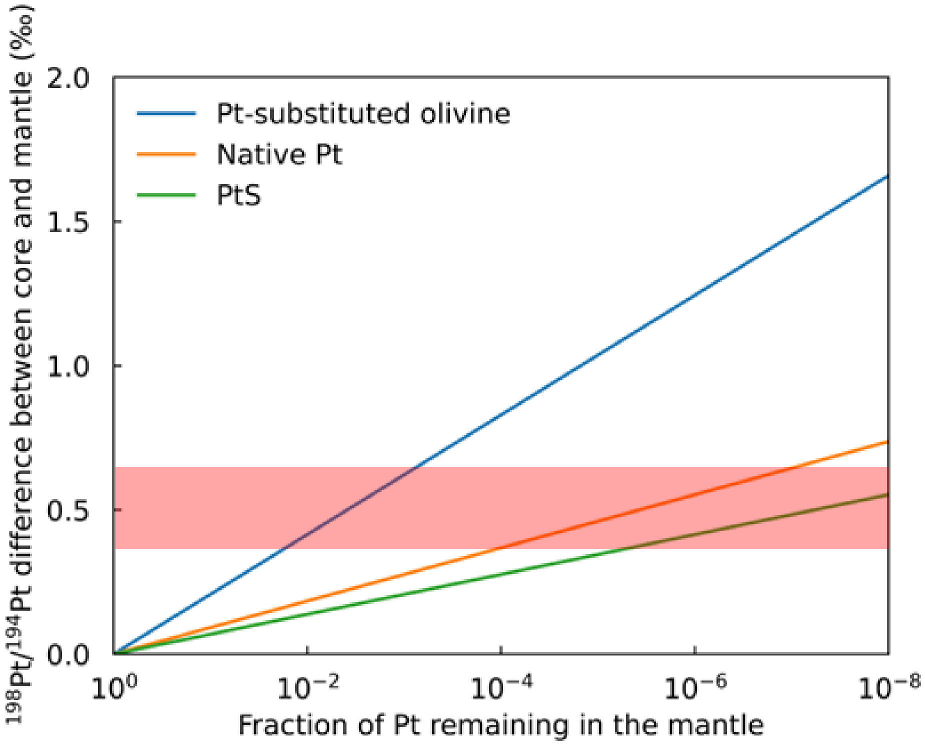

Figure 4-10: Rayleigh fractionation model for the solids Pt-substituted olivine, native Pt, and PtS fractionating relative to the species Fe_7Pt at 3000 K. The equilibrium fractionation factors for each species at this temperature are 0.09‰, 0.04‰, and 0.03‰ respectively. Shaded red area indicates composition of primitive Archean mantle from Creech et al. (2017).

References

Agresti D, Kankeleit E, Persson B (1967) Hyperfine Interaction and Isomeric Shift in Pt^{195}. Physical Review 155:1339. https://doi.org/10.1103/PhysRev.155.1339

Albarède F (2009) Geochemistry: an introduction. Cambridge University Press, Cambridge

Anbar AD, Wasserburg GJ, Papanastassiou DA, Andersson PS (1996) Iridium in Natural Waters. Science 273:1524–1528. https://doi.org/10.1126/science.273.5281.1524

Anders E, Grevesse N (1989) Abundances of the elements: Meteoritic and solar. Geochimica et Cosmochimica Acta 53:197–214. https://doi.org/10.1016/0016-7037(89)90286-X

Angeli I (2004) A consistent set of nuclear rms charge radii: properties of the radius surface R(N,Z). Atomic Data and Nuclear Data Tables 87:185–206. https://doi.org/10.1016/j.adt.2004.04.002

Angeli I, Marinova KP (2013) Table of experimental nuclear ground state charge radii: An update. Atomic Data and Nuclear Data Tables 99:69–95. https://doi.org/10.1016/j.adt.2011.12.006

Armytage RMG, Georg RB, Savage PS, et al (2011) Silicon isotopes in meteorites and planetary core formation. Geochimica et Cosmochimica Acta 75:3662–3676. https://doi.org/10.1016/j.gca.2011.03.044

Atzmony U, Bauminger ER, Lebenbaum D, et al (1967) Mössbauer Effect in Ir^{193} in Intermetallic Compounds and Salts of Iridium. Physical Review 163:314. https://doi.org/10.1103/physrev.163.314

Azaroual M, Romand B, Freyssinet P, Disnar J-R (2001) Solubility of platinum in aqueous solutions at 25 C and pHs 4 to 10 under oxidizing conditions. Geochimica et Cosmochimica Acta 65:4453–4466. https://doi.org/10.1016/S0016-7037(01)00752-9

Bayliss P (1990) Revised unit-cell dimensions, space group, and chemical formula of some metallic minerals. The Canadian Mineralogist 28:751–755

Beaton SA, Steimle TC (1999) Laser-induced fluorescence and Optical/Stark spectroscopy of PtC. The Journal of Chemical Physics 111:10876–10882. https://doi.org/10.1063/1.480452

Benczer-Koller N (1971) ^{195}Pt—A Survey of Mössbauer Spectroscopy. In: Platinum Group Metals and Compounds. American Chemical Society, pp 135–149

Bigeleisen J (1996) Nuclear Size and Shape Effects in Chemical Reactions. Isotope Chemistry of the Heavy Elements. J Am Chem Soc 118:3676–3680. https://doi.org/10.1021/ja954076k

Bigeleisen J, Mayer MG (1947) Calculation of Equilibrium Constants for Isotopic Exchange Reactions. The Journal of Chemical Physics 15:261–267. https://doi.org/10.1063/1.1746492

Błachowski A, Ruebenbauer K, Żukrowski J (2008) Spin- and charge density oscillations around Ir impurity in α-Fe studied by ^{57}Fe Mössbauer spectroscopy. Journal of Alloys and Compounds 464:13–17. https://doi.org/10.1016/j.jallcom.2007.09.133

Blöchl PE (1994) Projector augmented-wave method. Phys Rev B 50:17953–17979. https://doi.org/10.1103/PhysRevB.50.17953

Bolzan AA, Fong C, Kennedy BJ, Howard CJ (1997) Structural Studies of Rutile-Type Metal Dioxides. Acta Cryst B 53:373–380. https://doi.org/10.1107/S0108768197001468

Borisov A, Palme H, Spettel B (1994) Solubility of palladium in silicate melts: Implications for core formation in the Earth. Geochimica et Cosmochimica Acta 58:705–716. https://doi.org/10.1016/0016-7037(94)90500-2

Bostrom D (1987) Single-crystal X-ray diffraction studies of synthetic Ni-Mg olivine solid solutions. American Mineralogist 72:965–972

Brenan JM, McDonough WF (2009) Core formation and metal–silicate fractionation of osmium and iridium from gold. Nature Geosci 2:798–801. https://doi.org/10.1038/ngeo658

Brett R (1984) Chemical equilibration of the Earth's core and upper mantle. Geochimica et Cosmochimica Acta 48:1183–1188. https://doi.org/10.1016/0016-7037(84)90054-1

Bridgeman AJ (2008) Modeling the Vibronic Spectra of Transition Metal Complexes: The Ligand-Field Spectrum of $[PtCl_4]^{2-}$. Inorg Chem 47:4817–4825. https://doi.org/10.1021/ic800091y

Buchanan DL (1988) Current Platinum-Group Exploration Targets. SAE International, Warrendale, PA

Cabri L (1981) Platinum-Group Elements; Mineralogy, Geology, Recovery. The Canadian Institute of Mining and Metallurgy 267:

Cabri LJ, Wilson JMD, Distler VV, et al (2002) Mineralogical distribution of trace platinum-group elements in the disseminated sulphide ores of Noril'sk 1 layered intrusion. Applied Earth Science 111:15–22. https://doi.org/10.1179/aes.2002.111.1.15

Capobianco CJ, Jones JH, Drake MJ (1993) Metal-silicate thermochemistry at high temperature: Magma oceans and the "excess siderophile element" problem of the Earth's upper mantle. Journal of Geophysical Research: Planets 98:5433–5443. https://doi.org/10.1029/92JE02742

Carloni P, Andreoni W, Hutter J, et al (1995) Structure and bonding in cisplatin and other Pt (II) complexes. Chemical physics letters 234:50–56. https://doi.org/10.1016/0009-2614(94)01488-H

Chen X, Chu W, Wang L, Wu Z (2009) Geometry of Pt(IV) in H_2PtCl_6 aqueous solution: An X-ray absorption spectroscopic investigation. Journal of Molecular Structure 920:40–44. https://doi.org/10.1016/j.molstruc.2008.10.016

Chou C-L (1978) Fractionation of Siderophile Elements in the Earth's Upper Mantle. In: Proceedings of the 9th Lunar and Planetary Science Conference. Lunar and Planetary Institute, pp 219–230

Clarke FW (1920) The Data of Geochemistry. U.S. Government Printing Office, Washington, D.C.

Coll RK, Fergusson JE, Penfold BR, et al (1987) The Chloro and Bromo Complexes of Iridium(III) and Iridium(IV). III. The Crystal-Structures of $K_3[IrCl_6]$ and $Cs_2[IrCl_5H_2O]$ and

Interpretation of the N.Q.R. Data of Chloroiridates(III). Aust J Chem 40:2115–2122. https://doi.org/10.1071/ch9872115

Corcoran L (2016) Platinum stable isotope fractionation and adsorption on marine ferromanganese oxide substrates. Victoria University of Wellington

Cottrell E, Walker D (2006) Constraints on core formation from Pt partitioning in mafic silicate liquids at high temperatures. Geochimica et Cosmochimica Acta 70:1565–1580. https://doi.org/10.1016/j.gca.2005.11.021

Cottrell E, Walter MJ, Walker D (2009) Metal–silicate partitioning of tungsten at high pressure and temperature: Implications for equilibrium core formation in Earth. Earth and Planetary Science Letters 281:275–287. https://doi.org/10.1016/j.epsl.2009.02.024

Creech J, Baker J, Handler M, et al (2013) Platinum stable isotope ratio measurements by double-spike multiple collector ICPMS. Journal of Analytical Atomic Spectrometry 28:853–865. https://doi.org/10.1039/C3JA50022E

Creech JB, Baker JA, Handler MR, et al (2017) Late accretion history of the terrestrial planets inferred from platinum stable isotopes. Geochem Perspect Lett 3:94–104. https://doi.org/10.7185/geochemlet.1710

Creech JB, Baker JA, Handler MR, Bizzarro M (2014) Platinum stable isotope analysis of geological standard reference materials by double-spike MC-ICPMS. Chemical Geology 363:293–300. https://doi.org/10.1016/j.chemgeo.2013.11.009

Dauphas N, Marty B (2002) Inference on the nature and the mass of Earth's late veneer from noble metals and gases. Journal of Geophysical Research: Planets 107:12-1-12–7. https://doi.org/10.1029/2001JE001617

Day JMD, Brandon AD, Walker RJ (2016) Highly Siderophile Elements in Earth, Mars, the Moon, and Asteroids. Reviews in Mineralogy and Geochemistry 81:161–238. https://doi.org/10.2138/rmg.2016.81.04

Deeth RJ, Elding LI (1996) Theoretical Modeling of Water Exchange on $[Pd(H_2O)_4]^{2+}$, $[Pt(H_2O)_4]^{2+}$, and trans-$[PtCl_2(H_2O)_2]$. Inorg Chem 35:5019–5026. https://doi.org/10.1021/ic950335v

D'Orazio M, Folco L (2003) Chemical Analysis of Iron Meteorites by Inductively Coupled Plasma-Mass Spectrometry. Geostandards Newsletter 27:215–225. https://doi.org/10.1111/j.1751-908X.2003.tb00723.x

Dubiel SM (1988) Platinum-induced changes in the electronic structure of iron. Phys Rev B 37:1429–1434. https://doi.org/10.1103/PhysRevB.37.1429

Dunning TH Jr (1989) Gaussian basis sets for use in correlated molecular calculations. I. The atoms boron through neon and hydrogen. The Journal of Chemical Physics 90:1007–1023. https://doi.org/10.1063/1.456153

Dyall KG (2007) Relativistic double-zeta, triple-zeta, and quadruple-zeta basis sets for the actinides Ac–Lr. Theor Chem Acc 117:491–500. https://doi.org/10.1007/s00214-006-0175-4

Ertel W, Walter MJ, Drake MJ, Sylvester PJ (2006) Experimental study of platinum solubility in silicate melt to 14GPa and 2273K: Implications for accretion and core formation in Earth. Geochimica et Cosmochimica Acta 70:2591–2602. https://doi.org/10.1016/j.gca.2006.02.015

Farges F, Neuville DR, Brown GE (1999) Structural investigation of platinum solubility in silicate glasses. American Mineralogist 84:1562–1568. https://doi.org/10.2138/am-1999-1009

Feller D (1996) The role of databases in support of computational chemistry calculations. Journal of Computational Chemistry 17:1571–1586. https://doi.org/10.1002/(SICI)1096-987X(199610)17:13<1571::AID-JCC9>3.0.CO;2-P

Fitoussi C, Bourdon B, Kleine T, et al (2009) Si isotope systematics of meteorites and terrestrial peridotites: implications for Mg/Si fractionation in the solar nebula and for Si in the Earth's core. Earth and Planetary Science Letters 287:77–85. https://doi.org/10.1016/j.epsl.2009.07.038

Fortenfant SS, Günther D, Dingwell DB, Rubie DC (2003) Temperature dependence of Pt and Rh solubilities in a haplobasaltic melt. Geochimica et Cosmochimica Acta 67:123–131. https://doi.org/10.1016/S0016-7037(02)01047-5

Fricke G, Heilig K (2004) 78-Pt Platinum. In: Schopper H (ed) Nuclear Charge Radii. Springer-Verlag, Berlin/Heidelberg, pp 1–6

Frisch MJ, Trucks GW, Schlegel HB, et al (2009) Gaussian 09: Programmer's Reference. Gaussian Inc., Wallingford, CT

Furuseth S, Selte K, Kjekshus A, et al (1965) Redetermined Crystal Structures of $PdAs_2$, $PdSb_2$, PtP_2, $PtAs_2$, $PtSb_2$, alpha-$PtBi_2$, and $AuSb_2$. Acta Chemica Scandinavica 19:735–741. https://doi.org/10.3891/acta.chem.scand.19-0735

Georg RB, Halliday AN, Schauble EA, Reynolds BC (2007) Silicon in the Earth's core. Nature 447:1102–1106. https://doi.org/10.1038/nature05927

Gonze X, Amadon B, Anglade P-M, et al (2009) ABINIT: First-principles approach to material and nanosystem properties. Computer Physics Communications 180:2582–2615. https://doi.org/10.1016/j.cpc.2009.07.007

Grevesse N, Sauval AJ (1998) Standard Solar Composition. Space Science Reviews 85:161–174. https://doi.org/10.1023/A:1005161325181

Griffiths JHE, Owen J, Park JG, et al (1959) Exchange interactions in antiferromagnetic salts of iridium. I. Paramagnetic resonance experiments. Proceedings of the Royal Society of London Series A Mathematical and Physical Sciences 250:84–96. https://doi.org/10.1098/rspa.1959.0052

Hagen JC (1954) Some Aspects of the Geochemistry of Platinum, Palladium and Gold in Igneous Rocks with Special Reference to the Bushveld Complex, Transvaal. Massachusettes Institute of Technology

Hartmann WK, Ryder G, Dones L, Grinspoon D (2000) The time-dependent intense bombardment of the primordial Earth/Moon system. Origin of the Earth and Moon 1:493–512. https://doi.org/10.2307/j.ctv1v7zdrp.31

Helmy HM, Ballhaus C, Fonseca ROC, Leitzke FP (2020) Concentrations of Pt, Pd, S, As, Se and Te in silicate melts at sulfide, arsenide, selenide and telluride saturation: evidence of PGE complexing in silicate melts? Contrib Mineral Petrol 175:65. https://doi.org/10.1007/s00410-020-01705-0

Hin RC, Burkhardt C, Schmidt MW, et al (2013) Experimental evidence for Mo isotope fractionation between metal and silicate liquids. Earth and Planetary Science Letters 379:38–48. https://doi.org/10.1016/j.epsl.2013.08.003

Holzheid A, Sylvester P, O'Neill HSC, et al (2000) Evidence for a late chondritic veneer in the Earth's mantle from high-pressure partitioning of palladium and platinum. Nature 406:396–399. https://doi.org/10.1038/35019050

Jagoutz E, Palme H, Blum K, et al (1979) The abundances of major, minor and trace elements in the earth's mantle as derived from primitive ultramafic nodules. In: Lunar and Planetary Science Conference. Lunar and Planetary Institute, pp 2031–2050

Jain A, Ong SP, Hautier G, et al (2013) Commentary: The Materials Project: A materials genome approach to accelerating materials innovation. APL Materials 1:011002. https://doi.org/10.1063/1.4812323

Jollet F, Torrent M, Holzwarth N (2014) Generation of Projector Augmented-Wave atomic data: A 71 element validated table in the XML format. Computer Physics Communications 185:1246–1254. https://doi.org/10.1016/j.cpc.2013.12.023

Kimura K, Lewis RS, Anders E (1974) Distribution of gold and rhenium between nickel-iron and silicate melts: implications for the abundance of siderophile elements on the Earth and Moon. Geochimica et Cosmochimica Acta 38:683–701. https://doi.org/10.1016/0016-7037(74)90144-6

Kleine T (2011) Earth's patchy late veneer. Nature 477:168–169. https://doi.org/10.1038/477168a

Kroening RF, Rush RM, Martin DS, Clardy JC (1974) Polarized crystal absorption spectra and crystal structure for potassium tetrabromoplatinate (II). Inorganic Chemistry 13:1366–1373. https://doi.org/10.1021/ic50136a024

Labidi J, Cartigny P, Moreira M (2013) Non-chondritic sulphur isotope composition of the terrestrial mantle. Nature 501:208–211. https://doi.org/10.1038/nature12490

Li J, Agee CB (2001) The effect of pressure, temperature, oxygen fugacity and composition on partitioning of nickel and cobalt between liquid Fe-Ni-S alloy and liquid silicate: implications for the earth's core formation. Geochimica et Cosmochimica Acta 65:1821–1832. https://doi.org/10.1016/S0016-7037(00)00613-X

Li Q, Chen Z, Zheng X, Jin Z (1992) Study of photoreduction of hexachloroplatinate (2-) on cadmium sulfide. The Journal of Physical Chemistry 96:5959–5962. https://doi.org/10.1021/j100193a057

Liu W, Peng D (2009) Exact two-component Hamiltonians revisited. The Journal of Chemical Physics 131:031104. https://doi.org/10.1063/1.3159445

Lorand J-P, Alard O, Luguet A (2010) Platinum-group element micronuggets and refertilization process in Lherz orogenic peridotite (northeastern Pyrenees, France). Earth and Planetary Science Letters 289:298–310. https://doi.org/10.1016/j.epsl.2009.11.017

Lu S-J, Wang K (2024) Structural and bonding analysis of PtO_2^- anion and neutral clusters. Journal of Molecular Structure 1301:137432. https://doi.org/10.1016/j.molstruc.2023.137432

Lu Y, Tsegaw YA, Wodyński A, et al (2022) Investigation of Molecular Iridium Fluorides IrF_n (n=1–6): A Combined Matrix-Isolation and Quantum-Chemical Study. Chemistry – A European Journal 28:e202104005. https://doi.org/10.1002/chem.202104005

Macdonald AJ (1987) Ore Deposit Models #12. The Platinum Group Element Deposits: Classification and Genesis. Geoscience Canada 14:155–166

Mann U, Frost DJ, Rubie DC, et al (2012) Partitioning of Ru, Rh, Pd, Re, Ir and Pt between liquid metal and silicate at high pressures and high temperatures - Implications for the origin of highly siderophile element concentrations in the Earth's mantle. Geochimica et Cosmochimica Acta 84:593–613. https://doi.org/10.1016/j.gca.2012.01.026

McDonough WF (2003) Compositional Model for the Earth's Core. Treatise on Geochemistry 2:568. https://doi.org/10.1016/B0-08-043751-6/02015-6

Méheut M, Lazzeri M, Balan E, Mauri F (2007) Equilibrium isotopic fractionation in the kaolinite, quartz, water system: Prediction from first-principles density-functional theory. Geochimica et Cosmochimica Acta 71:3170–3181. https://doi.org/10.1016/j.gca.2007.04.012

Mkhonto PP, Ngoepe PE (2022) Reconstruction of Cooperite (PtS) Surfaces: A DFT-D+U Study. ACS Omega 7:43390–43410. https://doi.org/10.1021/acsomega.2c02867

Mondal SK (2011) Platinum group element (PGE) geochemistry to understand the chemical evolution of the Earth's mantle. J Geol Soc India 77:295–302. https://doi.org/10.1007/s12594-011-0039-y

Mössbauer RL, Lengsfeld M, Lieres WV, et al (1971) Nuclear Gamma Resonance Study of the Ir —Fe and Ir —Ni Alloy Systems. Zeitschrift für Naturforschung A 26:343–352. https://doi.org/10.1515/zna-1971-0303

Moynier F, Yin Q-Z, Schauble E (2011) Isotopic Evidence of Cr Partitioning into Earth's Core. Science 331:1417–1420. https://doi.org/10.1126/science.1199597

Muller O, Roy R (1968) Formation and stability of the platinum and rhodium oxides at high oxygen pressures and the structures of Pt_3O_4, β-PtO_2 and RhO_2. Journal of the Less Common Metals 16:129–146. https://doi.org/10.1016/0022-5088(68)90070-2

Murthy VR (1991) Early differentiation of the Earth and the problem of mantle siderophile elements: a new approach. Science 253:303–306. https://doi.org/10.1126/science.253.5017.303

Nadjakov EG, Marinova KP, Gangrsky YP (1994) Systematics of Nuclear Charge Radii. Atomic Data and Nuclear Data Tables 56:133–157. https://doi.org/10.1006/adnd.1994.1004

Ohgushi K, Matsushita Y, Miyajima N, et al (2008) $CaPtO_3$ as a novel post-perovskite oxide. Phys Chem Minerals 35:189–195. https://doi.org/10.1007/s00269-007-0211-5

Ohtani E, Yurimoto H, Seto S (1997) Element partitioning between metallic liquid, silicate liquid, and lower-mantle minerals: implications for core formation of the Earth. Physics of the Earth and Planetary Interiors 100:97–114. https://doi.org/10.1016/S0031-9201(96)03234-7

Parker SF, Forsyth JB (1998) K_2MCl_6 (M=Pt, Ir), location of the silent modes and forcefields. Journal of the Chemical Society, Faraday Transactions 94:1111–1114. https://doi.org/10.1039/A709215F

Perdew JP, Burke K, Ernzerhof M (1996) Generalized Gradient Approximation Made Simple. Phys Rev Lett 77:3865–3868. https://doi.org/10.1103/PhysRevLett.77.3865

Petaev MI, Jacobsen SB (2004) Differentiation of metal-rich meteoritic parent bodies: I. Measurements of PGEs, Re, Mo, W, and Au in meteoritic Fe-Ni metal. Meteoritics & Planetary Science 39:1685–1697. https://doi.org/10.1111/j.1945-5100.2004.tb00066.x

Pritchard BP, Altarawy D, Didier B, et al (2019) New Basis Set Exchange: An Open, Up-to-Date Resource for the Molecular Sciences Community. J Chem Inf Model 59:4814–4820. https://doi.org/10.1021/acs.jcim.9b00725

Righter K (2003) Metal-Silicate Partitioning of Siderophile Elements and Core Formation in the Early Earth. Annual Review of Earth and Planetary Sciences 31:135–174. https://doi.org/10.1146/annurev.earth.31.100901.145451

Righter K, Drake MJ (2003) Partition coefficients at high pressure and temperature. Treatise on geochemistry 2:568. https://doi.org/10.1016/B0-08-043751-6/02010-7

Righter K, Humayun M, Danielson L (2008) Partitioning of palladium at high pressures and temperatures during core formation. Nature Geosci 1:321–323. https://doi.org/10.1038/ngeo180

Ringwood AE (1966) Chemical evolution of the terrestrial planets. Geochimica et Cosmochimica Acta 30:41–104. https://doi.org/10.1016/0016-7037(66)90090-1

Ringwood AE (1977) Composition of the core and implications for origin of the earth. Geochemical Journal 11:111–135. https://doi.org/10.2343/geochemj.11.111

Rozhdestvina VI, Ivanov AV, Zaremba MA, et al (2008) Single-Crystalline cooperite (PtS): Crystal-Chemical characterization, ESR spectroscopy, and ^{195}Pt NMR spectroscopy. Crystallogr Rep 53:391–397. https://doi.org/10.1134/S106377450803005X

Saue T (2011) Relativistic Hamiltonians for Chemistry: A Primer. ChemPhysChem 12:3077–3094. https://doi.org/10.1002/cphc.201100682

Saue T, Visscher L, Jensen HA, et al (2011) DIRAC, a relativistic ab initio electronic structure program, release DIRAC10

Schauble EA (2013) Modeling nuclear volume isotope effects in crystals. PNAS 110:17714–17719. https://doi.org/10.1073/pnas.1216216110

Schauble EA, Ghosh P, Eiler JM (2006) Preferential formation of ^{13}C–^{18}O bonds in carbonate minerals, estimated using first-principles lattice dynamics. Geochimica et Cosmochimica Acta 70:2510–2529. https://doi.org/10.1016/j.gca.2006.02.011

Schauble EA, Young ED (2021) Mass Dependence of Equilibrium Oxygen Isotope Fractionation in Carbonate, Nitrate, Oxide, Perchlorate, Phosphate, Silicate, and Sulfate Minerals. Reviews in Mineralogy and Geochemistry 86:137–178. https://doi.org/10.2138/rmg.2021.86.04

Schuchardt KL, Didier BT, Elsethagen T, et al (2007) Basis Set Exchange: A Community Database for Computational Sciences. J Chem Inf Model 47:1045–1052. https://doi.org/10.1021/ci600510j

Shahar A, Ziegler K, Young ED, et al (2009) Experimentally determined Si isotope fractionation between silicate and Fe metal and implications for Earth's core formation. Earth and Planetary Science Letters 288:228–234. https://doi.org/10.1016/j.epsl.2009.09.025

Tagirov BR, Filimonova ON, Trigub AL, et al (2019) Platinum transport in chloride-bearing fluids and melts: Insights from in situ X-ray absorption spectroscopy and thermodynamic modeling. Geochimica et Cosmochimica Acta 254:86–101. https://doi.org/10.1016/j.gca.2019.03.023

Taylor SR (2001) Solar System Evolution: A New Perspective. Cambridge University Press

Tera F, Papanastassiou DA, Wasserburg GJ (1974) Isotopic evidence for a terminal lunar cataclysm. Earth and Planetary Science Letters 22:1–21. https://doi.org/10.1016/0012-821X(74)90059-4

Torrent M, Jollet F, Bottin F, et al (2008) Implementation of the projector augmented-wave method in the ABINIT code: Application to the study of iron under pressure. Computational Materials Science 42:337–351. https://doi.org/10.1016/j.commatsci.2007.07.020

Treviño A, Ermler WC (2023) Environmental considerations in ab initio calculations of electronic states of $PtCl_4^{-2}$ complexes. The Journal of Chemical Physics 158:024304. https://doi.org/10.1063/5.0113097

Wagner F, Klöckner J, Körner HJ, et al (1967) Isomer shift and quadrupole splitting in ^{191}Ir and ^{193}Ir. Physics Letters B 25:253–255. https://doi.org/10.1016/0370-2693(67)90002-0

Wagner F, Zahn U (1970) Mössbauer isomer shifts, hyperfine interactions, and magnetic hyperfine anomalies in compounds of iridium. Zeitschrift für Physik 233:1–20. https://doi.org/10.1007/bf01396512

Wagner FE, Karger M, Seiderer M, Wortmann G (1977) Change of the mean square nuclear charge radius for the $2^+–0^+$ transitions in ^{178}Hf, ^{182}W, and ^{186}Os. AIP Conference Proceedings 38:13–22. https://doi.org/10.1063/1.31062

Walker RJ (2009) Highly siderophile elements in the Earth, Moon and Mars: Update and implications for planetary accretion and differentiation. Geochemistry 69:101–125. https://doi.org/10.1016/j.chemer.2008.10.001

Walker RJ, Horan MF, Shearer CK, Papike JJ (2004) Low abundances of highly siderophile elements in the lunar mantle: evidence for prolonged late accretion. Earth and Planetary Science Letters 224:399–413. https://doi.org/10.1016/j.epsl.2004.05.036

Weigend F, Ahlrichs R (2005) Balanced basis sets of split valence, triple zeta valence and quadruple zeta valence quality for H to Rn: Design and assessment of accuracy. Phys Chem Chem Phys 7:3297–3305. https://doi.org/10.1039/B508541A

Wetherill GW (1975) Late heavy bombardment of the moon and terrestrial planets. In: Lunar Science Conference. Pergamon Press, Inc., Houston, Texas, pp 1539–1561

Widanagamage IH, Schauble EA, Scher HD, Griffith EM (2014) Stable strontium isotope fractionation in synthetic barite. Geochimica et Cosmochimica Acta 147:58–75. https://doi.org/10.1016/j.gca.2014.10.004

Wilburn DR, Bassett WA (1978) Hydrostatic compression of iron and related compounds; an overview. American Mineralogist 63:591–596

Wolbeck B, Zioutas K (1972) The g-factor of the 130 keV state in ^{195}Pt measured by the Mössbauer effect. Nuclear Physics A 181:289–297. https://doi.org/10.1016/0375-9474(72)90921-9

Wood BJ, Walter MJ, Wade J (2006) Accretion of the Earth and segregation of its core. Nature 441:825–833. https://doi.org/10.1038/nature04763

Woon DE, Dunning TH Jr (1993) Gaussian basis sets for use in correlated molecular calculations. III. The atoms aluminum through argon. The Journal of Chemical Physics 98:1358–1371. https://doi.org/10.1063/1.464303

Zhu Z, Meija J, Zheng A, et al (2017) Determination of the Isotopic Composition of Iridium Using Multicollector-ICPMS. Anal Chem 89:9375–9382. https://doi.org/10.1021/acs.analchem.7b02206

Zwanziger JW (2009) Computation of Mössbauer isomer shifts from first principles. J Phys: Condens Matter 21:195501. https://doi.org/10.1088/0953-8984/21/19/195501